SERVICEABILITY AND POST-FAILURE BEHAVIOUR OF LAMINATED GLASS STRUCTURAL ELEMENTS

Dissertation

submitted to and approved by the

Department of Architecture, Civil Engineering and Environmental Sciences
University of Braunschweig – Institute of Technology

and the

Department of Civil and Environmental Engineering
University of Florence

in candidacy for the degree of a
Doktor-Ingenieur (Dr.-Ing.) /
Dottore di Ricerca in Civil and Environmental Engineering[*)]

by

Lorenzo Ruggero Piscitelli
born 8 March 1986
from Bagno a Ripoli, Italia

Submitted on	20 February, 2018
Oral examination on	8 May 2018
Professorial advisors	Prof. Harald Kloft Prof. Maurizio Orlando Prof. Giovanna Ranocchiai

2019

*) Either the German or the Italian form of the title may be used.

Dottorato di ricerca in Civil and Environmental Engineering

Ciclo XXX, novembre 2014 - Ottobre 2017

Settore Scientifico Disciplinare ICAR/09

Dott. Lorenzo Ruggero Piscitelli

Tutor:

Prof. Maurizio Orlando

Prof. Harald Kloft

Prof. Giovanna Ranocchiai

Coordinatore del dottorato:

Prof. Fabio Castelli

Acknowledgements:

These pages are the result of a long time combined effort of many individuals. Perhaps, some of them are unaware of the significance and impact of their contributions on my work and education as a whole; it is now a privilege for me to release my feelings of profound gratitude to all of them.

To Prof. Orlando, "Maurizio", as you invited me to call you since day one, for the abiding support, advices and guidance. You've been the driver of my academic experience since 2009, I could never have wished for a better mentor.

To Prof. Giovanna Ranocchiai, for all the essential contributions to this work, for the time you always found to help me when I needed the most and for your unfailing assistance.

To Prof. Harald Kloft for the interest you showed immediately on this topic and your support during the many months spent at the ITE in Braunschweig.

To Marco Casucci for being the best co-worker a Ph. D student could ever dream for: curious, proactive, exceptionally resourceful and totally dedicated. I hope our paths may cross again very soon.

To Saverio Giordano, for sharing a lifetime of experience over the last… many years! I will try to treasure and put to good use everything that you left me.

To Enzo Barlacchi and Franco Bruni, for always going the extra mile for me; I look forward to working again side by side with the both of you.

To the research team in Milano: Prof. Luigi Biolzi for your precious guidance; to Prof. Sara Cattaneo for having me constantly involved in absolutely anything exciting taking place and for going above and beyond in supporting my work; to Gabriele D'Incertopadre and Luca Marini, for the precious help throughout many months of tests and data analysis; to Nicola Piazzolla and Daniele Spinelli for the joyful moments and their priceless assistance in the everyday life of the laboratory.

Also, my work would not have been possible without the precious contributions and support of many colleagues: Antonino "Ninni" Marra, Tommaso Massai, Andrea Giachetti, Enzo Marino, Luca Salvatori, Alessandro Giusti and Luca Pigolotti. There is an inestimable value in knowing that you can always find the right answer at the right time, I am grateful for all your help and suggestions.

Thank you my dearest friends, you know who you are, I'm blessed to count you on both hands. Thank you to my family, thank you "Nonna", for teaching me the respect for other people's work, the value of collaboration over competition, the importance of taking the time for a break when things get tense, for sitting together to share a meal… and five more minutes for a coffee.

"What do we mean by "understanding" something?

We can imagine that this complicated array of moving things which constitutes "the world" is something like a great chess game being played by the gods, and we are observers of the game. We do not know what the rules of the game are; all we are allowed to do is to watch the playing. Of course, if we watch long enough, we may eventually catch on to a few of the rules. The rules of the game are what we mean by fundamental physics. Even if we knew every rule, however, we might not be able to understand why a particular move is made in the game, merely because it is too complicated and our minds are limited. If you play chess you must know that it is easy to learn all the rules, and yet it is often very hard to select the best move or to understand why a player moves as he does.

So it is in nature, only much more so." [1]

Richard Phillips Feynman [2]

[1] Basic Physics, volume I; lecture 2, Introduction published by Jeffrey Robbins in "*The Value of Science*", part of the National Academy of Sciences.

[2] Richard Phillips Feynman, New York on the 11 May 1918, Los Angeles 15 February 1988, American physicist, Nobel prize in physics 1965. To the exceptional skills in many physics and science fields, he combined a sense of humour out of the ordinary, the passion for music and arts. He defined himself as a "Nobelist Physicist, teacher, storyteller, bongo player".

INDEX

ABSTRACT (GER)

Infolge des wachsenden Architekturtrends zu Licht und Transparenz, werden tragende Verbundglasselemente im Bauwesen immer öfter verwendet. Nichtsdestoweniger, zeigt eine Analyse des rechtlichen und wissenschaftlichen Stands der Technik einige Fachgebiete auf, die von gründlicher Forschung Nutzen ziehen könnten. Namentlich Eigenschaften von Plastik, innerhalb eines Scheibenpaars als Schicht verwendet, sind aus den bereits angeführten Gründen bisher kaum untersucht, Professionelle sind weit von einstimmigen und verlässlichen Techniken entfernt, um verschiedene Materialien zu vergleichen. Allerdings wird dieses Wissen, für verlässliches Design insbesondere im Baubereich, gebraucht.

Dieses Manuskript stellt die Ergebnisse einer experimentellen Multiskalenforschung für eine mechanische Reaktion von drei Zwischenschichten: PVC, SG und DG41 vor. Ersteres war der Standard in der Glaslaminierungsindustrie, während die beiden letzteren jünger sind und angeblich eine höhere Leistung in mechanischer Hinsicht aufweisen. Das hyperelastische Verhalten wird mit einfachen Zugversuchen an Zwischenschichtproben untersucht; am Ende wird ein neuartiges verallgemeinertes Reaktionsmodell vorgeschlagen, das so abgestimmt werden kann, dass es die komplexe Kurzzeit- und Enddehnungsreaktion eines beliebigen Thermoplasten mit wenigen Koeffizienten repliziert. Auch viskoelastische Parameter von Zwischenschichten spielen eine wesentliche Rolle bei der globalen Reaktion auf langfristige Verbundglaselemente. Das temperaturabhängige viskoelastische Problem wird in größerem Umfang mit Hilfe von Doppelschlag-Verbundglasverbindungen unter Druckbelastung untersucht. Es wurden Tests an Proben aus drei Glasschichten unter langzeitigen Einwirkungen in einem Temperaturbereich zwischen 0°C und 60°C durchgeführt. Ein bestehendes Verfahren wurde weiterentwickelt, um Erkenntnisse über die Kriech- und Relaxationseigenschaften zu gewinnen. Schließlich werden kalibrierte Prony-Reihen für viskoelastische Modelle zusammen mit Williams Landel Ferry-Koeffizienten für die Zeit-Temperatur-Überlagerung bereitgestellt, um die viskoelastischen Reaktionen der drei Zwischenschichtmaterialien bei beliebigen Temperaturen zu modellieren. Grenzen und Zuverlässigkeit solcher Modelle werden diskutiert; vereinfachte und gebrauchsfertige Tabellen werden bereitgestellt. Es wird eine Analyse des Zusammenhangs zwischen mechanischen Einwirkungen und dem Verlust der Haftung durchgeführt.

Die dritte Ebene der experimentellen Analysen untersucht das mechanische Verhalten von progressiv beschädigten, vollflächigen Verbundglasträgern. Risikoanalysen und anschließende ausfallsichere Konstruktionen werden oft in Normen und technischen Unterlagen erwähnt, aber es wurden nur wenige Studien über die Leistung nach dem Versagen und den Auswirkungen von Verbundträgern aus gehärteten Glasscheiben durchgeführt. Nach einem Teilversagen hängt die Tragfähigkeit von der Fähigkeit der Zwischenschicht ab, Kopplungseffekte zwischen gebrochenen und unbeschädigten Glaselementen durch Haftung und eigene mechanische Eigenschaften zu erzeugen. Ergebnisse aus dynamischen und statischen Tests werden verglichen und die spannungssteifende Wirkung von Zwischenschichten in teilweise beschädigten Elementen untersucht. Eine äquivalente thermische Ausdehnung wird vorgeschlagen, um die Wechselwirkungen zu modellieren, die zwischen gebrochenen und intakten Lagen im Falle eines Teilausfalls auftreten. Weitere Tests wurden unter völlig beschädigten Bedingungen durchgeführt, um die Resttragfähigkeit und die Auswirkungen der Alterung dieser Bedingungen zu bewerten. Es werden einachsige Zug- und Druckprüfungen an vollständig beschädigten Verbundglasproben durchgeführt. Die Ergebnisse werden verwendet, um das Verhalten von vollständig beschädigten Trägern zu modellieren.

Im letzten Teil des Manuskripts werden Anwendungsbeispiele für neu gefundene Ergebnisse in möglichen Verbundglaskonstruktionen verwendet: Anwendungen für Kaltbiegeverfahren und Sicherheitsbewertungen nach einem Versagen werden bereitgestellt.

ABSTRACT

Structural laminated glass elements are being used ever more frequently in the construction industry, following a growing architectural trend that looks for light and transparency. Nevertheless, an analysis of both regulatory and scientific state-of-the-art reveals several fields of inquiry which could benefit from deeper investigations. Namely, properties of plastics used as interlayer materials within the glass plies are scarcely investigated, professionals being far from unanimous on reliable techniques for comparing different materials on the same grounds. Yet, such knowledge is needed for reliable designs, especially in structural applications.

This manuscript presents the results of a multi-scale experimental research on the mechanical response of three interlayers: PVB, SG and DG41. The former has been the standard in glass lamination industry, while the latter two are more recent and supposedly more performing from a mechanical point of view. The hyperelastic behaviour is studied with simple tensile tests on interlayer specimens; in the end, a novel generalized response model is proposed, which can be tuned to replicate the complex short-term and finite-strain response of any thermoplastic using few coefficients. Also, viscoelastic parameters of interlayers play an essential role in the global long-term laminated glass elements response. The temperature-dependent viscoelastic problem is investigated on a larger scale, using double-lap laminated glass joints under compressive loadings. Tests were performed on specimens made of three glass plies under long-term imposed actions in a temperature range between 0℃ and 60℃. An existing procedure was further developed, to provide insight on both creep and relaxation properties. Finally, calibrated Prony series for viscoelastic models are provided together with Williams Landel Ferry coefficients for time-temperature superposition, allowing to model the viscoelastic responses of the three interlayer materials at arbitrary temperatures. Limits and reliability of such models are discussed; simplified and ready-to use tables are provided. An analysis on the correlation between mechanical actions and loss of adhesion is performed.

The third-level of the experimental analyses investigates the mechanical behaviour of progressively damaged, full-scale laminated glass beams. *Risk analyses* followed by *fail-safe* designs are often mentioned by standards and technical documents, but few studies have been carried out on the post-failure performance and effects of laminated beams made with tempered glass plies. After partial failure, the load-bearing capacity depends on the interlayers ability to generate coupling effects among fractured and undamaged glass elements through adhesion and its own mechanical properties. Results from dynamic and static tests are compared and the *tension stiffening* effect of interlayers in partially damaged elements is investigated. An equivalent thermal expansion is proposed to model the mutual effects which are generated among broken and intact plies in the event of partial failure. Further tests have been carried out in fully damaged conditions, to evaluate the residual load-bearing capacity and the effects of ageing such conditions. Uniaxial tensile and compressive test on fully damaged laminated glass specimens are performed. Results are used to model the response of fully damaged beams.

In the last part of the manuscript, examples of application of newly found results are used in possible laminated glass structural designs: applications are provided for cold-bending techniques and post-failure safety assessments.

WORKFLOW OF THE THESIS

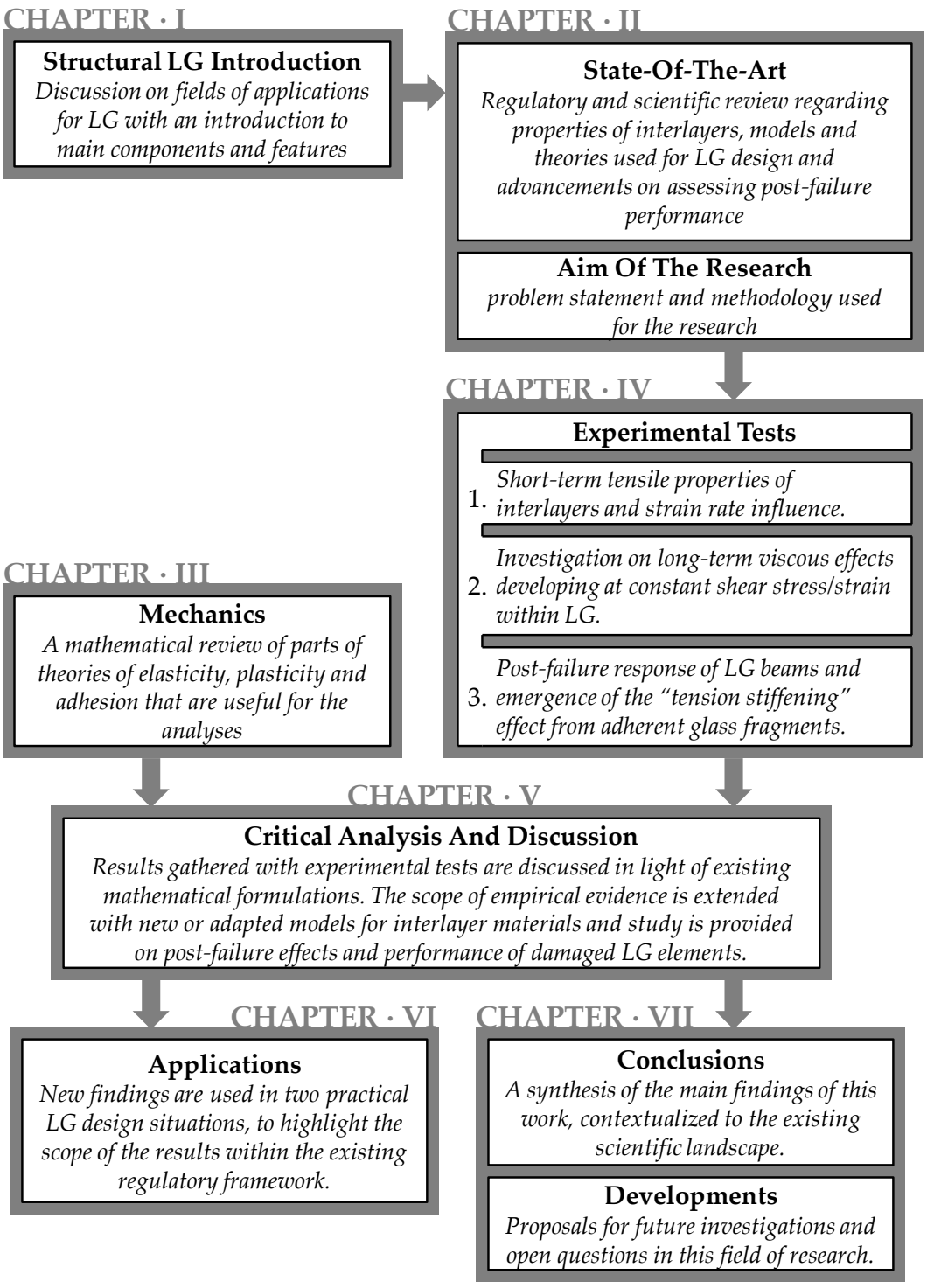

LIST OF ACRONYMS

DEM	Discrete Element Model
DG41	*DG structural PVB interlayer®*, Saflex (Eastman Chemical Co. subsidiary)
DH	damp heat
DOI	domain of influence (method) (cfr. §5.1.2.4 and Appendix I)
EET	enhanced effective thickness (model)
EPP	elastic perfectly plastic
ESM	equivalent stiffness model (cfr. §5.2.1)
ETEM	equivalent thermal expansion model (cfr. §5.2.3)
EVA	ethylene vinyl acetate
FDLG	fully damaged laminated glass
FE	finite elements
FFT	fast Fourier transform
GFRP	glass fibre reinforced polymers
GR	generalized response (model) (cfr. §5.1.1.2)
HE	hyperelastic / hyperelasticity (i.e. non-linear elastic theory)
HEVP	hardening elastic viscoplastic
HT	R. N. Haward and G. Thackray
IP	ionoplast polymer
LE	linear elastic / linear elasticity
LEFM	linear elastic fracture mechanics
LG	laminated glass
LVE	linear viscoelastic / linear viscoelasticity
MOR	modulus of resistance
MR	Mooney-Rivlin
NH	neo-Hookean
NLVE	non-linear viscoelastic / non- linear viscoelasticity
PDLG	partially damaged laminated glass
PV	photovoltaic
PVB	polyvinyl butyral
PVP	perfectly viscoplastic / perfect viscoplasticity
RH	relative humidity
SED	strain energy density
SG	*SentryGlas®* (previously known as SGP "*SentryGlas® Plus*"), Kuraray Ltd.
SLS	serviceability limit state
TCT	through crack tensile (test)
TS	tension stiffening
TSSA	transparent structural silicon adhesive
ULG	undamaged laminated glass
ULS	ultimate limit state
WLF	Williams Landel Ferry (equation)

A mio padre,

per il significato che ha dato
all'impegno, al sacrificio e all'onestà.

1 STRUCTURAL GLASS INTRODUCTION

The use of glass in the construction industry has been a part of human culture from centuries. Nonetheless, despite numerous advantages, glass and architecture inherently have to deal with compromises. While glass is stiff, it is brittle, although beautiful, it is costly. This first chapter introduces to the topic of architectural glass and issues related to glass design, contextualizing the aim of this manuscript and purpose of the presented researches.

"Don't build a glass house if you're worried about saving money on heating."

~Philip Johnson

Throughout history of building and construction, glass has always been a material fascinating both designers and the collective imagination. The research of light and transparency seems to be inborn in human kind and is often associated to healthy environments and high quality of life [1–3]. In fact, transparent or translucent elements in buildings are key for connecting interiors to natural lighting, allowing for natural environments heating through infrared radiation [4,5].

While in past centuries glass has been used in relatively small portions of buildings facades, gradual technical evolutions have allowed transparent elements to dominate most of the outer "skin" of buildings. This continuing transformation eventually redefined our very perception of many recent large structures with a feeling lightness, harmoniousness and environmental compatibility (Figure 1.1). Even so, while detailed properties of glass will be discussed in §1.1.1, it is well-known that brittleness and unpredictable failure are inherent features in the nature of this material. To allow for a safe use of glass in buildings (that has to do both with the perception of safety and structural safety itself), committing it to increasingly more demanding structural tasks, designers have to deal this fundamental Achilles' heel.

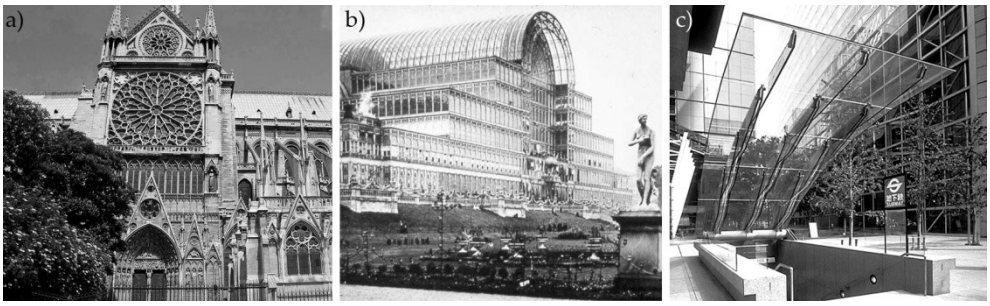

Figure 1.1 - a) North Rose of Notre Dame (Paris), 1270, still considered one of the largest windows in the world with its 13.1 m diameter b) The Crystal Palace (London), 1850, largest a cast-iron and plate-glass structure ever built c) International Forum glass canopy (Tokyo), 1997, among the first structural applications of laminated glass.

The invention of Laminated Glass (LG) by the beginning of the last century, with a French Patent filed in France in 1902 [1], was an essential milestone in glass

[1] Patent 321.651, filed in May the 31st 1902 by the "*société anonyme Le Carbone*", describing the process of applying a layer of celluloid on a glass object, through immersion and drying, to reduce the fragility of glass and shattering of fragments uprising from failure.

architecture: a turning point in shifting the role of glass elements from carried to self-sustained and eventually to structural ones [6]. In a nutshell, the lamination process consists in coupling glass plies to polymers which are generally –but not always- required transparency and must have prominent adhesive properties with the surface of glass. The main task of the polymer is to secure glass fragments in case of glass breakage, avoiding the scattering of potentially harmful shards. Beyond to this original intent of mere fragments-retaining property, the concept appeared to provide containing capacity to a glazing element, preventing to some extent the perforation of colliding bodies [7]. Moreover, assembling many glass plies in such arrays soon highlighted the structural coupling ability of interlayers, namely that the resistance and stiffness of LG elements is greater than the sum of the resistance and stiffness of the glass plies comprising this composite material. While these features were observed ever since the invention of LG, nowadays, more than a century later, the fundamental understanding and modelling of these effects is still an ongoing research field.

Architectural LG usage has progressively extended from secondary elements (e.g. windows and curtain walls) to structural elements with significant load-bearing capacity. Nowadays applications of structural LG include floors, stairs, balconies, canopies, point glazing systems, curtain walls, beams, pillars, sloped and overhead glazing and essentially any glazing application in which glass is required to be safe in case of failure and to be able to bear a substantial amount of load.

The architectural research for transparency has historically set the high road for external glazing and see-through façades, focusing on connecting the interior to the external environment. Figure 1.2 shows the evolution of the concept of seamless transparent façades and environmental connection in twenty years, interpreted by the design engineering firm Rice Francis Ritchie (RFR). In many recent buildings, with increasingly higher knowledge and confidence on LG resources, planar glass surfaces are progressively losing ground to curved, sinuous, shapes, aiming to impart a sense of delicateness and harmony.

Figure 1.2 - a) & b) Cité des Sciences et de l'Industrie greenhouses and reception, Parc de la Villette, Paris, RFR 1986 c) new TGV railway station in Strasburg, RFR-SNCF 2007

This increasing awareness and reliance on LG properties is helping architects and engineers to bridge the gap from viewing glass merely as an external interface, to a proper construction material. Numerous examples of practical LG applications can nowadays be found in staircases, internal walls, balustrades and walkable areas.

Taking to extremes this general tendency are concepts like the one shown in Figure 1.3 from *santambrogiomilano architects*, where all traditional structural elements have been replaced with LG counterparts, designed allow the occupant to be entirely immersed in the natural scenery. Nonetheless, apart from these architectural virtuosity exercises and touristic niches, arguably the housing market not nearly close enough to wild transitions like the ones showcased in such concepts. Besides, offices and public buildings often chose to actively rely on

transparent architectures to instil in the general public or potential customers the analogous sensation of transparency in relation to their conduct and behaviour. An architectural choice that was overtly guided by that philosophy was the design of the renovated *Reichstag* (seat of German parliament) by N. Foster in 1999:

> *"Some come to see democracy in action, but most come to wander up through the lofty glass and metal dome that crowns it. […] The glass dome above the assembly symbolizes a transparent government and that the republic's people are above it."*[2]

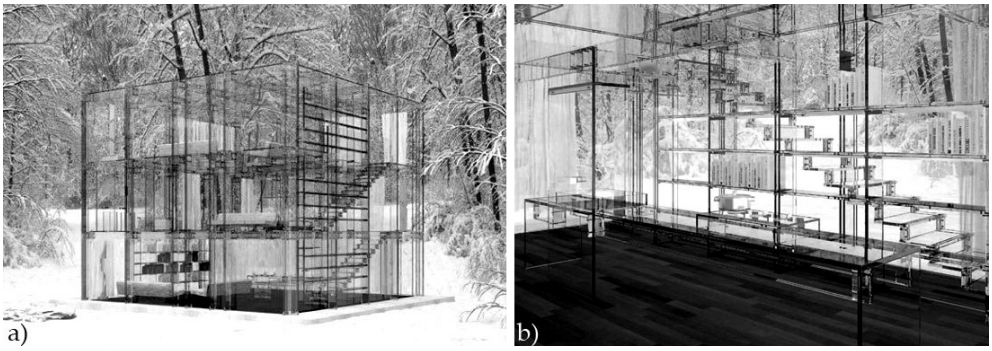

Figure 1.3 - "The Snow House" concept by Santambrogio & Arosio a) exterior b) interior

Over the past decades, an increase in the demand of structural load bearing glass elements has occurred [8], stimulating the formation of an organic institutional and regulatory framework. Transparent glass structures are required serviceability conditions, granting that the failure of any glass element does not turn out into an unexpected collapse of the structure and that sufficient load bearing capacity is available until substitution or evacuation (fail-safe response). From a standardization point of view, Europe is long time awaiting the approval of a dedicated *Eurocode*[3] on glass products and design, which is expected to be a cornerstone in glass industry. Aiming to fill this regulations void, provisional norms have been issued, namely prEN13474[4] and later prEN16613[5], ultimately dividing the LG market in two macro-sectors: laminated glass and laminated

[2] 2015, Michael Abrams, Photographer and journalist for *Stars and Stripes (www.stripes.com)*.

[3] A series of 10 Standards on different topics, providing a common approach for the design of buildings and other civil engineering works and construction products. For issues that are contained within its regulatory framework, *Eurocodes* are the recommended means of giving a presumption of conformity with the basic requirements of the *Construction Products Regulation* for construction works and products that bear the CE Marking, as well as the preferred reference for technical specifications in public contracts.

[4] prEN13474 "*Glass in buildings, Design of glass panes*" was the first European attempt to supply the glass professional and designers with general principles on the design of structural glass elements. The document was divided in three parts:

- prEN13474-1 "*Basis of design for glass*", January 1999,
- prEN13474-2 "*Design for uniformly distributed loads*", February 2000,
- prEN13474-3 "*Calculation of strength and load resistance of glass*", 2005, updated 2009.

While the general philosophy of the document was in accordance with the Eurocodes, the norm never saw a final approval and was ultimately replaced by prEN16612.

[5] prEN16612 "*Glass in buildings*" resumed the earlier regulatory attempt of prEN13474 in recent years, with the final aim to issue a dedicated *Eurocode* for glass design. The document is divided in two sections:

- prEN16612-2013 "*Determination of the strength of glass panes by calculation and testing*",
- prEN16613-2013 "*Laminated glass and laminated safety glass".*

To this day, this document has not yet received final approval.

safety glass: the first, doesn't require safety properties and can be used for acoustic isolation or decorative purposes, while the latter is required safety with respect of the adhesion of glass fragments to the interlayers and the ability to withstand the impact of colliding bodies according to standardized procedures. Lacking a strong central coordination, the regulatory framework on glass production and design has followed different - sometimes divergent - paths among European countries. Some have interpreted and reused part of the provisions of American[6] and Australian[7] standards, which arguably are some of the most organic attempts to a comprehensive regulation body. A list of applicable country-based regulations and technical documents follows:

- AS 1288-2006, Australia (2006),
- DIN 18008, Germany (parts 1/2/3/4 2010-2013, parts 5/6/7 in preparation),
- CSTB 3574, France (2011),
- CNR-DT210/2013, Italy (2013),
- ÖNORM B 3716, Austria (2016),
- ASTM E 1300, US (2016).

Alongside those and other documents, which are openly attempting a wide-ranging approach to issues related to glass design and production, lives a crowded universe of standards (ISO, EN, VDA, DIN, ETSI, etc.), regulating different aspects related to glazing. An extensive description of these norms, along with their Italian UNI EN counterparts, was made in a recent work by M. Blascone [9].

An outlook on the LG market can be obtained using *Google Trends*[8] for the query "laminated glass" (Figure 1.4). Results show a decreasing trend which has been stable for almost a decade, with higher peaks around 2004-2006. Small and rich emerging countries are leading the sector interest along with developed markets[9].

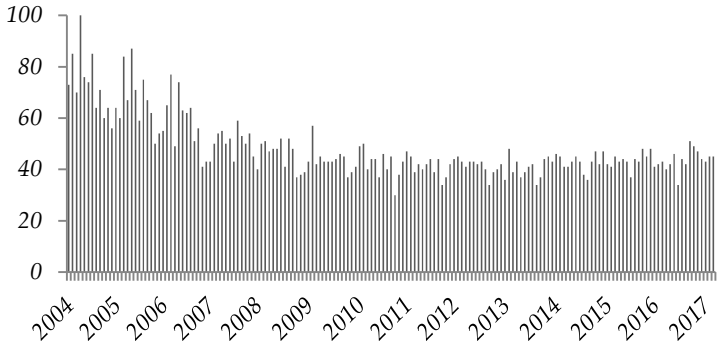

Figure 1.4 – worldwide interest in time for the query "laminated glass"

[6] ASTM E 1300 "*Standard Practice for Determining Load Resistance of Glass in Buildings*" for the US, currently used throughout the United States and parts of Canada.

[7] AS1288-2006 "*Glass in buildings*" prepared by the Joint Standards Australia/Standards New Zealand Committee BD-007, Glazing and Fixing of Glass, to supersede AS 1288—1994.

[8] A web facility of *Google* Inc., based on *Google Search*, that shows how often a particular search-term is entered relative to the total search-volume across various regions of the world.

[9] On a scale from 0 to 100, where 100 indicates the location with the highest frequency of search in proportion to the total number of searches in that location: Singapore (100), Australia (63), Hong Kong (63), U.A.E. (57), New Zeland (52), Malaysia (45), U.K. (42), South Africa (37), Philippines (24), U.S. (20), Canada (19), India (17), etc. [updated November 2017]

1.1 MATERIALS

LG products are assemblies of several glass plies, two at the very least, bound together with adhesive polymers. These plastic sheets are usually one order of magnitude thinner than the glass plies, and for their inner position among the composite material are usually referred to as "interlayers"[10].

Lamination was introduced in the automotive and aeronautical industries for the assembly of forward windshields, to prevent the scattering of sharp shards upon glass failure from inducing likely lethal injuries to pilots and drivers. As the first safety glass with cellulose interlayer turned yellow in a few years of light exposure, the bonding layer was replaced in 1933 by cellulose acetate, made from the reaction of cotton with acetic acid [10]. By 1939 this was again replaced by the cheaper polyvinyl butyral (PVB), which has then dominated the marked up to this day. Almost one century later, despite major improvements in manufacturing processes and increasingly more options for polymers to be used as interlayers, the basic concept of glass lamination has not yet been revolutionized: New LG products now conquering the construction industry are conceptually comparable to the earliest elements in cars and other means of transport.

Polymer/glass laminates are employed when safety and security preclude the use of monolithic glass [11]. Contrary to monolithic glass elements, these composite materials gain some level of impact resistance and ability to dissipate energy [12–16], along with post failure load bearing capacity. These and other properties, most of which are yet to be adequately modelled and understood, are always accompanied by the ability to hold glass fragments: a property connected to the adhesive properties of the glass/interlayers interface which is the first unalienable requisite of LG products.

Intuitively, the properties of LG composites derive from the properties of the comprising materials[11]. In the following paragraphs, a general overview of the key features and properties of the individual materials is presented. Bearing in mind the scope of this work, which is aimed primarily towards the use of transparent glass elements in construction industry from a civil engineering point of view, the reader should not be surprised not to find adequate mention of some among the known and important properties of the materials. For instance, optical or thermal transmittance properties of glass and interlayers will not be mentioned at all, while only a general overview of the fracture mechanics is discussed. Should the reader require more insight on those topics, references are provided to exhaustive scientific literature works.

Modelling the mechanical properties of LG from a structural engineering point of view is no easy task. To showcase some of the most relevant phenomena, the following scheme provides a broad overview of models and key properties that need to be mastered to perform a reliable and cost-effective LG design, divided for the three key fields of inquiry:

[10] from latin *intĕr* : in the middle, in the midst. As in: "situated between layers".

[11] In most applications, two materials are used: one type of glass and one of interlayer. Nevertheless, specific designs may require or suggest the adoption of several glass types, diverse interlayers or the embedding of instruments and various devices [309–311].

Glass	Interface	Interlayer
• Hookean elasticity	• delamination[$]	• viscoleasticity[†‡]
• toughness[‡$]	• chemical bonds strength[†]	• hyperelasticity[†]
• fracture mechanics	• boundary stress distribution	• viscoplastic flow[†‡]
		• cross-linking effect[†]
		• tension stiffening*[†‡]

While dependable models are known to understand and predict the response of glass elements, much work has yet to be done to improve knowledge on the mechanics of most interlayer materials and properties of the interface.

1.1.1 GLASS

Glass is a non-crystalline solid which is often transparent. As a material category, glass is often described as a *supercooled* liquid: amorphous solid whose formation depends upon the kinetics in the cooling from its liquid form. As a result, glass do not have a sharp melting point: gradually softening from a solid state to a state which can be described as a viscous liquid [17].

At ambient temperature ($-30 \div 60°C$) silicate glass[12] used in architectural applications [18,19] have properties typical of the solid state. Glass is a resourceful building material: it is permeable to light but impermeable to fluids and solids, it is recyclable [20,21], made of some of the most abundant substances on earth's crust [22] and has a reasonably low thermal conductivity[13] [23].

Optical properties of glass[14] are linked to the interactions of electromagnetic radiations [24]. Glass absorbs about 4% of the radiation in the visible spectrum[15] (but molecules may be tuned with metal oxides to absorb specific frequencies, resulting in coloured glass [25]). Glass is mostly impermeable to ultraviolet and far infrared radiation, for the presence of ions O^{2-} and groups Si-O respectively.

Glass is a liquid around 1500°C and a solid near 500°C.; in-between, it behaves like a viscous fluid. Being a poor thermal conductor, a rapid cooling of the outer surface does not transfer instantly to the inner core. This temperature differential, coupled with the thermal expansion properties, may result in a peculiar stress pattern, discovered in the early 17th century[16] [26]. This phenomenon can be

---

* only for post-failure, † temperature-dependent, ‡ time-dependent $ climatic-conditions dependent.

[12] Where silicon dioxide SiO_2 is the principal component ($69 \div 74\%$), principal others and usual concentrations being sodium oxide Na_2O ($12 \div 16\%$), calcium oxide CaO ($5 \div 12\%$), magnesium oxide MgO ($0 \div 6\%$) and aluminium oxide Al_2O_3 ($0 \div 3\%$) [28]. To follow up on the chemical composition of glass cfr. [5,6,24,63,268].

[13] Compared to metals, stone, masonry and regular concrete (i.e. non-lightweight).

[14] Reflection, refraction, absorption, scatter, etc.

[15] Even the purest of silicate glass is not perfectly transparent and colourless. It is not enough to choose materials produced with synthetic techniques or the purest natural ones: some elements, like iron and chromium, can slightly colour the material even in trivial quantities. To obtain a fully colourless element, specific bleach substances must be added to the blend, correcting the tonality either with a complementary colour superposition principle or chemical oxidation-reduction of the original colouring element (e.g. iron has a much higher colouring power if it belongs to a reduced state than in an oxidised one).

[16] Prince Rupert's drops, also known as Batavian tears, are made of a silicate glass of a high thermal expansion coefficient and have the shape of a tadpole [312].

harnessed to improve the mechanical properties of many glass products through a process called "thermal tempering".

Glass sheets are nowadays produced through an industrial process developed by A. Pilkington and K. Bickerstaff in the 1950s[17], resulting in seamless "float glass" elements that is later cut to pieces. During the cooling process, strong eigenstresses may remain within the glass plies; for this reason, an annealing process[18] is carried out in special furnaces at controlled temperatures to relieve internal stresses. "Float glass" sold on the market are always annealed according to standard procedures (for simplicity and to avoid redundant terminology, the term "annealed" will not be mentioned here on after). Standard glass thicknesses range from 2 to 25 mm (Table 1.1) [27,28] (although most manufacturer are able to produce only up to 19 mm thick elements, and exceptions can be found with thickness up to 30 mm). The maximum size of the plies depends on manufacturing and transportation capability of the manufacturers, the largest elements produced are usually $6000 \times 3210mm$ [29] (the latter being the width of the float bath).

Table 1.1 - standard glass plies sizes and thicknesses in construction indstry

	float (annealed)	**strengthened**	**tempered**
thicknesses[mm]	2-25[†]	4-12	4-19[*]
maximum size [m×m]	3.21×6.0[‡]	2.8×6.0	2.8×6.0

[†] *standards for most manufacturers are 3, 4, 5, 6, 8, 10, 12, 15 and 19 mm*
[‡] *often referred to as the "Jumbo" size.*
[*] *most manufacturers recommend 6-19 mm thickness for tempering.*

Chemical bonds comprising glass elements are extremely strong, in a way, comparable to the bonds found in the strongest metal alloys [19] (over 1 GPa, but by estimates of the theoretical strength of flawless glass are as much as 35 GPa [30]). Glass is a stiff and perfectly elastic material up to the ultimate failure, with a Young modulus around 70 GPa (about 30% the stiffness of steel used in the construction industry). Alas, contrary to metals for which plastic deformations precede the ultimate failure, the structure of glass is unable to rearrange its atomic dislocations in a ductile manner, thus the intrinsic brittleness [31]. Mechanical properties of glass, namely its tensile strength, are dependent on microscopical scratches and imperfections on the surface[19]. At the tip of those imperfections, stresses concentrate and can easily initiate the propagation of cracks [32]. To enhance this tensile strength, several approaches can be attempted [33]:

- reduce the severity of surface flaws,
- controlled environment near the crack tip,
- polymeric coatings to reduce surface abrasion,
- induced surface compression.

[17] Sir Alastair Pilkington and Kenneth Bickerstaff, pioneered the technique in St Helens, Merseyside in 1952. In this "float glass production process" (also known as the "Pilkington process"), molten glass rests on top a bed of molten metal, entering as a liquid around 1000°C and exits as a solid, at about 600°C. The cooling must be carefully controlled up to 450°C and can be sped up successively. This method gives the sheet uniform thickness and very flat surfaces. Due to this technique, glass plies have a "tin" side (because tin is often used as molten metal, but other metals can be chosen) and an "air" side, with slightly different properties.

[18] Process of slowly cooling hot glass after they have been formed.

[19] Often named ''Griffith flaws'', in the order of a few micrometers, produced during handling by the manufacturer as well as the user in ordinary ambient conditions.

While the first three approaches aim to reduce the various coefficients in fracture mechanics models [34–36], the introduction of surface compression remains the easiest, more reliable and cost-effective method for glass strengthening. Tempering and toughening processes were developed to induce compressive actions in the outer surface of glass, with an equilibrating tensile stresses in the inner part of the material, which is not affected by the same vulnerability to superficial defects [32,37]. This has beneficial effects in the overall tensile resistance, as it is mainly a function of stress concentrations around the imperfections. Tempering can be obtained either with a thermal process or a chemical one[20]: while thermal tempered products can be "fully tempered" or "thermally toughened"(essentially, a lighter form of thermal tempering), building codes only contemplate one type of chemically tempered product (Table 1.2). Other properties of interest for glass design are collected in Table 1.3.

Table 1.2 - characteristic tensile strength for glass (min. required [38]*)*

float (annealed)	45 MPa
thermally toughened	70 MPa
thermally tempered	120 MPa
chemically tempered	150 MPa

The release of the eigenstresses, induced to enhance the performance of glass elements with toughening or tempering, influences crack patterns and distribution upon failure. Figure 1.6 shows how the relief of internal stress distributions may result in widespread shattering patterns upon glass failure.

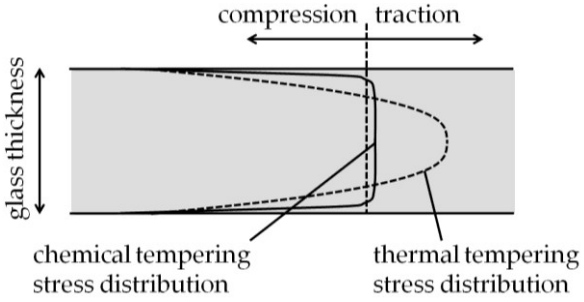

Figure 1.5 - stress distribution in chemically or thermal tempered (or toughened) glass

Cracks propagate in glass at the about speed of sound in the material[21]. From a

[20] The French Francois Barthelemy Alfred Royer de la Bastie is credited with first developing a method of thermal glass tempering in 1874 [313]. Nonetheless, inadvertent effects of glass tempering had been already observed in the past (cfr. footnote 16 p.6). Thermal tempering consists in re-heating the glass above its softening point (620-675°C) and following rapid cooling via compressed air jets. Because of the fast cooling the outer surface contracts while the core remains partially molten. When the core finally cools down, it must deal with a rigid outer surface that is therefore pulled toward the center and becomes tightly compressed.
In the chemical strengthening process, alkali-containing glass are immersed in an electrically heated bath of alkali salt KNO_3. During the bath, an ion exchange occurs between the host alkali ions of glass and invading ions from the salt. Because the invading ions are larger in size than the original ones, the resultant stuffing in the near-rigid atomic network of glass leads to the development of high surface compression and balancing by interior tension, whose distribution depends on the diffusion depth and glass thickness [33].

[21] The assumption in fracture mechanics is that the propagation of cracks occurs when the rate of energy return from fracture is greater than the energy necessary to create new surfaces. Once this happens, the incremental fracture energy grows while the incremental surface energy stays the same, and the system is unstable. Crack will then propagate "as fast as possible", which for an ideal continuous media is the speed of sound. Other works [35] used high-speed photography to reveals

safety-perspective, large fragments produced by failure of float annealed elements have sharper edges and greater mass. On the other hand, small tempered glass shards can rely upon a very limited surface for to adhering to an eventual substrate. Moreover, experimental evidence showed that a significant number of small glass fragments are expelled at high speed upon bending -induced failure of partially damaged glass elements.

Table 1.3 – list of the main properties of glass useful for LG design

property	**unit**	**value**
density	kg/m^3	$2250 \div 2750$
tensile resistance	N/mm^2	$20 \div 200$
compressive resistance	N/mm^2	$900 \div 1000$
Young modulus	N/mm^2	$63 \div 77 \cdot 10^3$
Poisson coefficient	$-$	$0.20 \div 0.24$
Hardness	$Mohs$	6
Toughness	$N \cdot m^{0.5}/mm^2$	0.75
Thermal conductivity	$W/(m \cdot K)$	$0.90 \div 1.10$
coefficient of thermal expansion	$\mu m/(m \cdot K)$	$3.1 \div 9.0$
maximum working temperature	℃	280

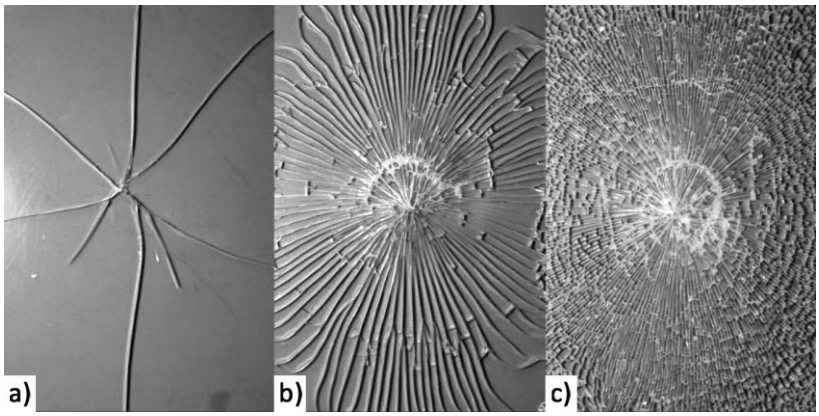

Figure 1.6 – typical failure patterns for a) annealed, b) heat-strenghtened and c) fully tempered glass (Overend, 2007 [39]*)*

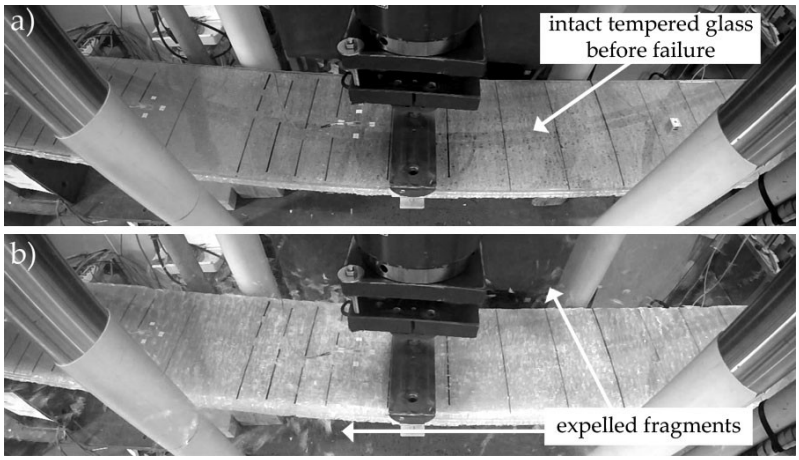

Figure 1.7 - tempered glass fragments expelled upon bending-induced failure (Laboratorio Strutture, Università degli Studi di Firenze, Italy 2017)

that cracks can spread through glass at speeds of hundreds of meters per second, or roughly half the speed of sound in glass.

As tempered glass products can be installed on very high buildings, it is useful to estimate of the terminal velocity and energy of free-falling fragments. Evidence showed that the size of tempered glass fragments is about the thickness of the ply. For a free-falling $1\ cm^3$ glass cube, the terminal velocity[22] in air is $20 \div 22\ m/s$ carrying a kinetic energy around $0.55\ J$, which is hardly harmful, let alone deadly.

1.1.2 INTERLAYER MATERIALS

Interlayers used in glass lamination are a class of synthetic resin material, able to form strong and reliable chemical bonds with the surface of glass[23]. The formation of these chemical bonds is generally made possible in an autoclave[24], under set conditions of pressure and temperature. The interlayers used in safety laminates are typically made from relatively thick polymer sheets, including complex, multi-component compositions based on poly(vinyl butyral), poly(urethane), and ethylene vinyl acetate or ionomer copolymers [40].

Since 1939, in the early days of glass lamination, PVB has undisputedly dominated the interlayer market for almost eighty years [11,41–44]. Nonetheless, the increasing demand for high-performance architectural LG and specific applications has pushed the breakthrough of new products [45–48]. Thus, the present interlayers panorama is much more diverse than it used to be no more than ten years ago. While ethylene-vinyl acetate (EVA) and other vinyl-ester polymers seem to dominate the market of photovoltaic (PV) laminates[25], polycarbonates [49–51] and ionoplast polymers (IP) and modified-PVB blends [52–55] all share a significant part of the architectural LG market, along with the more traditional PVB.

Interlayers are usually prepared in sheets with rough surfaces, required to prevent blocking (i.e., the tendency of the interlayer to stick to itself prior to lamination during transportation and handling). Rough surfaces are also beneficial for preventing premature adhesion to other components of the laminate (glass), and facilitating the expulsion of air bubbles during lamination [56]. The term "sheet" or "monolithic sheet" or "monolithic interlayer" refers to a single layer of material formed from the thermoplastic composition. Some interlayer sheets are produced

---

[22] Terminal velocity $V_t = [2mg/(\rho S C_d)]^{0.5}$ where m is the mass of the object, g is gravity, $\rho = 1.25\ kg/m^3$ air density, S is the external surface and $C_d = 0.8 \div 1.05$ the drag coefficient.

[23] While most LG products assembled for architectural purposes have the interlayers positioned *within* the glass plies (i.e. most of the external surface is glass), laminates may comprise a single sheet of glass included among synthetic resin sheets. In this latter type of laminated safety glass products, which constitutes a niche product and will not be further referenced or studied in this manuscript, the surface of the synthetic resin sheet which is not laminated to the glass may optionally be coated with or laminated to another synthetic polymeric material [56].

[24] In most production lines, pre-assembled components are heated in a chamber filled with oil or air to about $120 \div 150$°C and pressure of 10 to $15\ kg/cm^2$ to soften and fluidize the interlayer sheets and cause them to adhere intimately to the glass panes. Nevertheless, vacuum-enhanced [314] and non-autoclave [315] techniques have also been developed.

[25] "*Ethylene-vinyl acetate (EVA) is still the market leader and standard encapsulation material for solar cells […]. For a long time there have been no alternatives on the horizon, as finished modules produced since the Nineties have a service life of at least 20 years and all series products have to be certified. It is therefore difficult for other plastics to gain a foothold on the market if the points in their favour are rarely measurable.*" (Kuraray, 2009). Nevertheless, the research in PV laminates has literally boomed in the last decade [316] and numerous researchers are dedicated now more than ever to finding cheaper and more efficient products [101,317–319].

by extrusion, which is a cost-effective procedure but requires low viscosity in the melt state (see below). Stiffer interlayers are generally produced with casting procedures, thus resulting in much more expensive final products. Most interlayer sheets are supplied in thicknesses which are multiples of 0.38 *mm*, which is often the thickness of the product extruded from the melted compound. Single sheets can be folded multiple times yielding the four traditional interlayer thicknesses found on the market[26]: 0.38 *mm*, 0.89 *mm*, 1.52 *mm* and 3.04 *mm*. Except for some niche products or resins used for decorative purposes, all of the most widespread interlayers in architectural LG products materials are synthetic polymers.

Polymers (and copolymers) are a class of materials characterized by long chains of covalently bonded macromolecules with a carbon atoms backbone [57,58]. While Ceramic materials are comprised with ionic molecular bonds (i.e. the strongest molecular interaction) and metal alloys mostly rely on bonds between electropositive elements, polymers are made of long chains with weak chemical interactions among one another [7]. Nonetheless, the long structure of each molecule and its ability to branch and tie with neighbouring chains (Figure 1.8.a), may yields tough mechanical properties under certain conditions [59]. As schematized in Figure 1.8.b, some polymers are able to cross-link one another (i.e. to form strong chemical intermolecular bonds among different chains), provided enough time and right conditions (temperature, pressure, etc.). Mechanical properties of cross-linked polymers depend on density and spatial distribution of chemical bonds; a traditional classification has been established accordingly: heavily cross-linked materials called thermosets, thermoplastics, with long chains and low to null cross-link density and finally elastomers, which are also scarcely cross-linked but able to deform elastically and do not have the tendency to flow when heated [59,60].

Most interlayer materials used in LG industry belong to the thermoplastic group; but, to some extent, can exhibit rubber-like behaviour comparable to elastomers in specific circumstances. For instance, all interlayers studied in Chapter 4 and Chapter 5, further described in the following paragraphs, are strictly speaking thermoplastics. Nonetheless, tensile tests alike those performed for elastomeric materials can be performed, yielding useful insight on the materials properties. On the distinction regarding material properties, and the indomitable desire of scientists to divide and classify different phenomena according to human-scale observations, I believe it is worthy quoting an inspiring extract from the work of G. K. Gilbert (1892) [61] as a reminder of our limitations:

> *"To my mind, it appears that the difficulty is only imaginary and not real. Rigidity and plasticity are not absolute terms but relative, […] the apparent contrast between the two properties belongs to the laboratory and to those phenomena of nature involving small masses and small forces. When great masses and great forces are involved […], the distinction loses value."*

Polymers used in glass lamination are sometimes referred to through a variety of fancy names originating from commercial decisions, rather than a descriptive

[26] some manufacturers, resellers and professionals are used to call those "single thickness", "double thickness", "safety thickness" and "heavy-duty thickness" respectively. Intermediate thicknesses that multiples of 0.38 *mm* are not the product of simple multiple folds are also found in the market, but less frequently.

approach on molecular properties[27]. Moreover, when used as interlayers, pure polymeric matrixes are usually mixed with countless plasticizers, fillers and additives, in proportions that are well-guarded industrial secrets or patented trademarks. Any commercial blend is therefore prone to major changes with technological evolutions and chemical discoveries: if a new mixture or plasticizer proves to be more performing or cheaper than any previous one, it is very likely to overrun the market while still maintaining the former commercial name. Moreover, while some innovative interlayer materials are currently produced only by a specific company (e.g. on June 1, 2014, Kuraray Co., Ltd. became the exclusive licensee for the technology and trademark of *SentryGlas*® interlayer), more traditional ones like EVA or polyvinyl butyral (PVB) are manufactured in different – and undisclosed – blends by several companies[28]. Therefore, when talking about any interlayer material, one should often rather refer to families of products, each likely susceptible to a large spectrum of slightly different mechanical properties.

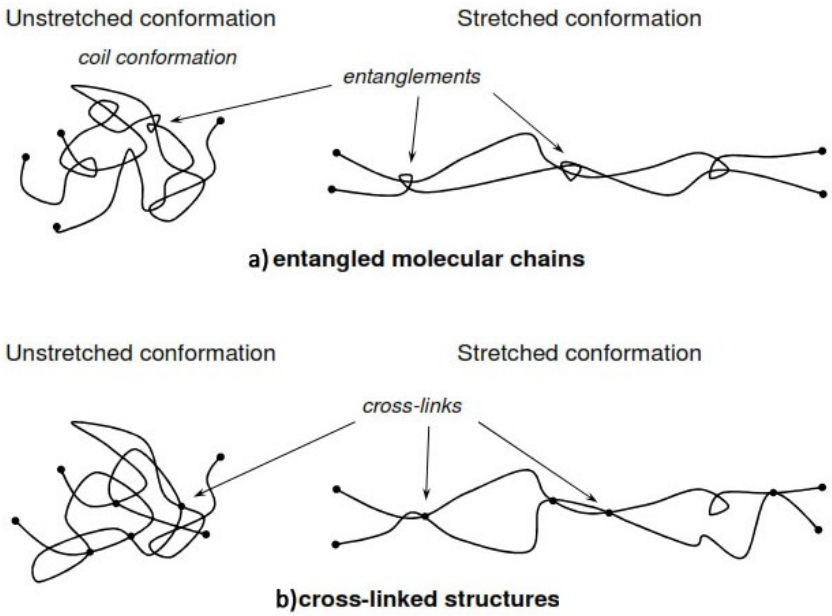

Figure 1.8 - a) entanglement and b) intermolecular cross-links (Delincé, 2014 [7]*)*

Key properties for understanding the mechanical response of interlayer materials in LG are viscoelasticity, hyperelasticity and viscoplastic flow [15,47,53,62–65]. Details on these mechanics will be shown, analysed and discussed throughout this manuscript. As a general idea, for sake of introducing the materials that will be studied hereon after, it is important to underline the profound differences with

[27] The most widely used polymeric films for glass lamination are: Polyvinyl Butyral (PVB) [168,320], Ethylene Vinyl Acetate (EVA) [321] Polycarbonate (PC, often used in combination with other interlayers for its limited adhesive properties) [84], *SentryGlas*® (SG) [54] and *DG41* (enhanced PVB). Examples of other interlayers and brands, sometimes with dedicated decorative or insulation properties, are *StormGuard*® (enhanced PVB interlayer alleges improved performance for hurricane-resistant applications), *Vanceva*® *Color* (decorative), *Saflex*® *SilentGlass* (acoustic), *S-LEC*™ (used mostly in the automotive sector as an UV shield with acoustic/thermal insulating properties). A fairly recent review on the research status, developments and applications of different polymers in LG was performed by M. Teotia and R. Soni [48].

[28] Just to name a few worldwide: 1. DuPont Co., Ltd (US). 2. Kuraray Co., Ltd. (Japan) 3. Solutia Inc. (US) 4. Huakai Plastic Co., Ltd. (China).

traditional building materials: experimentally-derived constitutive equations have been shown to be highly dependent on factors such as temperature, the rate of application of stress and strain, load and strain history, etc [66].

Two temperatures define transitions among different states for polymers: the glass transition temperature T_g and the melt temperature T_m (Figure 1.9) [7]. At low temperatures, polymers behave mostly like solids, with higher stiffness and sometimes major brittleness (it is not uncommon in everyday life to experience the sudden failure of some frozen plastic materials), a "glassy" state where the relative movements of molecules are blocked for the most part[29]. Corresponding to the glass transition temperature is a transitory "leathery" phase, in which the molecules are allowed increasingly more freedom of movement, usually ending in a "rubbery" plateau, where materials properties are fairly consistent. Closer and above the melt temperature, polymers behave like high-viscosity fluids.

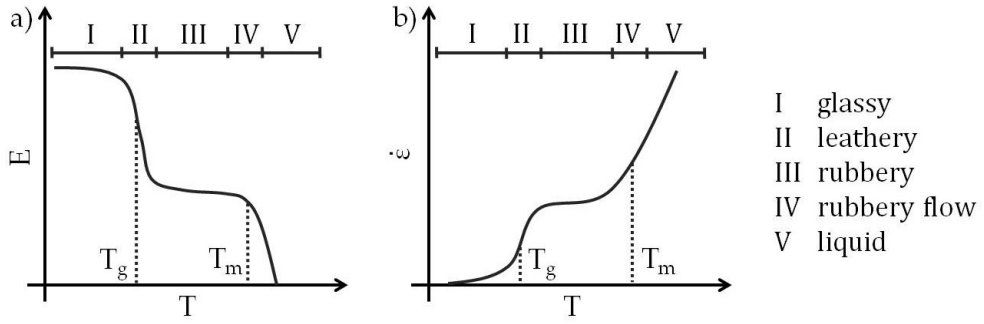

Figure 1.9 - thermo-mechanical curves for a) elastic modulus [67] *and b) strain rate* [68]

Working conditions of interlayers used in LG should never involve temperatures close or higher than the melt temperature, which corresponds to the states of the lamination process, one that should never be reached again during the lifetime of architectural LG elements. Operational temperatures for interlayers commonly correspond to the glassy, leathery and rubbery phases (I,II&III in Figure 1.9). For this reason, the glass transition temperature is usually an important and insightful parameter for LG design and is provided by manufacturers (Table 1.4), stressing the difference between very different responses of the material above and below. Note that, while SG and DG41 are patents from specific manufacturers, PVB and EVA are a classes of materials produced by many companies; as a consequence, results for those materials should be looked at as averages or likely ranges.

Table 1.4 – glass transition and (melt) temperature for some interlayer materials

SG	DG41	PVB	EVA
55.0[a] (94.0)[a]	46.0[b] (n/d)	19.5[c] (113.0)[c]	-43.0[d]/-33.1[e] (65.0[f]/80.0[e])

[a] *2014, Kuraray (www.kuraray.com)*; [b] *2014, Saflex (www.saflex.com) and* [69]; [c] *2016, Kuraray, confirmed by some researches* [70–72]*, values may vary for other manufacturers*; [d] *1983, Cuddihy et. al.* [73]; [e] *2012, Agroui et. al.* [74]; [f] *2006, Chen et. al.* [75].

Traditional methods and models used in civil engineering are scarcely able accurately predict the mechanical behaviour of most plastic materials; besides, a complete mathematical formulation able to describe such response is currently missing. For most design purposes, a phenomenological methodology appears to be the most reliable approach, with different empirical models which can be used to solve specific problems, under well-specified boundary conditions.

[29] Below the glass transition temperature, a reduced molecular mobility doesn't allow the polymer to reach a state of thermodynamic equilibrium [291].

Haward and Thackray in 1968 [76] (HT in the following) proposed that the response $\sigma(\varepsilon)$ of thermoplastic polymers could be divided is the sum of two terms, in turn describing different physical mechanisms. While cross-links among the molecules, along with and other weaker chemical actions, are accountable of the response for short-range deformations $\sigma_c(\varepsilon)$, those tend to be less relevant for higher strains, where the response is driven from the tethering and entanglement $\sigma_e(\varepsilon)$ of the long and branched polymeric chains[30].

$$\sigma(\varepsilon) = \sigma_c(\varepsilon) + \sigma_e(\varepsilon)$$

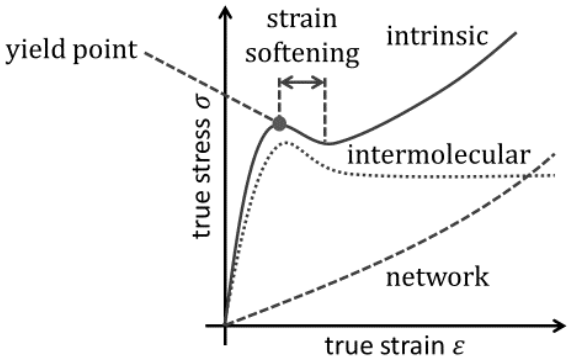

Figure 1.10 - classical stress decomposition (Haward and Thackray, 1968 [76]*)*

Viscoplasticity is the theory that describes the rate-dependent inelastic behaviour of solids. The bulk of the viscoplastic flow in thermoplastic materials (cfr. §3.2.1) is believed to be associated to the rupture of the intermolecular bonds, mostly after the measured load peak in the intrinsic curve (Figure 1.10) [77,78]. From that point on, a quota of accumulated strain is non-reversible. Besides, viscoelastic effects are believed to be correlated to the rearrangement of dislocations within the polymers network: the initial – unstressed -conformation of the network is the state of lower entropy, the one to which stretched thermoplastics have the tendency to return over time, in a behaviour also known as *entropic elasticity*[31] [59]. More details are given in §5.1.1.2.

1.1.2.1 PVB

For its excellent optical clarity and good adhesion with glass, polyvinyl butyral (PVB) is arguably the most common interlayer in safety glass laminates in the automotive, aerospace and architectural sectors [16,71]. Worldwide, 65% of PVB is used in automotive applications [11,41,42].

PVB is a polyacetal produced by the condensation of polyvinyl alcohol with butyraldehyde [10]. Plasticizers are major components polymer-containing products. For instance, PVB used in safety glass is typically composed mainly of

[30] While this model was issued for true stress-strain diagrams, an analogous decomposition can be made in an engineering-stress over engineering-strain diagram, neglecting the cross-sectional reduction due to Poisson effect [164]. In fact, multiple transitions between the two will be used for the analysis of tensile tests in §5.1. While the substance of this decomposition, its original idea, will be used within the upcoming analyses, the graphical interpretation brought by Haward and Thackray in Figure 1.10 is believed to have been originally flawed, having considered the presence of a strain softening region within true stress-strain diagrams. In the following §5.1.1.2, a discussion is brought regarding the fact that softening may only be visible in engineering diagrams.

[31] The key element that has been considered for the design of the viscoelastic investigation campaign (cfr. §3.3.7 and §4.1).

poly-(vinyl butyral) and about 30% plasticizers and softeners to enhance plasticity and toughness. Condensation leaves some free hydroxyl groups, which are then able to tie to similar groups originating from the Silicon atoms of glass [79]; these bonds are at the origin the origin of the good adhesive properties of PVB.

PVB is a recyclable material. In fact, no incompatibilities were observed in blending various grades of commercial and recycled PVB, suggesting that blends and recycled polymers themselves could be used as substitute materials in glass lamination [71].

PVB has been either described as an amorphous [80,81] or semi-crystalline [82,83] thermoplastic. The mechanical behaviour of PVB has been proven to be highly nonlinear, time- and temperature-dependent and capable of major extension. The scientific literature includes several experimental results on PVB, which will be referenced and compared throughout this manuscript to the newly presented results.

1.1.2.2 SG

SentryGlas® ionoplast Architectural safety glass interlayer (in short, SG) is the commercial brand of a Ionoplast Polymer (IP) produced by Kuraray Inc.[32], primarily composed of ethylene/methacrylic acid copolymers, with small amounts of metal salts. Compared with PVB, SG allegedly has higher stiffness and strength, so much that in an early announcing of the material in 1997 the company stated:

> *"SentryGlas® [Plus] interlayers are the building block for a new generation of structural laminated glass: a high-strength polymer used for glass laminators and window companies to make advanced safety glass for automobiles and buildings".*

Pioneering the present historic phase, witnessing a boom in interlayer material development, the genesis of this material was arguably due to the growing awareness among LG designers and architects that PVB had very limited mechanical properties, especially concerning long actions at higher temperatures.

SG belongs to the IPs family. Ionoplast polymers and copolymers have been proven useful in safety laminates intended for structures requiring a high degree of penetration resistance. Examples include hurricane-resistant glazing and structural elements such as glass staircases and glass balustrades. In particularly demanding applications, the use of IP interlayers such as SG in safety laminates have shown ballistic resistance [84]

In literature, SG has been described as a semi-crystalline thermoplastic material [45,81]. Ionic polymers like SG are synthesized by connecting ionic groups to a carbon chain backbone. If the ionic content within the non-polar polymer is at most 10%, the ionic polymer is defined as a ionomer [85,86]. While the production of SG is a patented and preserved secret, we known that IPs are synthesized by neutralizing the carboxylic acid groups of acid copolymers. Incomplete details on those chemical procedures are available in patents and scientific papers [40,87]. The final fabrication processes of SG incorporate an extrusion blow molding, resulting in a monolayer product of the desired thickness.

Arguably few details on the mechanical properties of SG are known, apart from those willingly disclosed by the manufacturer. Preliminary independent analyses

[32] This product was patented as SGP® by *DuPont Glass Laminating Solutions/Vinyl*, a segment of the *DuPont Packaging & Industrial Polymers company* acquired by Japanese chemical manufacturer *Kuraray* in 2014.

with tensile tests on material specimens have shown that this material has an elasto-plastic behaviour at room temperature (about 24°C), with a noteworthy initial modulus (480 to 580 MPa) [54,88,89] (cfr. Appendix D). From a thermo-mechanical point of view, this polymer appears to have major advantages over PVB for a large range of temperatures (0 to 60°C) [54]. Analyses within this manuscript aim to share more light on the properties of this material: as a material itself and most of all as component of LG elements.

1.1.2.3 DG41

Saflex® DG, also known as "DG41", is the most recent interlayer material among those studied in this manuscript. It is produced from plasticized PVB, so much that some [90], along with the manufacturer itself, have been referring to this new material as "structural PVB"; which is arguably a poor choice of words, given that PVB has been rightfully considered a structural material itself for over half a century. DG41 was announced by Solutia Inc. in 2012, allegedly suited for:

> *"applications in which increased interlayer rigidity and high glass adhesion are required relative to standard glazing interlayers"* [33].

Where the part "standard glazing interlayers" should be intended referred to the overwhelmingly popular use of PVB. DG41 is supposed to combine:

> *"the benefits of a rigid interlayer with the features of glass containment, UV screening, edge stability and clarity"* [33].

Upon release of this new product, J. Schimmelpenningh, manager for Solutia said:

> *"[…] Saflex DG interlayer tends to keep glass intact at high and low temperatures, even after impact and under load. Saflex DG is unique in that it combines the meaningful performance and processing characteristics of standard PVB interlayers while allowing for balanced engineering practices, which can lead to more efficient whole building design."*[33]

Such bold claims have not yet been adequately backed up by experimental evidence, hence the need for unbiased analyses and studies (cfr. Appendix D). DG41 is comprised by long and heavy molecules ($M_w \cong 170\,000$) [69] and is already difficult to process in extrusion, compared to other more highly plasticized polymers (plasticizer level is about 20 parts of per hundred parts resin [91]). This low plasticizer level in increases the melt state viscosity, resulting in a difficult extrusion process. For the current state-of-the-art production lines, attempting to increase further the glass transition temperature of DG41 interlayer by dropping the amount of plasticizer will result in an unacceptably low flowability for extrusion, therefore necessitating a casting procedure which is not cost-effective. Being a PVB-modified material, the good chemical adhesion of DG41 to the glass surface essentially relies on the same chemical bonds described in §1.1.2.1.

1.1.2.4 OTHER INTERLAYER MATERIALS AND MULTILAYER INTERLAYERS

For reasons that will be discussed in Chapter 2, this manuscript will focus on the three interlayer materials described in the previous paragraphs. Nonetheless, it is worth mentioning that along with PVB, SG and DG41, other resins have been and continue to be adopted in vast portions of the glass lamination industry. Polycarbonates [49,92], polyurethanes [93], vinyl resins and other polymers or

[33] Solutia® press conference, St. Louis (US-MO), 9 February 2012.

copolymers include a wide range of applications; also, extensive efforts are being made to replace PVB films with alternate films.

Some polymers are not included in this treatise have found thriving and wide success in specific applications. Namely, because of its UV-screening and ageing properties [73], EVA is leader in the PV sector. EVA is a polymer which fluctuates from partial crystalline and thermoplastic to amorphous and rubber-like, but an amplified amount of vinyl acetate increases strength and ultimate elongation.

A fairly recent and extensive review of most interlayers used for glass lamination, most of whom will not be dealt with in this manuscript, can be found in the work of M. Teotia, R. K. Soni [48].

Lastly, as this topic will be present in part of the following discussion, it is worth mentioning the existence of so-called "multilayer interlayers" [69], interlayers comprising several coextruded or pre-laminated polymeric layers. Most applications of this technique aim to include within the whole interlayer thickness polymers with prominent mechanical properties but poor adhesion with glass. In doing so, the adhesion is dealt with traditional and reliable materials such as PVB, while the bulk of the mechanical resistance is assigned to the core layers (e.g. polycarbonate).

1.1.3 ADHESION BETWEEN GLASS AND INTERLAYERS

Adhesion is the macroscopic measure of the chemical attraction molecules of one kind exert on molecules of a different kind on an atomic level. According to the properties of the surfaces, adhesion can rely upon several mechanisms [94–96]: mechanical interlocking, chemical bonding, physical adsorption and electrostatic effects [96,97].

Within LG elements, adhesion between glass and polyvinyl-based interlayers is primarily due to the chemical bonds that form between alcohol groups comprised within the polymeric chains and the silanol groups on the surface of the glass (Figure 1.11). These combine to form a reversible but dense network of weak hydrogen bonds and beyond this point to some extent true chemical bonds [79,98].

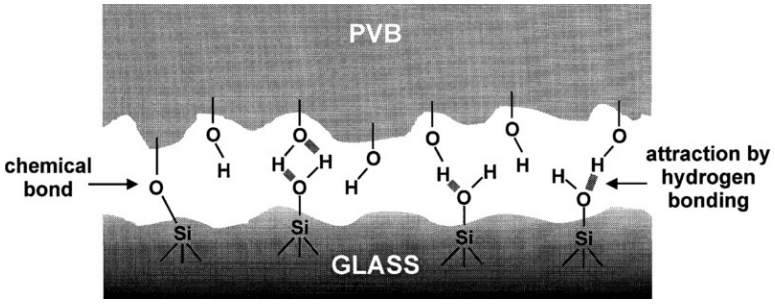

Figure 1.11 - PVB-glass chemical bonding mechanisms (Keller and Mortelmans, 1999 [79]*)*

A first discussion on non-mechanical factors influencing adhesion has been carried out by Keller and Mortelmans in 1999 [79] and further developed by Froli and Lani [98] for the influence of moisture during interlayer storage prior to lamination. A first glance on mechanical effects on PVB, after degradation in damp heat (DH) conditions[34], was given by Chapuis et al. [99] showing that ultimate failure in those conditions is always of adhesive nature rather than cohesive. While numerous

[34] 85°C and 85% R.H.

techniques have been employed to measure the strength of the adhesive bond, no single test has proved to be superior, more general or reliable than the others. In the last decade, effective non-destructive adhesion monitoring techniques (NDT) have been developed [100].

CST tests have been used to investigate the strength of the adhesion bond for PVB and EVA blends [99], showing that the layers of EVA exhibit a hyperelastic deformation until catastrophic delamination of the interface takes place and that hydrogen bonds among glass and PVB are easily degraded by moisture leading to a large decrease in adhesion after DH.

While the research on EVA and PVB (and DG41, as its adhesion is owed to the same molecular interactions than PVB) allowed to draw guidelines for degradation conditions, details on the chemical adhesion mechanisms of ionoplast interlayers have not been disclosed by the manufacturer nor yet seem to have been sufficiently investigated. Comparative observations on post-breakage effects of weathering on LG elements with PVB and SG showed that the strength of the adhesion bond for ionoplast-laminates is weaker than for polyvinyl-based polymers. Moreover, experimental analyses at high temperatures (40°C ÷ 60°C) showed that the strength of the adhesion bond for ionoplast-laminates is weaker than the internal cohesion.

As adhesion is an essential requirement for LG (it is the reason for which glass lamination was invented in the first place), Even though the analyses within this work were not directly focused in investigating the causes of delamination nor modelling its final effects, a description of the observations was deemed to be both useful and necessary (cfr. §4.2.4.5, §5.1.3 and Appendix C).

2 STATE-OF-THE-ART AND AIM OF THE RESEARCH

The expansion of the LG market in the construction industry, together with the development of an ever-growing number of interlayer materials, comes with new problems and questions. Most of these open topics are related to the contribution of interlayers to the performance on laminates. The scientific community and the standardization bodies are working to find reliable methods for safety assessment, characterizing materials properties and devising cost-effective production technique. In this Chapter, the scope of the manuscript is put into perspective after an overview on these efforts and a review of the state-of-the-art.

At point in time, most of the architectural LG is being manufactured by using PVB interlayers [8]. Since several researchers and companies are making efforts in developing alternative interlayers [69,101,102], more efforts should also be made for conceiving techniques for assessing these material properties in a consistent and reliable way. The specifics of these test methods should be designed according to the general principles of the Eurocode (Basis of structural design) [103] and to the design function within the final structural system[1] [7].

Glass being a brittle material, prone to sudden failure sometimes in the event of minor collisions, the partial- and complete-failure scenarios ought to be considered in a thorough and reliable LG design process. Few studies have been made on this topic; and while predictive post-failure models supported by experimental analyses have been asked for by some researchers [104,105], still few works have produced dependable results [13,88,106]. Further work should be made for developing models for LG fracture analysis and post-failure behaviour [48].

The following two paragraphs summarize the state-of-the-art in this field: first dealing with this topic from the perspective of standards and regulations, then from the perspective of the scientific research[2]. Finally, put into perspective within both these frameworks, the aim of the research and proposed methodologies are presented.

[1] For instance, the performance of interlayers to be used in glass lamination should rather not be evaluated for compressive or flexural actions nor for direct impact, as those properties are not primarily tied to the role of the material within the sandwich structure of LG. On the other hand, tensile or shear tests could yield useful results for practical applications.

[2] In the LG field, it appears that the standardization bodies are guiding behind the scenes the scientific research the toward increasing levels of detail. Namely, standards are providing researchers with a framework of basic assumptions, ways of thinking and methodologies that can be accepted by the housing market. A similar scientific evolution path is described by T. Kuhn in [322] in terms of shifting paradigms: *"the paradigm determines the kinds of experiments scientists perform, the types of questions they ask, and the problems they consider important. A shift in the paradigm alters the fundamental concepts underlying research and inspires new standards of evidence, research techniques and pathways for theory and experiment."* Such paradigm-shifting revolutions produce *"a shift in the standards by which the profession determined what should count as an admissible problem or as a legitimate problem-solution."*

While the topic of structural elements made with glass can be wide and multifaceted, according to the intended purpose of this work, the discussion will exclusively address issues related to LG and specific aspects connected to interlayer mechanics. Therefore, the reader should not be surprised if other topics, which are also debatably needing improvement or refinement, will not be mentioned or thoroughly analysed (e.g. general design principles, properties of glass as a structural component, issues related to sealants and other adhesives, insulated glazing, etc).

2.1 SHORTCOMINGS IN THE REGULATORY FRAMEWORK

A brief but wide-ranging review of regulations on architectural LG has been discussed when introducing the topic in Chapter 1. Nonetheless, it appears that providing a complete overview on the regulatory framework is a complicated task for at least three reasons: first, numerous European standards or guidelines live side-by-side with former regulation, some active and others outdated or withdrawn (but still used in practice) [7]; second, while the glass industry can rely upon internationally acknowledged manufacturing standards, regulating the LG industry involves the necessity to standardize an emerging interlayer market, populated by a multitude of new products along with traditional ones; third, while several simplified models exist[3], a fundamental approach for LG design, one that should be based on strong theoretical bases, is still missing.

While some standards do not officially attribute to interlayers any structural capacity within LG elements[4], even those who do are not providing nearly enough information for actual model implementation. Italian technical document CNR-DT210 [38] is arguably among of the latest and most complete attempts for standardization of LG design. Nonetheless, the document states:

> *"Mechanical properties of the elastomers [used as interlayers] are strongly dependent from time and temperature; in any case the stiffness of these polymeric materials is much lower compared to glass, so even provided the adhesion is effective, polymers are subject to high angular sliding." 5*

And,

> *"[…] the viscoelastic behaviour of polymeric interlayers is modelled as linear elastic materials. In particular, the shear modulus G, which generally varies according to the operating temperature, loads duration and aging, is considered constant." [5]*

Statements like these, considering the outcomes of the experimental campaigns presented within this manuscript, will likely be seen as oversimplifying the response of a diverse and complicated panorama of interlayer materials.

---

[3] Examples of standard-adopted models for LG response are: *Épaisseur équivalente des vitrages feuilletés* (CSTB 3488, 2011), *Interlayer stiffness family model* (prEN16612, 2013), *Wölfel-Bennison* (sandwich model [323], 1987, also adopted by ASTM E1300), *Effective Laminate Thickness* (2009, [89]), *Enhanced Effective Thickness* (EET, 2012 [113], adopted and integrated by CNR-DT210).

[4] On the other hand, such standards may propose an increase in the maximum design stress for glass plies in LG elements, which means they are indirectly accounting for the collaboration between glass slabs, due to the coupling effect provided by the interlayers (e.g. TRLV ,2006, *"Technische Regeln für die Verwendung von linienförmig gelagerten Verglasungen"*).

[5] Translated from Italian.

Throughout the past two decades, with a remarkable acceleration in the last five years, the scientific community has been progressively moving towards a more rigorous approach in dealing with LG load bearing capacity. This new paradigm is based on first principles for laminates mechanics and on proper, time-dependent, constitutive equations for the interlayers [64,107,108]. While this approach seems promising, it also appears at this time excessively complicated and lengthy for most practical LG structural applications, inevitably requiring complex numerical models (provided the materials properties have been established in a reliable way). Standards and technical documents on occasion mention to these numerical analyses as level-2 and level-3 models, with 2-D shells and three-dimensional solid elements respectively. Comments and examples come with a few prescriptions, but mostly relate on geometric or numerical issues. So far, for instance, requirements and suggestions have not included specific details on the constitutive equation to be used for defining the interlayer elements response[6], which is understandably one of the key issues at stake.

For the sake of presenting features and voids in the existing regulatory framework, along with perhaps some misleading instructions, the aforesaid Italian standard is taken as case-study. From the point of view of a structural engineer attempting a design over LG, it appears that two choices may be source of decisive dilemmas:

- choice of the model for LG response among the many available,
- selection of the most appropriate constitutive equations for interlayers: linear elastic (LE), linear viscoelastic7 (LVE), non-linear elastic (hyperelastic HE), non-linear viscoelastic[7,8] (NLVE).

An often-underestimated aspect to bear in mind, is the general lack of understanding of polymers and adhesives peculiarities by structural engineers and architects. Training in material science guided those professions toward arguably simpler – or at least different - materials, that are only marginally influenced from variables like time and temperature. With that in mind, it is of paramount importance that standards and guidelines help them in choosing the most appropriate design path. Besides, the awareness is growing that polymer particularities might require adapted assessment methods of corresponding building products and applications, specifically regarding time-dependant behaviour and ageing phenomena [109]. For instance, scientific evidence has shown that viscoelastic models are capable to describe the evolution of interlayer properties over time [37,64,110–112], while hyperelastic models may be more suited for the interpretation of brief effects [14–16]. Simple distinctions and directions like this one seem to be missing in the existing standards framework.

[6] More precisely, there are references to elastic approaches *à la* Newmark (Newmark et al. [160]), but no mention is made relatively to constitutive equation other than LE.

[7] For linear viscoelastic materials, the isochronous response is linear, but the effective modulus decreases with time, so that the stress-strain curves at different times are separated from one another. When a viscoelastic material behaves nonlinearly, the isochronous stress-strain curves begin to deviate from linearity at a certain stress level [324].

[8] Non-linear viscoelastic models for interlayer materials have already been adopted in LG studies, so it made sense to include them in this list, as they appears to be the frontier of the research in this field [108,325]. Nonetheless, such models are not mentioned in standard and guidelines (e.g. CNR-DT210), as neither are mentioned some more complex models such as the visco-elasto-plastic ones (linear and non linear, that to my understanding have not yet been successfully adopted).

In dealing with time and temperature effects for the polymeric interlayers response, standardization bodies seem to have at least partially acknowledged the inherent difficulty of designers to deal with those matters with a rigorous approach. Therefore, as previously hinted in the quote from the Italian standard, linear elastic simplified models (e.g. EET model by L. Galuppi & G. F. Royer [113]) are being provided, which can account for constant values of the interlayer shear modulus G_{int}. To deal with a diminishing modulus over time and as a function of temperature (due to the viscous deformations of the polymers), a designer ought to perform multiple analyses for varying values of the shear modulus.

Provided a reliable formulation to calculate the effective thickness of laminated glass can be identified, a significant obstacle arises when attempting to find reliable values of G_{int} for given time and temperature.

$$G_{\text{int}} = G_{\text{int}}(\text{time}, \text{Temperature})$$

While standards take on the linear viscoelastic approach and time-temperature superposition principles [68,114,115] (cfr. §3.1.3.1 and §3.1.3.5), few mentions are made on techniques for assessing interlayer properties from experimental analyses, in a way which is compliant with practical LG applications[9]. In theory, the Eurocode Annex D (design assisted by testing) is always valid for testing of new materials or obtain specific material properties using specified testing procedures. Nonetheless, this document does neither includes procedures for load-bearing polymers nor deals with dependency upon time and temperature. A general framework on the planning of tests is given in terms of (among others): specifications of specimens and sampling, testing arrangement, evaluation and reporting. Alas, some have complained [7,105] that the provided instructions are not specific enough to set up for standardized, relevant and economically-viable experimental programs for definite polymer components and LG systems.

Various documents suggest the use of dynamic tests to characterize the long-term properties of interlayer materials [38,116,117]. Such procedures, taking advantage from a correlation among dynamic tests and viscoelastic parameters (cfr. §3.1.3.4) [114,118], are well-established among plastic material industry standards, but fundamental questions remain on whether or not it is always justifiable to extrapolate very short- and very-long term properties from cyclic tests. Besides, some authors and technical documents suggest that the most appropriate way to deal with interlayer mechanics is to test them under conditions which are as related as possible to those encountered in practical applications [7,109,119].

Naturally, (full scale[10]) bending tests are also deemed to be good performance indicators for LG units [38]. Sadly, prescriptions seem to fall short once again: while in the absence of accurate data there is mention of temperatures of $50℃$ and $-10℃$, no instruction on parameters like strain and strain rate can be found.

[9] At an international level, the European Committee for Standardization (CEN) has issued the draft standard prEN-16613 *"Glass in building - Laminated glass and laminated safety glass - Determination of interlayer mechanical properties"* (first issued in 2013, updated in April 2017), proposing a classification of polymers in "interlayer stiffness families". This ranking system has been said by many to be taken with great caution, because while being very simple and easy-to-use, it is deemed to be excessively inaccurate and flawed [326] (for instance, it neglects the influence of known important factors such as the loading conditions, typology and size of the LG element, cross-sectional details on the laminated assembly, etc).

[10] The term "full-scale" is not explicitly adopted in [38], but it seem implied by the context.

2.2 SCIENTIFIC LITERATURE OVERVIEW

Aside from patents filed in the first half of the 20th century, few researches can be found regarding dedicated scientific works on LG. Among the first, at least two start to deal with this topic on a performance-based level: one by J. Widman in 1965 [120] and one by R. Reiser and J. Chabal in 1967 [121]. Nevertheless, both documents were openly dedicated to the automotive sector, focusing on the correlation between interlayer thickness and penetration of impacting objects.

At that time, few examples of architectural LG applications could be found [122]; only by the end of the 60's and the beginning of the 70's works on architectural LG start to show up. Namely, M. Barakat and J. Hetherington in 1970 are the first to mention "laminated glass" among architectural building materials [123], while the first performance-assessing study in that field is due to the work of J. Hooper in 1973 [43] with a paper titled *"On the bending of architectural laminated glass"*.

From this point on, scientific works on LG start to proliferate. To provide a comprehensive but non-dispersive handling of the issue, I believe it makes sense to divide the pertinent scientific body in five macro-categories, depending on the approach on laminated architectural glass and corresponding research goals:

- interlayer chemical and mechanic properties,
- sandwich models for LG,
- reinforced LG,
- pre-stressed LG,
- safety and post-failure LG performance.

For all these topics, evidence has emerged of a major increase in the interest of the scientific community and volume of published researches in the last 10-15 years.

2.2.1 PROPERTIES OF INTERLAYERS USED FOR LG

Research on interlayer properties for LG, oriented towards structural - construction industry - applications, has only really started to show up in the last two decades. Experimental works within the last century were typically more oriented towards transportation and safety with respect glass fragments expulsion, with little interest in assessing other mechanical properties. Nevertheless, significant works (mostly published in books rather than research papers) laid the ground for all recent studies on the complex mechanical properties of both interlayers and LG.

Mathematical models have been proposed throughout the last century, to understand the polymer response to small and large deformations, along with the viscoelastic and hyperelastic effects and the dependency of those upon temperature. Details on these theories will be recalled and discussed throughout this manuscript when needed, and it feels redundant to reference them here one by one.

Regarding the study of plastics used as interlayers in LG, the acknowledgement of the importance of modelling mechanic effects other than simple adhesion was first acknowledged in 1980 by K. Katsuki et al. in a pioneering work *"Laminated sheet composed of thin glass and plastic sheets"* [124]. The research underlined the central role of glass in such composites from the point of view of functional properties such as transparency, hardness and chemical durability. From there, the authors tried to use thin glass plies ($1\,mm$) as protecting interfaces for a thicker core of polycarbonate (up to $3\,mm$), bonded to glass using EVA or PVB. In the conclusions, the authors inevitably admitted that much had yet to be done for the correct use understanding of thermoplastic materials within LG elements.

Even though the fundamental origin of all properties of interlayer materials could be - in principle - reunited with a unified theory, this has so far proven to be out of the reach for the current scientific understanding. Far from such research of a fundamental truth, investigations on interlayer properties for architectural purposes have mostly shifted towards a phenomenological level of understanding, splitting up different properties (i.e. interface and bulk responses, chemical and optical properties, etc). To introduce to the aspects which are most relevant for this work, a breakdown in two categories seems useful:

- investigations on the interface strength and effects of weathering and ageing,
- works oriented towards assessing bulk properties of interlayers.

While a traditional classification system exists, dividing plastics in thermoplastics, thermosets and elastomers according to the type and density of the cross-links [10] (cfr. §1.1.2), such division will not be used for this treatise of the scientific research state-of-the-art for three reasons: first, it is not always obvious which category a product belongs, as pointed out by other researchers [7,59], therefore the classification might emerge as equivocal or inconsistent, second, most of the scientific research has been made on PVB, with far less investigations on other materials, and third, this classification is rarely mentioned by the scientific works which will be mentioned in the following.

As a general idea, good practice would be to design and perform experimental analyses which are a good representation of the final design, rather than trying to extrapolate mechanical properties from different – although standardized – testing techniques. Joined to a cautious indication of safety factors, a comprehensive overview of meaningful properties for well-defined applications is the most reliable approach when designing an experimental campaign on thermoplastics.

> *"The necessity is stressed to converge to as limited a number of test methods as possible that are also adequately simple and can therefore be applied in most research laboratories." (Ranocchiai et al., 2017 [118])*

The structural contribution of interlayers within a LG element essentially sets upon balancing two properties: the inner cohesion/response and the strength of the adhesive bond with glass. Neglecting either one of those aspects may lead to dangerously overestimate the performance of the LG layered structure.

adhesion, ageing and weathering effects

The durability of LG being a relevant problem in all sectors of the industry, observations, patents and researches have always paid attention to factors affecting the properties of the materials over time. Since the dawn of glass lamination for automotive and aeronautical purposes, it has been known that weathering and radiation are parameters which can facilitate the loss of adhesion. In recent years, researchers have accepted the challenge to tackle several different aspects related to delamination: temperature, humidity, UV radiation, boundary conditions, mechanical actions and combinations of these. While all seem to be co-factors, it is fairly accepted that humidity plays a greater role in undermining the strength and reliability of the chemical bonds[11], that UV radiation is primarily responsible for chromatic changes but can also affect mechanical properties of interlayers (along

[11] Mainly during the lamination process, but also throughout the whole life span of the LG elements, due to infiltration of water and moisture along the outer borders.

with the chemical ones) and that a mechanical action is ultimately needed to detach the materials, even with a severely jeopardized adhesion.

The great influence of storage humidity for interlayers, prior to the lamination with glass, which appears to be vastly exceeding the effect of moisture and weathering for laminated elements [65]. An almost dedicated research in that direction was performed by M. Froli and L. Lani from University of Pisa in 2011 [98], concluding that the most important parameter in the lamination process is the humidity storage of the PVB.

Among the latest researches on investigating adhesion in LG in 2012, Y. Sha et al. [125] studied the correlation between the peak load and the mechanism of debonding for PVB, resulting in a relationship which could be fed to FE models. Using peel tests, and a different approach, a study on glass-PVB interface properties was performed a few years after by J. Pelfrene et al. [126], highlighting that there seems to be no clear relationship between the peeling force and the Mode I activation of fracture for characterization of the interface strength [34–36]. Moreover, this work underlined that no certain correlation could be established among the presented experimental results and other publications in this field, because the large-strain behaviour of PVB interlayer is yet to be satisfactorily documented and understood. Adhesive resilience of specimens with initial delamination at different regions and ratios was recently carried out by E. Dural in 2016 [127]. Using a high-resolution camera and a numerical morphological analysis, Dural was able to obtain a relationship between delamination ratio and the residual strength of delaminated glass units. The analysis concluded that the behaviour of LG units is highly nonlinear, and that the strength of laminated glass is influenced by the location and extent of the delaminated surface.

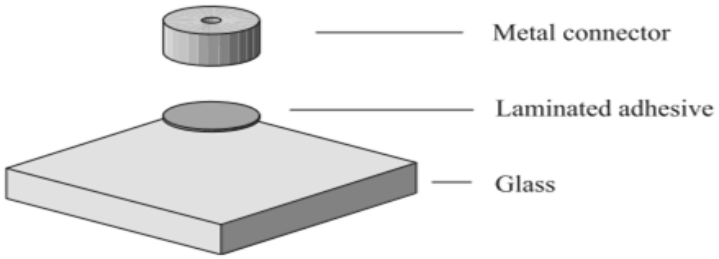

Figure 2.1 - specimens used in the tensile tests (Santarsiero, 2017 [128]*)*

C. Louter and other researchers have also shown interest in the topic of adhesive properties of interlayers in a series of recent works between 2014 and 2017. First, effects of environmental impacts on durability of laminated glass plates with interlayers were investigated for three types of interlayers: SG, EVA and PVB [129]. This initial research opened to two relevant "twin" publications for shear [130] and tensile [128] strain rate correlations with temperature for laminated connections between glass and metallic connectors. In these two researches, the authors investigated both properties of a Transparent Structural Silicon Adhesive (TSSA) and SG interlayer, observing two interesting phenomena with the loss of adhesion: the whitening in TSSA and the development of bubble within the SG adhesive, hinting to the hypothesis of a dominant hydrostatic component of the stress tensor as the consequence of the large confinement state of the adhesive. The experimental investigations also showed that temperature and strain rate variations have important effects on the mechanical response of the connections; namely, that resistance is proportional to the logarithm of the strain rate, and decreases at high temperature. More specifically, a logarithmic law was proposed

for the strain rate effects for both TSSA and SG connections, while linear and inverse hyperbolic-tangent-based laws were instead proposed for the TSSA and SG temperature effects, respectively.

Results of the last experimental analyses suggest that much has yet to be done for understanding and reliably anticipate the adhesive properties of interlayers used for LG. Besides, while the research on PVB can boast many researches, those are admittedly not yet fully relatable for the numerous aspects of interlayer rheology which come into play. Conversely, research on new interlayer and adhesives is not yes sufficiently developed to yield wide-ranging conclusions.

Led by L. Andreozzi, within 2013 and 2015 a team of researchers from Universities of Pisa and Firenze also delved into the mechanics of interlayer adhesion and correlations to environmental effects [131–133]. In their project, the authors presented studies on thermo-viscoelastic properties of PVB, for varying weathering actions (humidity, thermal cycles and UV radiation). The analysis highlighted distinct damage mechanisms, promoted in different extents by the different exposure to environmental effects. Results proved for the first time that RH can influence both the adhesive and bulk properties PVB, calling for further investigations to separately analyse these features. The authors concluded that degradation related to solar radiation can produce major changes to mechanical properties of PVB interlayers, to an extent that originally reliable numerical evaluations on the response of LG structures may become incorrect over time.

bulk properties

Among the first works to show interest in bulk properties of interlayers, a research issued in 1981 by J. R. Huntsberger included a study of mechanical performance of PVB [134]. As usual, boosted by the needs of the automotive department rather than the architectural one, a model for windshield fracture event was described in terms of interactions among mechanical responses of interlayers and fracture characteristics of glass. Anyhow, this pioneering research still seems very much oriented towards taking steps for increasing safety with respect of the expulsion of glass fragments in the event of colliding bodies.

The first work to openly mention PVB properties for architectural glazing is possibly the paper from C Vallabhan et al. published in the *Journal of Materials in Civil Engineering* in 1992 [135]. Shear force-deformation characteristics of PVB were studied via direct-shear tests (Figure 2.2), similarly to those performed by geotechnical engineers for determining soil characteristics in a specified plane. While failing to emphasize temperature effects and openly reference to viscoelastic properties, the major conclusion of the research was that the shear modulus of PVB interlayer is *"very dependent on the amount shear strain, and not on its thickness"*.

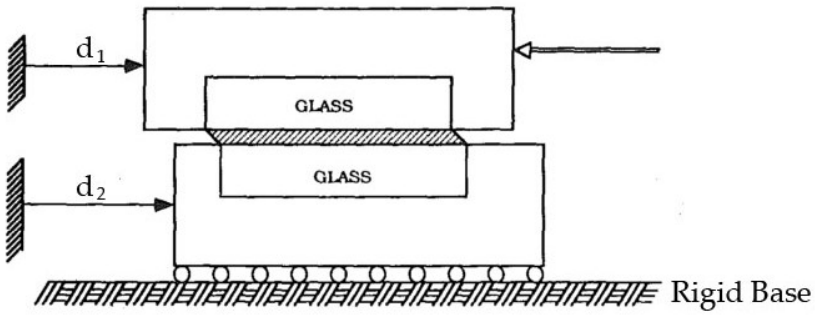

Figure 2.2 – scheme of a setup used for direct shear tests (Vallabhan, 1992 [135]*)*

Thermal properties and the dependency on those of the mechanic response of PVB were investigated a few years later by Egyptians N. M. S. El-Din and M. W. Sabaa [136]. While the research was certainty more oriented towards a chemical and optical analysis of degradation rather than dependency of mechanical properties, the conclusions discussed how the intrinsic viscosity decreases with increasing temperatures. According to the authors, this indicates that the thermal degradation is mostly accompanied by a main-chain scission, rather than splitting of the cross-links (cfr. §1.1.2).

Apart from similar trailblazing works, of which other examples can also be found, as indicated in the first part on this paragraph, the largest part of the research on interlayers properties is found within the last two decades. A detailed comparative study, complete with a state-of-the-art of researches and methods used for assessing of the mechanical interlayers, was recently issued from the same Italian team from Pisa and Firenze mentioned for their analyses on adhesive and durability properties of interlayers (see above). As the panorama of techniques and hypotheses is admittedly extremely variegated, the authors took a first effort for classifying test methods used for the characterization of interlayers, according to the time load history. The convenient scheme proposed within the work of G. Ranocchiai et al. [118] is re-proposed in Figure 2.3 with some integrations.

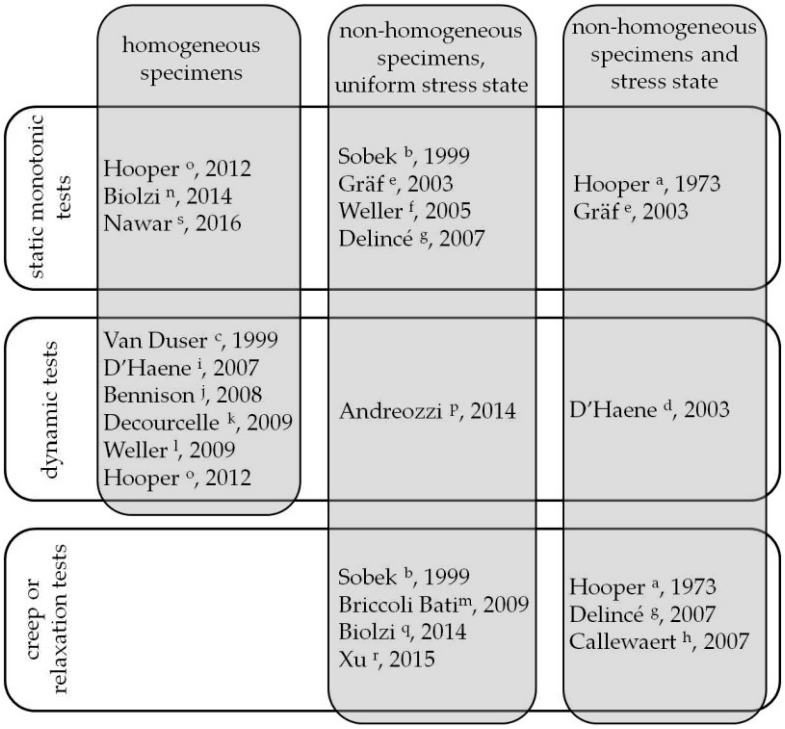

Figure 2.3 - schematic representation of the interlayer studies proposed by Ranocchiai et al. in 2017 [118]*, integrated with a few additional and relevant works.*

References for studies cited in Figure 2.3: [a][43], [b][137], [c][11], [d][138], [e][139], [f][140], [g][141], [h][142], [i][143], [j][54], [k][144], [l][83], [m][145], [n][146], [o][147], [p][148], [q][65], [r][149], [s][150].

The article provides a detailed discussion on methods used to determine the viscoelastic behaviour of interlayer polymers in all those studies, to a point that reporting those once again within this work would be undoubtedly redundant. Individual researches will be mentioned again in the following when appropriate, to support the both the design and results of experimental investigations carried out throughout Chapters 4 and 5.

Form a conclusive analysis, having looked at most of the researches on the mechanical characterization of interlayers, the following emerges:

- almost all the researches on bulk properties focus either on hyperelastic response or viscoelastic properties,
- while the linear thermo-viscoelastic correlation is widely accepted, no studies are found for effectively correlating temperature and hyperelastic response,
- most of mechanical characterizations deal exclusively with PVB, while other interlayers are rarely dealt with,
- researchers agree on the necessity to converge on a limited number of accepted test methods for the characterization of different aspects of interlayers response; such envisaged unification could help in the process of comparing properties of different materials on a similar scale, which would be advisable considering that these materials have ultimately identical roles in LG elements, therefore need be chosen knowing to *pros* and *cons* of each one of them.

Regarding the emerging macroscopic properties of interlayers, studies have attempted to derive the engineering properties from the microscopical interactions. Still, several open questions remain to this day for fully understanding how the microscopical interactions work to govern the measured macroscopic effects. One of those, is the proportion to the overall response between intermolecular and network effects (cfr. §1.1.2), which is directly concern the interpretation of many experimental tests. Namely, the standard tensile ones.

> *"The distinction between the viscoelastic or viscoplastic nature of the deformations is however difficult to establish univocally and depends on the conditions of measurement"*[12] ~ Sharpe 2008 [57]

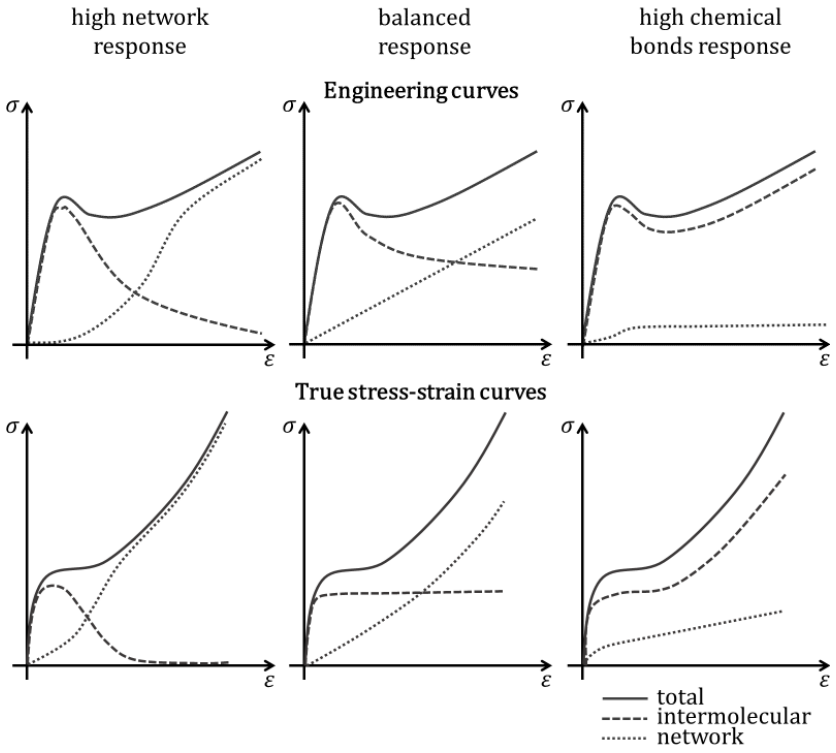

Figure 2.4 - intermolecular and network interaction scenarios (Vegt, 2002 [59]*)*

[12] Visser in 2009 seems to address the same question with regard to the distinction between reversible and irreversible deformations. [7,270]

Figure 2.4 shows a few qualitative examples of plausible decompositions for some hypothetical thermoplastic materials on both *engineering* and *true* stress-strain correlations (indeed, for a given material and testing conditions, there only is *one* correct decomposition).

As an empirical rule, studies have confirmed that intermolecular effects, are dominant for small and very small strain, while network effects, when present and significant, govern the response for large deformations [72,151–154]. Likewise, the emerging viscous properties of thermoplastics are believed to be related to these two microscopic mechanisms [57,155]:

- viscoelasticity due to the uncoiling of the molecules network,
- viscoplasticity ascribable to breaking of intermolecular cross-links.

An attempt for a combined description of intermolecular and network response was proposed by Klompen in 2005 [156] and recently re-discussed by Delincé in 2014 [7] (in the following, KD approach/decomposition). This analysis incorporates both the thermo-mechanical history (represented by the parameter S [157]) and softening kinetics, attempting to decompose the total response into different terms, each dependent only on some of the known influential parameters. The proposed constitutive model was then used to study polycarbonate response [50,156], distinguishing the contribution of secondary interactions due to molecular interactions σ_s from the network effect σ_r [13]. In turn, a further decomposition was proposed for the driving stress in a strain-rate dependent *rejuvenated yield stress* $\sigma_{rej,0}$ and a *yield-drop* $\Delta\sigma_y$, function of the thermomechanical history S (Figure 2.5).

$$\sigma = \sigma_s + \sigma_r$$

$$\sigma(\varepsilon, \dot{\varepsilon}, S) = \overbrace{\sigma_{rej,0}(\dot{\varepsilon}) + \Delta\sigma_y(S)}^{\sigma_s} + \sigma_r(\varepsilon)$$

This decomposition assumes that both the yield-drop[14] and "rejuvenated" stress-hardening functions are independent from the strain rate[15].

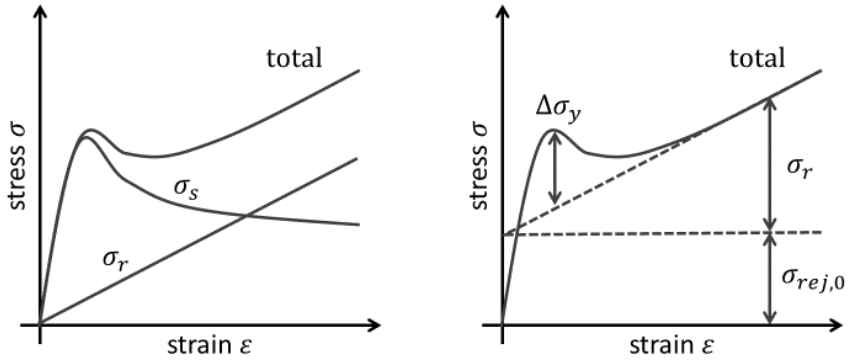

Figure 2.5 - stress decomposition (Klompen, 2005 [156]*)*

[13] This method is consistent with the original 1968 Haward and Thackray (HT) approach [76]

[14] The softening part of the curves in Figure 4.4, well recognizable in the experimental analyses for SG and to some extent also for DG41.

[15] Both hypotheses that doesn't seem to be accurate in our analyses (cfr. Figure 5.2 123 with comments in §5.1.1.2). Moreover, the yield-drop function would be required to output initial negative values to correctly describe the material response for very small strains, something that doesn't seem to have an intuitive physical meaning, if any.

2.2.2 LG MODELS AND FULL-SCALE EXPERIMENTAL ANALYSES

The field of modelling the mechanical response of laminated elements is, by itself, a very complicated challenge, let alone having to deal with complicated materials such as thermoplastic interlayers. Structural response of LG elements stands amid two limiting cases: a *layered* limit, where all glass plies are allowed to slip freely one over the other and the interlayer contribution in entirely neglected, and *monolithic* limit, where the plane sections conservation hypothesis stands and the interlayer is assigned the same properties of glass [11,41,158,159]. Since the middle of the 20th century, two approaches have been carried out and progressively refined, to provide accurate and/or simple tools for predicting where the actual LG stands between these two limit cases: a numerical approach and an analytical one (exact or simplified), both supported by experimental analyses. To overview the path of the research leading to the current state-of-the-art, the two approaches – which are nevertheless deeply interconnected – will be examined separately.

Analytical approach

Equations for modelling three-layered sandwich structures, with a thick and soft inner core, were developed in the early 1950s by N. M. Newmark [160], E. Reissner [161] and C. Wang [162]. While the first was conceived of for steel-concrete structures, and could hardly be applied to LG elements, the latter two models accounted for transverse deformation and compressibility of the central layer, but they neglected the bending stiffness external plates and were thus also of little use for practical LG design. At the end of the decade, K. S. Pister and S. B. Dong [163] developed a set of equations for large deflection in laminated plates, but - like the Newmark model - used the hypothesis that plane sections remain plane [164]. As hinted in Chapter 1 and further discussed in the following, this hypothesis can hardly be applied to LG structures for out-of-plane bending scenarios.

A kick-start to the investigations in this field, specifically thinking about LG and practical applications, was brought more than 20 years after by American researchers R. A. Behr, J. E. Minor and C. V. G. Vallabhan between 1985 and 1993. In collaboration with others, this group issued many pioneering works for characterizing the response of architectural LG under lateral pressure [165]. By the end of their investigations, a mathematical model was developed using an energetic approach. The comparison between the mathematical model (which could only be used for uniformly distributed loads) and the experimental analyses proved to be good, but still needed large improvements to cater a variable shear modulus of the interlayer and different boundary conditions. Experimental and theoretical investigations within this decade-long project took stock of a 20-year period by several other investigators, to ultimately provide a predicting model for architectural LG under lateral pressures, validated for practical engineering purposes[16]. Notable works of this research group are:

- 1985, *Laminated Glass Units Under Uniform Lateral Pressure* [41] (Behr, Minor, Linden & Vallabhan)
- 1986, *Load Duration and Interlayer Thickness Effects on Laminated Glass* [166] (Behr, Minor, Linden & Magnus)
- 1987, *Stresses in Layered Glass Units and Monolithic Glass Plates* [167]

[16] Using these results, the effect of different interlayers and temperatures have been studied in recent years by El-Shami et al. [327], comparing them with FE models and new experimental data.

(Vallabhan, Minor & Nagalla)
- 1990, *Failure Strengths of Laminated Glass* [159]
  (Minor & Reznik)
- 1993, *Structural Behaviour of Architectural Laminated Glass* [158]
  (Behr, Minor & Norville)
- 1993, *Analysis of Laminated Glass Units* [168]
  (Vallabhan, Das, Magdi, Aşik & Bailey)

After those contributions, the investigations seem to have stalled for a few years and no major advancements is to be found. With the turn of the century and the decisive growth of the architectural LG market, the volume of research in the field of glass lamination has certainly moved up a gear, as already observed in the previous paragraph when talking about properties of interlayers. An analytical approach to determining the impact strength of laminated glass was proposed by A. I. Shutow et al. [169], while S. J. Bennison et al. were the first to publish a research about LG with a "stiff" interlayer (SG[17]), which was explicitly indented to enhance properties of architectural LG [102]. Based on experimental analyses, the first correlations between bending stiffness and temperature were provided by S. H. Pang et al. [170], for ambient temperatures close to usual indoor environments (18°C to 35°C).

LG plates and beams (where the sandwich structure is loaded in its own plane) laminated with several interlayer materials, were investigated by C. Louter et al. at Delft University of Technology. The researchers studied both reinforced and non-reinforced LG elements at different temperatures with four-points bending tests [47,171]. Among other results, the investigations showed that SG-laminated elements had the lowest midspan deflection, volatile displacements and longitudinal strains under different temperature conditions. Similar tests were also proposed by L. Briccoli Bati et al. [145], comparing experimental results to the Hooper[18] [43] and numerical models.

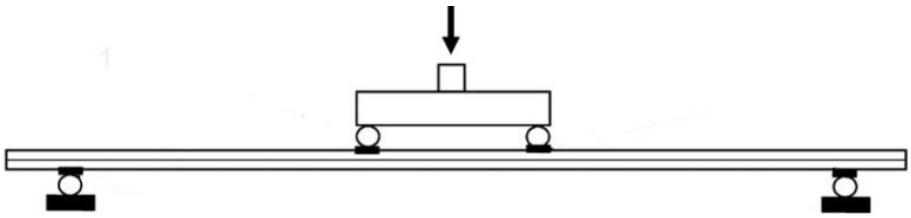

Figure 2.6 - scheme of four-point bending tests used by Louter [171] *and Briccoli Bati* [145]

By means of similar tests, K. Pankhardt and G. L. Balázs investigated the effects of temperature and fracture pattern on the residual load bearing capacity of partially damaged LG using EVA and PVB [172]. The researchers observed that if one glass ply fails within an n-glass plies LG element, the residual load-bearing capacity is higher than that of laminated glass consisting of $n-1$ glass plies, suggesting that the interlayer on the top of the fractured glass layer may function as a kind of strengthening element[19].

[17] At that time known with the commercial name of SGP, where the "P" stands for "Plus".

[18] By the means of which an approximate solution to the elastic problem of the composite glass beam subjected to four-point bending test was proposed.

[19] Even if the authors never mentioned this term, the effect observed called "tension stiffening" by other researchers in succeeding works.

The state-of-the-art of analytical models for LG sandwich structures is set by two approaches, both issued by Italian researchers in 2012: an analytical, exact and explicit model developed by P. Foraboschi [173], and the *effective thickness*[20,21] approach by L. Galuppi and G. F. Royer-Carfagni [113], embracing classical formulations as particular cases but allowing any constraint- and load-condition. Among others, both models accept the same assumptions, namely:

- glass and interlayers are LE materials,
- perfect adhesion between the layers (i.e. no delamination occurs).

Both models can certainly coexist, having two different goals and fields of application. The Foraboschi model provides a full description of the mechanical phenomena of bending in sandwich structures, and despite its arguable complexity it can be used to validate both numerical and approximate models (such as the Galuppi-Royer one). Conversely, as P. Foraboschi alleged, among all approximated solutions, an *effective thickness* (EET) approach can provide the best approximation. Moreover, it has been shown that results from the EET method are close to results from the exact model (with a guaranteed maximum relative error limited to 10%), but it is also typically conservative, providing overestimations of both deflections and stresses. While practical expressions [174], a time-dependent load analysis [112] and applications to viscoelastic interlayers [64] have been provided by the same authors of the EET, a fairly recent and successful validation of the model has been provided by F. Pelayo et al. [112] for buckling of LG beams.

Numerical approach

Unsurprisingly, because of the difficulty in dealing with the problem in a rigorous way, studies of sandwich structures have embraced numerical models since the early days of FE applications. Reports can be found dating back to the late 1960s, with the FE method extended to LE analyses of multilayer beams and shells.

Contributions on numerical models are countless[22], and the prospect of giving a comprehensive review of all researches is out of the reach of this work; besides, numerical models will only be dealt with marginally. Also, differently from analytical approaches to the theory of sandwich structures, numerical models have hardly been developed especially for LG applications. Often, numerical models are developed for multi-purpose applications, to be later used, validated and commented on differently in all engineering fields. Concerning LG applications, numerical models have been used for the study many of the aspects which are not yet covered with reliable analytical solutions. Among these:

- glazing resistance to blast-loads,
- buckling of compressed columns and beams,
- point-supported structures,
- concentrated actions,
- colliding bodies (impulsive effects),

[20] Possibly for its user-friendly characteristics and adaptability to numerous practical design situations, this is the approach is proposed in the Italian technical document CNR-DT210 [38].

[21] The "effective laminate thickness" idea draws from the intuition of Bennison et al. [89], in turn elaborating on the work of E. Wolfel n 1987 [323], to introduce an equivalent moment of inertia for the LG cross section. Once the effective stiffness is established, deflection and curvature can be calculated and, consequently, the maximum stress in the single glass plies.

[22] [14,98,211,220,328–331,104,106,108,139,141,145,158,171], only to reference a few.

- visco-elastic decay due to interlayers mechanics,
- non-linear analyses,
- crack initiation and post-breakage behaviour,
- reinforced elements,
- delamination,
- complicated or varying boundary conditions.

Just to mention some researchers that have openly dedicated much of their attention to the application of numerical models to LG structures, M. Z. Aşik, a computational mechanics specialist from Middle East TU (who also had been involved with C. V. G. Vallabhan at Texas TU in the early 1990s) presented several relevant studies between 2003 and 2009 [175–178]. In more recent years, C. Bedon and C. Amadio have studied several LG properties using FE models with Abaqus[23] and occasionally previous experimental analyses (Figure 2.7) [179–185].

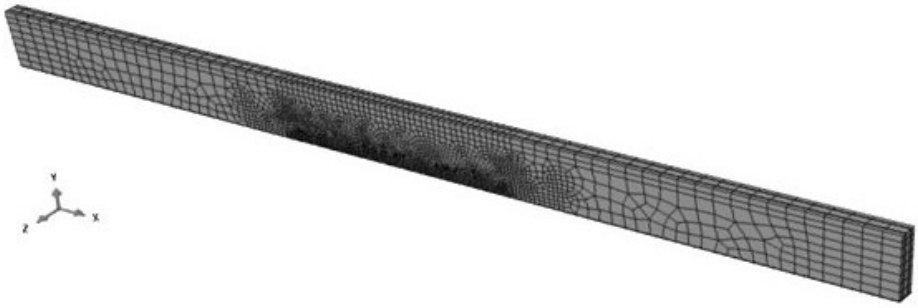

Figure 2.7 - 3D FE model by C. Bedon, 2017 [184]*, for the numerical interpretation of 2014 tests by C. Louter et al. on pre-stressed LG beams* [186] *(cfr §2.2.3)*

2.2.3 REINFORCED LG

In literature, with the term *"reinforced laminated glass"* scientists and engineers are generally referring to composite elements based on a LG core, with the addition of stronger and/or more ductile materials which are either able to enhance the SLS or ULS performance. The knowledge about synergistic features of LG reinforced composites relates varies depending on materials and techniques used. Numerous examples of such performance-enhanced LG can be found across the body of international researches, once again with a decisive increase in the last decade.

The interest in reinforcements for LG structures start to come up by the end of the last century. A concept for a steel-glass-polycarbonate beam presented in 1997 by F. A. Veer et al. in the bi-annual *Glass Performance Days conference* was later on updated in 2001 and once again in 2003 [187]: a three-ply LG with polycarbonate interlayers and a stainless steel profile in the tension zone. In later years, more examples and similar ideas have been proposed and tested; namely: plain or perforated metallic plates and flanges (2003-2008) [188–190], steel-reinforced concrete (2004) [191], plain or hollow steel bars (2005-2012) [45,192], stainless steel-wire meshes, thin perforated metal sheets and fabrics of high strength fibres (2008) [193], carbon fibre (2009-2016) [5,194], glass fibres [195], pultruded Glass Fibre Reinforced Polymers (GFRP) [196,197] or timber (2010-2016) [198–200]. Some of those concepts are presented in Figure 2.8.

[23] Abaqus Unified FEA - SIMULIA™ by Dassault Systèmes®

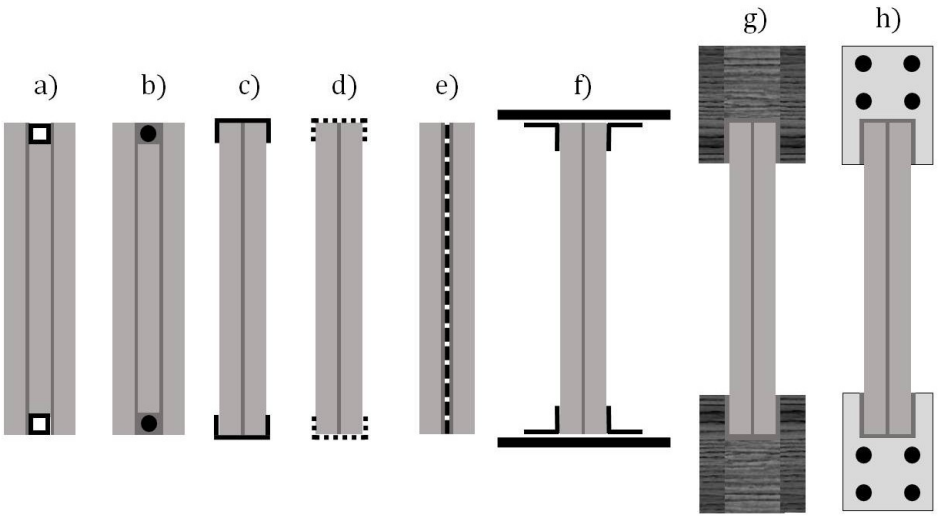

Figure 2.8 - a) & b) embedded hollow/plain steel c) steel or GFRP profiles d) carbon-fibre e) embedded perforated metal plate f) steel flanges g) timber h) reinforced concrete[24]

For most of those studies, the whole purpose of the reinforcements was to enhance the post-failure performance of LG elements, by avoiding sudden collapses. Therefore, such reinforcements had been charged with minor – if any - structural responsibilities for serviceability conditions.

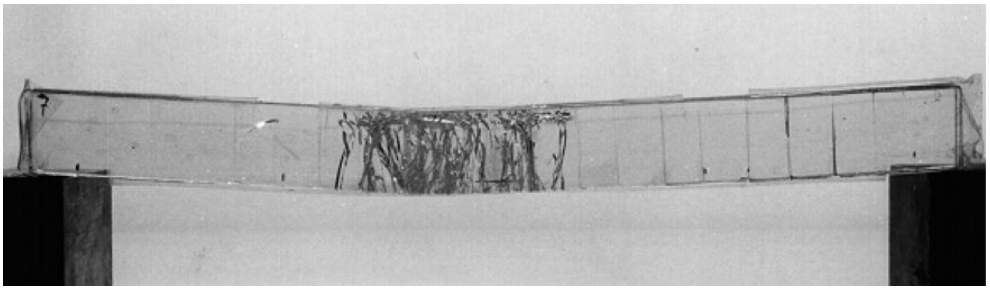

Figure 2.9 – tenting the "Zappi1" beam specimen[25] *in 4-points bending (Veer, 1997* [201]*)*

Among the first to methodically take on the challenge of glass reinforcements, within the years 1992-2003 the *Zappi research group* of the faculty of architecture in Delft[26] developed a research where the design philosophy progressively evolved in

[24] All of the examples proposed are shown in a vertically symmetric configuration. Nonetheless, it is not uncommon in LG beams to find reinforcements only on the lower part of the cross-section, which is affected by tensile actions in most SLS and whose post-failure behaviour can hardly account any structural contribution from glass. On the other hand, it is known and it will be shown again within this manuscript, that fractured glass is still able to withstand substantial compressive actions (cfr. §4.3.4 and §5.2.4). For each of the presented solutions, the number of glass plies is indicative and may in fact vary for different studies and applications.

[25] A special method of laminating glass plates in an overlapping pattern, with the advantages that failure is concentrated in the individual segments and specimens of any size can be made by manufacturing them out of smaller components. While this techniques didn't use steel reinforcements, the same concept of segmented LG beams was used with stainless steel reinforcements in later researches from the same team (Delft, 2003) [187], concluding that reinforced LG is a safer structural material.

[26] The origin of this group is ascribable to Prof. D. Dicke (1924 - 2003) in 1989, who asked to describe "the ideal transparent structural material". He proposed to design a structure with an imaginary material having a motley set of characteristics, derived from those of well-known structural materials. *The quest for Zappi*, this still unknown transparent wonder material, was

using glass as a sort of transparent concrete using steel reinforcements[27]. This decade-long research concluded that it is possible to design and manufacture transparent composite materials with metal-like properties (i.e. ductile failure) using steel-reinforced LG. The authors went as far as stating that such structural elements will be used to replace metallic beams in load bearing constructions; and that the research would eventually result in a family of reliable transparent building components which are structurally safe, with a long lifespan [201,202].

Regarding other reinforcement materials, while researches on strategies using timber and concrete seem not to have led to major follow-ups, significant advances in the domain of embedded steel-reinforcements in LG can be ascribed to the work of C. Louter and J. Belis, who took part of the conclusions of the *Zappi* research; since 2009, sporadically joined by others, the two researchers have been collaborating on this topic. The conceptual development of the research over the years emerges from the vast amount of papers published. The first analyses were made for metal-to-glass bonding properties using acrylate adhesives or SG at a range of temperatures [96], showing that the bonding strength of both plastics is dependent on temperature and that the residual strength after bond failure which is ascribable to friction is still significant. Analyses on SG-laminated and steel reinforced beams followed right away, studying the effects of glass type, reinforcement percentage and beam size [203]. Successive investigations on the effects of temperature, thermal cycling, humidity and load-duration, showed that temperatures in the range of -20 to $+60$°C do not endanger the safety performance of such elements, and that a significant post-breakage strength is reached at all tested temperatures [45]. Both fragile and ductile structural aspects of reinforced glass beams were analysed [204], before extending the study to statically indeterminate reinforced glass beams (Figure 2.10) [205] and FE analyses [184]. The last papers showed that the static determination status of the LG system is not influential towards the determination of the load-carrying capacity nor the failure mechanisms, and that the mechanical properties of glass can be exploited using tendons to pre-stress LG beams. However, these researches also highlighted that, if the ratio between reinforcement and glass surface exceeds a given threshold, the reinforcement benefits can vanish, ultimately concluding that further investigations are still to be expected for optimizing such concepts.

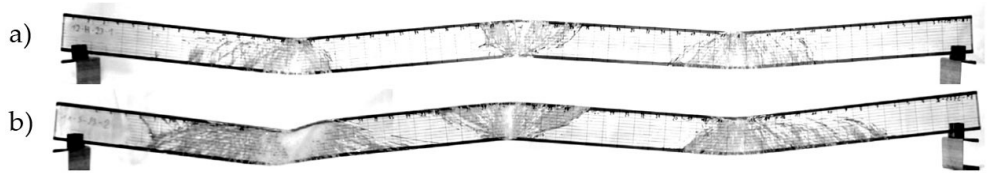

Figure 2.10 – five-points bending tests for SG-laminated beams reinforced with a) solid- and b) hollow-steel profiles (martens, 2017 [205]*; cfr. Figure 2.8)*

Promising results in terms of ductility were obtained by E. Speranzini and S Agnetti using pultruded GFRP elements in combination with LG [197]. Thick combinations of reinforced six-layers LG made with tempered or float glass plies were tested (Figure 2.11).

officially announced in the inaugural speech in 1992.

[27] Initially, the goal was to find a material with the mechanical properties of steel and the transparency of glass.

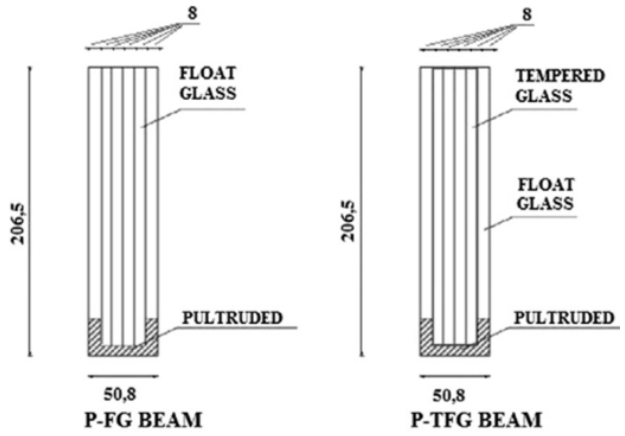

Figure 2.11 - cross section of the GFRP-reinforced FL tested (Speranzini, 2015 [197]*)*

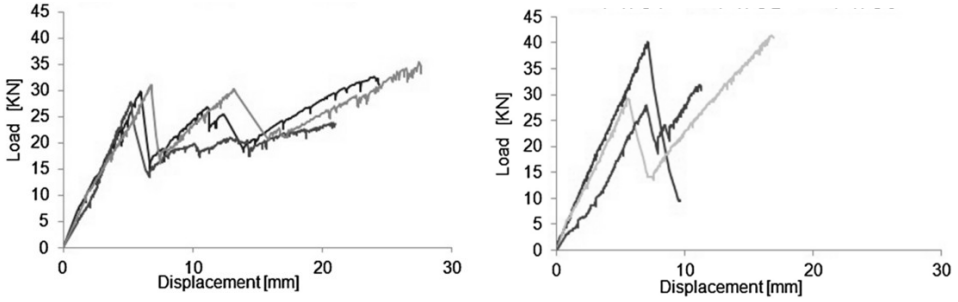

Figure 2.12 - four-point bending results on P-FG (left) and P-TFG specimens (right)

For both solutions, the structural behaviour is similar; however, the mode of failure is different: for P-FG the load increases after the first failure and diminishes progressively with increasing number of cracks, until the final collapse, for of P-TFG specimens, the initial failure is reached because of fragmentation of the whole array of tempered glass plies. Overall, this solution proved that some kind of ductile and hardening structural response can be obtained for reinforced LG beams, with load-displacement curves which are similar to the desired load-carrying behaviour described by K. Martens et al. [206] for pre-stressed LG (see below).

2.2.4 PRE-STRESSED LG

The term *"pre-stressed laminated glass"* can be used to refer to LG elements whose glass is subject by design to a – significant - tensile state prior to the application of external loads. Two macro-categories of elements can be identified:

- elements with axial self-balancing loads, designed to induce a compressive state in the glass plies (*"pre-stressed"* or *"post-tensioned"* LG[28]),
- out-of-plane *"cold-bent"* LG structures, whose internal stress distribution is proportional to the extent of the curvature, thickness of the sandwich structure and coupling abilities of the interlayer.

[28] The term *post-tensioned* has been extensively used in scientific literature referring to such LG elements. Anyhow, in my opinion this choice ay be slightly confusing and the term *pre-stressed* should be always preferred. As a matter of fact, "post-tensioning" refers to the act of applying a tensile force to some tensile-resistant component of a composite LG material after (i.e. *post-*) the lamination process is concluded. Arguably, because the goal of the whole procedure is not to tear those accessory elements, but rather to put the glass - or part of the glass - in a compressive state before (i.e. *pre-*) the application of the design live loads, the term *pre-stressed* (or *pre-compressed*) is more suited and less prone to misunderstandings.

While the study of pre-stressed LG is inherently connected to reinforced LG (cfr. §2.2.3), cold-bent LG is usually comprising only glass and interlayers. In fact, mention of a study concerning pre-stressed LG has already been made within the overlook on reinforced LG works: the research on FE numerical models carried out by C. Bedon and C. Louter [184], used results of a previous investigation on pre-stressed LG beams with steel tendons [186] to numerically explore the effects of the pre-stressing action, as well as the overall performance steel-reinforced LG beams.

The concept of pre-stressed glass beams has currently been explored in only a limited number of researchers projects within the last decade [207]. The main goals of pre-stressed LG structures are: first, to improve the ultimate flexural strength, second, to yield considerable post-fracture load-bearing capacity. Many researchers have issued methods and techniques to improve LG elements in general - and specifically LG beams - using materials with prominent tensile-resistant properties, like steel bars [208] or FRP bars [194,209,210]. Using epoxy resins to secure the reinforcements, these techniques yielded promising results, underlining that the strength and reliability of the reinforcements-resins and glass-resins adhesion are critical parameters for assessing the response of such elements [211]. Despite investigations are still in a preliminary phase and despite their limited number, such researches have shown the potential of post-tensioned LG.

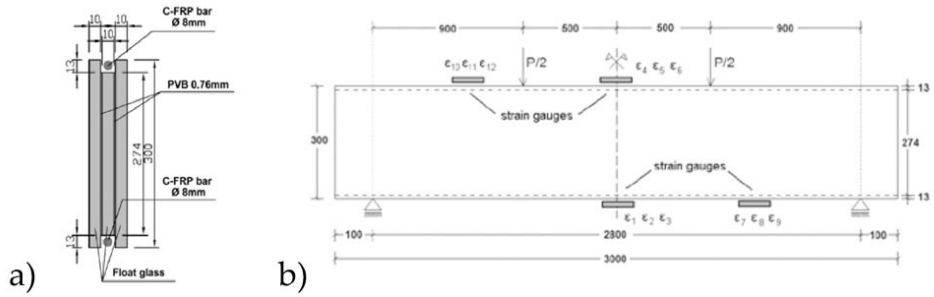

Figure 2.13 - a) cross-section and lateral view of LG reinforced and pre-stressed using FRP pultruded bars (Cagnacci, 2009 [211]*)*

Limits of adhesive reinforcements bonding have been pointed out in 2014 with the research of Louter et al., showing that pre-stress can be achieved by means of mechanically anchored or adhesively bonded tendons. Due to the actions of the tendons, initial fracture loads of pre-stressed LG elements can be increased up to 230% compared to reference beams. Also, with the bridging of the glass cracks, a post-fracture load-carrying mechanism is created. Therefore, the residual load-carrying capacity is enhanced up to 140– 180% of the initial fracture load [186,207].

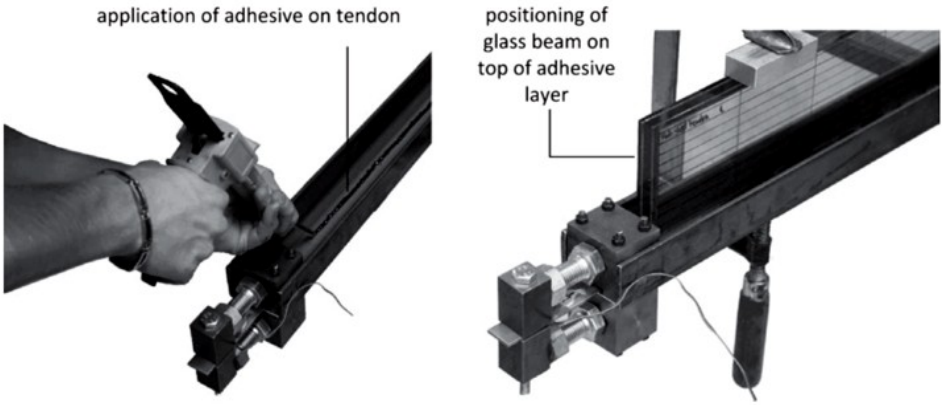

Figure 2.14 - method for bonding pre-tensioned tendons to the lower edge of laminated glass beams (Louter, 2014 [186]*)*

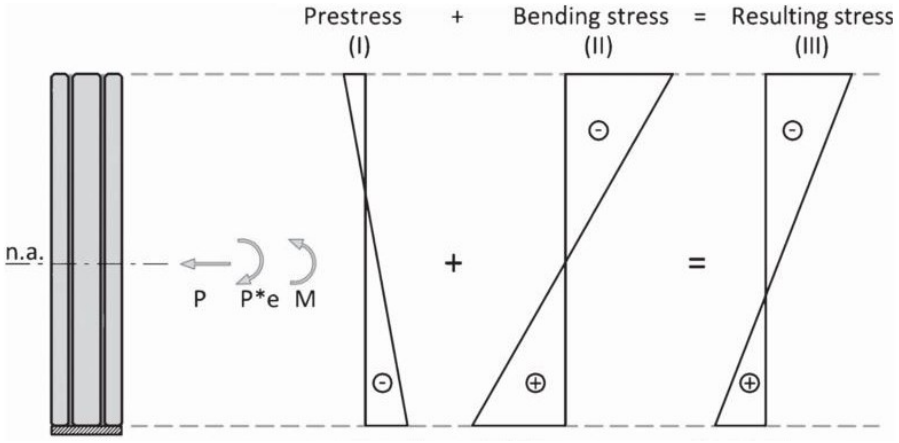

Figure 2.15 - stress distribution in pre-stressed LG beams (Louter, 2014 [186]*)*

A good choice of reinforcement/pre-stressing material and a good design of the cross-section will yield structural glass beams with safe failure behaviour. Figure 2.16 provides a schematic presentation of the desired load-carrying behaviour for pre-stressed LG which has been given by K. Martens et al. in 2015 in [206], within a comprehensive process of reviewing the state-of-the-art of pertinent researches.

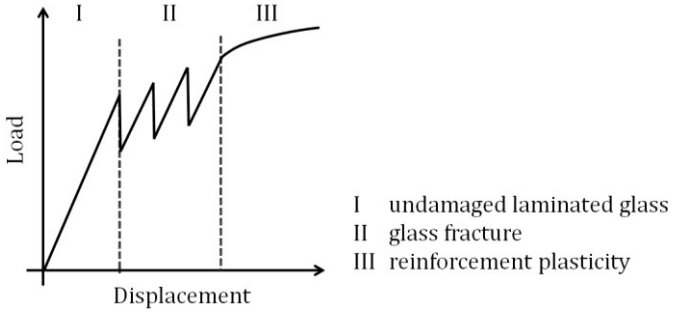

Figure 2.16 - desired load-carrying behaviour for LG beams (Martens, 2015 [206]*)*

On the other hand, regarding cold-bent LG elements, the act of forcing a single-curvature shape after the lamination process is concluded gives also birth to *pre-stressed* LG elements: structures which need to cope with an internal state of stress prior to the application of external live loads. The behaviour of such elements is not easy to model, as the stress distribution in the glass plies varies with time after the initial bending phase because of the viscoelastic properties of the interlayers, which causes the decay of the shear-coupling effect [212].

The possibility to cold-bend LG has been used for less than twenty years, with the earliest scientific reports dating back to the start of the century [213]. The distinction between short-term and long-term response of this technique has been clear since the early days: while at short term the glass panes "work together", and the sandwich structure will act approximately as a single layered pane of the thickness of the whole sandwich, at long term the panes of the sandwich act mostly independently from one another as separate panes (Figure 2.17).

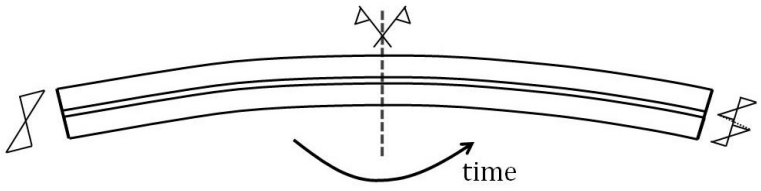

Figure 2.17 – qualitative stress distribution in cold-bent LG at short (left) and long term behaviour (right) respectively (Vakar and Gaar, 2004 [213]*)*

While long-term effects of cold-bending have yet to be properly understood [146], the proven reliability of completed constructions which were only concepts when the first papers were issued is proof that the creation of transparent, curved surfaces comes within reach of designers and clients with an affordable price tag.

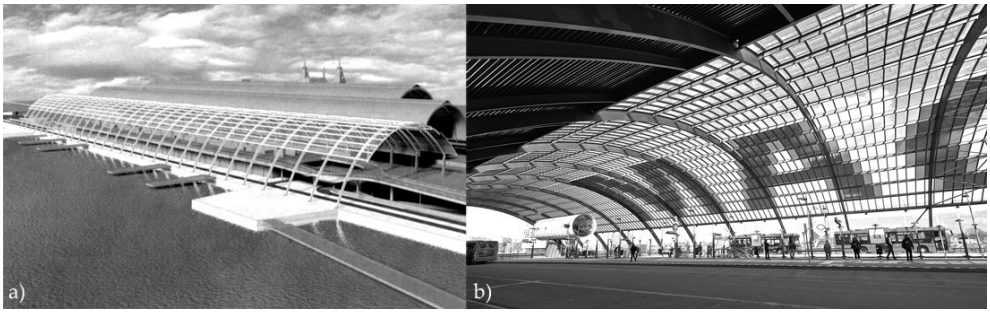

Figure 2.18 – Roof over the IJsei bus station in Amsterdam in a) an early 2004 concept, which was completed in 2011 and b) a picture in 2017.

Despite its complicated behaviour, cold-bending is an alluring prospect for glass designers being a much cheaper alternative to the expensive hot-bending process[29]. Conversely, cold-bending allows for the construction of curved free-form surfaces[30] with better optical properties at a lower cost. While the general principle is to leave the glass properties unaltered, different manufacturing solutions are possible:

- flat lamination and in-site bending with clamps[31] [214] (cheap, small curvature),
- cold-lamination-bending [212] (moderately expensive, large curvature),
- flat-lamination- relaxed-bending [146] (moderately expensive, large curvature),

The latter two methods bring into play of the interlayer mechanical properties to keep the LG panels in the desired shape (or at least in a shape which is closer to the final installation). In both cases, once bending devices are removed, the LG element holds the deformed shape thanks to the interlayer stiffness. Hence, dependable data of long-term properties of such materials is of paramount importance for the implementation of these techniques. Equally to axially pre-stressed LG elements, researchers agree that cold-bending is worth a deeper investigation, as there appears to be a general lack of understanding and reliable long-term data.

2.2.5 POST-FAILURE LG PERFORMANCE

Over their lifetime, buildings are likely to be subject to actions such as impacts, abrasions and localized temporary loads. While the overall intensity of localized effects may be far lower compared to design ULS load combinations, such stress

[29] Where curved glass plies are first obtained by heating them up to the material softening point (cfr. §1.1.1) and curved individually into the desired shape using moulds. Hot-bent glass plies are then successively laminated to form LG elements. While this process allows to shape virtually any kind of curved glass elements, either single-curvature and double-curvature ones, it is very expensive and doesn't leave a perfectly reflective glass surface.

[30] Cold-bending a double curved shape is possible, but typically results in very high stresses in glass, so that the economic advantage of cold-bending in manufacturing is lost. However, recent advances in theoretical algorithms allow for the discretization of any surface using only single curvature panels, thus allowing the construction of smooth double curvature glazing of any form [332–334].

[31] This technique can already count some practical application, like the Strasbourg Railway Station (cfr. Figure 1.2.c) and the aforementioned bus station in Amsterdam (Figure 2.18).

concentrations can kick-start the uprising of cracks, thus influencing the maximum load which can be carried by structural LG. As peak stress concentrations are independent from the type of element and can affect any type of glass product (cfr. §1.1.1), localized loads induced failures cannot be safely included into the design process. Besides, what happens to the glass after it has failed is an important design concern; and both designers and customers must accept that LG *can* fail, at least partially, due to concentrated impacts and actions. Ultimately, a successful and widespread strategy to avoid catastrophic effects is to include sacrificial plies on the outer layers on LG [42,192,215]. Therefore, the understanding and modelling of damaged LG elements must be seen as fundamental parts of the design process. While studies on the behaviour of unreinforced LG beams are available [62,211,216,217] (also cfr. §2.2.2), those rarely delve in performance assessments after the failure of the glass plies [11,158,159,166].

In the last decades, researchers have picked up the challenge of understanding the post-failure response and properties of LG. Once again, the research started from the automotive department. One of the first research on post failure LG performance can be traced back to the year 2000, in a work by Japanese J. Oda et al. [218], studying variously damaged automotive windshields residual impact resistance. Mechanisms of crack initiation and propagation were investigated by Chinese team J. Xu, Y. Sun et al. between 2011 and 2017 with a couple of noteworthy papers [219,220]. In the former, with preliminarily impact fracture experiments, authors investigated crack propagation in PVB-LG; in the latter, an explanation to the basic crack propagation mechanism on radial multi-crack was proposed, providing guidance for retroactive impact information extraction and improving cracking-resistant structural design and material selection.

Models have been proposed for in-plane and out-of-plane bending. The latter can account for decisively more in-depth analyses, having yield in the last years both an homogenized analytical model by L. Galuppi and G. Royer [104] and a Non-linear discrete modelling proposal [215] by D. Baraldi, A. Cecchi and P. Foraboschi. Both researches focused on tempered glass failure. Arguably, while influencing dramatically the post-failure LG configuration, tempered glass failure produced a more homogeneous material in the post-failure phase, compared to annealed glass failure. Major research conclusions were that fully-damaged tempered LG elements can still give rise to a resisting system, with a degree load-bearing capacity and stiffness strongly dependent on the interlayer material. Results of the analysis also showed that the interlayers are "stiffened" by the contact with the adherent glass shards, but a degree of delamination is supposed to occur at the glass-polymer interface. From a numerical point of view, it was shown that non-linear Discrete Element Modelling (DEM) is a practical solution for analyzing the behaviour of fully damaged LG elements made with tempered glass plies.

Compared to out-of-plane analyses, far fewer works seem to have been performed on the post-failure behaviour of in-plane loaded LG. A recent experimental paper, issued by Chinese X. Huang et al. [221], described an experimental campaign which was carried out on a significant number of full-scale PVB- and SG-laminated beams in short term three-point bending at room temperature. While PVB-laminated were found to have very poor post-failure performance, the research was able to produce a simple analytical model to predict the post-failure strength of the SGP LG beams. Still, this work seems to be the only example regarding studies in this area of research.

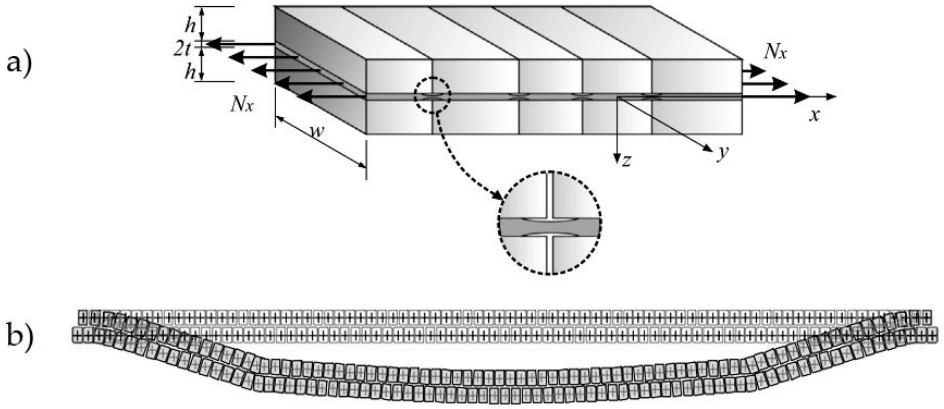

Figure 2.19 - a) homogenized model problem by Galuppi-Royer [104] *with hint to interface delamination and b) DEM example from Baraldi-Cecchi-Foraboschi* [215]

2.3 AIM OF THE RESEARCH

In the analysis of regulatory and scientific state-of-the-art, several open questions have been highlighted. While new researches in many of these fields may lead to interesting results, for the breakdown of the most pressing questions to be investigated within this work, the focus will be set from the perspective of a LG designer, an architect or an engineer, proficient with the currently available design tools and aiming to find more reliable answers to given architectural applications.

From interlayers properties on a microscopic level, to local effects within the cross section, to the response large architectural structures, the topic of interlayer mechanics within LG elements represents a multi-scale problem. Accordingly, a multi-scale approach will be carried out within the research framework: from small interlayer specimens, to small LG specimens, to full-scale LG structural elements.

The research presented within this manuscript is set on two main goals, in turn articulated in multiple analyses:

1: Assessing and comparing interlayer mechanical properties

Among the most compelling and still unresolved topics, one certainly deals with the assessment of interlayer mechanical properties. Problems related to LG design have typically to deal either with long-term actions and short-term effects, which trigger two very different responses. For LG structures charged with out-of plane actions, long-term effects are mostly defined by the viscoelastic flow within the bulk of the interlayers, critically affecting both stiffness and load-bearing capacity. Conversely, viscoelastic properties are less relevant for short-term effects like blasts and vibrations; there, the instantaneous, and possibly large-strain response may be best represented by means of hyperelastic models.

Taking advantage of a substantial lack of a coherent regulatory structure for architectural applications of interlayer materials, newly developed interlayers such as DG41 (and, to a minor extent, SG) are put forward by manufacturers supported by very modest technical information (while supposedly alleging prominent mechanical properties). To establish a simple baseline, allowing to compare these new products to more traditional ones, tensile tests (cfr. §4.1.1) will be carried out using the exact same procedure for specimens of three materials (Figure 2.20.a): PVB, SG and DG41.

While short-term effects can be studied with tensile or dynamic tests (cfr. §3.1.3.4, not performed in this research), some have pointed out that correlations used to

extrapolate long-term viscoelastic properties from imposed sinusoidal actions may yield incorrect results, and that shear tests should be preferred instead for both isotropic and non-isotropic materials (cfr. Délince [7], Van Der Vegt [59] & §4.2.1). Embracing this approach, an experimental technique developed within a previous research with Prof. L. Biolzi at the Politecnico di Milano and used for two diverse applications [65,146], will be perfected and enhanced in this work (cfr. §4.2.1). This method is used to investigate the viscoelastic properties of same materials studied with tensile tests, this time in a small-scale LG structure (Figure 2.20.b).

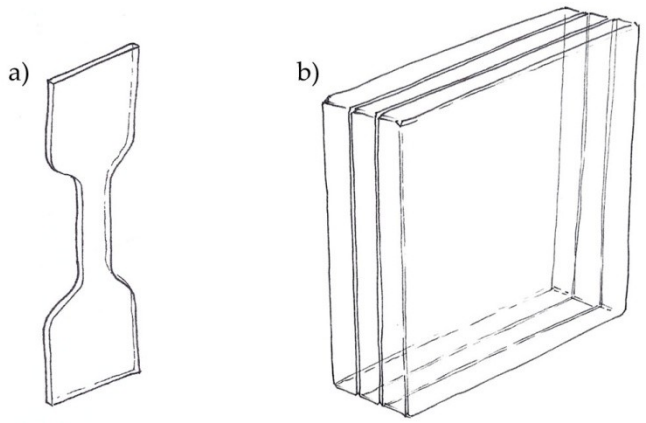

Figure 2.20 - a) interlayer specimens for tensile tests and b) LG specimens tested for assessing the viscoelastic properties of interlayers ($10 \times 10 \times 3.3\ cm$*)*

2: Investigating the progressive damage effects of LG beams

Except for requiring safety with respect to the collapse of safety LG structures, the standardization bodies make no mention of quantitative mechanical properties which are required to partially- or totally-damaged LG elements. On the other hand, relevant studies on the structural performance of architectural laminated LG have been experimentally and numerically performed, including lamination combined with embedded reinforcements, but no experimental analyses could be found on progressively damaged LG beams (i.e. in-plane loaded elements). While the interlayer doesn't have a significant influence on the flexural response of undamaged LG beams under in plane loading, it is believed that the use of "stiff" interlayers may significantly enhance the post-failure response.

This research will tackle the problem of experimentally investigate the performance of SG- and DG41-laminated glass beams, made with three fully tempered glass plies, to assess their post-failure behaviour. Static and dynamic tests will be performed, with the goal of deepening the understanding of the *tension stiffening* (TS) effect, recently observed by some researchers (cfr. §2.2.5), and the decay of bond adhesion between glass and interlayers around tempered glass fragments, which is supposed to induce a drastic reduction of the TS over time and over large strains.

Multilayer interlayers will be investigated, by comparing DG41-laminated beams with twin elements with an extra polycarbonate sheet amid the interlayers matrix. The goal of the comparison is to establish whether a thin foil of "stiff" plastic material can significantly enhance the properties of such laminates.

3 MECHANICS

Laminated glass is a composite material whose components present several elements of novelty for most architects and engineers. Here more than anywhere else, designers are forced to think in terms of viscosity and fragility. While those subjects are often circumvented and avoided in traditional applications, the desire for transparent glass structures forces us to tackle those topics more in depth, understanding the mechanics to propose new solutions to new problems.

Despite its intrinsic brittleness, glass itself can be included in the category of "traditional" solid building materials. Most of increased complexity when dealing with LG is due to the peculiar behaviour of thermoplastic interlayers. This complexity is well introduced by A. Ali:

> *"Elastomers present a very complicated mechanical behaviour that exceed linear elastic theory and contain large deformations, plastic and viscoelastic properties and stress softening"*. A. Ali et al., 2010 [222]

In the following, an overview of the fundamental mechanics needed to understand the response of LG is provided. While some chapters are openly more dedicated glass and others are dealing with interlayer mechanics, it is once again useful to recall the words of K. Gilbert (cfr. p.11): observations and models are generally dependent on the scale of human problems, so that mechanics can vary once the scale is changed to larger perspectives.

This chapter deals with the following topics:

- small strains linear elasticity,
- large deformations non-linear elastic response,
- time- and temperature-dependency of solids,
- non-reversible processes and plastic deformations,

Despite being essential to the understanding of the response of brittle materials such as glass, the topic of fracture mechanics is not dealt with in this manuscript, as countless dedicated works on this topic can be found in literature [32,34,36].

3.1 ELASTICITY

The *theory of the elastic solid* is briefly introduced, deriving the relations and laws by which an elastic material transforms because of externally applied actions.

Elastic materials share the ability to deform under external actions and the property to restore the initial shape when freed from said actions, independently from the conditions upon which those were applied. The rule according to which loads are applied is called *loading process* [223].

An elastic material or body is described as a reversible system, where energy spend throughout the deformation is internally stored and entirely released upon removal of the external actions. The ability of such materials to naturally restore their initial state allows to acknowledge the existence of an entity such as the *elastic energy* or *strain energy*, capable to produce (at its expenses) negative work from a

combination of forces. In short, mechanical work needed to transition from the initial configuration to a deformed one is stored as elastic energy, which transforms back in a positive work during the inverse transition. A biunivocal relation can be identified among stress and strain components for elastic materials:

$$\sigma_{ij} \Leftrightarrow \varepsilon_{ij}$$

Different materials may store elastic energy in different ways. From a macroscopic point of view, a distinction of interest for this work may be performed according to materials showing a linear elastic response, a non-linear elastic response and a time-dependent elastic response [224].

The treatise in the following paragraphs will first briefly mention linear elastic solids, which are a good model for glass in the pre-failure phase, while non-linear elasticity and time-dependent elasticity will be functional for understanding the response of thermoplastic interlayers. On occasion, when presenting the various mathematical formulations, specific mechanics will be immediately referred to a specific component of LG, to clarify and synthesize the discussion.

3.1.1 LINEAR ELASTICITY

Among elastic materials (see above), a *Linear Elastic* (LE) one is defined by linear constitutive equations, meaning that the relations between stresses σ_{hk} and strains ε_{ij} are linear and homogeneous [223]. For LE isotropic materials, the correlation between the components of tensors σ and ε allows for the formulation of the so-called *generalized Hooke's laws*[1] :

$$\varepsilon_{11} = \frac{\partial \phi}{\partial \sigma_{11}} = \frac{1}{E}[\sigma_{11} - \nu(\sigma_{22} + \sigma_{33})] \quad ; \quad \gamma_{12} = 2\varepsilon_{12} = \frac{\partial \phi}{\partial \sigma_{12}} = \frac{\sigma_{12}}{G}$$

$$\varepsilon_{22} = \frac{\partial \phi}{\partial \sigma_{22}} = \frac{1}{E}[\sigma_{22} - \nu(\sigma_{11} + \sigma_{33})] \quad ; \quad \gamma_{13} = 2\varepsilon_{13} = \frac{\partial \phi}{\partial \sigma_{13}} = \frac{\sigma_{13}}{G}$$

$$\varepsilon_{33} = \frac{\partial \phi}{\partial \sigma_{33}} = \frac{1}{E}[\sigma_{33} - \nu(\sigma_{11} + \sigma_{22})] \quad ; \quad \gamma_{23} = 2\varepsilon_{23} = \frac{\partial \phi}{\partial \sigma_{23}} = \frac{\sigma_{23}}{G}$$

Where E is the *Young modulus*[2] and the ν the *Poisson's coefficient*[3]. These relations are valid for the small strain domain and will be used frequently throughout this work when dealing with glass; as their use is common practice in engineering, these will be usually implied without direct reference.

3.1.2 NON-LINEAR ELASTICITY (HYPERELASTICITY)

The demand of predictive models for mechanics of rubber-like materials has been pushing the research since the beginning of the 20th century, overcome the limits of linear elastic models that have guided many of the technical developments throughout the industrial revolution (namely, the restriction to infinitesimal strains). This progress has led to the development and critical assessment of constitutive equations for the nonlinear elasticity of rubber materials known as *hyperelastic models* [225]. Such mathematical formulations can be used to model materials exhibiting a non-linear but reversible response (Figure 3.1). Primary applications of these models have been dedicated to rubbery polymeric materials

[1] Robert Hooke, Wight 1635 – London 1703

[2] Thomas Young, Milverton 1773 - London 1829

[3] Simeon Denis Poisson, Pithiviers 1781 - Paris 1840

and foams exposed to large, reversible shape changes (e.g. tires, seals, conveyor belts, base isolations of buildings, etc) [226,227].

Hyperelastic models are suited for situations in which the non-linear response of a material is mostly independent from strain rate and, more generally, from the strain history. Alike elastic materials, the hyperelastic response only depends on the strain (i.e. any work done deforming an hyperelastic material is stored as potential energy in a thermo-dynamically reversible process).

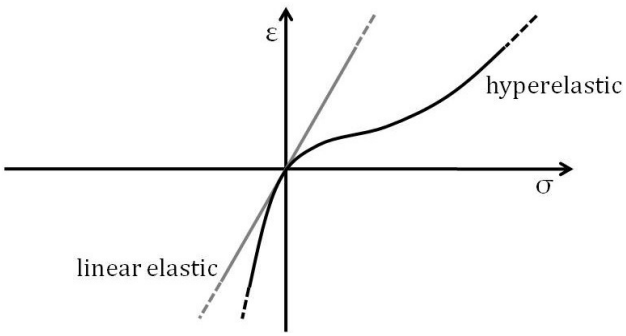

Figure 3.1 – typical linear elastic and hyperelastic response

Hyperelastic models are defined in virtue of a functional called *strain energy density* (SED) for finite strain. Several SED functions have been proposed: some are deeply intertwined with the theory of finite elasticity [222,228,229], whereas others rather result from phenomenological observations, with less ties to fundamental phisics. These empirical models are frequently used, mostly aiming to a simplified and design-oriented approach[4] [222,229,230].

The existence of a SED functional Φ was postulated by G. Green and perfected by Rivlin within the *Phenomenological Theory of Rubber Elasticity* [231], relating the potential strain energy content of a material to its state of deformation. Some properties of the SED are [230–234]:

- it is a scalar function of the strain,
- its derivative with respect to the strain is the stress,
- it is independent from deformation history,
- for anisotropic materials, it depends implicitly on the directions defining the structure of the material (i.e. orientation of fibres or layers),
- for small strains in isotropic materials, the function specializes to:

$$\Phi = \frac{1}{2}\sum_{i=1}^{3}\sum_{j=1}^{3}\sigma_{ij}\varepsilon_{ij} = \frac{1}{2}\left(\sigma_x\varepsilon_x + \sigma_y\varepsilon_y + \sigma_z\varepsilon_z + \sigma_{xy}\varepsilon_{xy} + \sigma_{yz}\varepsilon_{yz} + \sigma_{xz}\varepsilon_{xz}\right)$$

- for isotropic materials in finite strains, a function is usually defined using the invariants I_1, I_2 and I_3 of the Cauchy-Green tensor, and sometimes through the elongation components λ_i in the three spatial dimensions:

$$\Phi = \Phi(I_1, I_2, I_3) \quad \text{or} \quad \Phi = \Phi(\lambda_1, \lambda_2, \lambda_3)$$

Dealing with rubber elasticity in this work, namely, with the response of interlayer polymers used in glass lamination, the large strain domain of isotropic materials must be considered. To choose the most appropriate SED functions to work with, we first need to assess how the compressibility of such materials come into play, both from a mathematical point of view and from the perspective of practical

[4] Some models postulate the existence of an arbitrary SED function, then derivate the formulation the constitutive material equations; some other bypass the definition of a SED function and directly provide empirical constitutive mathematical formulations instead.

applications in LG elements. The compressibility of a material is a functional which can be defined because of volumetric changes due to an isotropic stress state. Conversely, an incompressible material is only allowed distortions with constant volume. As such, SED functions can be addictively decomposed two parts, respectively correlated to the hydrostatic and deviatoric part of the stress tensor. While examples can be found involving tests on compressible rubbery materials under homogeneous, hydrostatic strain [233], interlayers used in LG hardly experience significant volumetric changes [48]. As the formulation of hyperelastic models for compressible materials usually comes at the price of major complications on a mathematical level, greater emphasis will be given to models providing a reliable approach to incompressible hyperelasticity.

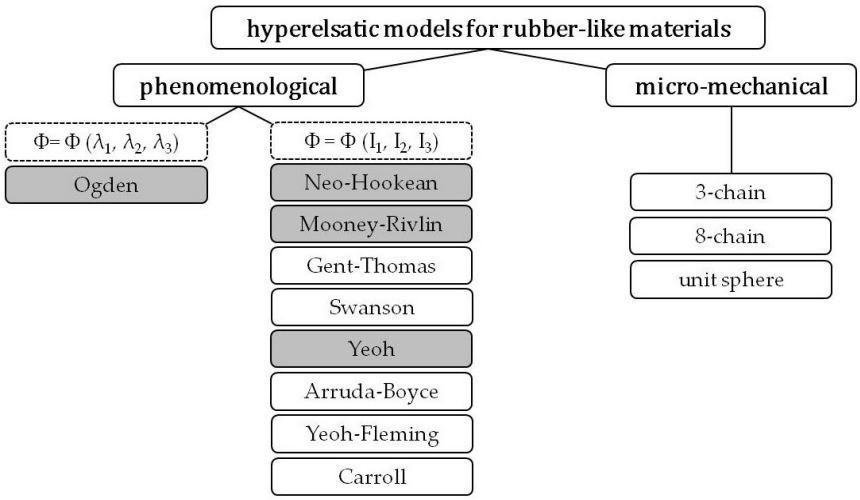

Figure 3.2 - hyperelastic models used within this manuscript, highlighted among some popular ones (references can be found in the work by Steinmann et al., 2012 [225]*)*

Polymers used as interlayer materials in LG transition among various regimes of mechanical behaviour depending on the temperature: glassy, leathery and rubbery (cfr. §1.1.2). Densely cross-linked polymers are the most likely to show the "ideal" rubbery behaviour [227], that hyperelastic expression are intended to approximate.

Within this manuscript, hyperelastic models will be used extensively in Chapter 5, to elaborate on tests results of Chapter 4. Mathematical formulations of the used phenomenological models (Figure 3.2) are presented in the following paragraphs.

Starting from the SED formulations proposed by various authors, a walkthrough on the analytical developments needed to calculate the stress-strain relations in uniaxial tensile tests is carried out in the following.

Neo Hookean model

Among phenomenological hyperelastic models, the Neo-Hookean (NH) is significant for two reasons: it is the simplest and does not involve arbitrary constants. The SED for is defined as follows:

$$\Phi = C_1(\bar{I}_1 - 3) + D_1(J-1)^2$$

Where $\bar{I}_1$ is the first invariant of the isochoric part of the right Cauchy-Green tensor $C = F^T F$ from the deformation gradient F, $J = \det(F)$ is correlated to the variation of volume for compressible materials, and the constants $C_1 = 0.5G$ and $D_1 = 0.5\kappa$ are depending on the shear modulus G and the bulk modulus κ respectively.

$$I_3 = \lambda_1^2\lambda_2^2\lambda_3^2 = J^2$$
$$\bar{I}_1 = J^{-2/3}\, I_1 = J^{-2/3}\,(\lambda_1^2 + \lambda_2^2 + \lambda_3^2)$$
$$\lambda_i = 1 + \varepsilon_i$$

In an uniaxial stress test with the force applied in the λ_1 direction, the transversal elongations are equal $\lambda_2 = \lambda_3$. With this relation and the previous equations, one finds I_1 as a function of the principal elongation component λ_1 and J:

$$J^2 = \lambda_1^2\lambda_2^4 \qquad \rightarrow \qquad \lambda_2 = \sqrt{\frac{J}{\lambda_1}} \qquad \rightarrow \qquad \bar{I}_1 = J^{-2/3}\left(\lambda_1^2 + \frac{J}{\lambda_1}\right)$$

Substituting the expression of I_1 in the formula of Φ and then differentiating for the three elongation components λ_i (proof in [234]) yields the expression of the principal stress components for a compressible material in an uniaxial stress test:

$$\Phi = C_1\left(J^{-2/3}\left(\lambda_1^2 + \lambda_2^2 + \lambda_3^2\right) - 3\right) + D_1(J-1)^2$$

$$\sigma_i = \frac{\partial \Phi}{\partial \lambda_i} = 2C_1 J^{-5/3}\left(\lambda_i^2 - \frac{I_1}{3}\right) + 2D_1(J-1)$$

$$\sigma_1 = \frac{4}{3}C_1 J^{-5/3}\left(\lambda_1^2 - \frac{J}{\lambda_1}\right) + 2D_1(J-1)$$

$$\sigma_2 = \sigma_3 = \frac{2}{3}C_1 J^{-5/3}\left(\frac{J}{\lambda_1} - \lambda_1^2\right) + 2D_1(J-1)$$

If no action is applied on the sides, radial stress components σ_2 and σ_3 are null; thus, it is possible to subtract the last two expressions and get rid of the term in D_1:

$$\sigma_1(\lambda, J) = 2C_1 J^{-5/3}\left(\lambda_1^2 - \frac{J}{\lambda_1}\right)$$

The relation between J and λ_1 can then be found solving the nonlinear equation in J with numerical methods. To highlight the variation of $J(\lambda)$ for changing G and κ, the Newton–Raphson method was used for results in Figure 3.3.

$$\frac{4}{3}C_1 J^{-5/3}\left(\lambda_1^2 - \frac{J}{\lambda_1}\right) + 2D_1(J-1) = 2C_1 J^{-5/3}\left(\lambda_1^2 - \frac{J}{\lambda_1}\right)$$

$$\frac{G}{2}J^{8/3} - \frac{G}{2}J^{5/3} + \frac{\kappa}{6\lambda}J - \frac{\kappa\lambda^2}{6} = 0$$

For many engineering purposes, $J(\lambda)$ is consistently close to 1 for any stretching value, and the compressible problem ultimately equals to the uncompressible one. The *true* stress, is calculated on the effective "stretched" cross-section. Besides, it is common in engineering practice to simplify the small elongations problem looking for the *engineering* relation between stress and strain on the original cross-section. If P_1 is the applied force and A_0 is the area of the original cross-section:

$$\sigma_1 = \frac{P_1}{A} \quad ; \quad \sigma_{1,eng} = \frac{P_1}{A_0} \quad ; \quad A = A_0\lambda_2\lambda_3 = A_0\lambda_2^2 = A_0\frac{J(\lambda)}{\lambda_1} \quad ; \quad \sigma_{1,eng} = \sigma_1\frac{J(\lambda)}{\lambda_1}$$

Table 3.1 - stress in uniaxial elongation for a Neo-Hookean material

	true stress	**engineering stress**
compressible	$\sigma_1(\lambda) = \frac{1}{GJ(\lambda)^{\frac{5}{3}}}\left(\lambda_1^2 - \frac{J(\lambda)}{\lambda_1}\right)$	$\sigma_1(\lambda) = \frac{1}{GJ(\lambda)^{\frac{5}{3}}}\left(\lambda_1 - \frac{J(\lambda)}{\lambda_1^2}\right)$
incompressible	$\sigma_1 = G\left(\lambda_1^2 - \frac{1}{\lambda_1}\right)$	$\sigma_1 = G\left(\lambda_1 - \frac{1}{\lambda_1^2}\right)$

with $\lambda_1 = 1 + \varepsilon_1$

Figure 3.3 shows the effects of varying values of the bulk and shear moduli on the function $J(\lambda)$ and a qualitative representation of the NH models described in Table 3.1 for given values of moduli G and κ.

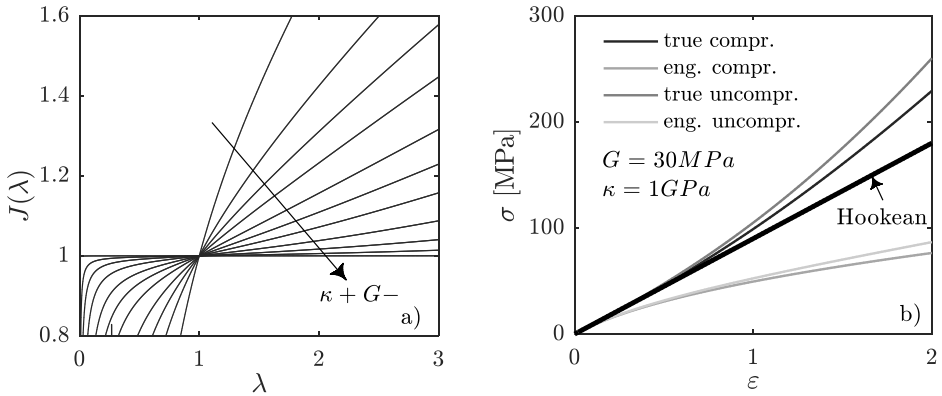

Figure 3.3 – a) function $J(\lambda)$ for varying G, κ and b) hyperelastic Neo-Hookean models

Mooney-Rivlin model

The Mooney-Rivlin (MR) hyperelastic model proposed in 1951, is a special case of the generalized MR polynomial model [235]. Based on empirical descriptions, this is today one of the most regularly used models [230]; the SED function is:

$$\Phi = C_1(I_1 - 3) + C_2(I_2 - 3) + D_1(J - 1)^2$$

Where I_2 is the 2nd invariant of the isochoric part of the left Cauchy-Green tensor:

$$I_2 = J^{-4/3} I_2 = J^{-4/3}(\lambda_1^2\lambda_2^2 + \lambda_2^2\lambda_3^2 + \lambda_1^2\lambda_3^2)$$

Constants C_1, C_2 and D_1 are empirically determined: while $D_1 = 0.5\kappa$ is linked to the bulk modulus κ, C_1 and C_2 have no physical meaning other than being an additive decomposition of half the shear modulus G.

$$C_1 = \frac{G}{2}\alpha \quad ; \quad C_2 = \frac{G}{2}(1-\alpha) \quad ; \quad 0 \le \alpha \le 1$$

Closed form expressions for a compressible problem are scarcely used, involving the solution of complex differential equations with arbitrary parameters. For an incompressible material, using the same relations introduced for the NH model, the principal stresses for a MR incompressible material are shown in Table 3.2.

Table 3.2 - uniaxial elongation stress for incompressible Mooney-Rivlin material

true stress	**engineering stress**
$\sigma_1 = G\left(\alpha + \frac{1-\alpha}{\lambda_1}\right)\left(\lambda_1^2 - \frac{1}{\lambda_1}\right)$	$\sigma_1 = G\left(\alpha + \frac{1-\alpha}{\lambda_1}\right)\left(\lambda_1 - \frac{1}{\lambda_1^2}\right)$
	with $\lambda_1 = 1 - \varepsilon_1$ *and* $0 \le \alpha \le 1$

Note that for $\alpha = 1$ the MR model degenerates in the NH incompressible one, and that for any other value of α the MR model results in softer material behaviour for finite strain, while still having the same initial tangent modulus.

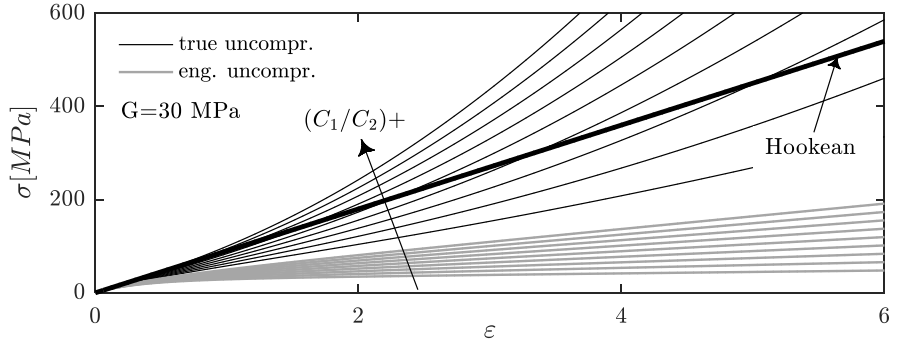

Figure 3.4 - hyperelastic Mooney-Rivlin models for varying C_1 over C_2 ratio

Yeoh model

Like the MR one, the Yeoh model also provides a phenomenological description of the material response. The model is based on R. Rivlin's observation that the elastic properties of rubber may be described using a strain energy density function which is a power series in the strain invariants [230]:

$$\Phi = \sum_{i=1}^{N} C_i (I_1 - 3)^i + \sum_{i=1}^{N} \frac{1}{D} (J-1)^{2i}$$

The constant D is related to the bulk modulus, so the right sum is non-null only for compressible materials. Alike to the MR model, despite compressibility being included in the SED formulation, a closed form solution is unknown using the complete expression of Φ. Hence, the Yeoh model is normally applied for incompressible materials only ($J = 1$) choosing $\mathrm{N} = 3$:

$$\Phi = C_1 (I_1 - 3) + C_2 (I_1 - 3)^2 + C_3 (I_1 - 3)^2$$

The constant C_1 is linked to the shear modulus by the relation $C_1 = 0.5G$, while C_2 and C_3 are phenomenological constants without a physical meaning. For an incompressible material in an uniaxial test:

$$\sigma_1 = \frac{\partial \Phi}{\partial \lambda_1} = \frac{\partial I_1}{\partial \lambda_1} \frac{\partial \Phi}{\partial I_1} = 2\left(\lambda_1^2 - \frac{1}{\lambda_1}\right) \frac{\partial \Phi}{\partial I_1}$$

Table 3.3 - uniaxial elongation stress for incompressible Yeoh material

true stress	**engineering stress**
$\sigma_1 = 2\left(\lambda_1^2 - \frac{1}{\lambda_1}\right) C_1 \sum_{i=2}^{3} i C_i (I_1 - 3)^{i-1}$	$\sigma_1 = 2\left(\lambda_1 - \frac{1}{\lambda_1^2}\right) C_1 \sum_{i=2}^{3} i C_i (I_1 - 3)^{i-1}$
with $\lambda_1 = 1 + \varepsilon_1$ *and* $I_1 = \lambda^2 - 2\lambda^{-1}$	

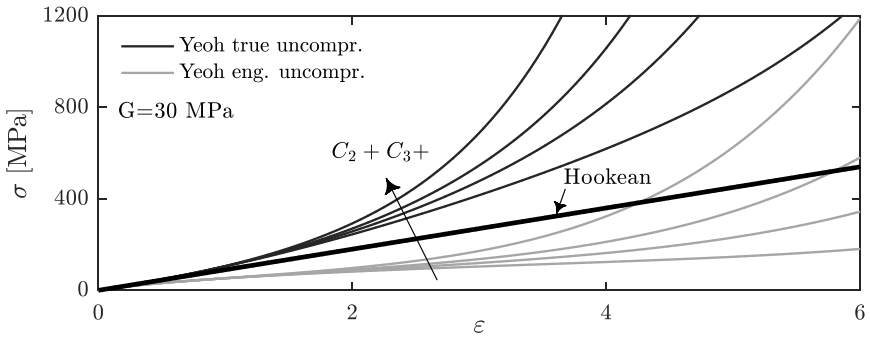

Figure 3.5 – hyperelastic Yeoh model dependency from coefficients C_2 and C_3

Ogden model

Unlike most empirical hyperelastic models, the 1972 Ogden model [236] does not define a SED functional from invariants of the deformation tensor, but rather through elongation components λ_i in the three spatial directions.

$$\Phi = \sum_{i=1}^{N} \frac{\tilde{G}_i}{a_i} \left(\lambda_1^{a_i} + \lambda_2^{a_i} + \lambda_3^{a_i} - 3\right)$$

Materials can be described by means of properly arranged set of $2N + 1$ constants $\tilde{G}_i$, a_i and N, all correlated the initial shear modulus by the relation:

$$G = \frac{1}{2}\sum \tilde{G}_i a_i$$

For an incompressible material in an uniaxial test, the SED simplifies as follows:

$$\Phi = \sum_{i=1}^{N} \frac{\tilde{G}_i}{a_i}\left(\lambda_1^{a_i} - \frac{2}{\lambda_1^{a_i/2}} - 3\right)$$

Table 3.4 - uniaxial elongation stress for incompressible Ogden material

true stress	**engineering stress**
$\sigma_1 = \sum_{i=1}^{N} \tilde{G}_i\left(\lambda_1^{a_i} - \frac{1}{\lambda_1^{a_i/2}}\right)$	$\sigma_1 = \sum_{i=1}^{N} \frac{\tilde{G}_i}{\lambda_1}\left(\lambda_1^{a_i} - \frac{1}{\lambda_1^{a_i/2}}\right)$
	with $\lambda_1 = 1 + \varepsilon_1$

3.1.3 TIME-DEPENDENT LINEAR ELASTICITY (LINEAR VISCOELASTICITY)

Many polymers show a mixture of elastic, viscous and inelastic responses when external actions are applied. In this paragraph, the focus will be given non the second ones, and on models used to describe the rheology of *linear viscoelastic* (LVE) materials [237].

Rheology is the study of flow and deformation of matter under applied forces, a field whose mathematical foundations have been extensively studied throughout the last decades of the 20th century [114,238]. While some authors are at times discordant on the terminology, the distinction used by P Perzyna in 1966 [239][5] will be used throughout this manuscript to separate plastic and rheologic properties: the first, dealing with inelastic deformations and power dissipations (cfr. §3.2), the latter associated to reversible processes.

The foundation of LVE lie in the *Boltzmann*[6] *superposition principle*, by virtue of which it is accepted that *"each loading step makes an independent contribution to the final state"*. By means of this statement, linear viscoelastic correlations can be written down for both creep and relaxation phenomena, which will be properly introduced and further discussed on in the next paragraph:

$$\sigma(a \cdot \varepsilon) = a \cdot \sigma(\varepsilon) \qquad \textit{linear relaxation}$$

$$\varepsilon(a \cdot \sigma) = a \cdot \varepsilon(\sigma) \qquad \textit{linear creep compliance}$$

meaning that strain resulting from applying a stress $a\sigma$, where a is an arbitrary constant, is a times the strain resulting from applying a stress σ (the same works the other way around for strains over stresses).

3.1.3.1 CREEP AND RELAXATION: THE WIECHERT MODEL AND PRONY SERIES

When dealing about time-dependent effects in solid continuum mechanics, *Creep* is looked at as the tendency to deform over time under the influence of constant stress, while the diminishing resistance observed in some materials in response to a fixed amount of imposed strain is called *stress relaxation* (generally referred to only as *relaxation*). Figure 3.6 shows conceptual representation of both phenomena.

Creep tests are typically easier to enforce compared to relaxation ones, because holding a perfectly steady strain over time is arguably more complex. For the former, a load is applied to a test specimen and its length is measured as a function of time. In stress-relaxation measurements test specimens is rapidly stretched to a

[5] Cited in over two thousand scientific works at the time this manuscript is written.

[6] Ludwig Eduard Boltzmann, Vienna 1844 - Triest 1906.

given value, and the stress required to hold the length constant is recorded as a function of time [240]. As a result, most of the data available for viscous properties of materials is available as (creep) *compliance* vs. time. In a creep test, strain ε is proportional to the applied constant stress $\bar{\sigma}$, and depends from time t according to the properties of the material through a *creep compliance*[7] *function* $C(t)$ [241]:

$$\varepsilon(t) = \bar{\sigma} \cdot C(t)$$

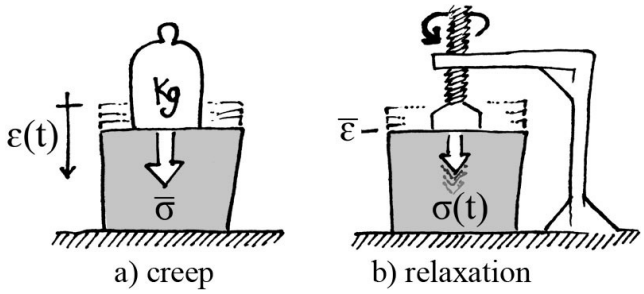

Figure 3.6 - conceptual visualization of a) creep and b) stress relaxation

Conversely, a *relaxation modulus function* $E(t)$ can be defined to link the imposed strain $\bar{\varepsilon}$ to the generated stress $\sigma(t)$ in a relaxation test[8].

$$\sigma(t) = \bar{\varepsilon} \cdot E(t)$$

The response to a creep or relaxation test for $t = 0$ is the elastic response (cfr. §3.1.1 and §3.1.2), which depends from the instantaneous moduli $C_0 = C(0)$ and $E_0 = E(0)$. Alas, although both creep and relaxation ultimately issue from the manifestation of the same physical effect[9], there is no known closed form for connecting the mathematical formulations of the two functions [114,237,240], hence:

$$E_0 = \frac{1}{C_0} \qquad but \qquad E(t) \neq \frac{1}{C(t)}$$

Relaxation $E(t)$ moves toward its equilibrium quicker than creep $C(t)$, and the shape of the function can be substantially different [114,241]. Therefore, if one has available creep data (e.g. the C_i coefficients for the discrete formulations) it is not easy to get insight on the relaxation model (and vice-versa).

If strains are small, the partitioning hypothesis is applicable; ε_{e} being the elastic strain and $\varepsilon_{\mathrm{vp}}$ the viscoplastic strain [242]:

$$\varepsilon = \varepsilon_{\mathrm{e}} + \varepsilon_{\mathrm{vp}}$$

The analytically exact creep compliance function $C(t)$ can be found by solving the convolution integral [241]:

$$C(t) = C_0 + C \int_0^{\infty} \boldsymbol{f}(\tau) \left(1 - e^{-\frac{t}{\tau}}\right) d\tau \qquad \textit{creep compliance}$$

Where C is the creep compliance coefficient, τ represents retardation time and $\boldsymbol{f}(\tau)$ is the compliance distribution of retardation times. This formulation poses a tough challenge for practical applications; instead, a convenient way of developing the

[7] To the letter "the act of complying"; as creep itself is the measured effect, the compliance is intended as the way the effect is measured and mathematically contextualized.

[8] As one can deduct from the equations, the creep function C is expressed in m^2/N, while the relaxation modulus is in N/m^2 .

[9] For polymers, the reversible sliding process of macromolecules over time.

viscoelastic problem is to set up discrete "spring-dashpot" systems, which provide approximate solutions. Such physical approximations use of *Hookean springs* (cfr. §3.1.1) to describe the instantaneous bond deformations between the molecules. The uncoiling of molecules is represented by *Newtonian*[10] *dashpot elements*, in which the applied stress produces a stable strain rate with constant applied stress.

a) spring, following Hooke's law $\sigma(t) = E \cdot \varepsilon(t)$

b) dashpot, following Trouton's law $\sigma(t) = \eta \frac{d\varepsilon(t)}{dt}$

Figure 3.7 - spring and dashpot elements

Constants E and η in Figure 3.7 stand for the spring stiffness and the fluid viscosity respectively. A common notation for dashpot elements combined in series with springs uses the ratio of viscosity to stiffness $\tau = \eta/k$ to represent the viscous flow of strain. Such element goes under the name of Maxwell model (Figure 3.8.b).

With an approach based on the *Wiechert model*[11] (which is a special case of the generalized Maxwell model, when one dashpot is assigned infinite viscosity), using the combination of springs and dashpots shown in Figure 3.8.b, it is possible to find an approximated description of the creep compliance by transforming the integral part of the equation to a finite sum of a of terms.

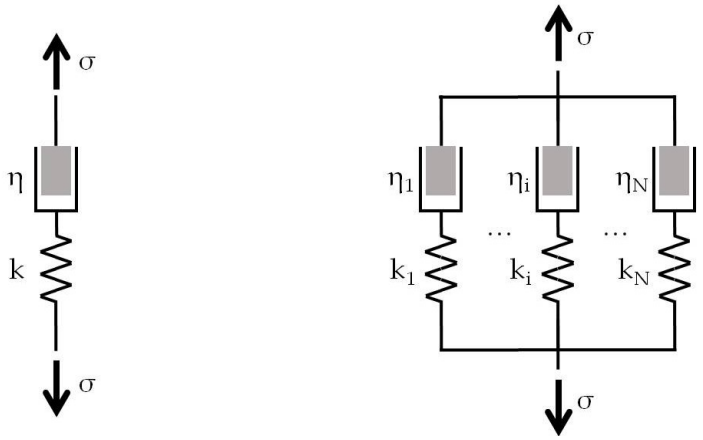

a) b)

Figure 3.8 - rheological representation of a) the Maxwell element and b) the generalized Maxwell model, of which the Wiechert model is a special case if $\eta_i = \infty, \forall i[1; N]$

$$C(t) = C_0 + \sum_{i=1}^{N} C_i \left(1 - e^{-\frac{t}{\tau_i}}\right)$$ *"instantaneous" Wiechert creep compliance*

This formulation can be referred to as an "instantaneous" formulation, because the term C_0 on the right side of the equation is correlated to the material response at

[10] Sir Isaac Newton, Woolsthorpe 1642 - Kensington 1726.

[11] Emil Johann Wiechert, Tilsit 1861 - Göttingen 1928

the instant actions are applied. In the sum, C_i are the creep compliance coefficients, and τ_i the retardation times associated with those coefficients[12]. For $t \to \infty$, an infinite compliance modulus J_∞ can be defined:

$$C_\infty = \lim_{t\to\infty} C(t) = \sum_{i=0}^{N} C_i = C_0 + \sum_{i=1}^{N} C_i$$

If all terms of the sum are known, this allows to find C_∞ from C_0 and vice-versa:

$$C_\infty = C_0 + \sum_{i=1}^{N} C_i \quad \leftrightarrow \quad C_0 = C_\infty - \sum_{i=1}^{N} C_i$$

Therefore, the model allows for a different and equivalent "infinite" formulation:

$$C(t) = C_\infty - \sum_{i=1}^{N} C_i e^{-\frac{t}{\tau_i}}$$

"infinite" Wiechert creep compliance

To summarize, upon loading the material immediately deforms according to the "glassy", instantaneous compliance C_0 ; which for polymers corresponds to the elastic distortion of the chemical bonds. Over time, the compliance rises to an equilibrium value C_∞, corresponding to the rubbery extension of the material[13].

Stress relaxation tests are performed by monitoring the time-dependent stress resulting from a steady imposed strain. As it is generally hard to hold a constant strain, relaxation tests are usually ran with digitally controlled instruments, able to adjust the displacement according to the design strain [241]. Initially, the resulting stress is at a high plateau corresponding to a "glassy" instantaneous modulus E_0 , which progressively decays to an equilibrium "rubbery" modulus E_∞ [240].

---

[12] Note that a coefficient τ_0 is not defined, because the instantaneous compliance C_0 -as the name suggests- occurs instantaneously.

[13] Example: given $C_0 = 7\,mm^2/N$, $C_i = [7,7,9,4,6]\,mm^2/N$ and $\tau_i = [2,8,18,35,60]s$, the infinite creep compliance is $C_\infty = (7+7+7+9+4+6)\,mm^2/N = 40\,mm^2/N$. Any given term i of the sum has accumulated only a fraction its final viscous effect when $t = \tau_i$. Because of the mathematical formulation of the Wiechert compliance, this fraction is equal to $(1 - e^{-1}) \cong 0.63$. From a practical point of view, the viscous effect of each term can be considered complete when $t > 3\tau_i$, which yields a completion ratio > 0.95. Note that the time τ_i also corresponds to the change in the curvature from positive to negative for each creep coefficient contribution in the $\log(t)$ time domain. To better explain this property, a comparative figure is shown with the compliance function (left) and the curves relative to each element i of the sum (right); points where each term has achieved 95% of the its final viscous contribution to the compliance are highlighted.

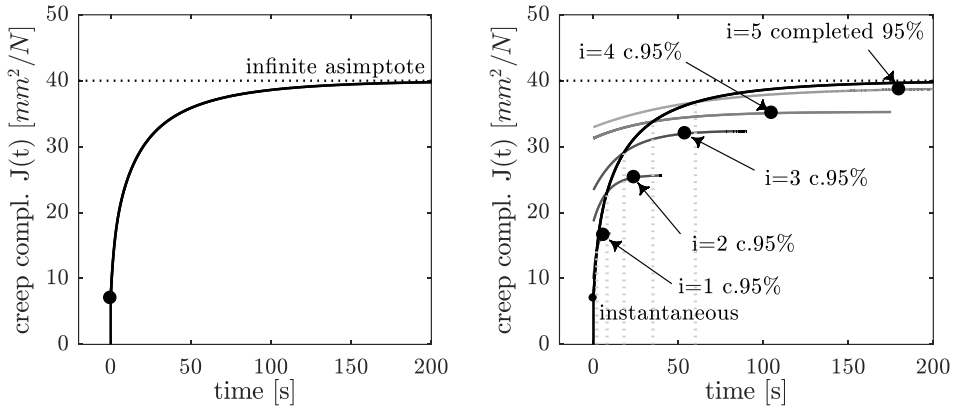

Like creep compliance, relaxation allows for a discrete mathematical formulation based on the Wiechert model, simplifying the analytical solution of the problem which would require the relaxation distribution of retardation times $\boldsymbol{g}(\tau)$:

$$E(t) = E_0 - E\int_0^{\infty} \boldsymbol{g}(\tau)\left(1 - e^{-\frac{t}{\tau}}\right) d\tau \qquad \textit{relaxation modulus}$$

$$E(t) = E_0 - \sum_{i=1}^{N} E_i\left(1 - e^{-\frac{t}{\tau_i}}\right) \qquad \textit{"instantaneous" Wiechert relaxation modulus}$$

$$\boxed{E(t) = E_\infty + \sum_{i=1}^{N} E_i e^{-\frac{t}{\tau_i}}} \qquad \textit{"infinite" Wiechert relaxation modulus} \text{ (Prony)}$$

The correlation between the different coefficients of the modulus can be found by calculating $E(0)$ in an analogous way as in the creep tests, yielding:

$$E_\infty = E_0 - \sum_{i=1}^{N} E_i \quad \leftrightarrow \quad E_0 = E_\infty + \sum_{i=1}^{N} E_i$$

The previous equation for the "infinite" Wiechert relaxation modulus, which allows for a simple representation of the relaxation problem [14], is presented in a formulation which is equivalent to a *Prony series*[15] [243]:

> *"A linear viscoelastic model with a given Prony series is identical to a multi-network Maxwell model"*. J. S. Bergstrom, 2015 [237]

3.1.3.2 METHODS FOR FITTING EXPERIMENTALDATA TO PRONY SERIES

Prony series allow for accurate modelling a decay which is monotonic in nature and eventually reaches a steady state value. While this representation fits perfectly with a generic experimental relaxation modulus $E(t)$, the inverse creep compliance $J^{-1}(t)$ also fits the description and could be dealt with accordingly (this is the approach used in the following Chapter 4 & Chapter 5 when elaborating on shear tests on LG specimens at various temperatures). Several methods have been proposed for fitting experimental viscoelastic data to Prony series coefficients:

[14] Example: given $E_0 = 40\,N/mm^2$, $E_i = [7,7,9,4,6]\,mm^2/N$ and $\tau_i = [2,8,18,35,60]s$, we find the infinite creep compliance is $E_\infty = (40 - 7 - 7 - 9 - 4 - 6)\,mm^2/N = 7\,mm^2/N$, using the same considerations discussed in footnote #13 above, the shape of the compliance function is:

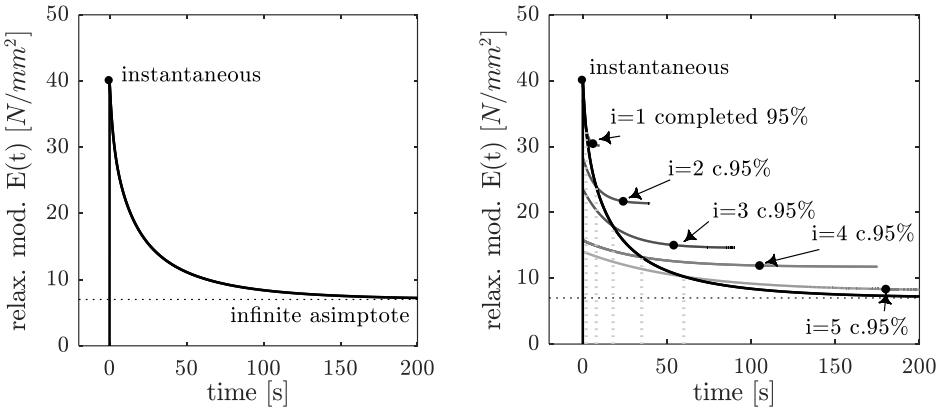

[15] Gaspard Clair François Marie Riche de Prony, Chamelet 1755 - Asnières-sur-Seine 1839.

- *constrained coefficients* method, J. E. Soussou et al., 1970 [244],
- *multidata method*, T. L. Cost & E. B. Becker, 1970 [245,246]
- *domain of influence* (DOI) method, F. S. Gant & M. V. Bower, 1997 [243],
- *weighted nonlinear regression*[16], C. Tzikang, 2000 [247],
- *power-law pre-smoothing*, S. W. Park & Y. R. Kim, 2001 [248].

While all these techniques have edges and weaknesses; the DOI method seems to be a powerful tool, to the extent that it allows fine-tuning a fitting algorithm with a fixed number of coefficients. Nevertheless, this technique needs a cured array of experimental data to perform a reliable fit, so pre-processing is sometimes needed.

The DOI method has been thoroughly explained and discussed by Gant and Bower in their work: *Domain of Influence Method: A New Method for Approximating Prony Series Coefficients and Exponents for Viscoelastic Materials* [243], so a walkthrough of all steps would be redundant within this manuscript (cfr. Appendix I).

3.1.3.3 HEREDITARY INTEGRALS FOR LINEAR VISCOELASTICITY

Creep and relaxation tests are usually conducted aiming to hold steady quantities of stress or strain in the materials; nonetheless, sometimes the experimental data is scattered or irregular in such a way that it is not accurate to consider either the stress or strain a fixed quantity over time.

To determine the stress state in a viscoelastic material at a given time, the deformation history must be considered. For LVE materials, a superposition of hereditary integral describes the time dependent response [247]:

$$\sigma(t) = E(t)\varepsilon_0 + \int_0^t E(t-\xi)\frac{d\varepsilon(\xi)}{d\xi}d\xi$$

In this situation, one may use a finite-difference form to find a convenient approximated solution [114,241] (the compliance function may be approximated in an analogous way for a time-dependent load history):

$$\sigma(t_i) = k_0\varepsilon(t_i) + \sum_{j=1}^{N}\frac{k_j\left(\varepsilon(t_i) - \varepsilon(t_{i-1}) + \sigma_j(t_{i-1})\right)}{1 + \frac{t_i - t_{i-1}}{\tau_j}}$$

Another approach to deal with varying input functions by means of the superposition principle could be to compute the solution by approximating the input function with a succession of short contributions constant actions. For instance, starting with the instantaneous formulation of the creep compliance:

$$\varepsilon(t) = \left\{k_0 + \sum_{i=1}^{N} k_i\left(1 - e^{-\frac{t}{\tau_i}}\right)\right\}\bar{\sigma}$$

If one can identify a finite number of time intervals $\Delta t_i = t_{i+1} - t_i$ in which the strain σ_i can be considered a constant value, it is possible to compute the solution in the time domain referring to that contribution by adding the effect of σ_i at the time t_i and subtracting the same amount induced at t_{i+1} .

$$\varepsilon_{\Delta t_i}(t) = \left\{k_0 + \sum_{j=1}^{N} k_j\left(1 - e^{-\frac{t-t_i}{\tau_j}}\right)\right\}\sigma_i - \left\{k_0 + \sum_{j=1}^{N} k_j\left(1 - e^{-\frac{t-t_{i+1}}{\tau_j}}\right)\right\}\sigma_i$$

[16] Based on the Marquardt-Levenberg Method [335].

$$\varepsilon_{\Delta t_i}(t) = \left\{ \sum_{j=1}^{N} k_j \left[-e^{-\frac{t}{\tau_j}} \left(e^{\frac{t_i}{\tau_j}} - e^{\frac{t_{i+1}}{\tau_j}} \right) \right] \right\} \sigma_i$$

3.1.3.4 DYNAMIC TESTS

Dynamic tests can be used to get insight on the viscoelastic properties of materials in the small-strain domain [148,237] (Figure 3.9). In virtue of the viscous properties of polymers, when a sinusoidal strain $\varepsilon(t)$ is imposed, a similar steady stress state $\sigma = \sigma_0 \sin(\omega t - \delta)$ with the same angular frequency ω and retarded phase δ is reached after a transient period [114,115,241]. By imposing a cyclic shear strain:

$$\begin{cases} \varepsilon_0 \sin(\omega t) & \text{if } t \geq 0 \\ 0 & \text{if } t < 0 \end{cases}$$

If $\lim_{s\to\infty} E(s) = 0$, the stress can be computed using the hereditary integral shown previously in §3.1.3.3 (also, $G(t) = E(t)/2(1+\nu)$ is the *shear relaxation modulus*):

$$\sigma(t) = \int_0^{\infty} G(s)\omega\varepsilon_0 \cos[\omega(t-s)]\, ds$$

Where $s \overset{\text{def}}{=} t - \xi$. Using $\cos(\alpha - \beta) = \cos\alpha\cos\beta + \sin\alpha\sin\beta$ yields:

$$\sigma(t) = \varepsilon_0 \sin(\omega t)\left[\omega \int_0^{\infty} G(s)\sin(\omega s)\, ds\right] + \varepsilon_0 \cos(\omega t)\left[\omega \int_0^{\infty} G(s)\cos(\omega s)\, ds\right]$$

Defining the s*torage modulus* E' and *loss modulus* E'', the equation can be simplified:

$$G'(\omega) = \omega \int_0^{\infty} G(s)\sin(\omega s)\, ds \qquad \begin{matrix} \textit{(relaxation)} \\ \textit{Storage modulus} \end{matrix}$$

$$G''(\omega) = \omega \int_0^{\infty} G(s)\cos(\omega s)\, ds \qquad \begin{matrix} \textit{(relaxation)} \\ \textit{Loss modulus} \end{matrix}$$

$$\sigma(t) = \varepsilon_0[E'(\omega)\sin(\omega t) + E''(\omega)\cos(\omega t)]$$

As the steady state strain response is $\sigma = \sigma_0 \sin(\omega t - \delta)$, one can use $\sin(\alpha+\beta) = \sin\alpha\cos\beta + \cos\alpha\sin\beta$ to write $\sigma(t) = \sigma_0 \sin(\omega t)\cos\delta + \sigma_0 \cos(\omega t)\sin\delta$. Therefore:

$$G'(\omega) = \frac{\sigma_0}{\varepsilon_0}\cos\delta \qquad \text{and} \qquad G''(\omega) = \frac{\sigma_0}{\varepsilon_0}\sin\delta$$

The storage modulus, defined as the stress in phase with the strain in a sinusoidal shear deformation divided by the strain, is a measure of the energy stored and recovered per cycle. Since both $G(t)$ and $G'(\omega)$ are measurements of the stored elastic energy, a dynamic measurement at frequency ω is qualitatively equivalent to a transient one at $t = 1/\omega$, so the graphs for G' over ω and G' over t are approximately mirror images with respect to a vertical axis (Figure 3.10). In particular, when $G(t)$ is changing very slowly, $G(t) \cong G'(1/t)$ [114].

Nevertheless, it has been pointed out that relationships among LVE functions such as storage and relaxation moduli have bases in the theory of linear differential and integral equations [249]. While several approximate interconversion methods can be found [248,250,251], Mun et al. [252] proposed an exact interconversion procedure for LVE functions of asphalt concrete from frequency-domain to time-domain (although details on calculations are not given).

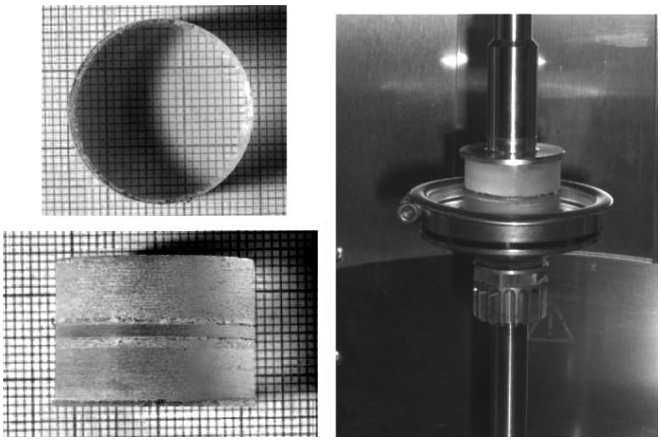

Figure 3.9 – LG specimen and testing in a torsional rheometer (Andreozzi, 2014 [148]*)*

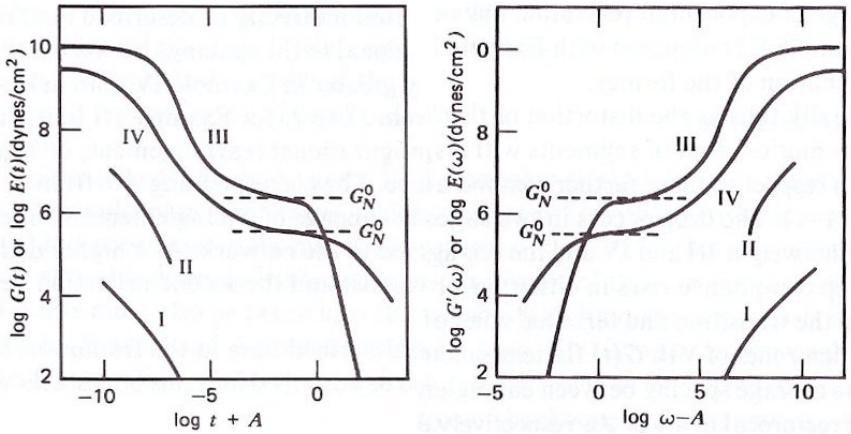

Figure 3.10 - relaxation & storage moduli plotted against t and ω axes (Ferry, 1980 [114]*)*

3.1.3.5 TIME-TEMPERATURE SUPERPOSITION (REDUCED VARIABLES METHOD)

Plotting on the same graph viscoelastic functions such as compliance/relaxation or loss/storage moduli (cfr. §3.1.3.1 & §3.1.3.4), it has been observed[17] that empirical shifts of data obtained at different temperatures along a logarithmic time or frequency domain may result in a unique, smooth and composite curve [114]. The significance of this empirical *shift factor* a_T in terms of molecular parameters became evident a few decades later with the work of P. E. Rouse in 1953 [253]:

$$a_T = \frac{[a^2\zeta_0]_T \cdot T_{\text{ref}}}{[a^2\zeta_0]_{T_{\text{ref}}} \cdot T}$$

where ζ_0 is the internal friction coefficient, a the characteristic molecules length and T is temperature (the subscript ref stands for reference conditions). The time-temperature superposition resulting from this empirical time-shifting procedure results in a reduced variables method, also known as "*viscoelastic corresponding states*", to the extent that the materials response at a given temperature is traced back to an equivalent response at a different time/frequency at a reference temperature. The original theory on which the method is based on has been developed in a linear viscoelastic context, for superposing storage and loss moduli of dynamic tests. The nowadays standard empirical correlation used in polymer

[17] Observations were made in the first decades of the 20th century by K. W. Wagner and applied to dielectric measurements.

science between temperature T and shift factor a_T has been proposed in 1955 by M. L. Williams, R. F. Landel and J. D. Ferry [254]:

$$\log a_T = \frac{-C_1(T - T_{ref})}{C_2 + (T - T_{ref})}$$

This expression, sometimes called WLF equation, is an empirical formulation for a curve $a_T(T)$ with whom many polymers have been reduced to standard states at reference temperatures T_{ref}. Coefficients C_1 and C_2 can be computed in a closed form with tests carried at three temperatures, using one as reference; if the number of investigated temperature is higher than three an interpolation criterion must be defined[18]. It has been observed that if the glass transition temperature T_g is lower than the reference temperature, coefficients C_1 and C_2 are positive[19].

Accounting for both time t and temperature T dependencies, a refined version of the creep compliance C and stress relaxation E is obtained. Using "instantaneous" formulations rather than the "infinite" ones introduced in §3.1.3.1 (although the procedure can be applied analogously for the latter), yields:

$$C(t,T) = C_0(T,T_{ref}) + \sum_{i=1}^{N} C_i(T,T_{ref})\left(1 - e^{-\frac{t}{\tau_i(T,T_{ref})}}\right) \qquad \textit{"instantaneous" Wiechert creep compliance}$$

$$E(t,T) = E_0(T,T_{ref}) - \sum_{i=1}^{N} E_i(T,T_{ref})\left(1 - e^{-\frac{t}{\tau_i(T,T_{ref})}}\right) \qquad \textit{"instantaneous" Wiechert relaxation modulus}$$

More details will be introduced on the time-temperature superposition principle in Chapter 5, paragraphs §5.1.2.1 and §5.1.2.3, with a practical application on three interlayer materials used for LG: SG, DG41 and PVB (cfr. §1.1.2).

3.2 PLASTICITY

While elastic materials will always internally store a form of energy, able to restore their initial configuration when external actions are removed (cfr. §3.1). In opposition, another class of materials can be defined for those which undergo non-reversible changes under certain conditions. From a thermo-mechanical point of view, this inability to restore the original shape is ascribed to the activation of dissipative mechanisms within the material structure. The power dissipated during plastic flow is called *power of dissipation* D, and is essentially positive [255]:

$$D = \sigma_{ij}\varepsilon_{ij} \geq 0 \qquad i,j = 1,2,3$$

In engineering, the study of plasticity has often been related to the study of metals, for which it has been observed that plastic deformations consist of slip in crystal dislocations [256]. Hence, it is generally assumed that the onset of yielding and power dissipation occurs when a fixed value of the maximum stress is reached:

$$\sigma = \pm\sigma_Y$$

[18] Most of the times, the least-squares differences method is used.

[19] While in first applications of the WLF equation, averages for many polymers of coefficients C_1 and C_2 had been used, it later became clear that the variation among different materials were too large to allow for the use of such "universal" values. In a slightly better approximation, fixed values $C_1 = 8.86$ and $C_2 = 101.6$ can be used, in conjunction with an adjustable reference temperature T_s, which usually fell about 50°C above the glass transition temperature T_g.

Several criteria can be used to define yield conditions, *Tresca*[20] and *von-Mises*[21] ones being the most commonly accepted for metals. A perfectly plastic solid can thus be described as a solid which undergoes unlimited plastic strains under constant reference stress, when subjected to a homogeneous stress state $\sigma_R = \sigma_Y$ [255].

Nevertheless, the theory of perfect plasticity seems to be not particularly relevant and helpful when dealing of LG structures, as neither glass or interlayer materials fill the profile for perfectly plastic solids (cfr. §1.1.1 and §1.1.2).

3.2.1 VISCOPLASTICITY

The fundamental time-independence assumption of all theories of plasticity does not allow for a simultaneous description of both plastic and rheologic properties of materials. In fact, there is no yield function for viscoplastic solids, but a stress- or strain-rate-dependent inelastic behaviour is observed instead, this means that when permanent deformations are produced, those are dependent on the rate at which external actions are applied [239,257].

Constitutive equations for viscoplasticity can be based on springs, dashpots, sliders and other elements, to model different responses such as perfectly viscoplastic, elastic perfectly viscoplastic and elasto-viscoplastic hardening solids (Figure 3.11).

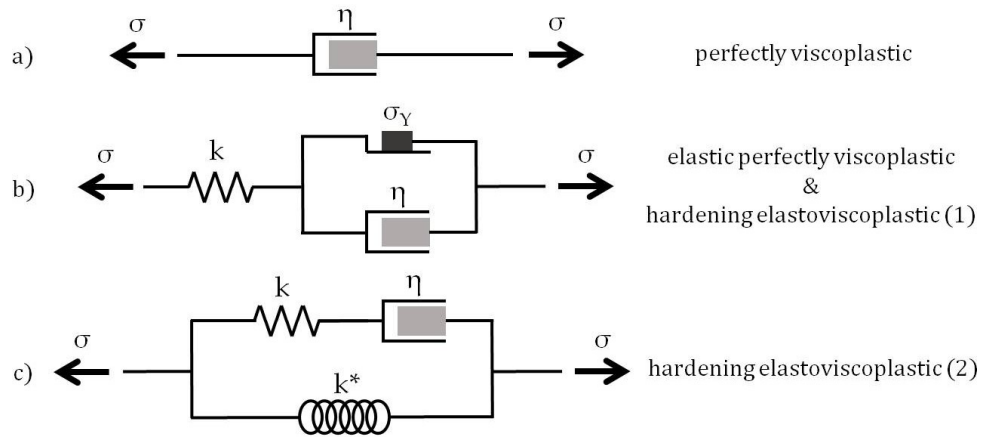

Figure 3.11 - one-dimensional constitutive models for viscoplasticity [242,258]

Perfect Viscoplastic fluid (PVP)

In a perfect viscoplastic solid the stress follows the Trouton's law (cfr. §3.1.3), hence σ is a linear function of the strain rate $\dot{\varepsilon}$ (Figure 3.11.a):

$$\sigma = \eta\dot{\varepsilon}$$

A creep test yields linear plot, while a relaxation test has a vertical asymptote for $t = 0$ and an horizontal one at zero for $t \to \infty$.

Elastic perfectly plastic solids (EPP)

The rate of plastic strain in EPP materials is a function of the yield stress σ_Y of the slider element. A constant stress flows through the slider element when the elastic limit is exceeded; otherwise, the plastic strain is nil. The Bingham-Maxwell[22] model is shown in Figure 3.11.b [255,259]:

[20] Henri Édouard Tresca, Dunkirk 1814 - Paris 1885

[21] Richard von Mises, Lemberg (now Lviv) 1883 - Boston, 1953; the yield surface is also known under the name of *Maxwell, Huber, Hencky and von-Mises yield condition*.

[22] Eugene Cook Bingham, Cornwall 1878 - Easton 1945, and James Clerk Maxwell, Edinburgh 1831 - Cambridge 1879.

$$\begin{cases} \sigma = E\varepsilon & \text{if } \|\sigma\| < \sigma_Y \\ \dot{\varepsilon} = \dfrac{\dot{\sigma}}{E} + \dfrac{\sigma}{\eta}\left[1 - \dfrac{\sigma_Y}{\sigma}\operatorname{sign}(\sigma)\right] & \text{if } \|\sigma\| \geq \sigma_Y \end{cases}$$

Hardening elastic viscoplastic solids (HEVP)

An elastic-viscoplastic material with strain hardening can be assembled in a similar array of an EPP material (Figure 3.11.b), provided that the yield stress σ_Y in the sliding element is not constant anymore, but instead increases with the viscoplastic component of strain ε_{vp}. Consequently, the stress now depends both on the strain rate $\dot{\varepsilon}$ and from a function f which includes ε_{vp}:

$$\begin{cases} \sigma = E\varepsilon & \text{if } \|\sigma\| < \sigma_Y \\ \dot{\varepsilon} = \dfrac{\dot{\sigma}}{E} + f\left(\sigma, \sigma_Y, \varepsilon_{\text{vp}}\right) & \text{if } \|\sigma\| \geq \sigma_Y \end{cases}$$

This classical formulation is not the only one proposed for HEVP materials, besides, the function f is not specified a priori, opening to an array of possible mathematical interpretations. As this research field is still looking for definitive models for finite strain response of polymers, a few studies have concurrently tried to tackle this topic, either with a reinterpretation of classical models or introducing new approaches[23].

3.3 ADHESIVE BONDS

While *cohesion* refers to the strength of the bonds within homogeneous materials, *adhesion* is a measure of the tendency of different particles (or surfaces) to "stick" one another. In engineering practice, adhesive joints can be designed to endure a certain set of loads or displacements. In LG industry, adhesion is a relevant factor for assessing structural performance in three situations:

- securing glass to interlayers,
- securing LG to an external frame or supports (seals),
- bounding of reinforcements.

In fact, the purpose and most of the times the behaviour of LG ultimately originates from strength of the adhesive bond between glass and interlayer materials (cfr. §1.1.3). While adhesive properties of different resins[24] to a variety of reinforcements have been investigated (e.g. steel profiles and tendons, glass or carbon fibres, concrete, wood, GFRP, etc. cfr. §2.2.3 and §2.2.4 for more), these properties are of limited interest for this research. Regarding external adhesive joints for LG elements, traditional seals are made using silicone-based compounds (*silicone structural glazing*) [38]. This field is also far from the aim of this work, where the focus will be set to studying interactions among glass and interlayers, in which loss of adhesion is relevant for two orders of reasons:

[23] The *affine network* hypothesis [336–338], based on the assumption that the number of entangled points in the molecular chains remains constant during deformation [339]; multi-scale models for semi-crystalline polymers in finite- [340,341] and infinitesimal-strain regimes [342,343], using a spherulitic morphology with a radial assembly of crystalline lamellae and amorphous layers [339]; generalized yield surfaces [339], based on the Drucker and Prager criterion, including invariants of the stress tensor and deviatoric part of the stress tensor; hyperelastic strain-hardening springs in HEVP one-dimensional arrays similar to the one in Figure 3.11.c [258], intended to reproduce the finite strain elasto-viscoplastic non-linear response of polymeric materials.

[24] Most of the times epoxy resigns [209].

- the stiffness and resistance may be compromised,
- delamination can be detrimental from an aesthetic point of view.

Surprisingly, relevant standards rarely mention the adhesion strength between glass and interlayers [79] (cfr. §2.1), let alone recommending specific values[25]. While standardized ageing tests can be performed according to EN ISO 12543-4[26] [260], as an indirect way for assessing expected long-term effects of varying temperatures and humidity [146], observations of LG delamination induced by mechanical effects can only rely on few studies (some referred to metal-interlayer glass joints) [65,128,130,146,261].

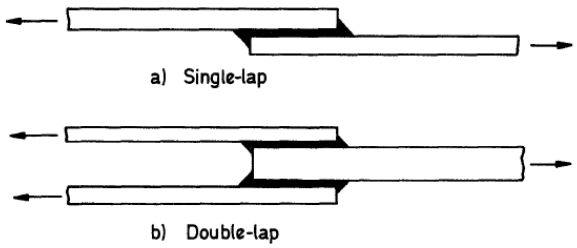

Figure 3.12 - geometry of common adhesive joints for LG (Adams and Wake, 1984 [38,94]*)*

A single-lap joint model shown in Figure 3.12.a can be used to understand the mechanics of multi-layered LG elements connections with any number of glass plies (e.g. three- or four-layered LG elements loaded transversally with flexural actions can be imagined as series of single-lap joints among adjacent plies).

While several arrays may be considered for adhesion of LG elements to the substructure (e.g. step, butt, butt strap and double butt strap [94]), for the purpose of this work and understanding the experimental analyses, it is only of interest to focus on some specific aspects related to double-lap adhesive joints of the kind described in Figure 3.12b. As the figure suggests, loads in single- and double-lap joints are parallel but not perfectly collinear with the interlayers. Therefore, the bending moment generated perpendicularly to the plane must be resolved within the joint with stresses normal to the direction of the applied loads. Tearing and compressive stresses are higher at the end of the joint and smaller in the middle. The relative influence of these normal stresses is a function of the geometry of the joints: for a fixed thickness of the glass plies, the longer the joint, the smaller the normal stresses compared to shear ones. For long joints compared to glass plies thickness, normal stresses are very small and can be neglected [65].

Parametrical study at varying temperatures for the shear stress distribution in SG used as an adhesive for metals on LG elements has been performed by M. Santarsiero et al. [130] (Figure 3.13). The analysis shows that the shear stresses

[25] For instance, the Italian technical document CNR-DT210 [38], one among those attempting a wide-ranging approach to LG design (cfr. §1 and §2.1), doesn't provide numerical specifications regarding the strength of the adhesion between glass and interlayers. Instead, the document states (translated from italian): "*It is necessary to point out that adhesion between glass and interlayer involves a chemical bond; this circumstance requires* […] *to perform mechanical tests on stratified specimens for the evaluation of the overall behavior. Since there are currently no regulatory indications in this regard,* […] *tests on plastic materials only are allowed*".

[26] For high temperatures, LG elements are heated to $100°C$, a temperature held constant for two hours; for humidity tests, specimens are put for two weeks in saturation conditions ($RH = 100\%$) at a temperature of $50°C$.

factor $\alpha_V = (A \cdot \tau_{\max})/F_V$, calculated for the nominal maximum stress $\tau_{\max}$ resulting from an applied shear force F_V on an adhesive area A is lower than 1.11 for $T > 0$°C. Besides, the stress distribution in Figure 3.13.a shows that a peak in the shear stress is found close to the edges, and is higher for lower temperatures. In any case, the actual distribution of shear stresses can be confused with the average value with limited error, especially for temperatures above 30°C.

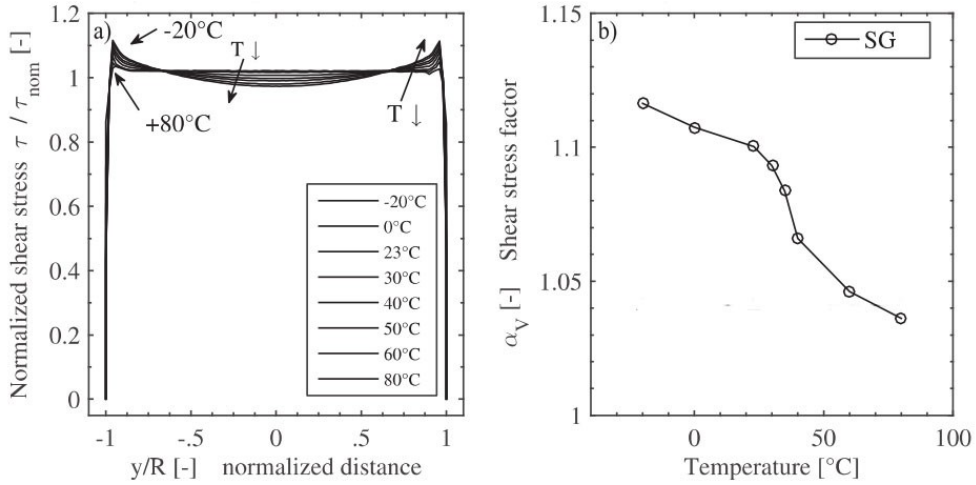

Figure 3.13 - a) shear stress distribution in SG for varying temperatures b) shear stress factor at different temperatures (Santarsiero, 2016 [130]*)*

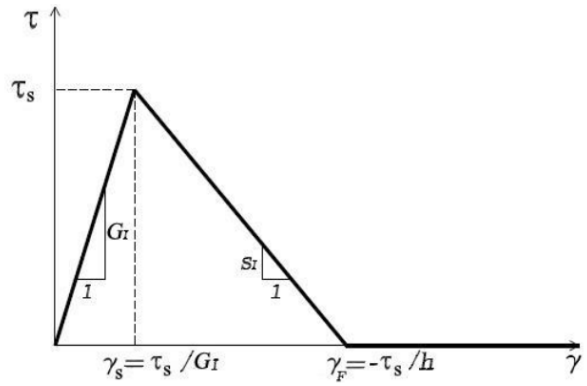

Figure 3.14 – tri-linear adhesion diagram (Cottone, 2010 [262]*)*

Knowing the stress distribution, to evaluate the risk of delamination and joint safety margins, a tri-linear model like the one shown Figure 3.14, can be used, where the horizontal segment corresponds to the loss of adhesion among surfaces.

This mechanical problem is talked using a zero-thickness interface concept, for which two adherents come into contact through an interaction surface. The local interface response in *mode II* [34] is adopted: a LE branch up to the adhesion strength a_0, followed by softening to the final displacement γ_F corresponding to the perfect fracture formation. The response for a monotonic displacement is [262]:

$$\begin{cases} \tau = E_I u & \text{for } 0 \le u \le u_E \\ \tau = s_I(u_F - u) & \text{for } u_E < u \le u_F \\ \tau = 0 & \text{for } u > u_E \end{cases} \qquad \text{where} \qquad s_I = -\frac{E_I h}{E_I + h}$$

In which s_I is the *interface softening modulus*, E_I the interface tangential elastic stiffness and $h < 0$ the softening parameter.

4 EXPERIMENTAL TESTS

LG composites bear an inherent complexity, for their non-homogeneous and anisotropic structure, but also for the intrinsic properties of the thermoplastic materials used as interlayers. Direct experimental tests are often used to address the lack of reliable theoretical models. Within this research, extensive and different experimental investigations have been carried out, regarding some of the less known mechanisms which are significant in LG design.

A synthesis of test methods used by the scientific community to model interlayer properties has been provided in §2.2.1. Attempts to provide a complete characterization of thermoplastics did not yet produce satisfying results, and experimental tests which aim to produce a full description of all possible combinations of boundary conditions (e.g. time, temperature, stress and strain rate, etc.) would lead to unreasonably high cost/benefit ratios [263].

Standard tensile tests were carried out in the *Politecnico di Milano*. The testing procedure was defined with Prof. S. Cattaneo and carried out with the help of a local undergraduate. Known issues regarding the extension of results of these simple and fairly cheap tests to LG design have been raised by D. Delincé in [7] and others [59,263]. Those tests are known to be unable to provide data on viscous properties and actual operating conditions of interlayers within LG elements [59]. Therefore, these will be looked at with a critical eye as a sort of "snapshot" of a more complex behaviour[1]. Three thermoplastic materials are tested: PVB, DG41 and SG (cfr. §1.1.2).

Viscoelastic properties are investigated in a subsequent campaign, described in §4.2 and further discussed in §5.1.2. Using small LG specimens in which the interlayers are assigned uniform[2] shear stress and strain, long-term tests are carried out in a climatic chamber at various temperatures. The same interlayer materials investigated with tensile tests have been studied (cfr. §1.1.2 and §4.2). These investigations were re-designed from the work of E. Cagnacci [261] and also carried out in Milan, with the help of another undergraduate student.

Full-scale tests on post-failure response of LG structural beams were designed in collaboration with Prof. Orlando and carried out in Firenze in the *Laboratorio Strutture* of the *Scuola di Ingegneria* in S. Marta. Part of the experimental analyses could benefit from the assistance of a masters degree student in civil engineering.

4.1 SHORT-TERM TENSILE PROPERTIES OF INTERLAYERS

Simple tensile tests, designed to assess the properties of plastic materials, can provide useful data with little effort [11,66,83,118,150,264]. These *conventional*[3] uniaxial tests are regularly used to look into the mechanical properties of materials with tensile load-carrying capacity such as polymeric interlayers.

[1] Obtaining viscoelastic or hyperelastic parameters requires a number of various tensile testing procedures and a very large number of specimens [118,137,152,344,345].

[2] Details on the uniformity of stress and strain are discussed in §4.2.1.

[3] The term "conventional" is used by numerous researchers, as such tests are often prescribed when dealing about plastics materials and are detailed by ASTM and ISO standards [66,264].

Outcomes of tensile tests are presented in the following paragraphs, while a critical analysis an discussion is provided in §5.1.1.

4.1.1 DESIGN AND AIM OF TENSILE TESTS

Short-term properties of interlayer materials have been investigated following the standards guidelines applicable to uniaxial tensile tests of plastics [66,264]. Throughout tests, the end grips of flat, *dog-bone*[4] shaped, material specimens are pulled apart at constant velocity, inducing an increasing strain which is mostly concentrated within the narrow section of the body (Figure 4.2). The average strain is measured between two points which are at a distance G on the un-deformed specimens.

Tested specimens were extracted out of larger, $0{,}76mm$ thick, interlayer sheets: half the thickness of layers used for laminating specimens for the campaign dedicated to study the viscoelastic properties (cfr. §4.2). According to the standards [66], "Type IV" specimens are suited when *direct comparisons are required between materials with different rigidity cases (that is, nonrigid and semirigid)* [66], which appears to be the case in our study (cfr. §1.1.2.1, §1.1.2.2 and §1.1.2.3). For $T \leq 4.06mm$, specimen dimensions shown in Figure 4.2 are fixed[5]: $W = 6mm$, $L = 33mm$, $W_0 = 19mm$, $L_0 = 115mm$, $G = 25mm$. A conveniently shaped manual die-cutter was used to provide identical specimens from the larger interlayer pieces. Once extracted, specimens were checked for scratches and imperfections. Flawed specimens were discarded.

Figure 4.1 - a) cutting of the specimens and b) manual finishing

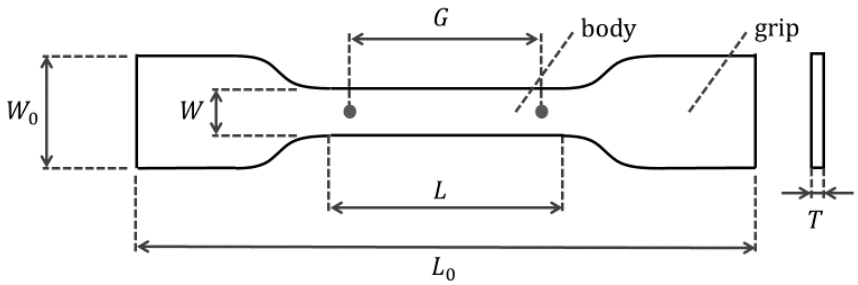

Figure 4.2 – Type IV dog-bone specimen according to ASTM D638-14

[4] A technical term often used in literature for such specimens, due to the visual analogy with a stereotypical bone (also sometimes called "dumbbell" shape).

[5] Radii of fillets, along with several other geometric specifications, are also provided in the aforementioned ASTM standard [66], they are not reported here for brevity.

Tests have been performed in a room with electronically-controlled humidity and temperature: 23.5°C and 50% RH. The same room was used for storage of materials before testing, complying with norm prescriptions [66] (23 ± 2°C , 50 ± 10% RH).

An Instron-3300[6] testing machine was used, complying with both ISO 7500-1 and ISO 9513. The machine has a stationary claw and a moving one, both connected to one grip of a dog-bone specimen. The position of the grips and claws is arranged in such a manner that the longest axis of tested specimens is aligned with the direction of relative displacement among the machine claws (i.e. a resulting pure normal force is transferred trough any cross-section of the specimen). A load-indicator is built-in within the lever system moving the claws, while an extensometer was used for measuring the distance among reference points on the specimen (Figure 4.2).

Testing velocity (i.e. speed of the relative movement of the claws) has specific and matching designations in both standards ISO [264] and ASTM [66], depending on specimen types. Tests were repeated for three different velocities:

- $v_1 = 5$ mm/min,
- $v_2 = 50$ mm/min,
- $v_3 = 500$ mm/min.

The minimum data acquisition frequency in Hz was [264]:

$$f_{\min} = \frac{v_i}{60} \cdot \frac{L_0}{L \cdot r} = 1.77 v_i \qquad i = 1,2,3$$

where v_i is claws relative displacement velocity in mm/min, L_0/L the ratio between initial and transient grip separation and r is the resolution in mm. Acquisition frequencies of 10, 100 and 1000 Hz were chosen for increasing velocity.

Standards prescribe a minimum number of specimens and a number of strain rates to be investigated, depending on the material properties (isotropic or anisotropic) [66,264]. The limitation could not always be fully respected for the limited amount of raw material which was available from suppliers of SG and PVB. Instead, DG41 specimens satisfactorily met requirements for the minimum number at the three velocities (Table 4.1).

Table 4.1 - number of specimens per material per test velocity

speed	SG	DG41	PVB
v_1	2	5	2
v_2	5	5	5
v_3	5	5	5

Four quantities were electronically measured throughout tests: time t , displacement d, force f and relative displacement d between reference measure points (G in Figure 4.2).

4.1.2 EXPERIMENTAL RESULTS

Specimens had been stored for about one week before testing, in the same temperature-controlled room used for tests (cfr. §4.1.1). Figure 4.3 shows a photographic follow-up for a PVB specimen: the remarkable elongation capacity and necking due to Poisson effect [164] is evident through parts a) to f), up to the final break in g).

[6] Instron Illinois Tool Works Inc. Canton, Massachusetts

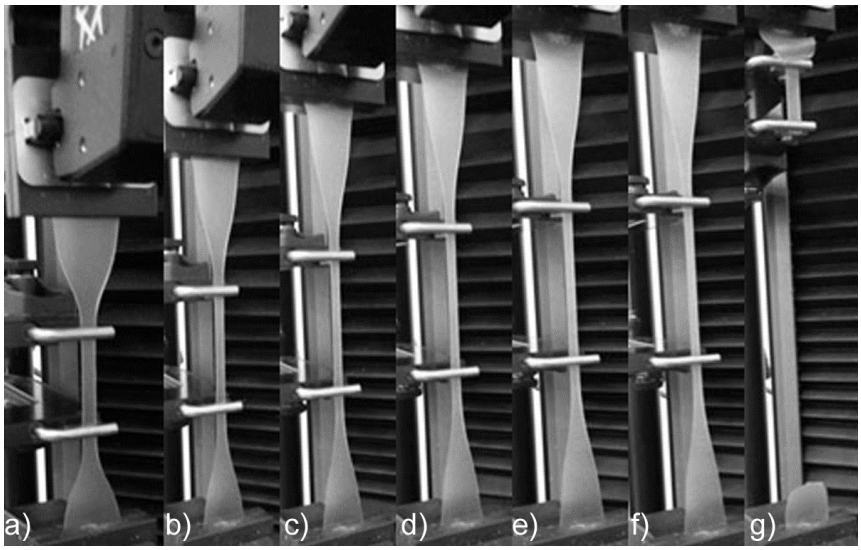

Figure 4.3 - progression of tensile tests on PVB

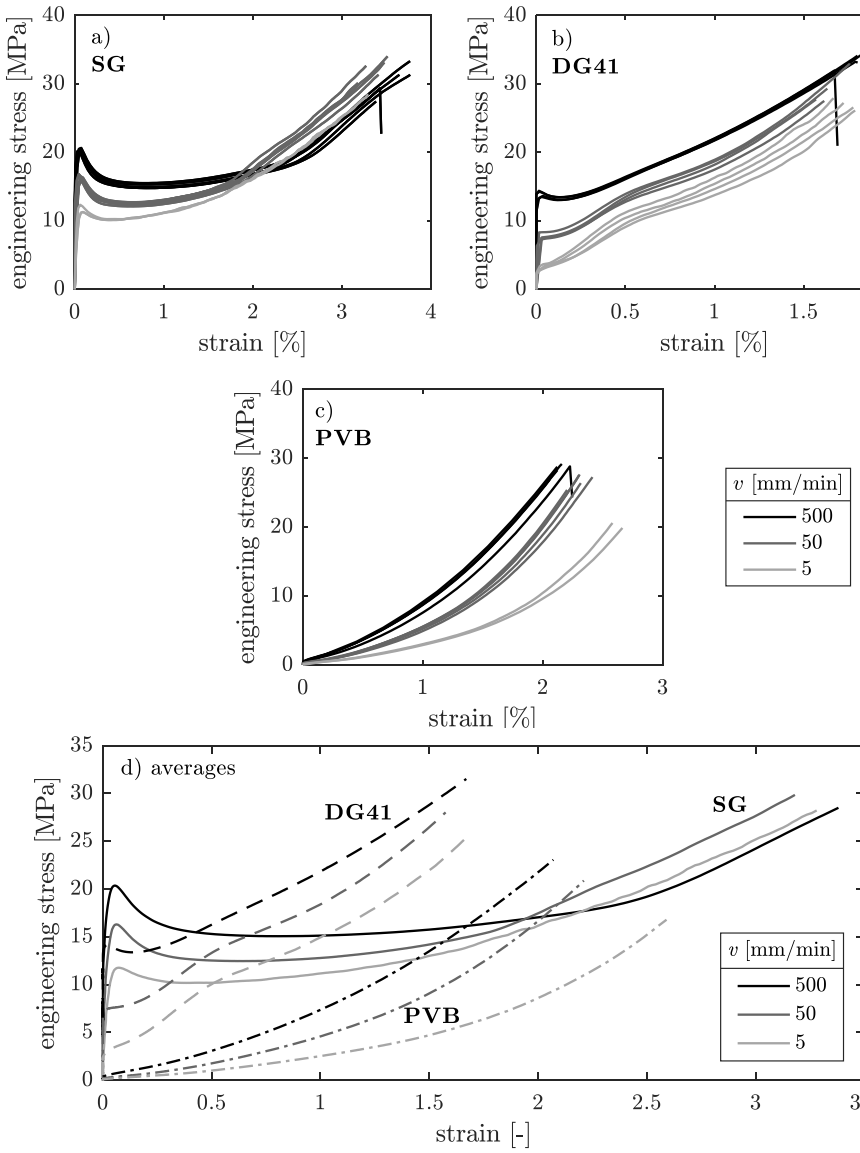

Figure 4.4 - stress-strain curves: a) SG, b) DG41, c) PVB and d) averages

The failure of specimens always originated in a point within the narrow area, never in the grip parts nor at the interface with the machine clamps.

Tests duration of was in the order of twenty minutes for v_1, two minutes for v_2 and fifteen seconds for v_3.

The engineering stress in the narrow area has been computed, knowing the applied force and original geometry of the specimen: with a cross-sectional nominal area $A_n = 4{,}56\ mm^2$ (cfr. §4.1.1), $\sigma_1 = f/A_n$. The mean strain in the narrow area can also be calculated knowing the initial distance and the relative displacement d of the two measure points: $\varepsilon = (G + d)/G$.

Stress results of performed tests are presented in Figure 4.4. Results show that the influence of the strain rate is more relevant for DG41 and PVB interlayers, while SG has a more consistent response at different strain rates.

Maximum tearing strength is usually of little interest for architectural LG applications, as it is reached for very high strains which are not compatible with serviceability limit states imposed by design. Nonetheless, for completeness in the discussion of experimental results, results in terms of ultimate strain ε_u and engineering stress $\sigma_{eng,u}$ are given in Table 4.2.

Table 4.2 – experimental minimum ultimate strain and engineering stress

claw displacement velocity v	**ultimate failure**	**SG**	**DG41**	**PVB***
5 mm/min	$\varepsilon_u\ [-]$	3,28	1,67	2,59
	$\sigma_{eng,u}\ [MPa]$	28,2	25,4	16,8
50 mm/min	$\varepsilon_u\ [-]$	3,18	1,57	2,21
	$\sigma_{eng,u}\ [MPa]$	29,8	28,1	20,9
500 mm/min	$\varepsilon_u\ [-]$	3,38	1,67	2,07
	$\sigma_{eng,u}\ [MPa]$	28,5	31,5	22,8

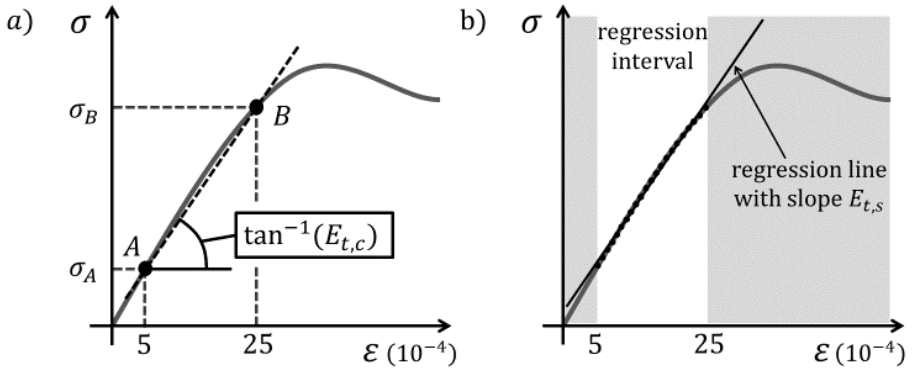

Figure 4.5 - construction for a) chord- and b) regression-slope tensile modulus

Since the existence of an elastic limit for plastics has been debated [7,78,114], the term "elastic modulus" is indicative, only to measure a quantitative value of the rigidity. Standards suggest two supposedly equivalent approaches to evaluate the elastic tensile modulus of polymers. The first method, also called *chord slope method* [264], is illustrated in Figure 4.5.a: two points A and B are found on the stress-strain curves, corresponding to fixed values of strain. The slope of the straight line interpolating the points defines the tensile "chord" modulus $E_{t,c}$:

$$E_{t,c} = \frac{\sigma_B - \sigma_A}{\varepsilon_B - \varepsilon_A} = 500 \cdot (\sigma_B - \sigma_A) \qquad \begin{matrix} A = [0.05\%; \sigma(0.05\%)] \\ B = [0.25\%; \sigma(0.25\%)] \end{matrix}$$

The regression slope method is illustrated in Figure 4.5.b: the least-squares difference regression line $\sigma(\varepsilon)$ is found using points in the interval $0{,}0005 \leq \varepsilon \leq 0{,}0025$ as a regression base. Once again, the slope of the line defines the tensile "regression" modulus $E_{t,s}$:

$$E_{t,s} = \frac{d}{d\varepsilon}\sigma(\varepsilon)$$

A close-up view on the average experimental results for small strains is shown in Figure 4.6. Dashed lines represent the slope of the tensile modulus calculated with the chord slope method (the regression method yields very similar results).

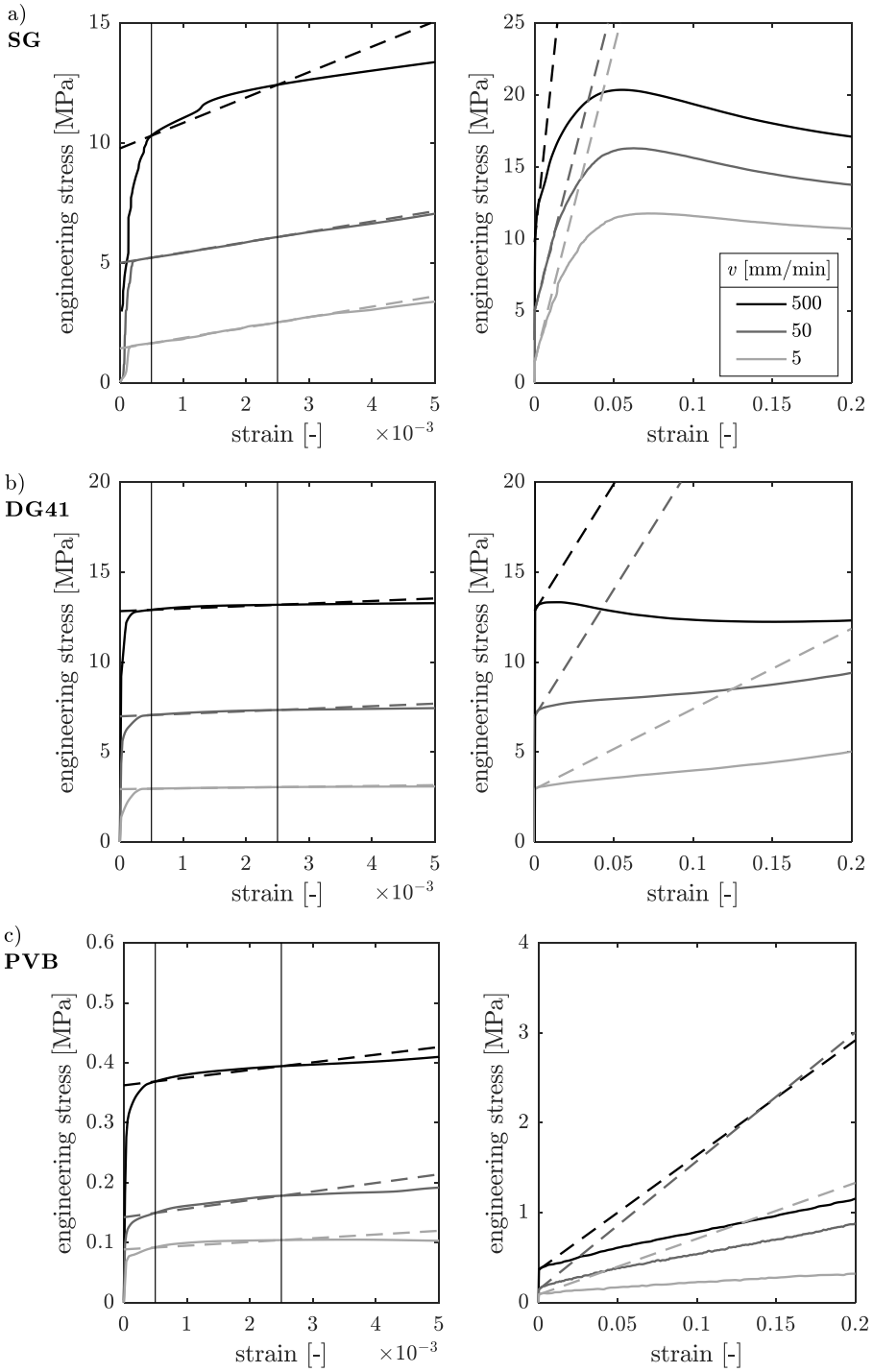

Figure 4.6 – mean engineering stress-strain curves and resulting chord-slope moduli according to ISO 527 [264] *for a) SG b) DG41 and c) PVB*

While curves obtained for SG, the hardest among the three materials, are arguably fit to be studied with both methods proposed by the standards, the same can hardly be said for the other materials (Figure 4.6.b and Figure 4.6.c). For very small strains ($\varepsilon < 0.5‰$) both PVB and DG41 initially exhibit a very stiff response, qualitatively comparable to SG and even higher in the case of DG41 for high strain rates (i.e. v_1 and v_2). Nonetheless, this very high initial stiffness is immediately followed by a quasi-constant load over strain segment, containing the whole strain interval $0.5‰ < \varepsilon < 2.5‰$, proposed by the standards to compute the tensile elastic modulus. The right part of Figure 4.6 shows that the tensile chord modulus[7] is an acceptable approximation of the initial tangent modulus for SG, but is neither very telling or consistent for both DG41 and PVB. Mean values of moduli calculated with both standard-proposed approaches are in Table 4.3; results show that the difference among the two methods is minor and, for this case study, the regression modulus is always slightly lower than the chord modulus. The convenience of using standard methods to define the tensile properties will be further discussed in Chapter 2.

Table 4.3 – mean chord- and (regression)-slope tensile modulus in MPa

claw displacement velocity v	**SG**	**DG41**	**PVB**
5 mm/min	431 (430)*	5.209 (5.209)	0.725 (0.704)*
50 mm/min	435 (435)	16.45 (16.38)	1.671 (1.660)
500 mm/min	1060 (996)	16.50 (16.45)	1.489 (1.412)

***** *statistically non-fully reliable according to* [66,264] *due to limited number of specimens*

Compared with traditional building materials, engineering interpretation of uniaxial tensile tests on polymers can be difficult for the large and non-homogeneous deformations involved [78,263]. For instance, the non-homogeneity has been observed experimentally by several researchers [7,78,263] and is believed to be either associated to the relation between test temperature and glass-transition temperatures [153] (cfr. Table 1.4 p.13) or to the presence of a softening region in the intrinsic stress-strain functions, causing the formation of localized necking [7,78,155] (cfr. §1.1.2).

Experimental observations of non-homogeneous deformations in SG specimens are shown in Figure 4.7 with the transverse contraction and necking in the narrow area of the dog-bone specimens. While the behaviour of DG41 is not shown, it has been observed to be somehow intermediate between SG and PVB, although much more similar to the latter (i.e. formation of a slightly visible necking region, but overall a quasi-uniform strain within the whole narrow area). These observational results agree with remarks of Meijer and Govaert [78] for similar tests on polycarbonate.

Results suggest that a median approach on the strain in the narrow section could be used for both PVB and DG41 to obtain a true stress diagram, given the material Poisson's ratios[8]. On the other hand, because of the presence of a localized neck,

[7] Tensile regression moduli curves are not shown, though they yield similar conclusions.

[8] The Poisson's ratio is defined within the infinitesimal strain theory [164], it has been questioned whether the concept and definition of may be extended to large deformations [346]. For an incompressible isotropic material, the relative error between the infinitesimal and finite strain domain can be estimated by $E = 1 - 2\varepsilon^{-1} + 2\varepsilon^{-1}(\varepsilon + 1)^{-0.5}$.

the same straightforward approach used for SG would yield a conservative lower bound value of the same diagram.

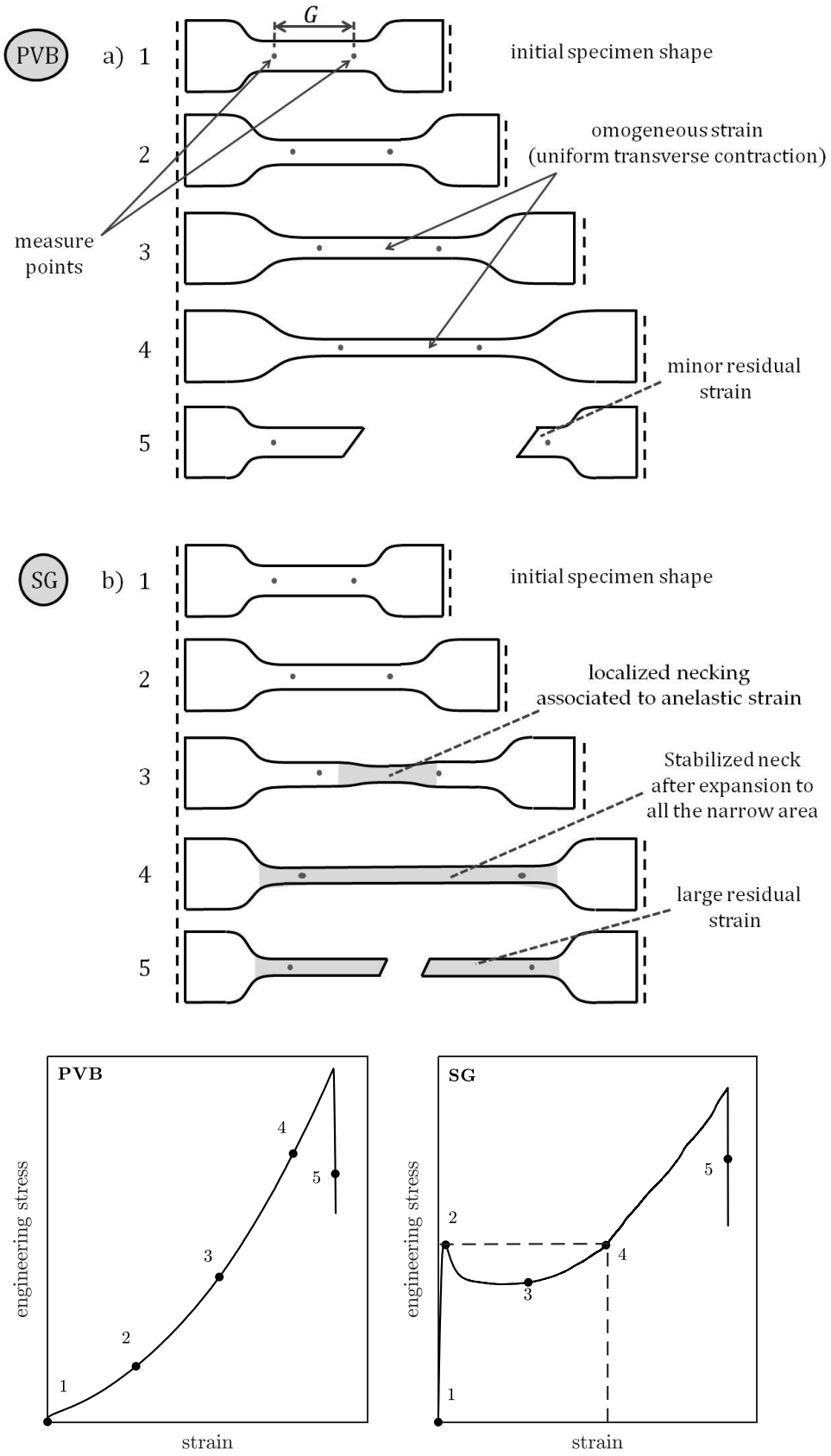

Figure 4.7 - experimental observations on non-homogeneous deformations

To further investigate the progression of non-homogeneous deformations within the narrow area of specimens, a time-lapse photographic system[9] was added to the setup to better understand results of SG specimens (Figure 4.8).

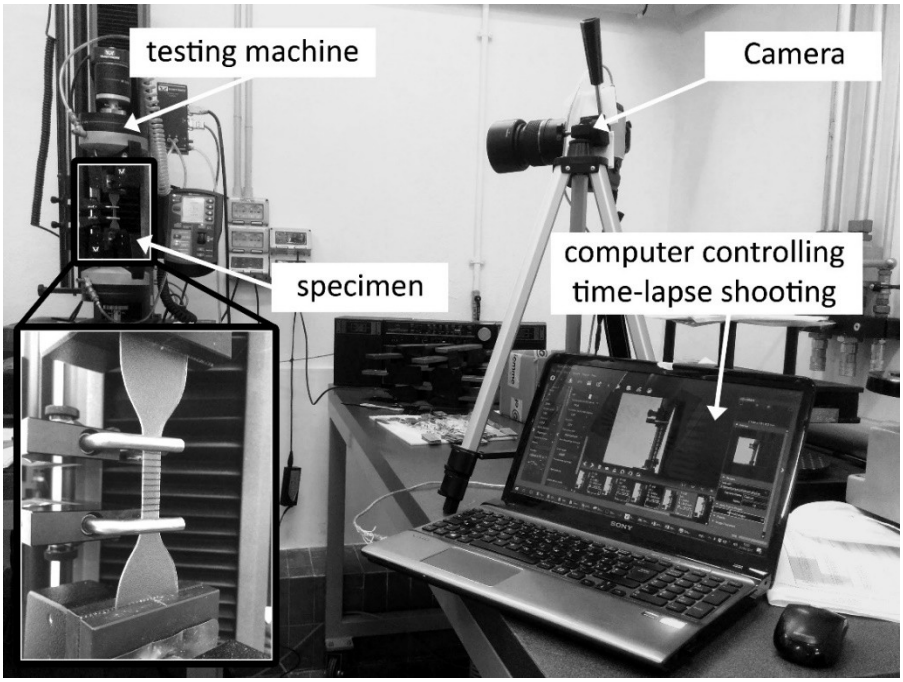

Figure 4.8 - setup for time-lapse photogrammetry

The time-lapse shooting frequency was limited by the data acquisition system to a maximum of one shot every two seconds (Table 4.4). To allow for a practical use of the time-lapse images, reference measurement lines have been manually drawn[10] on specimens as shown in Figure 4.9.

Table 4.4 – SG tensile tests photographic time-lapse shooting details

v	**shooting freq.**	**duration**	**shots**
5 mm/min	1 shot every 5s	29′28″	355
50 mm/min	1 shot every 2s	2′35″	79
500 mm/min	1 shot every 2s	19″	11

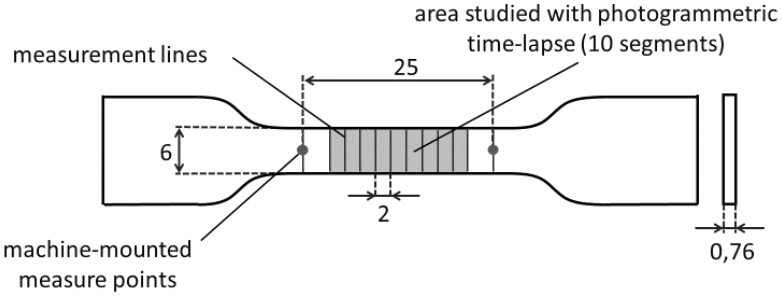

Figure 4.9 - measurement lines used for photogrammetric analysis

[9] Optical device used is a *Tamron* SP AF 90mm F/2.8 Di MACRO 1:1 on a Nikon D90 camera with CMOS 12,3-megapixel sensor. Software for time-lapse control is open-source *digiCamControl* © 2015 Duka Istvan.

[10] A thin permanent marker was used, the kind of those used to write on CDs.

Figure 4.10 shows the complete shooting sequence for the higher test speed (500 mm/s), including a final after-failure picture.

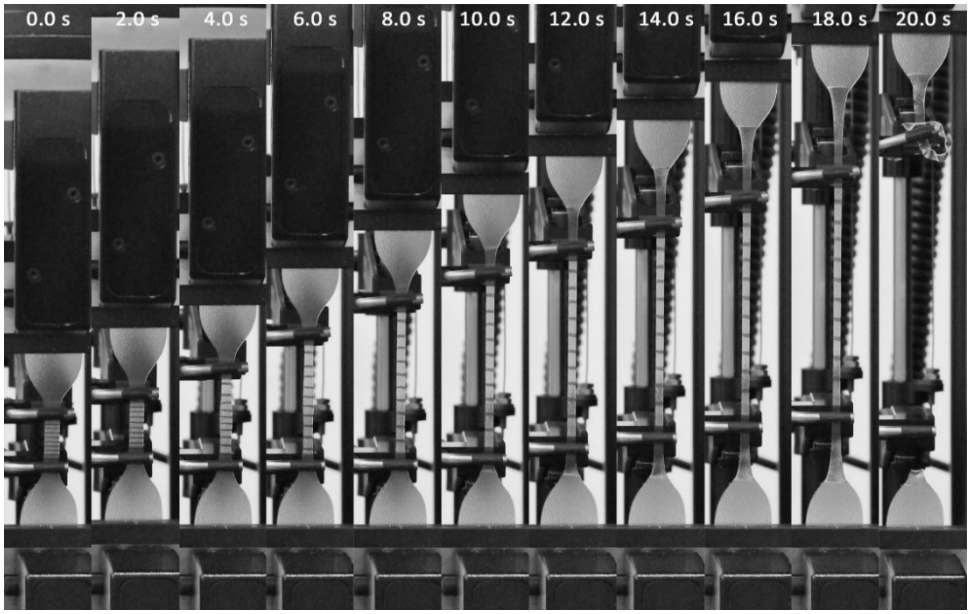

Figure 4.10 – SG tensile test at 500 mm/min time lapse, all shots[11]

4.2 LONG-TERM VISCOELASTIC PROPERTIES OF INTERLAYERS

Interlayers used for LG are known for having significant viscous properties, strongly dependent on their temperature (cfr. §1.1.2). Nevertheless, understanding and quantifying the long- and short-term effects of external actions on those materials, either being imposed loads or imposed displacements, is of paramount importance for a reliable and economically viable LG design.

To model and understand relaxation and creep for three among the most widely used interlayers (cfr. §1.1.2), an existing procedure[12] was adopted with several improvements (cfr. §2.2.1 and Biolzi et al., 2014 [65,146]). The aim is to provide a wide range of useful data for architectural LG design involving long-term effects.

4.2.1 AIM AND DESIGN OF TESTS

This experimental campaign was designed to investigate long-term effects of imposed loads and displacements on the mechanical properties of three different thermoplastics at different temperatures. Following, a selection of three interlayer materials to be tested was made, for their relevance and diffusion in LG industry:

- PVB (cfr. §1.1.2.1),
- SG (cfr. §1.1.2.2),
- DG41 (cfr. §1.1.2.3).

With the intent to provide useful data for LG design, the range of investigated temperatures was chosen to be as useful as possible to actual use in architectural applications, thus ranging between 0°C and 60°C [5,265–268].

The importance of testing interlayer materials in their laminated configuration, after both the internal cross-linking process and the chemical adhesion with glass

[11] The time-lapse video can be seen at https://www.youtube.com/watch?v=O17Q_z9DZ7U

[12] Prior to this campaign, a similar procedure was implemented with good results by the author and other colleagues in a previously published paper [65] and other works still to be published.

have been achieved, has been highlighted by numerous researchers [7,263] and in a previous campaign carried in 2013-2014 [65]. In the conclusions of his 2014 manuscript, Didier Delincé stated (cfr. [7] §VI.3):

> *"The determination of the contribution of the interlayer should be assessed by considering it as a component rather than as a material, and test configurations should be designed in accordance. In particular, separate characterization of adhesive properties and bulk material properties of the interlayer seems not really useful with purpose of assessing the end performances of products."*

Rather than focusing on the interlayer alone, the design of tests, starting from the setup itself and then defining the procedure, aims to investigate a scaled version of the actual LG beam. The mindset is to carry out simple and well-controlled tests which are a good representation of in-situ working conditions for interlayer materials. LG specimens were assembled using three $10mm$-thick plies, $100 \times 100mm$ wide, with two 1.52 mm-thick interlayers (Figure 2.20.b p.42).

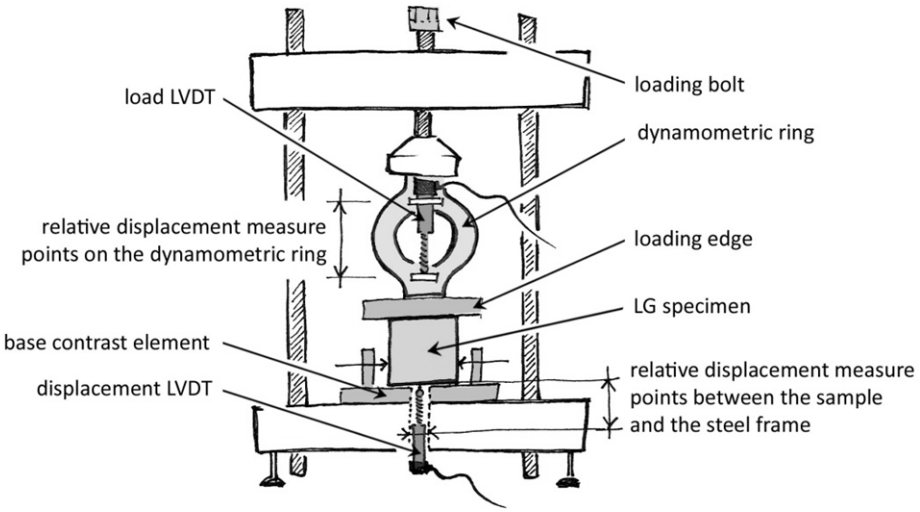

Figure 4.11 – testing frames

Drawing from the basic concept behind shear tests for bolted double-lap joints for steel elements and/or other composites [269], tests for LG specimens were designed to apply a vertical force on the central ply. For the geometric properties of the cross-section and the large difference in stiffness between polymers and glass, this procedure induces almost exclusively shear actions through the interlayers, with minor tensile and compressive stresses at both ends of the specimen [118,226]. The setup in Figure 4.11 is similar to the one used in 2014 (cfr. Biolzi et al. [65]), with the addition of the base contrast element, which will prove essential for the improved design of the procedure.

The three-layered LG specimens being loaded vertically through the central glass ply, actions normal to the interlayer surface were deemed to be minor, and a procedure to record or quantify these actions was not put in place. Besides, local shear forces transferred through the interlayer can be confused with the mean shear stress under some conditions[13]; this assumption was used to gather stress information from the load recordings.

[13] cfr. §2.2.1, the outcomes of the work by C. Vallabhan et al. [135] and also E. Viola [223]. This topic is further discussed in §4.2.4.4.

Figure 4.12 - testing devices with specimens inside the climatic chamber before the tests

Four identical testing devices[14] were designed to perform shear tests on LG specimens (Figure 4.12 and Figure 4.11 p.73). The number of devices was decided to allow for an analysis as statistically reliable as possible to be performed, while concurrently coping with the available financial resources and the volume of the climatic chamber (Figure 4.12). Thanks to the multiple presses available, tests were performed simultaneously on multiple specimens under identical loading conditions (cfr. Table 4.5 p.84). After some remarks emerging from preliminary tests (see below §4.2.2), one device was used to compensate for temperature effects (cfr. §4.2.2); therefore, the total number of available devices to test specimens at any given temperature was reduced to three.

Relaxation-creep test

A test procedure has been designed to investigate creep and relaxation properties of polymeric interlayers used in LG (cfr. §3.1.3.1). The separation among the nature of viscous rearrangements of the material structure – namely, viscoelastic and viscoplastic- is usually very complicated. In fact, both phenomena cooperate in parallel to the measured strain, in proportions which depend on factors such as temperature, strain rate, strain extent (small/finite), etc [57,270] (cfr. §1.1.2).

Drawing from the very high stiffness of the stainless steel dynamometric rings (about $0.6kN/\mu m \pm 5\%$ for all devices), the initial idea was to perform tests which in displacement-controlled conditions (differently from those performed in 2014 [65], which required periodic adjustments to reach a roughly consistent stress state).

The first part of tests consists in a quasi-relaxation[15] phase, in which a nearly constant strain $\gamma_I(t)$ and decreasing shear stress $\tau_I(t)$ are recorded. This *phase I* is shown in Figure 4.13.a. Being LG specimens well-secured to the steel frame

[14] Testing devices were built by *Officine Meccaniche Rinaldi Srl* in Milan and delivered to the laboratory in the Politecnico di Milano, were tests were performed.

[15] The term "quasi" is used in the sense that strain is not properly consistent, as a proper relaxation test would require, but varies slightly over time.

structure through the base contrast elements shown in Figure 4.11[16], highly reliable data $\gamma_{II}(t)$ could be gathered on the viscous recovery in a second phase, contrary to previous testing methods [65]. The applied load in *phase II* is null, as the dynamometric rings are physically disconnected from LG specimens, which are left free to return over time to their lower-energy state (Figure 4.13.a). Using the superposition principle [114,237,240,241], it is possible to look at the load removal as to the application of an inverse, "virtual" load (upwards), which is equal to the load recorded at the end of phase I. Conversely, the "virtual" strain $\gamma'_{II}(t) = -\big(\gamma_{II}(t) - \gamma_{II}(0)\big)$, essentially a re-scaled and flipped version of $\gamma_{II}(t)$, can be looked at as the creep compliance effect of a constant, "virtual" load step $\tau'_{II} = \tau_I(t_1)$, as shown in *phase II'* in Figure 4.13.b.

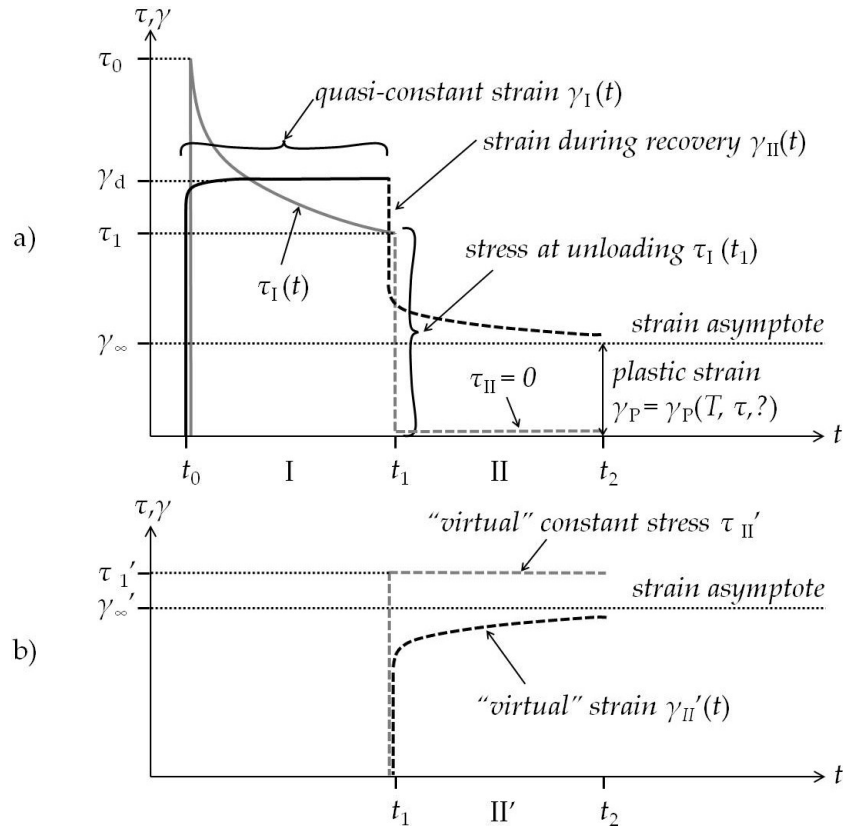

Figure 4.13 - design two-phases test output for stress and strain a) expected data to be recorded and b) conversion of a recovery phase II to a "virtual" creep phase II'

Such testing technique aims first and foremost to gather data on LVE parameters for creep and relaxation of three interlayers: PVB, SG and DG41 (cfr. §1.1.2). In addition, some permanent plastic strain is expected, especially at high temperatures (γ_P in Figure 4.13.a, whose scale may only be considered indicative), if a significant pattern can be detected, further analyses can be made in that sense using known models for PVP or HEVP (cfr. §3.2.1), always bearing in mind that such tests are not specifically designed to investigate viscoplastic parameters.

The launch of tests is achieved by adjusting the loading bolt (Figure 4.11) to a fixed design displacement δ_d, correlated to the design strain γ_d. More details are discussed with the presentation of preliminary results in the next paragraph.

[16] More details on the mounting and securing technique are shown in Figure 4.14 and Figure 4.15, and further discussed in the following.

4.2.2 PRELIMINARY TESTS AND HIGHLIGHTS

While all interlayer manufactures produced some data regarding the properties of their products (cfr. §1.1.2 and sub-paragraphs), no comparable data are available regarding viscoelastic properties of PVB, DG41 and SG. A preliminary test phase was therefore arranged between October and December 2016, prior to the start of the actual experimental campaign (cfr. Figure 4.24 p.85). Preliminary tests were meant to calibrate testing devices and define an order of magnitude for different actions and timings.

As expected, preliminary tests showed to be of paramount importance in laying the groundwork for the actual campaign, providing a general understanding of all key elements involved and highlighting several problems to troubleshoot. While some of the factors which came to light were arguably trivial and were only required to ease the various tasks throughout testing operations, other factors of major importance could not have been ignored. A list of main conclusions of the preliminary test phase is presented, with more in-depth comments and explanations in the following.

Trivial highlights, calibrations and improvements:

a) the need for a re-calibration of all transducers,
b) importance of manual finishing of LG specimen surfaces,
c) introduction of aluminium-lead angular shims to help distributing confining actions on lateral glass plies,
d) positioning of neoprene guiding dowels on top of specimens for easier installation of the loading edge in the correct position.

Important additions to the procedure:

e) insertion of an unloaded testing device in the climatic chamber to account for thermal effects on dynamometric rings,
f) preparatory cycles of elevated load ramps (up to $40 \div 50\ kN$) on the lateral plies for adjustment of the plastic dislocations in the interface lead foils,
g) calibration of the setup deformation of with a swift load step on the lateral plies only (up and down to $35\ kN$ in about $1\ min$),
h) correction of the linear drift of some load instruments readings.

Using results of the preliminary test phase, testing technique and limits were decided accordingly. Working under the hypothesis of linear viscoelastic materials (cfr. §3.1.3) [114,115,151,241], such procedure was designed to allow for the three thermoplastics to be tested at all design temperatures:

Testing procedure:	Relaxation-creep test
maximum imposed displacement:	1.0 mm [17]
maximum imposed load:	25.0 kN [17]
steps for max. load/displacement:	4
Conditioning time:	minimum 4 hrs.

[17] As properties of interlayer materials vary significantly with changing climatic conditions, for higher temperatures the limit was usually defined by the maximum displacement, while at lower temperatures the maximum load was reached for significantly lower values of the displacements ($0.2 \div 0.3$ mm). The number of steps to reach the target load/displacement was achieved accordingly (e.g. first load step imposed is imposed up to 5kN or 0.25 mm, whichever comes first, then a second load step up to 10kN or 0.50mm, whichever comes first, etc.). All load steps were performed by alternating the fastening of the three testing devices, for the whole loading process to be performed in about three to five minutes.

While a precise lower limit for the conditioning time was defined, to allow setup and specimens to reach thermal equilibrium, the duration of phases I and II was not defined a priori. Tests were carried out for the longest amount of time, while simultaneously managing several factors: opening hours of the laboratory, rate of load decay at a given temperature, upcoming tests, etc.

As tests were carried out from the highest temperatures to the lowest ones (Figure 4.24 p.85) the duration of *phase I* and *phase II* shown in Figure 4.13.a was adjusted on-the-fly for each test. The aim of this way of proceeding was to provide data that could be later joined in a general *mastercurve* (cfr. §3.1.3.5) with the lowest amount and extent of "gaps". This apparently confusing and arbitrary criterion will be clarified with the data analysis performed in §5.1.2.1.

4.2.2.1 CALIBRATIONS

A verification of the calibration for all LVDT transducers was performed, both the displacement ones[18] and those connected to the dynamometric rings[19] (Figure 4.11). Effects of temperature on the measurements of displacement transducers were also investigated in the full range of test temperatures by laying a still object at half the stroke of the instrument ($\sim 5\ mm$) and cyclically varying the temperature in the chamber. Minor variations in the instrument readings were observed in a range of $\pm 0.01\ mm$, but most importantly for tests, at each temperature the conditioning time interval for consistent readings ($\pm 0.001\ mm$) was observed to be lower than $60\ s$, allowing for reliable readings throughout tests (cfr. §4.2.4.3 and §5.1.2.6).

4.2.2.2 PREPARATIONS OF SPECIMENS

Due to the way LG glass is manufactured [271,272], the edge of the interlayer was not always spot-on the edge of the glass plies (Figure 4.14). Protrusions of interlayer outside the perimeter of the specimens was generally in the order of $1.0 \div 1.5\ mm$, although not always present. Cutting out of the excess interlayer was only needed in some areas, to allow for convenient contact among all surfaces: between the glass plies and the base contrast elements, between the upper loading edge and the central glass ply and between the specimens and the lateral fastening angular shims. Excess of interlayer outside those areas was usually deemed to be irrelevant to the outcome of tests and therefore not always completely removed.

This cleaning procedure was mostly needed for all the SG-laminated specimens, as they have been individually laminated by superposition of three 100x100mm glass plies and two interlayer foils of the same size. On the other hand, PVB- and DG41-laminated specimens were produced by partitioning larger LG elements[20]. Therefore, those specimens already presented adequate finishing and didn't require extensive manual finishing.

[18] Calibration curves for displacement transducers were given by the HBM certification body, supplier of Politecnico di Milano, for a 10mm range and 0.001mm accuracy, within an operating temperature range of 10÷60°C.

[19] Dynamometric rings calibration was done by means of a 50kN Wheatstone bridge load cell, in turn calibrated by the same certification body of the LVDT transducers. The resulting calibration curve for the dynamometric ring itself showed good linearity, with maximum deviation of ±0.5% in a 0÷25kN range, and an accuracy of 0.05kN.

[20] Partitioning was achieved by slicing of large LG elements through a diamond band saw, to produce smaller pieces the size of the design specimens.

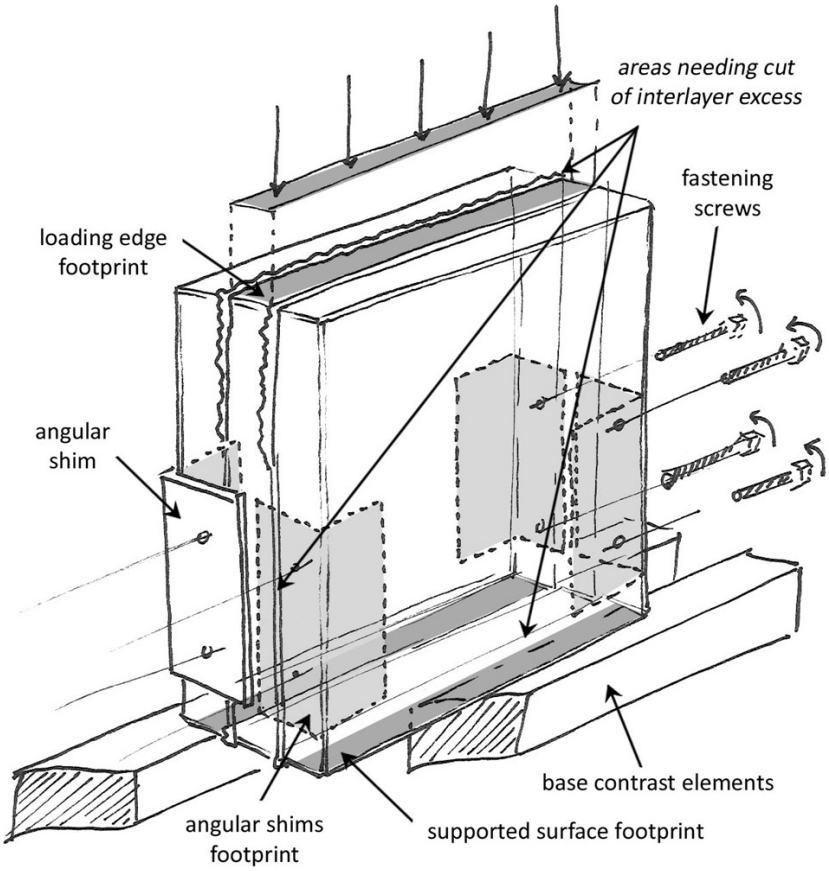

Figure 4.14 – scheme of the elements in contact with LG specimens

4.2.2.3 STRESS DISTRIBUTION IMPROVEMENTS

A thin lead foil was introduced at the interface among lateral glass plies and aluminium angular shims (Figure 4.14 and Figure 4.15). This addition was thought out after the local failure of glass when tightening the fastening screws, whose force could apparently not be sufficiently distributed by the aluminium layer alone. The mounting of shims consisted of four phases described in Figure 4.15: 1) the aluminium foil is connected to the aluminium shim by means of a cyanoacrylate glue, 2) metallic elements are glued to the specimen using a hot-melt adhesive (HMA), 3) specimens are installed on the devices and 4) fastened by means of lateral screws.

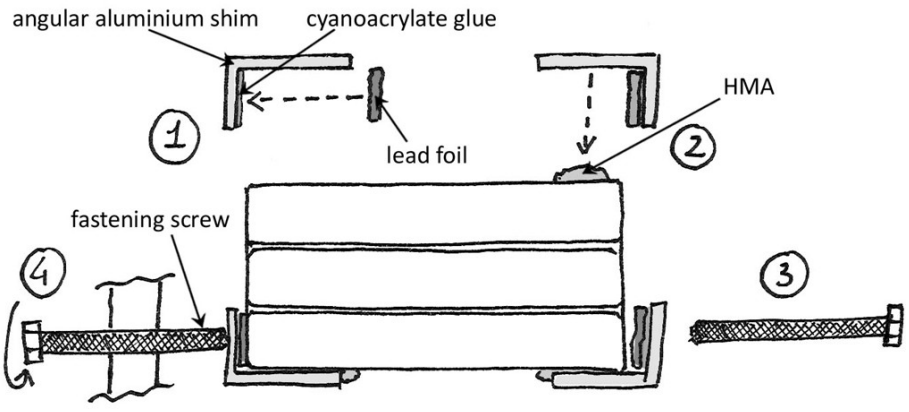

Figure 4.15 – four phases (clockwise) for the installation of angular shims

4.2.2.4 IMPROVEMENTS OF CHAMBER OPERATIONS

Four neoprene guiding dowels were installed on top of specimens to speed up and simplify the placement of loading edges in the correct position inside the climatic chamber. Those elements were glued by means of the same cyanoacrylate adhesive used to assemble angular shims. The guiding dowels ought to cover both the lateral glass plies and the interlayer (Figure 4.16), for the loading edge to properly apply its effect on the central glass ply only.

The introduction of the guiding dowels allowed for the loading edge to be put in the optimal position in the setup phase in a loose configuration (not applying any load except for self-weight), before conditioning and loading, eliminating the need for further handling ever since. This choice was a turning point in managing operations inside the climatic chamber; due to the limited time between opening and closing, minor improvements to minimize handling of devices proved to be ultimately very significant. Considering the high temperatures some tests were run at (notably, the ones at $T > 50℃$), all the steel elements had become very hot after the initial conditioning period; therefore, eliminating the need to touch or adjust any of them proved to be very convenient.

Details on the installation of dowels are shown in Figure 4.16: on the left side, the position of dowels highlight their role for guiding the $8\,mm$ wide loading edge in the right position, corresponding to the middle of the central glass ply. On the right side, the loading edge is shown in the testing position, but the shot is taken just at the end of the setup phase, so that the central glass ply is not currently loaded.

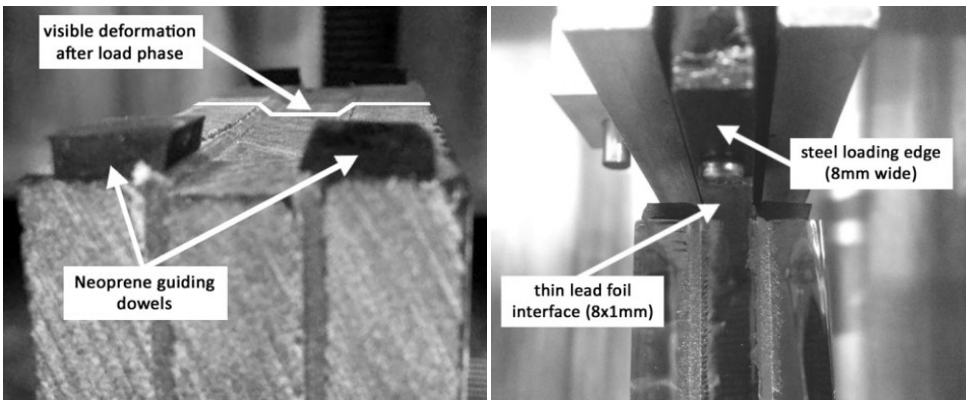

Figure 4.16 - guiding dowels a) on a tested specimen and b) before a test

4.2.2.5 THERMAL EFFECTS ON DYNAMOMETRIC RINGS

Effects of swift temperature variations on testing devices was observed to be significant only during chamber openings. More specifically, thermal effects on the load measuring devices (dynamometric ring, aluminium pads, extension shaft and LVDT transducer) were observed to be remarkable when compared to the loads involved in the actual testing process ($0 \div 25\,kN$). This effect is ascribable to the high sensitivity of devices to small changes in size. As the temperature of the parts composing the devices varies, their size adjusts accordingly because of the thermal deformations, with speeds and extents depending on their thermal properties. As the load acquisition system converts relative displacement readings into loads (cfr. §4.2.2.1), variations of the size of elements are read as artificial or "virtual" loads Figure 4.17 shows the thermal effects measured by the dynamometric rings upon opening of the chamber at various temperatures.

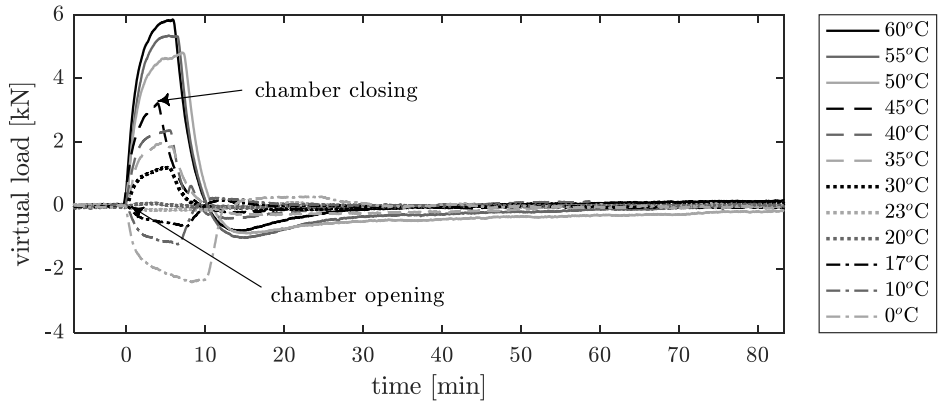

Figure 4.17 - thermal effects recorded by load-monitoring devices

Results in Figure 4.17 are referred to an unloaded load measuring device. Being the ambient temperature generally close to 20°C, one can observe that higher test temperatures have a greater influence in creating a fictitious load measurement. A thermodynamic model was calibrated to understand why the recordings have such an odd shape, details are in Appendix A.

For some tests, multiple load measuring devices were not used to perform actual tests on laminated glass specimens, but were nonetheless inserted in the climatic chamber and subject to the same temperature variations. Compared results showed good consistency among all non-loaded devices, implying that results from one device can be successfully used to correct another, which was the assumption adopted in the following data analysis.

4.2.2.6 ANELASTIC LEAD INTERFACE SETTLING

Although the design maximum load was well under the limit deemed to be critical for the formation of fractures due to compressive actions, preliminary tests highlighted that glass plies comprising LG specimens could occasionally crack during tests, typically near the edges.

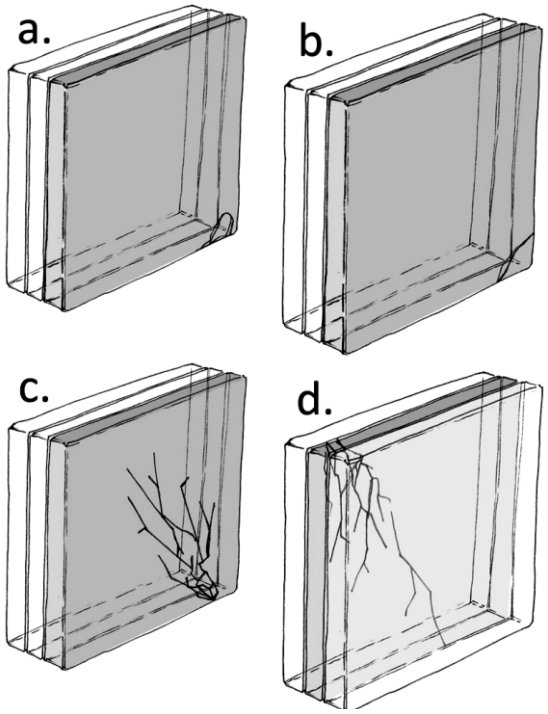

Figure 4.18 – typical position and evolution of cracks in laminated glass specimens

Typical crack patterns and starting points of fractures are presented in Figure 4.18. Most cracks were very minor: either affecting just the outer surface of the glass to a depth of a few millimetres (Figure 4.18.a), either affecting a limited volume of the whole ply (Figure 4.18.b). In both of those cases, the interlayer interface was not severely affected by the failure of the glass plies, thus results regarding the viscoelastic properties of the interlayer could have been accepted anyway. On the other hand, a few cracks were much larger, affecting a vast portion of the plies and the interface, possibly influencing the tests (Figure 4.18.c and Figure 4.18.d).

The starting point of cracks was always observed close to the edges, suggesting that this phenomenon may be connected to defects in the alignment of plies or minor tolerances in the finishing of surfaces: stresses which were meant to be transferred through a large contact surface were in fact redirected and concentrated into significantly smaller regions in proximity of the edges.

A noteworthy remark is that the finishing of the edges did not seem to be correlated to the formations of cracks. The uprising of cracks was observed only for some specimens and for loads higher than $18 \div 20\,kN$, translating in nominal compressive stresses around $22 \div 25\,MPa$ for the central ply and $10 \div 12\,MPa$ for the lateral ones. This was an odd result, as those stresses are even lower than the tensile limit of glass [273–276].

To prevent the glass from cracking, a thin lead foil was inserted between the bottom of the lateral plies and the base contrast elements (Figure 4.20). The downside of this choice is that the recorded displacement at the base of the central glass ply now must account for some plastic deformations of the lead interface. To allow for correct readings, the plastic deformations in the lead foils were addressed before the beginning of tests (i.e. before the conditioning phase). To this aim, several very high load ramps of 50kN were imposed with the testing devices on the lateral plies alone, with the temporary introduction of lead foils also on top of them.

Figure 4.19 shows that increments in lead plastic deformations gradually reduce with an increasing number of cycles. When the relative displacement between the beginning and the end of a high-load cycle was smaller than 5μm, a verification cycle was performed up to 25kN, the maximum design force. Lead plastic strains were deemed to be settled with a residual deformation lower than 1μm.

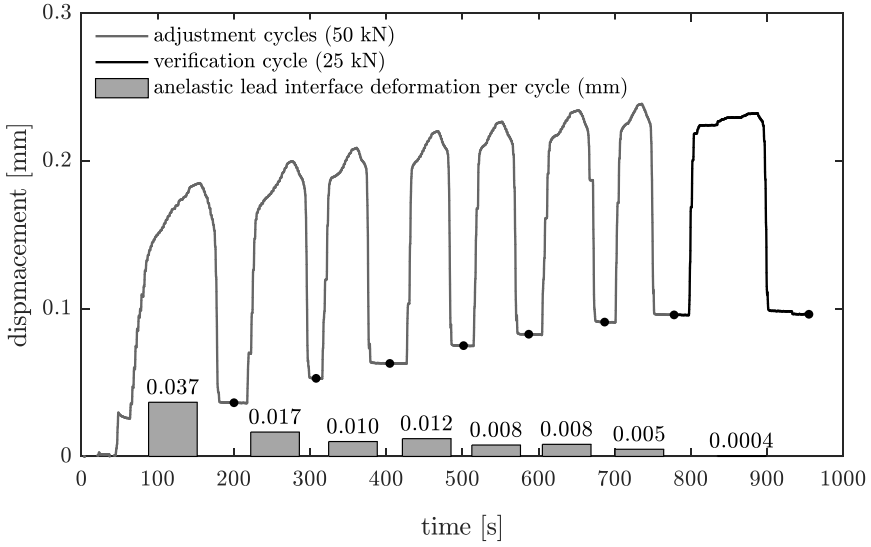

Figure 4.19 - displacement monitoring for the adjustment cycles

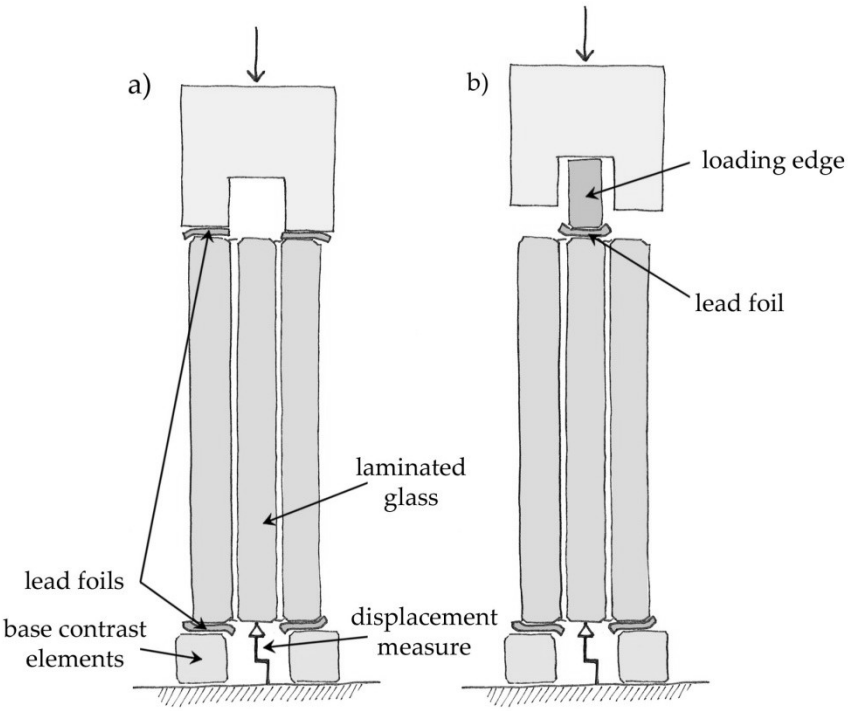

Figure 4.20 – a) setup for adjustment of deformations in lead foils and b) test setup

4.2.2.7 DEFORMATION OF TESTING DEVICES

An unexpected phenomenon involving properties of the setup was observed in preliminary tests: measured displacements slightly exceeded the expected values[21] (i.e. the deformations which could be ascribed to interlayers shear strain).

Several hypotheses were made regarding the origin of this unexpected phenomenon: issues in fastening of the displacement transducers, imperfect contact between glass plies and the base contrast elements, shielding and grounding of monitoring instruments and properties of the base contrast elements.

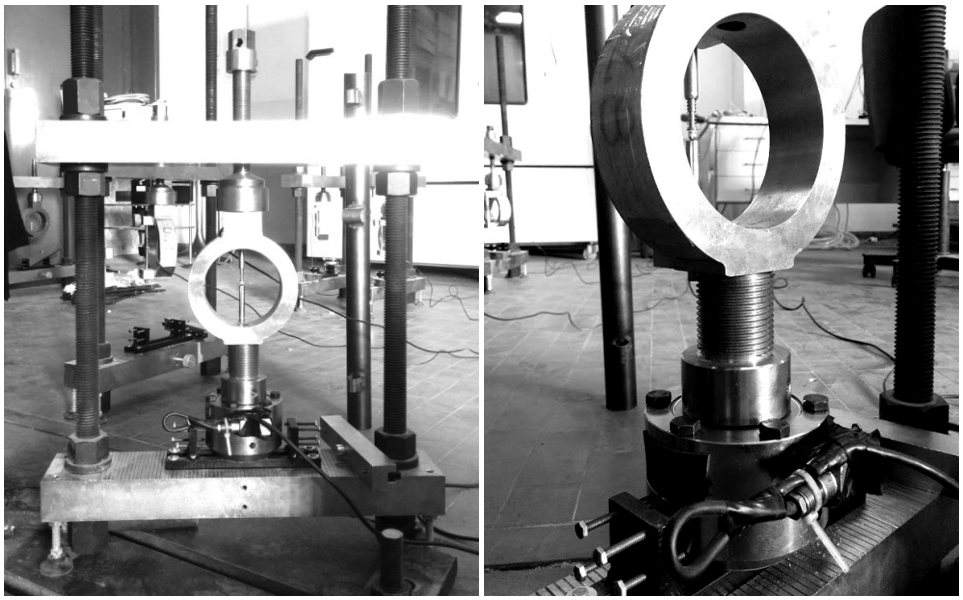

Figure 4.21 – setup for calibration of rings and base contrast elements

[21] The first remarks were made comparing preliminary PVB tests to available data [38,65].

No hypothesis could be excluded *a priori*; nonetheless, by double checking all those connected to the recording devices themselves, the key factor had to be ascribed to properties of the steel contrast elements. As those parts were hand-crafted by the *Structures Laboratory* in Florence, the possibility of an imperfect contact with frames was taken in consideration. Rather than presenting a very high compressive stiffness, as one would expect from simply compressed steel, tests in Figure 4.22 highlighted that small loads induced a significant non-linear elastic deformation.

Tests were made assembling the setup in Figure 4.21, then swiftly fastening and releasing the tightening bolt connected to the dynamometric ring. The procedure was repeated up to six times for all devices[22]. While displacements were recorded with the same "displacement LVDT" transducers shown in Figure 4.11 p.73 (now pointed to the bottom of the load cell), the load was simultaneously recorded with the load cell and the dynamometric ring[23].

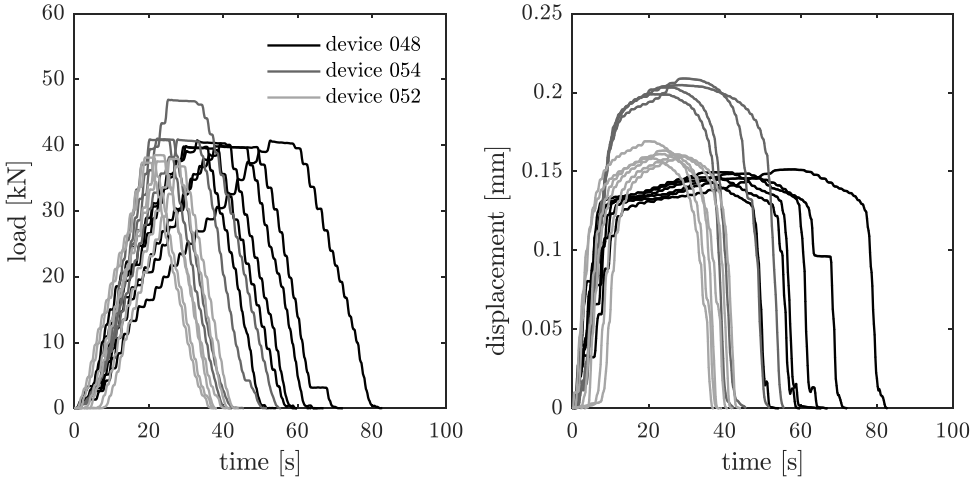

Figure 4.22 – a) load and b) displacement curves for base elements calibration

Curves shown in Figure 4.23 are the result of this calibration process; details on the construction of these mathematical models are discussed in Appendix B.

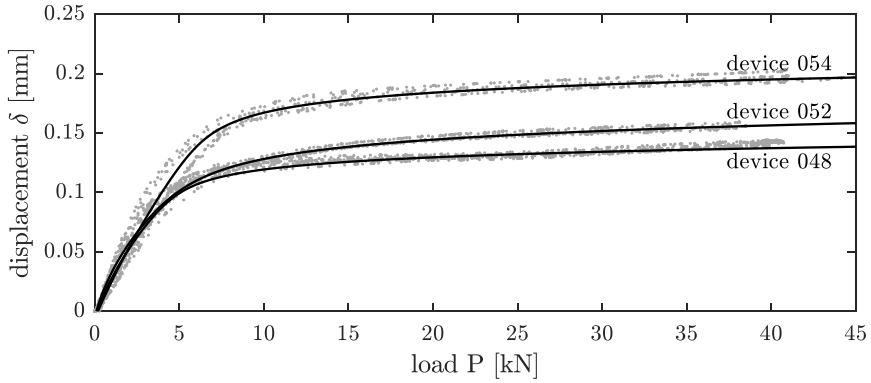

Figure 4.23 - non-linear deformations of the base contrast elements

[22] Each time a test was performed, the load cell was removed and reinstalled, to ensure that results were not influenced by some peculiar arrangement of the elements.

[23] To grant full consistency with the following tests, the dynamometric ring readings were used to calibrate model. Redundant load recordings must be looked at as an internal feedback.

4.2.2.8 LINEAR DRIFT OF LOAD READINGS

On occasion, load-recording instruments exhibited a linear drift during tests, easily detectible in the last part of the data[24] (Figure 4.28).

Causes of the drift were thoroughly investigated; even so, the fundamental origin of this phenomenon could not be identified. As this effect was observed independently from any likely connectable variable (i.e. temperature, testing device, elapsed time, reset of the data acquisition device), it was concluded that it may most likely have been generated within the data acquisition system itself.

Studying the last part of the curves, measured drifts were rectified by subtracting a linear interpolation of the data. More details on the exact procedure are presented in the following with a case study.

4.2.3 PERFORMED TESTS

After the preliminary phase, the actual campaign to investigate long-term properties of interlayers at different temperatures was started. Tests were arranged in the materials laboratory of *Politecnico di Milano*, using a climatic chamber which was available for a two-months period. Specimens were classified using a convenient code: SG-laminated specimens were listed as SXX[25], DG41-laminates as DXX[25] and PVB-laminates as PXX[25] (cfr. §1.1.2.1, §1.1.2.2 and §1.1.2.3).

Table 4.5 - list of performed tests and tested specimens

mat.	Temp. [°C]	dates		phases duration [h] cond.	I†	II†	tested specimens		
SG	20	20/1	23/1	2	67	5	S27	S28	S29
	30	19/1	20/1	12	6	4	S25	-	S24
	35	24/1	26/1	4	21	17	S19	S17	S18
	40	06/2	07/2	4	18	9	-	S26	S23
	45	17/1	19/1	6	19	24	S15	-	S13
	50	26/1	30/1	5	17	67	S22	S20	S21
	55	11/1	13/1	15	8	16	S09	-	S12
	60	13/1	17/1	6	66	23	S14	-	S16
DG41	10	16/2	17/2	15	4	4	D13	D15	D14
	14	20/2	22/2	15	15	5	D19	D22	D20
	17	07/3	8/3	4	17	4	D23	D26	D25
	20	17/2	20/2	4	70	24	D16	D18	D17
	23	14/2	16/2	4	23	8	D11	D10	D12
	30	7/2	9/2	15	10	13	D06	D08	D07
	40	2/2	3/2	4	17	9	D01	-	D02
	50	3/2	6/2	4	17	46	D03	D04	D05
PVB	0	10/2	14/2	65	23	23	P03	P05	P04
	10	2/3	3/3	4	17	4	P14	-	P15
	20	6/3	7/3	4	8	14	P16	-	P17
	30	28/2	2/3	4	24	23	P11	P13	P12
	40	24/2	28/2	5	70	24	P08	P10	P09
	50	22/2	24/2	5	25	21	P06	P02	P07

† *cfr. Figure 4.13 p.75*

[24] In the last part, the applied load is null, as the dynamometric ring is physically disconnected from any surrounding object and the temperature is constant.

[25] *XX* is a progressive two-digits number.

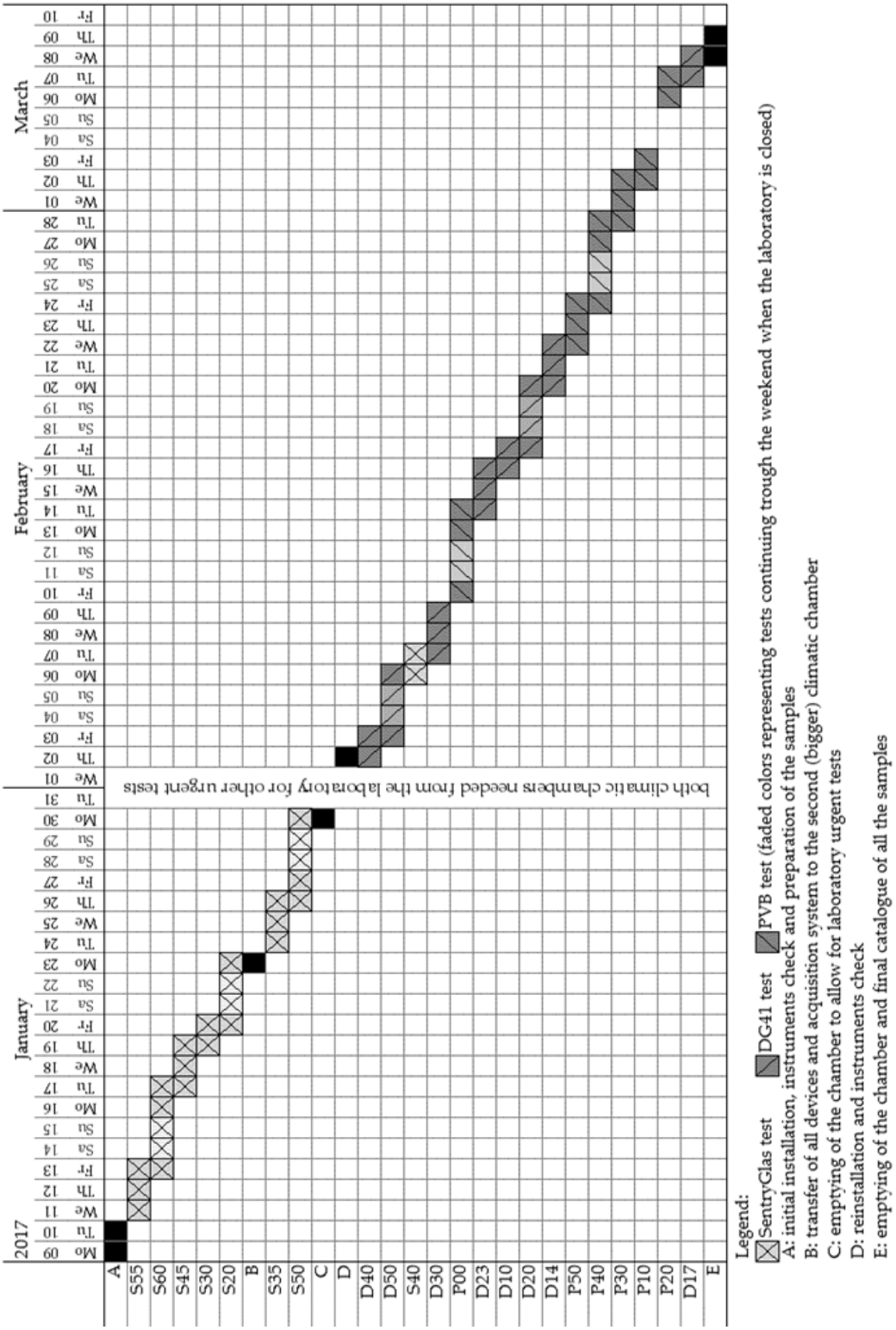

Figure 4.24 - Gantt diagram of performed tests

The list of tests and specimens is presented in Table 4.5, while Figure 4.24 shows a Gantt diagram of the campaign progression[26].

[26] The list is "missing" some specimens (e.g. tests for SG start with the S09 and S12), in part due to those used in preliminary tests and in part to the rejection of specimens for assembly flaws (e.g. glass plies not perfectly aligned).

4.2.4 EXPERIMENTAL RESULTS AND FIRST DATA ANALYSIS

A case-study is presented to detail all the steps in the data analysis, according to previously described goals and highlights (cfr. §4.2.1 and §4.2.2). Tests on two SG-laminated specimens at 55°C were chosen to describe all phases (cfr. Table 4.5).

Raw numerical results collected by the data recorder[27], are presented in Figure 4.25 for measured loads from the dynamometric rings and in Figure 4.26 for the measured vertical displacement of the central glass ply. As testing device 041 was used solely for thermal correction, displacement was not recorded.

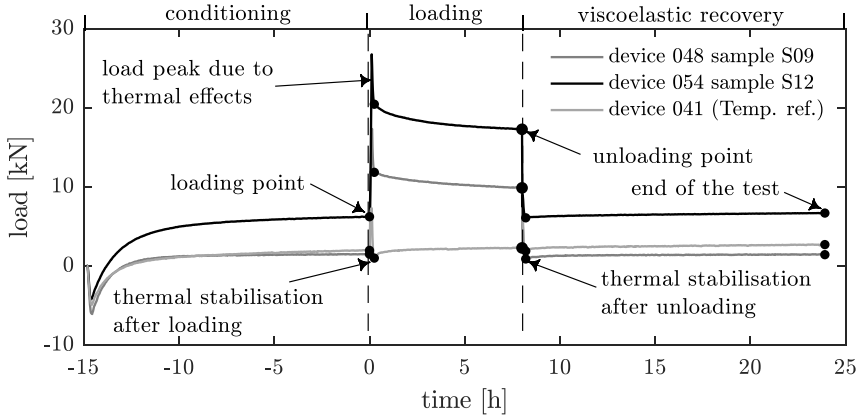

Figure 4.25 – recorded loads trough dynamometric rings

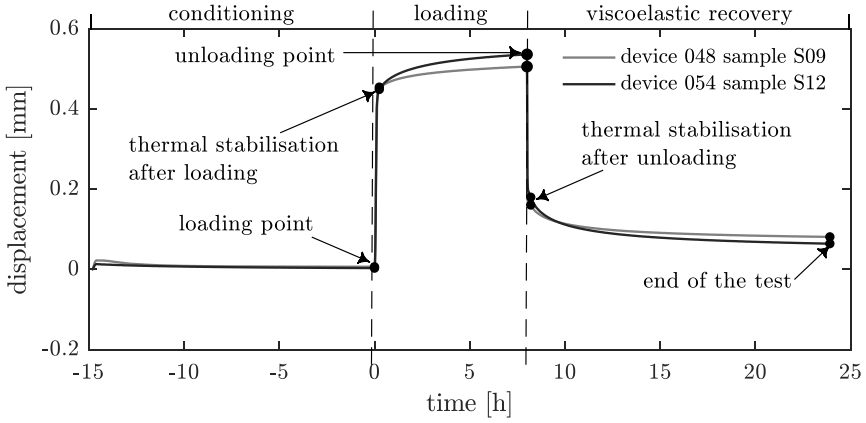

Figure 4.26 - recorded displacements at the bottom of the central ply

On top of both Figure 4.25 and Figure 4.26, conditioning, loading and recovery phases divide the time axis (cfr. §4.2.1). The duration of the phases matches what is shown in Table 4.5. Significant points have been highlighted:

- loading point — end of the conditioning phase, prior to the chamber opening and specimens loading by fastening of the tightening bolts,
- thermal stabilization after loading — after closing the climatic chamber, when the dynamometric rings are in thermal equilibrium (Figure 4.27),
- unloading point — end of the loading phase, before the opening of the chamber for loosening testing devices and unloading the specimens,

[27] HBM QuantumX CX22B-W (www.hbm.com)

- thermal stabilization after unloading — after closing the climatic chamber, when thermal effects on dynamometric rings are settled for the most part (cfr. Figure 4.27),
- end of the test — end of data recording, before the final opening of the chamber.

Thermal effects were introduced in §4.2.2.5 and are discussed in Appendix A. To define the moment when such effects start to be negligible, points were identified on the measured load curves: the thermal stabilization was assumed to be reached in the loading and recovery phases when $t_{stab} = 2t_B - t_A$ (Figure 4.27).

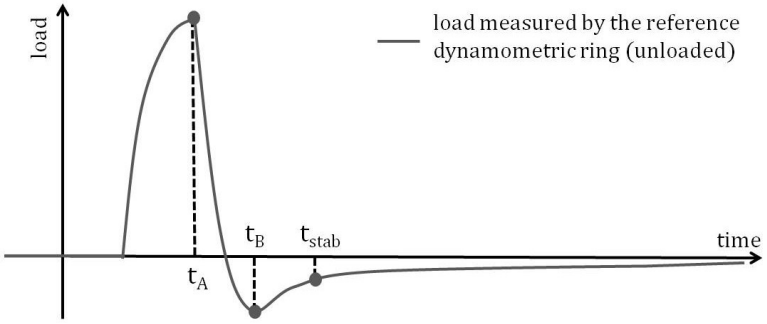

Figure 4.27 - load measured by the reference dynamometric ring upon chamber opening

Figure 4.25 shows that even starting from the so defined stabilization point, some thermal effects must still be considered (line for device 041 after thermal stabilization at loading/unloading); this has been taken care of in the following by subtracting the load recorded by the reference dynamometric ring from the readings of the instruments used for testing the LG specimens.

4.2.4.1 LOAD DRIFT CORRECTION AND INITIAL DISPLACEMENT

The problem was introduced in §4.2.2.8. Figure 4.28 shows what the load drift looks like, and how it affects the loaded dynamometric rings and the reference one. Dotted lines are superimposed to the recorded measurements to highlight the linear trend of the drift, calculated by linear regression of the load curves in the viscoelastic recovery phase[28]. Figure 4.29 shows the result of the correction, where the linear drift effects are subtracted from the original load readings.

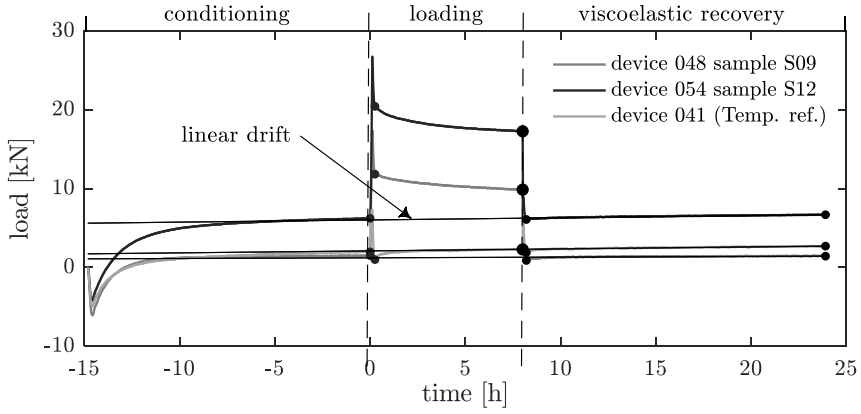

Figure 4.28 – linear drift superimposed to load readings

[28] The regression base for the linear drift curve is defined by all the points comprised in the interval within the thermal stabilisation point after unloading and the end of the test point shown in Figure 4.25. The choice was made for all dynamometric rings to be effectively disconnected by all surrounding effects in that time interval and in thermal equilibrium.

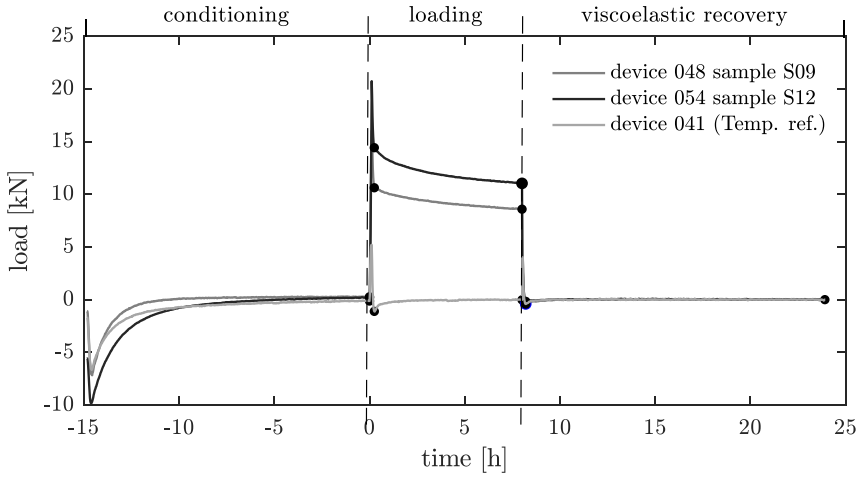

Figure 4.29 - load readings corrected for linear drift

The comparison Figure 4.28 and Figure 4.29 shows that the slope of viscous load decay in the loading phase is more consistent after the drift correction.

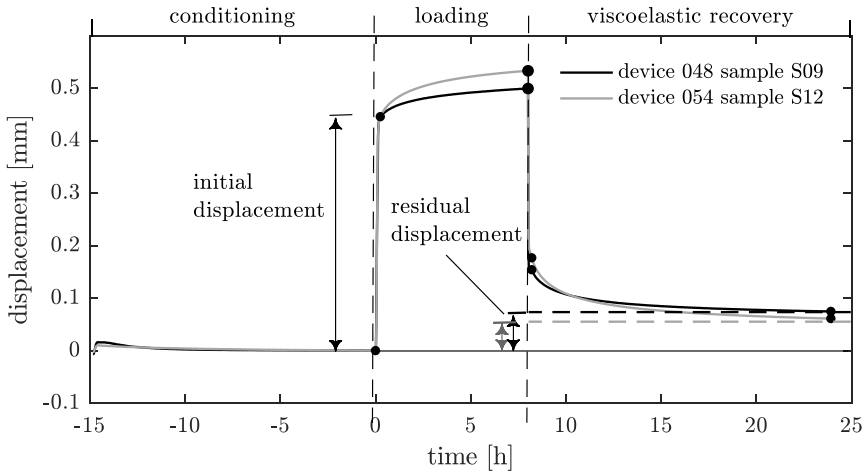

Figure 4.30 - displacement readings corrected for initial measurements

Figure 4.30 shows the normalized recordings for the displacement curves, obtained by subtracting the displacement at the loading point (cfr. Figure 4.26).

The imposed displacement during the loading phase is not perfectly constant, as it should be instead by theoretical design of a stress relaxation test (cfr. §4.3.2). Instead, the imposed displacement slowly rises after the initial imposed value, due to the elastic deformations of the dynamometric ring. Nonetheless, it is important to note that this example is willingly referred to SG (cfr. §1.1.2.2) to show the worst case scenario: SG being the stiffest among tested interlayers, results for other materials are more concordant to the hypotheses.

4.2.4.2 ELASTIC SETUP DEFORMATION CORRECTION

As in §4.2.2.7, the displacement at the base of the specimens had to be corrected to account for the non-linear elastic deformation of the base contrast elements. The functions correlating load and displacement for the different devices have been used to rectify the curves, by subtracting the deformation of the base contrast elements. Figure 4.31 shows the result of the correction. Note that, because the correction is a function of the load, the curves in the viscoelastic recovery phase are unaffected by the procedure.

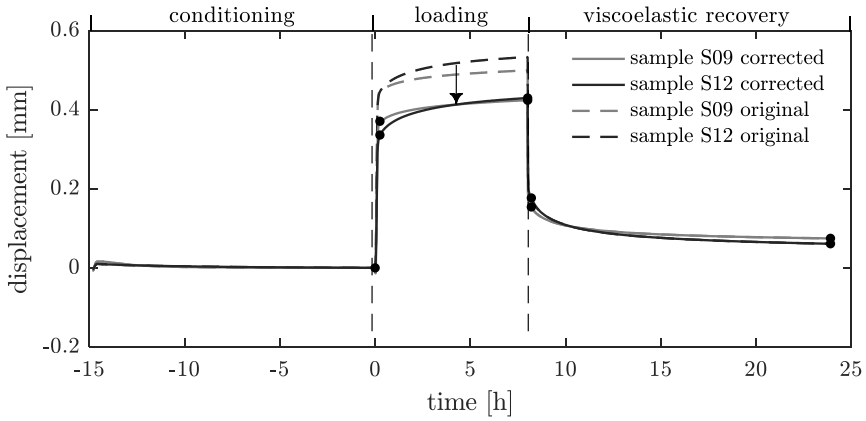

Figure 4.31 - displacement readings corrected for base deformation

4.2.4.3 THERMAL EFFECTS

Thermal effects on the dynamometric rings and associated transducers have been illustrated in §4.2.2.5 and further analysed in detail in Appendix A.

Figure 4.32 compares dotted lines for original load readings (accounting for previous corrections) to plain lines for measures adjusted for thermal effects. The correction is achieved by subtracting the virtual load recorded by the reference device (device 041 in Figure 4.29). Points representing the thermal stabilization thresholds are also shown in Figure 4.32 (cfr. §4.2.4).

In all tests, the importance of the thermal correction seems to be greater in the loading phase, rather than in the viscoelastic recovery phase. This is likely due to the duration of the chamber openings: at the beginning of the loading phase, the climatic chamber had to be left open for about three to five minutes, whether at the beginning of the viscoelastic recovery phase chamber operations could usually be concluded in less than a couple of minutes. This allowed for a minor variation in the temperature of the dynamometric rings during the openings and consequently a lower amount of time for the return to the design operating temperature.

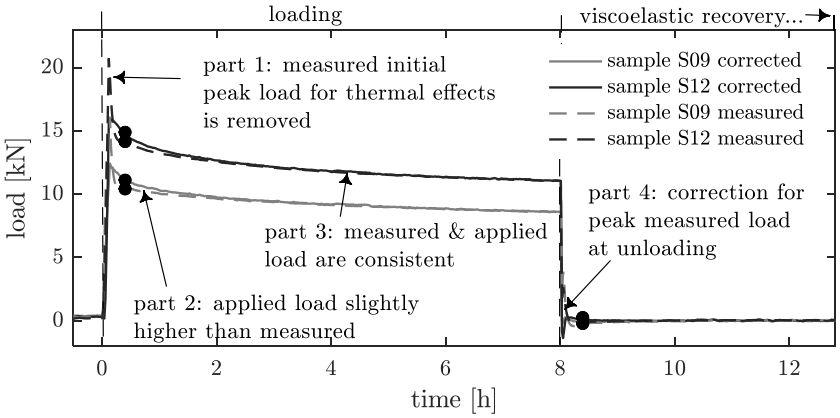

Figure 4.32 – correction for thermal effects on dynamometric rings

4.2.4.4 RELAXATION AND CREEP

Knowing the geometry of the specimens[29] (total interlayer surface $2A$ and thickness s), the mean shear stress $\bar{\sigma}_{12} = \overline{\tau}$ and strain γ_{12} can be calculated from the corrected

[29] Not all specimens had identical geometry, some were slightly wider or shorter than design.

load P and displacement d (Figure 4.31 and Figure 4.32), assuming a linear variation of the displacements[30] [223].

$$\overline{\tau}(t) = \bar{\sigma}_{12}(t) = \frac{P(t)}{2A}$$

$$\gamma(t) = \gamma_{12}(t) = 2 \cdot \varepsilon_{12}(t) = \tan^{-1}\left(\frac{d(t)}{s}\right)$$

Figure 4.33.a shows stress results for the case study: for the viscoelastic recovery phase, the virtual – constant – load $\overline{\tau}_u = \overline{\tau}(t_u)$ has been set equal to the last recorded load in the relaxation phase just before unloading: the dash-dot line, representing the virtual load, intersects the end of the corresponding curve in the loading phase. The time axis for the creep curve has been shifted, the new origin is the unloading point at time t_u (cfr. Figure 4.25 p.86).

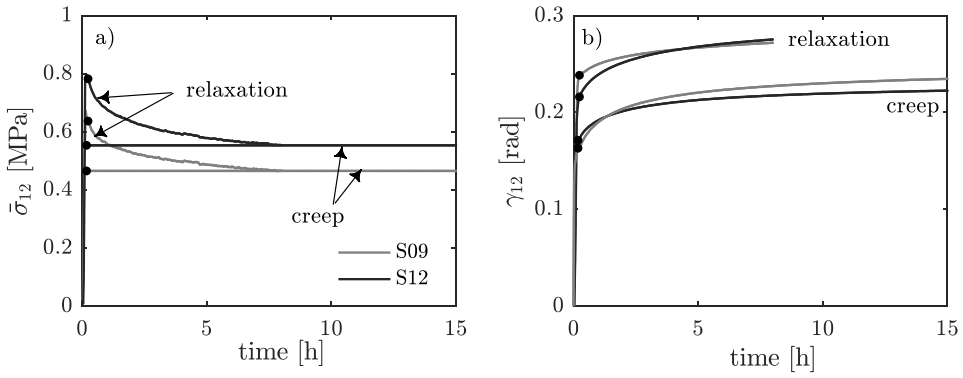

Figure 4.33 – a) stress and b) strain in loading and viscoelastic recovery phases

Shear strain curves shown in Figure 4.33.b for the unloading phase have been shifted, normalized and turned upside down according to the procedure (cfr. §4.2.1). The new time origin is once again the unloading point at time t_u (black dot in Figure 4.31 p.89).

Shear strain and stress data over time allow to compute the values two experimental moduli $G^*(t)$ and $J(t)$ [114,241]:

$$G^*(t) = \frac{\bar{\tau}(t)}{\gamma(t)} \cong G(t) \qquad \textit{Stress Relaxation}$$

$$\frac{1}{J(t)} = \frac{\bar{\tau}_u}{\gamma(t)} \qquad \textit{Creep Compliance}$$

The modulus G^* is an approximation of the relaxation modulus G: the fundamental discrepancy with the theory is due to the fact that the strain $\gamma(t)$ used to compute $G^*(t)$ is not constant throughout the loading phase, but varies slightly over time (Figure 4.33.b).

The modulus G^* is neither a pure relaxation modulus G, neither the creep compliance. Rather, it is a combination of both in varying proportions hard to decouple. Nonetheless, the steadier the strain in the loading phase, the more the

[30] While values of shear strain are way larger than those found for more conventional building materials, a definition of shear strain like that shown in the equations can be successfully used to represent the interaction of the interlayer in the LG element in models, aiming to compute shear strain and the corresponding shear stress transferred among the glass plies [135,167].

experimentally calculated G^* will approach the relaxation modulus G. Increasing strains in the loading phase are due to the finite stiffness of the setup, more specifically the finite stiffness of the dynamometric rings. Per definition, dynamometric rings can only record varying applied loads with some deformation. Hence with this setup, varying size of the dynamometric rings will always be associated to varying stain in the interlayer (i.e. one cannot read vary the load without – even so slightly - varying the strain when using a dynamometric ring). This setup didn't allow for on-the-fly modifications to the stiffness of the dynamometric rings; however, as the ratio r between setup and interlayer stiffness increases, the experimentally computed value of G^* approaches the exact value of the relaxation modulus G:

$$\lim_{r\to\infty} G^* = G$$

Even so, looking at the slope of the strain curves in the loading phase in Figure 4.33.b and remembering that this case study is referred to the stiffest among tested materials, it seems not completely unacceptable to confuse the experimentally calculated modulus with the relaxation modulus. In the proceeding of the dissertation, this approximation will be accepted, and the consequences will be carried on knowingly, up to the final conclusions. Therefore, by concisely referring to the *relaxation modulus* G, in all the following discussions, we will in fact be referring to the *experimental approximation of the relaxation modulus* G^*, rather than to its true definition.

The experimental creep compliance modulus $J(t)$, calculated over a constant "virtual" load step $\bar{\tau}_u$, is not affected by the same approximation.

Figure 4.34 shows both the relaxation and creep compliance moduli over time; to ease the comparison among them and dimensionally uniform the graph, the inverse of the creep modulus J^{-1} is presented. Finally, note that the time axis has now been converted to seconds, a choice which will also be carried on for all following analyses (cfr. §5.1.2).

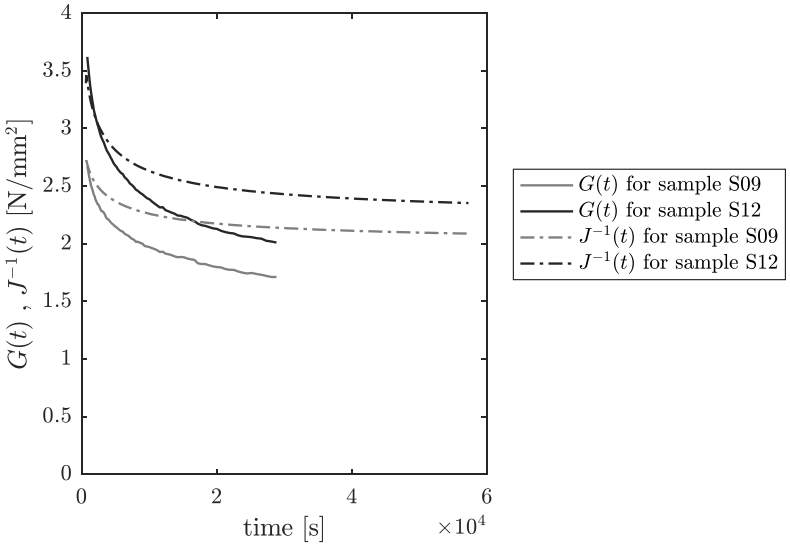

Figure 4.34 – relaxation and creep compliance moduli for the case-study

Final results for all tests are displayed in Figures 4.35 to 4.37. Values are displayed in a log-log scale plot, helping to compare quantities ranging among several orders of magnitude.

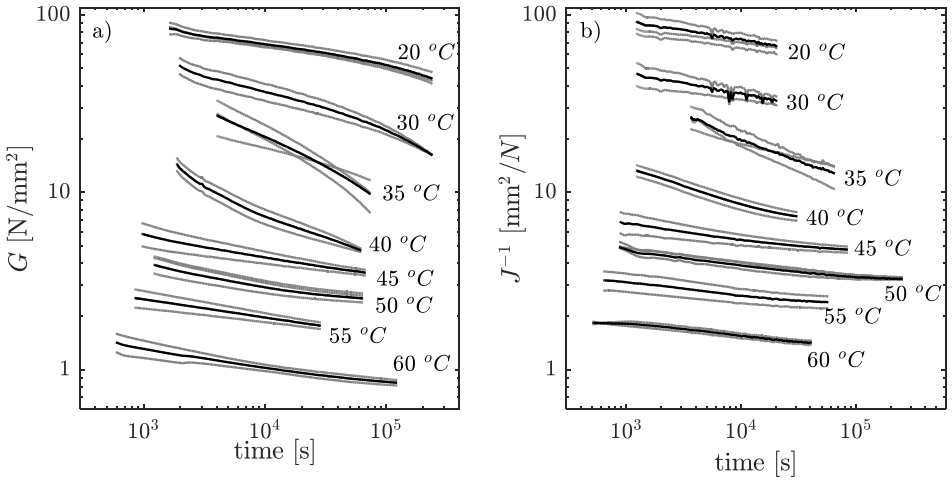

Figure 4.35 – a) relaxation and b) inverse compliance moduli for SG interlayer†

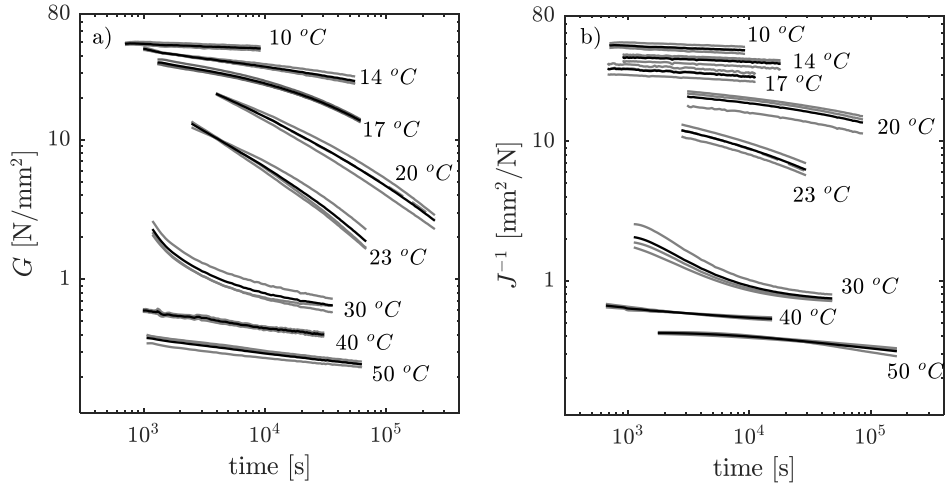

Figure 4.36 – a) relaxation and b) inverse compliance moduli for DG41 interlayer†

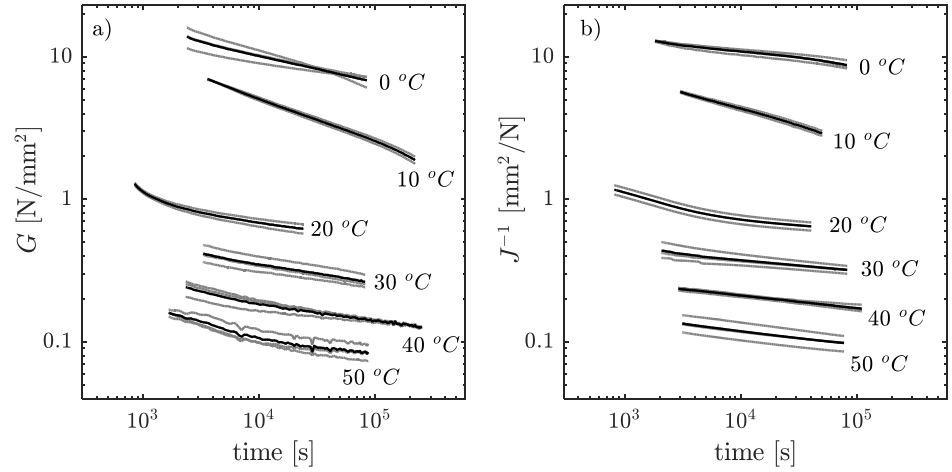

Figure 4.37 – a) relaxation and b) inverse compliance moduli for PVB interlayer†

---

† Dotted lines are the results for each different tested specimen (cfr. Table 4.5). For each temperature, the mean value is presented as a thick plain line.

4.2.4.5 EXPERIMENTAL DELAMINATION

Laminated glass specimens were assembled by the manufacturer with a traditional process at high pressure and temperature[31] in an autoclave: a method which allows for the formation of chemical bonds between the glass surface and the interlayer (cfr. §1.1.3).

Before the start of the campaign, a foreseen scenario was the possibility that the imposed shear stress on the specimens may exceed the capacity of the bonding forces among glass and interlayers, while these remain internally cohesive. The result of this event is a phenomenon known as "delamination", which has been described in §3.3 as the loss of adhesion between the materials forming a LG element. Previous research showed how similar tests may result in partial delamination, suggesting that both temperature and shear stress play an important role in facilitating the loss of adhesion [65,110].

Throughout the experimental campaign on laminated specimens, after each series of tests was performed, the laminated elements were extracted from testing devices (cfr. §4.2.1) and classified accordingly with labels for the name, test duration and temperature. A simple photographic technique was developed, to investigate the extension of the delamination among the specimens which suffered from partial loss of adhesion.

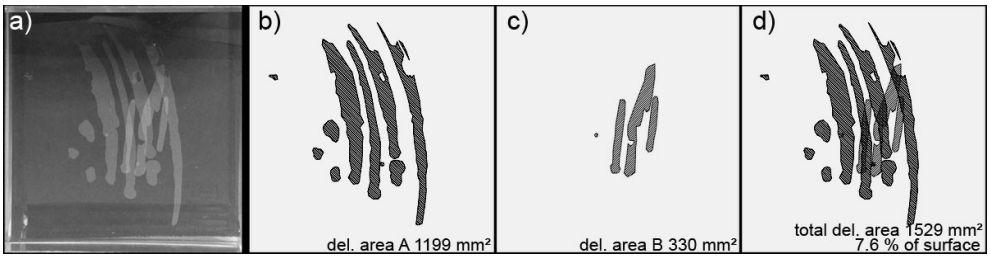

Figure 4.38 - example of delamination analysis for specimen S09

An example of the photogrammetric analysis is presented in Figure 4.38, while details on the technique and results for all other specimens are in Appendix C.

4.3 PROGRESSIVE DAMAGE IN LAMINATED GLASS BEAMS

The layered LG arrangement, consisting in the combination of stiff glass plies and softer interlayers, causes this composite material to behave in a peculiar manner [47,277]. While interlayers properties are crucial in defining the mechanical response and resistance of Undamaged Laminated Glass elements (ULG) [159], those are even more relevant when the structural integrity of the glass plies is compromised [11,221]. Safe LG design asks for reliable structures even after partial or complete glass failure, avoiding injuries and collapses. Two binding serviceability conditions are to be met:

1. abrupt and unanticipated collapses must be avoided and
2. adequate residual load-bearing capacity must be provided until evacuation and replacement (fail-safe response).

As glass itself loses structural integrity with propagation of cracks, both safety requirements must draw from the mechanical properties of interlayers (cfr. §4.2

[31] Typically, around 120-150°C and 10-15 atm, depending on the manufacturer and interlayer material [93,347].

and §4.1 with further discussion in §5.1). While the increase in tensile strength brought by such performance-enhancing processes is unquestionably beneficial for ULG, the fragmentation after glass failure might not be advantageous from a structural point of view. Depending on several factors that will be discussed in the following, Partially Damaged- and Fully Damaged Laminated Glass (PDLG and FDLG) can still withstand significant loads prior to the final collapse.

Studying properties of progressive damage among a LG element is significant for assessing safety and performance for Ultimate Limit State (ULS) and Serviceability Limit States (SLS) as well. As a matter of fact, it is common design practice to include *sacrificial glass plies* within those LG elements that bear the most responsibility or those which are more likely to be exposed to accidental failure. Foraboschi in [42] provided a definition of the characteristics of sacrificial plies:

> *[The sacrificial ply] collects the live loads [and] is allowed to fracture in service. [The sacrificial ply] is redundant to the serviceability and ultimate limit states of the LG member and is included only to allow for the possibility of accidental glass breakage due to contact damage. The sacrificial ply may be kept in service also in fractured condition; it has to be substituted only when it has lost the capacity of shielding the others layers.*

4.3.1 PURPOSE OF TESTS

Interlayers are believed to have a negligible influence over the response of in-plane loaded ULG elements, due to the vast mechanical differences between the two materials (i.e. the glass is generally orders of magnitude stiffer compared to any interlayer). Nonetheless, stiff interlayers are known to enhance significantly the post-failure response [102]. The goal of this experimental campaign[32], is to investigate and quantify the effects of the *tension-stiffening* (TS) mechanism which arises once one or more glass plies break. The insight that kick-started the investigation is that glass fragments adherent to interlayers can still provide a beneficial effect on the global properties of damaged LG.

Architectural LG elements can be designed to bear transversal loads (e.g. glazing, roofing, etc.) or loads in their own plane (e.g. beams, columns, etc.). From a structural point of view, elements which bear greater load-carrying responsibilities are generally the latter. As a safe design of in-plane loaded LG could benefit from better understood and quantified levels of resilience, a focus on such elements was chosen for this research[33].

Structural LG elements are often comprising several – if not only – fully tempered glass plies. Tempered glass undergoes thermal or chemical treatments which increases its strength and influences the breakage texture, producing a denser and more widespread crack patterns compared to annealed of heat-strengthened glass (cfr. §4.3). While residual properties of damaged LG elements ultimately rely upon the strength of the adhesion bond and the intrinsic properties of interlayer

[32] Presented studies are actually part of two separate campaigns with similar goals, carried out in different time spans: a first campaign on SG-laminates was performed in summer 2015 and a second one on DG41- and *reinforced* DG41-laminates in summer-fall 2016.

[33] Research on post-failure response and progressive damage regarding transversally-loaded elements is ongoing at the Structures Laboratory of the DICEA by the time this manuscript is being completed. More information on the results of those tests and comparisons with the ones presented within this manuscript can hopefully be expected soon, within dedicated research papers.

materials [104], as a general rule of thumb, the bigger size of the glass fragments, the better the overall post-failure performance [77]. Performance analyses of damaged LG made with tempered glass plies can therefore be regarded as a worst-case scenario.

4.3.2 DESIGN AND SETUP

Tests were designed to assess the post-failure behaviour of simply supported SG-laminated beams (type A), DG41-laminated beams (type B) and *reinforced* DG41-laminated beams (type C). The "reinforcement" within type C specimens consisted in 0.2 mm thick polycarbonate (PC) foils between two layers of DG41. A total of eight specimens were assembled (Table 4.6), each using three 10 mm thick tempered glass plies. Figure 4.39 shows details of specimens with nominal sizes and thicknesses.

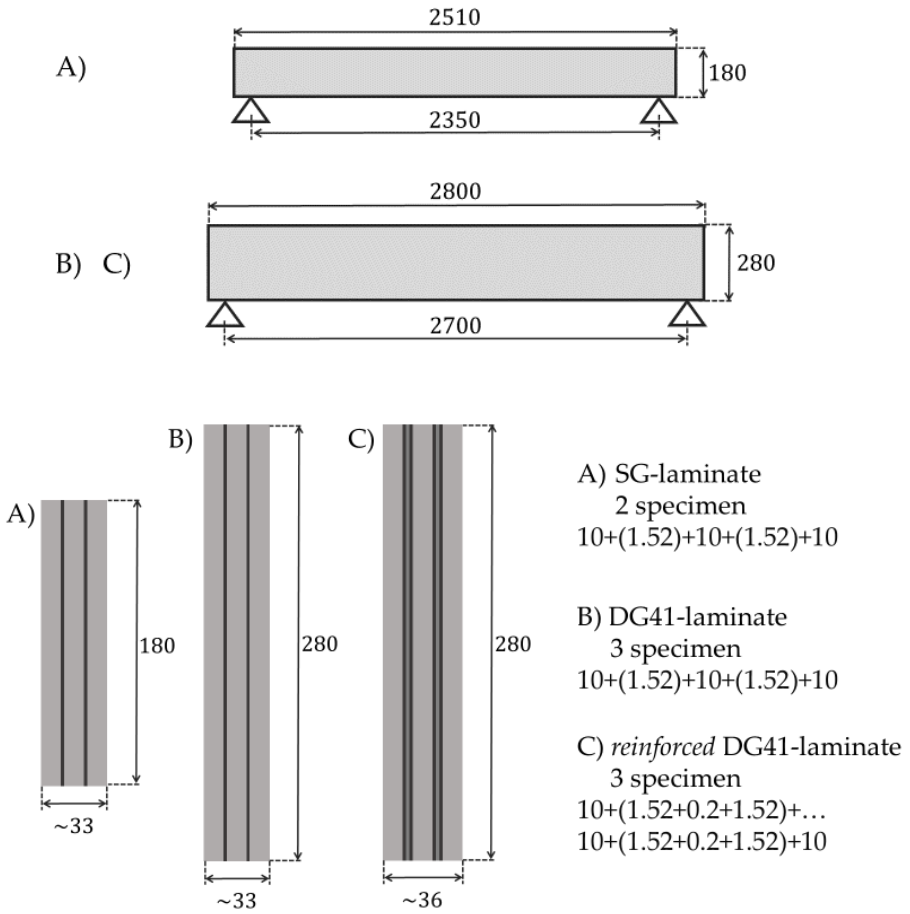

Figure 4.39 - full-scale LG beams specimens type A, B and C [mm]

Table 4.6 - specimens type and nomenclature

interlayer material	**SG**		**DG41**			**DG41 + PC**		
type	A		B			C		
specimens	A1	A2	B1	B2	B3	C1	C2	C3

Figure 4.40 illustrates the design damage progression: first failure of the central ply, then the lateral plies, one at a time. Rather than reproducing the most common

failure mode within real structures[34], this *modus operandi* was chosen to safeguard the instruments, allowing for the collection of a larger amount of data. Moreover, this procedure allowed for studying a symmetrical PDLG configuration, which is convenient for reasons that will be discussed throughout the critical analysis and discussion of experimental results.

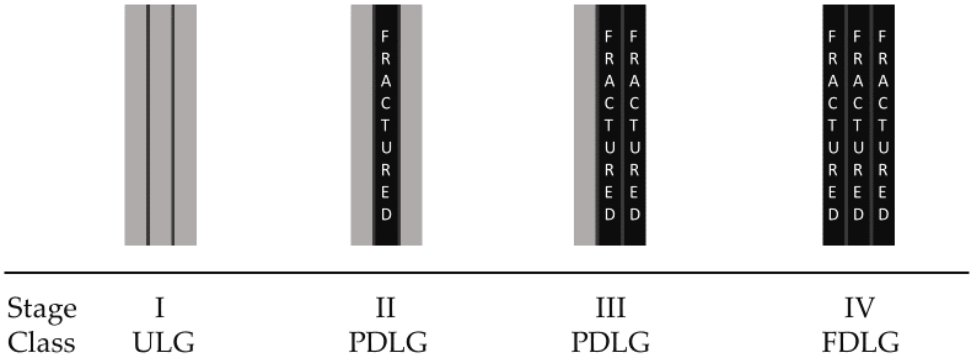

Figure 4.40 - damage progression imposed by design

Figure 4.41. shows the two experimental setups which were designed around an MTS hydraulic press, used to apply vertical loads in three-point bending tests. To allow specimens to be simply supported, a HE300B steel beam was inserted within the press columns, to serve as a base for steel rollers, in turn used as punctual supports for the specimens. Vertical struts were needed to provide additional vertical support, while lateral torsional restraints were installed for safety reasons: preventing damage and injuries in the event of sudden lateral-torsional buckling[35].

As the manufacturing process did not allow for a perfect glass plies alignment, two solutions were adopted to rectify the contact surfaces: at both ends, aluminium pads were placed on top of the steel rollers and a stiff epoxy resin was used to fill the interface between the pads and the glass surface; at midspan, where the vertical load is applied, a third aluminium element was inserted between the top of the specimen and the hydraulic jack. A thin lead foil under the central aluminium pad was used to compensate for small plies misalignments and help to evenly distribute the applied load.

As illustrated in Figure 4.44 for type A and Figure 4.45 for type B&C specimens, several instruments were used to monitor the LG response along the different stages.

Piezoelectric accelerometers were installed on the specimens and the setup for dynamic tests, to detect the response of impulse-induced vibrations.

For bending tests, vertical displacements were monitored at midspan (F1) and both ends (F2 and F3) with LVDT sensors. For FDLG elements, the midspan transducer was replaced with a cable potentiometer transducer, to cope with the higher sag expected.

[34] Which are likely to have the external plies fail first, due to local contact actions.

[35] Apart from asymmetrical failure configurations, when the lateral sag didn't allow for the beam to rest on a vertical position by itself, torsional restraints were intentionally distanced from the specimen surface, allowing it to move freely.

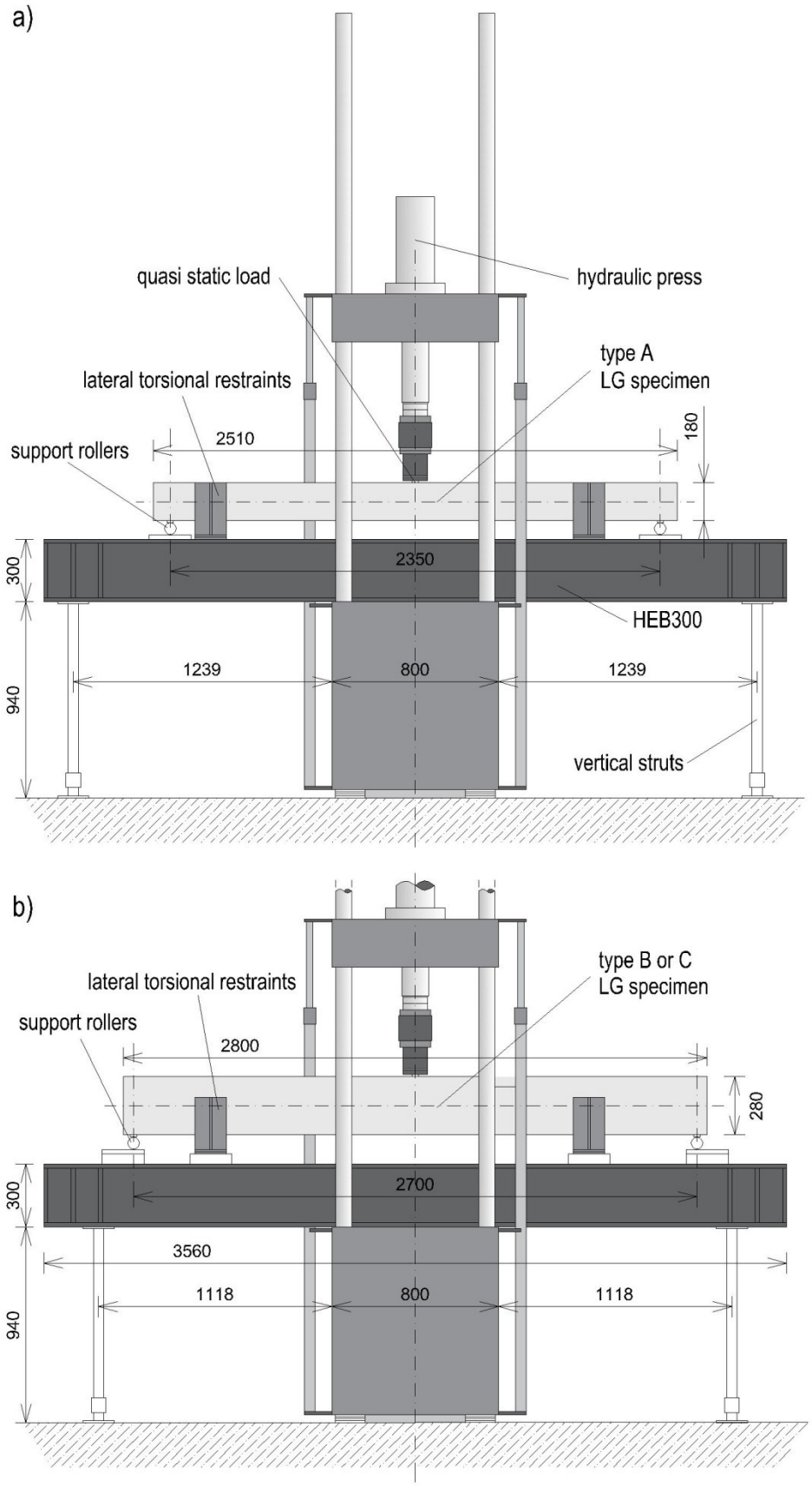

Figure 4.41 – lateral setup scheme for a) type A and b) type B or C specimens

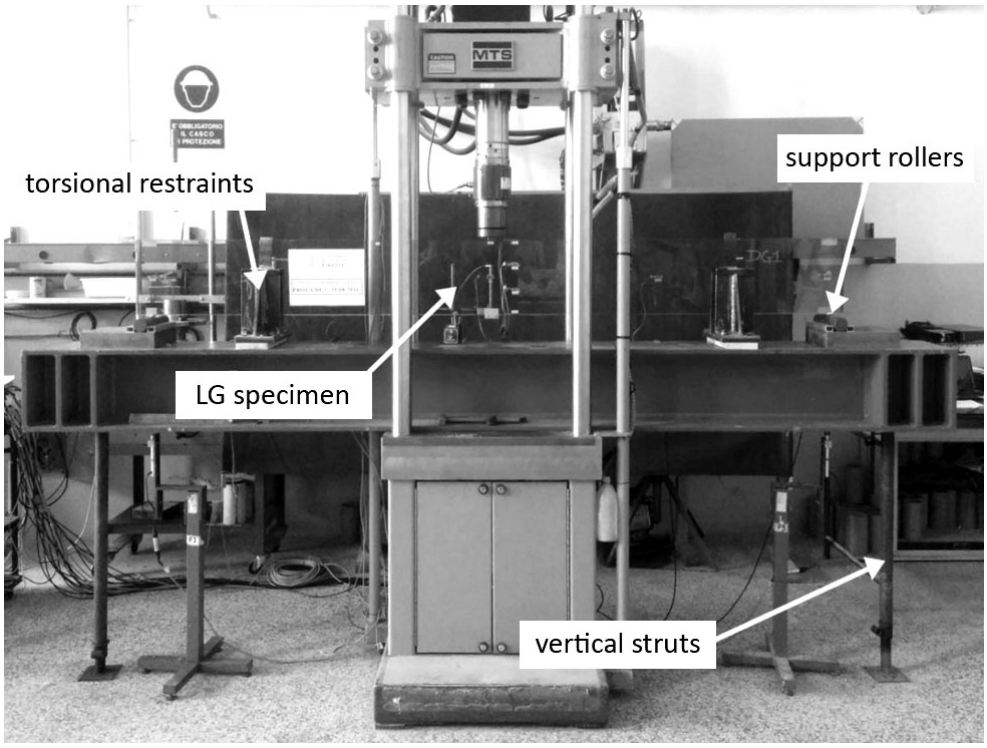

Figure 4.42 - picture of the setup arranged for specimen B1

Specimens were equipped with strain-gages on the outer surface of the glass plies: 8 were used for type A ($e1$ to $e8$) and 15 for type B&C ($e1$ to $e15$). A cross-section close to midspan was equipped with most strain-gauges, to investigate the varying position of the neutral axis for increasing levels of damage. The exact midspan cross-section was not chosen, to avoid the influence of local effects of localized load application. As the damage level increases, data from strain-gauges is progressively lost. Readings collected by strain-monitoring instruments connected to glass fragments are affected by the distribution of cracks: as the number and distribution of crack can affect those instrument readings in unpredictable ways, the interpretation of such measurements is a very difficult task. Data originating from instruments on damaged plies have therefore never been accounted for.

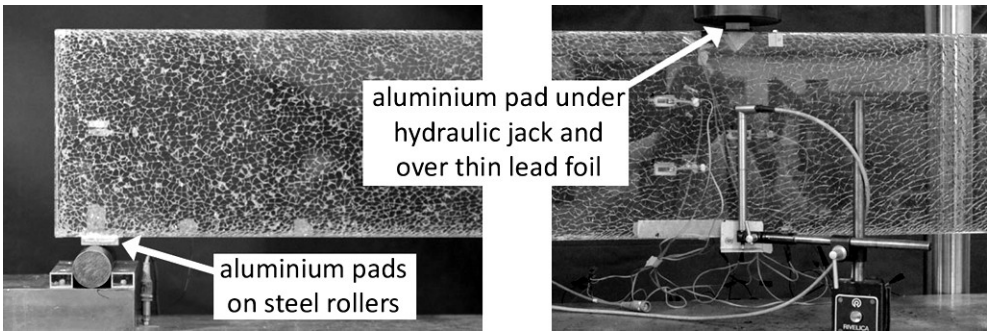

Figure 4.43 –pads used for the setup interfaces (on stage II PDLG specimen B2)

To cope with the loss of strain-gauge measurements on FDLG specimens, omega transducers were installed on the central - fractured - glass ply, close to midspan. The confinement effect due to the presence of interlayers on both sides, together with the good adhesion between the two materials, allows for using the relative displacement readings of the base points of the omega transducers to compute the mean strain (Figure 4.46): knowing the base distance $b_0 = 50\,mm$, the mean strain is $\bar{\varepsilon} = b/b_0$.

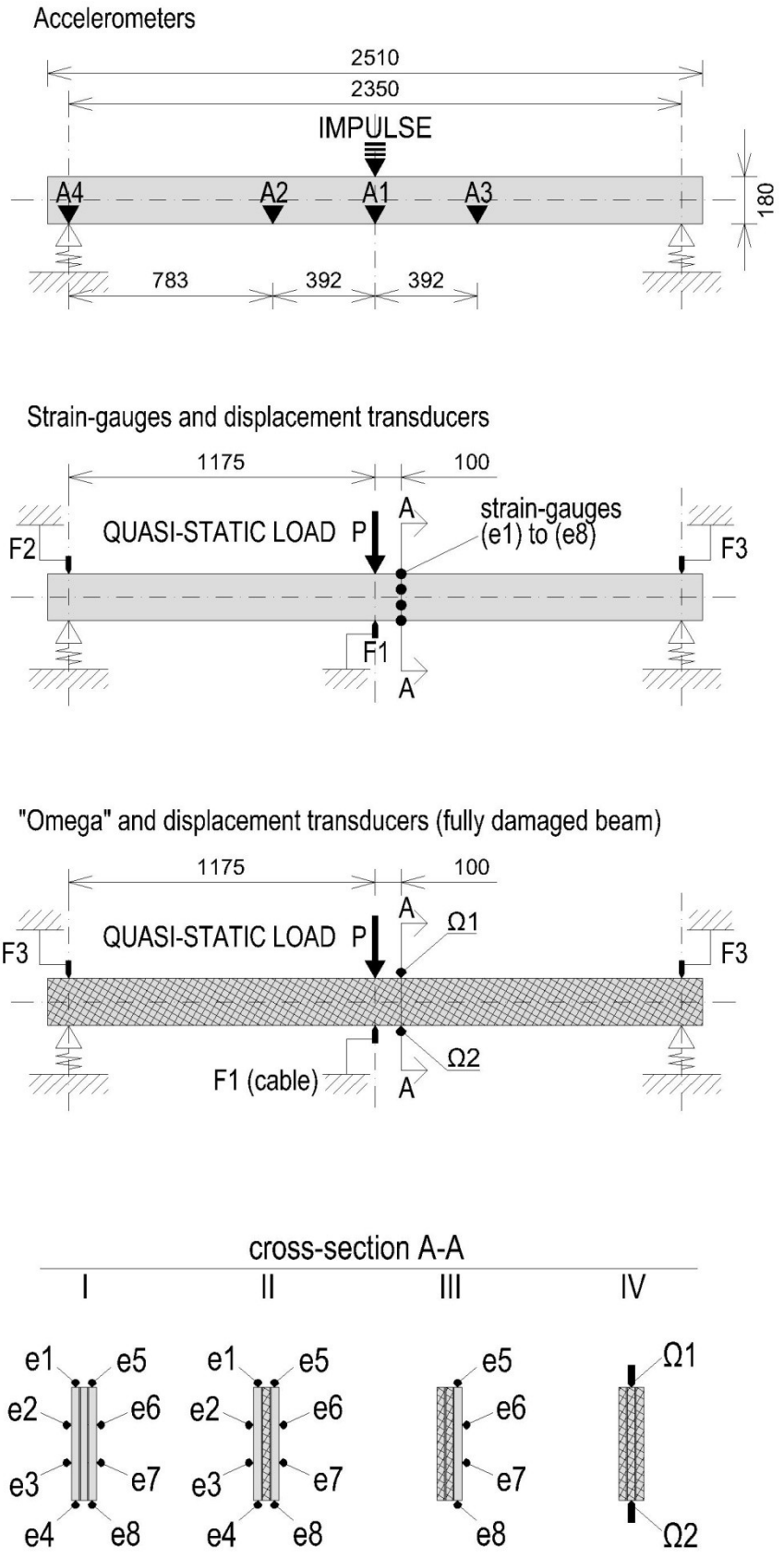

Figure 4.44 – measure instruments installed on type A beams

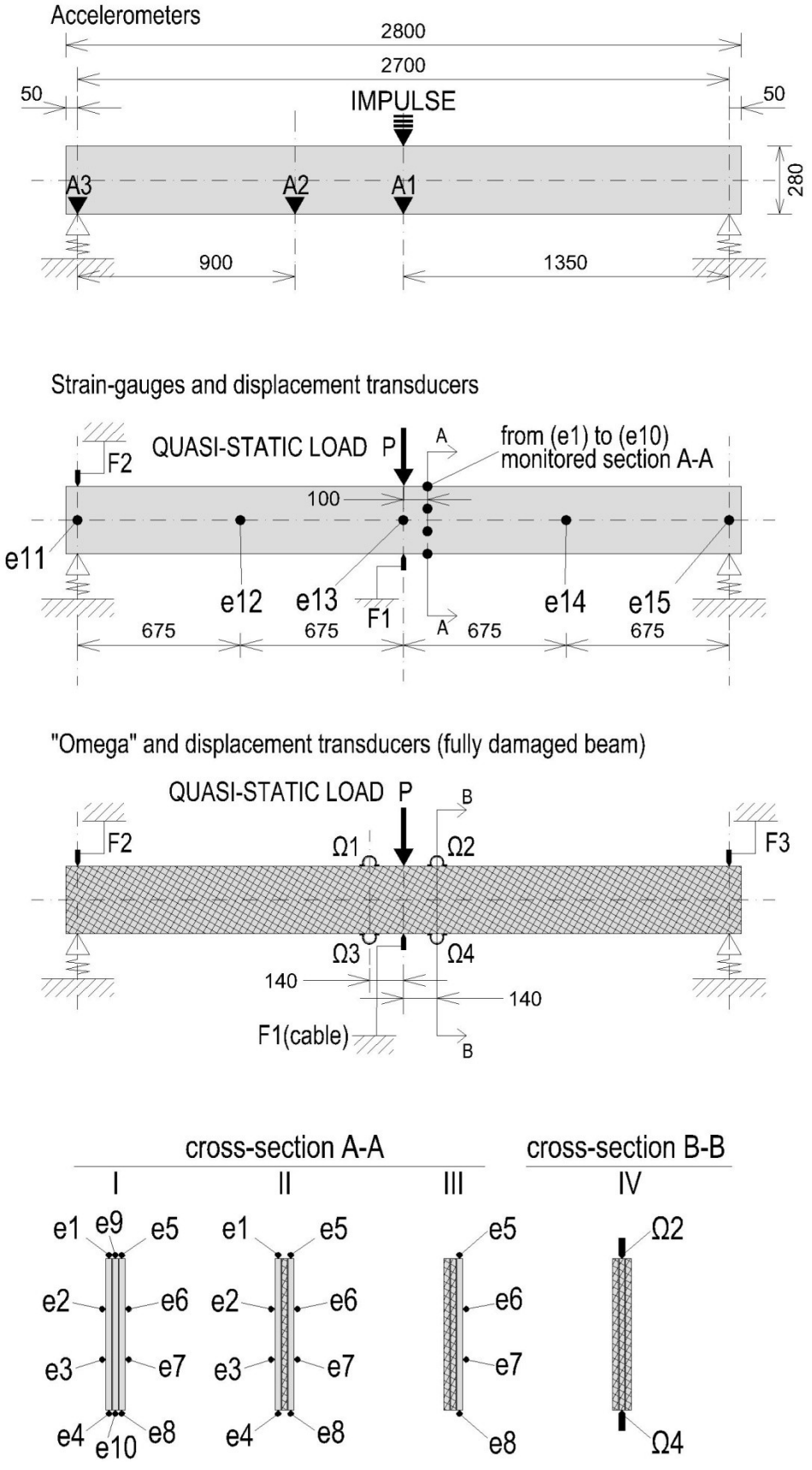

Figure 4.45 – measure instruments installed on type B and C beams

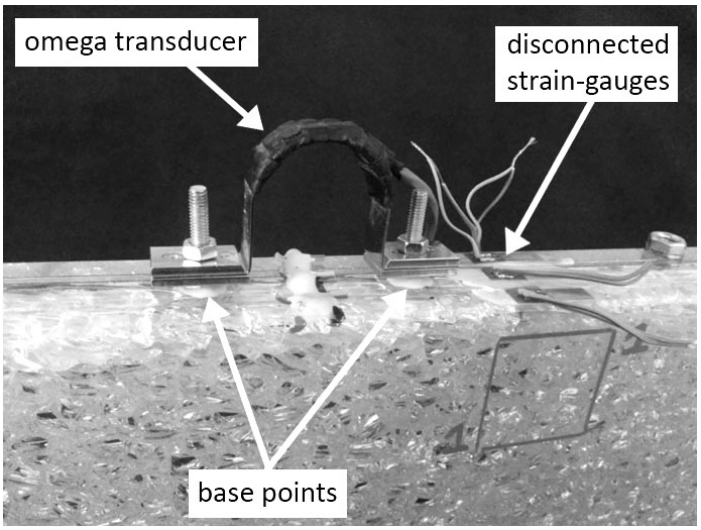

Figure 4.46 - omega transducers installed for FDLG tests

Table 4.7 lists all tests designed to investigate the effects of progressive failure on LG beams[36]. Individual tests are described in the following.

Table 4.7 - tests performed on LG beam specimens

Test stage	Test #	type	SG		DG41			rDG41		
			A1	A2	B1	B2	B3	C1	C2	C3
I	1	*dynamic response*	✓	✓	✓	✓	✓	✓	✓	✓
	2	*3-p. bending*	✓	✓	✓	✓	✓	✓	✓	✓
II	1	*failure effects*			✓	✓	✓	✓	✓	✓
	2	*long-term strain*			✓	✓			✓	✓
	3	*dynamic response*	✓	✓	✓	✓	✓	✓	✓	✓
	4	*3-p. bending*	✓	✓	✓	✓	✓	✓	✓	✓
III	1	*failure strain*			✓	✓	✓	✓	✓	✓
	2	*lateral sag*			✓	✓	✓	✓	✓	✓
	3	*long-term strain*			✓	✓				✓
	4	*dynamic response*	✓	✓	✓	✓	✓	✓	✓	✓
	5	*3-p. bending*	✓	✓	✓	✓	✓	✓	✓	✓
IV	1	*ultimate failure*							✓	
	2	*dynamic response*	✓	✓	✓	✓	✓	✓	✓	✓
	3	*3-p. bending*	✓	✓	✓	✓	✓	✓	✓	✓
	4	*5mo. 3-p. bending*	✓	✓						

I-1 Dynamic response test: multiple vertical impulses are applied at 10 *s* time intervals at midspan and L/4 [37]. Accelerometers data is recorded.

[36] As mentioned when introducing these experimental analyses, results discussed in this paragraph and listed in Table 4.7 are referred to tests carried out during two distinct experimental campaigns. Therefore, one should not be surprised observing that type B and C specimens are listing a larger number of tests (and carry a larger measurement equipment), as those investigations could benefit from the experience gathered during the analyses of type A specimens in the first campaign.

[37] At the beginning, impulses were given with a rubber hammer. However, this technique proved to be sub-optimal during the first tests, for the formation of a feeble sonic wave propagating through the beam and the setup, affecting the accelerometers accuracy. After several attempts, impulses given with a swift palm hand strike showed to yield the best results, this technique was then used for all other tests.

I-2 Three-point bending test: with hydraulic jack speed 0.01 mm/s, a load ramp is performed up to the design maximum load, held for two minutes, and an unload ramp at the same speed back to zero load. Repeated twice. Design maximum load is 5 kN for type A and 40 kN for type B and C. Strain data are collected from the strain-gauges, applied load from the load cell, and vertical displacements at midspan and both ends through LVDT transducers.

II-1 Failure of the central glass ply: failure of the central glass ply is induced with a glass-breaker pick and a hammer. Strain gauges data are recorded during failure and for 10 minutes after failure.

II-2 Long-time strain recording: while the specimen is left undisturbed, resting on the supports at both ends, strain-gauges data is recorded continuously for 24 hrs after the glass ply failure. In the same room, an additional strain-gauge is installed on a separate glass surface in the same room, to allow for *a posteriori* compensation of thermal effects.

II-3 Dynamic response test: same procedure of test I-1.

II-4 Three-point bending test: similar procedure of test I-2, the design maximum load is now 5 kN for type A and 25 kN for type B and C. Strain-gauges data are now only collected from instruments installed on non-broken glass plies.

III-1 Failure of one lateral glass ply: the first lateral ply is broken with the same procedure of test II-1. The first lateral ply designated to be broken is the one not equipped with the strain gauges $e11$ to $e15$.

III-2 Measure of the lateral sag: a caliper is used to measure the lateral sag at midspan, induced by the shattered glass expansion in an asymmetrical failure configuration. A thin spring steel cable is used to collimate the ends of the beam during the measurement.

III-3 Long-time strain recording: same procedure of test II-2.

III-4 Dynamic response test: same procedure of test I-1.

III-5 Three-point bending test: Same procedure than test I-2, the design maximum load is now 2.5 kN for both type A, B and C.

IV-1 Flexural failure: failure of the last glass ply is induced with a continued three-point bending test. Lateral torsional restraints are placed close to midspan and used to hold the cross-section in vertical position.

IV-2 Dynamic response test: similar procedure of test I-1, except vertical impulses are applied at 20 s intervals.

IV-3 Three-point bending test: similar to the procedure of test I-2, the design maximum load is not set a priori, while a maximum sag of 10 cm is imposed to safeguard the measure instruments. Strain-gauges data is replaced newly installed "omega" transducers in a position close to midspan. Before testing, specimens were supported on multiple points (two at least) with wooden wedges, to prevent the onset of significant viscous deformations. Wedges have been removed moments before the beginning of tests.

IV-4 Repeated three-point bending test: same procedure of test IV-3, performed 5 months after the previous test.

4.3.3 EXPERIMENTAL RESULTS

Experimental results are presented separately for increasing levels of damage: starting from analyses on undamaged specimens in stage I up to the experimental outcomes for FDLG in stage IV, when all glass plies are shattered.

4.3.3.1 UNDAMAGED LG

The undamaged mechanical properties of glass have been drawn from experimental analyses, specifically, by interpretation of tests I-2 (Table 4.7). According to European Standards, the elastic modulus of glass is allowed to ranges between 63 and 77 GPa [38,278]. Experimental values of the Young modulus have been obtained assuming that interlayers – in virtue of their very low modulus - do not give a significant contribution to the response of in-plane loaded LG beams. For a simply supported element of span L, composed of n glass plies, of thickness t_g with moment of inertia $J_{1,g} = h^3 t_g/12$ about the strongest axis, with a load P_m at midspan, the elastic modulus of glass can be obtained as:

$$E_g = \frac{1}{48}\frac{P_m L^3}{\eta_m n J_{1,g}}$$

Experimental values of E_g have been evaluated on the second ramp load plateau of tests I-2, when the design action is held constant for two minutes. Table 4.8 displays experimental values of the elastic modulus for glass. Tests on materials coming from different manufacturers yielded comparable results.

While the interlayer modulus was neglected, the presence of the PC reinforcement for type C specimens has been considered with an elastic modulus of 2.39 GPa [66,279]. Figure 4.47 shows how the experimental modulus defined with this procedure is consistent over the whole loading plateau; final listed in Table 4.8 for all specimens are referred to the experimental point in the middle of the plateau. It is worth pointing out that such values must be looked at as average moduli for the three plies comprising each specimen.

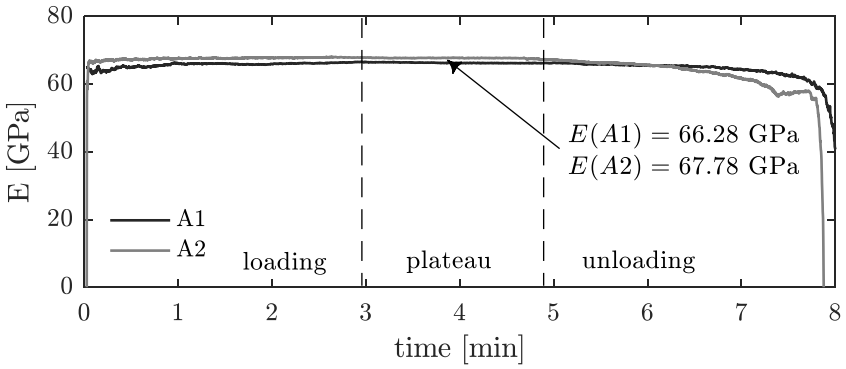

Figure 4.47 - glass modulus evaluation over the 2nd load ramp for type A specimens

Data recorded by accelerometers in dynamic tests I-1 have been analysed using a one-sided Fast Fourier Transformation (FFT), to evaluate the frequency content. As an example, Figure 4.48 shows the result of this procedure for the undamaged specimen A2.

The first natural frequency is easy to be found at 72.95 Hz, with a mutual effect also measured by accelerometer $a4$ placed on the setup. Similarly, the effect of the natural frequency of the setup, and its effect on all three instruments installed on the specimens, are found around 32 Hz. At higher frequencies, between 110 and

170 Hz, a second natural setup frequency appears o be inducing a disturbance on the specimen vibrations, while clear peaks at 239 Hz for instruments $a2$ and $a3$ spectra (but not $a1$) give a possible insight on the second vertical modal form of the specimen.

Table 4.8 – experimental elastic modulus of glass

manufacturer	specimen	Young modulus E [GPa]
1	A1	66.28
	A2	67.81
2	B1	66.39
	B2	65.83
	B3	68.45
1	C1	66.69
	C2	67.71
	C3	69.11

manufacturers: 1) Novavetro S.r.l. 2) Saint-Gobain Glass Italia S.p.a.

After the first campaign, evidence showed that accelerometers $a2$ and $a3$ were giving redundant results. Therefore, as shown by comparison of Figure 4.44 and Figure 4.45, a slightly different instrument choice was made for the second campaign on type B&C specimens: former instrument a3 was removed, while $a2$ was installed at $L/3$, rather than $L/4$. This choice was motivated by the fact that, while the second modal form displacements are not massively different between $L/3$ and $L/4$, one can hope to glance at the third modal form. Unfortunately, this approach did not give satisfactory results in practice.

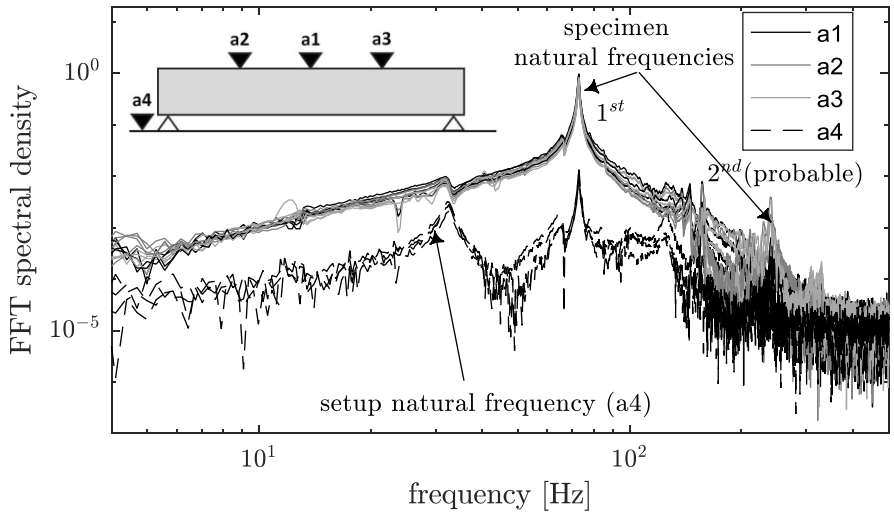

Figure 4.48 – normalized FFT response spectrum for undamaged specimen A2

Figure 4.49 shows the same analysis for a specimen of type B, investigated within the second campaign, with the new instrument configuration. While insight on the second modal form could still be gathered for most specimens, those results seemed overall less reliable with respect of the first campaign results. Ultimately, the data analysis focused on results for the first modal form only, which was always very easily identifiable.

By analysing data from strain-gauges on the monitored cross-section close to midspan (A-A in Figure 4.44 for type A specimens and Figure 4.45 for type B&C specimens), information can be gathered on the likely position of the neutral axis throughout bending tests.

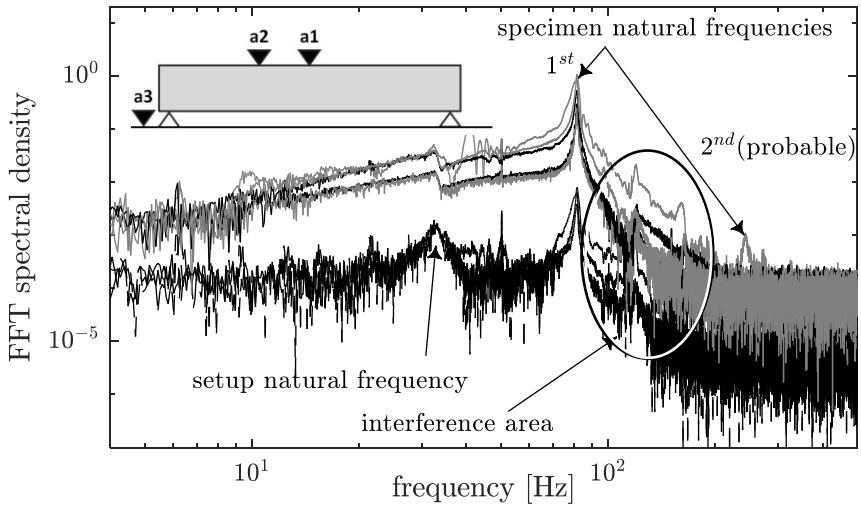

Figure 4.49 - normalized FFT response spectrum for undamaged specimen B2

Figure 4.50.a shows recorded data for the two load ramps, according to the procedure for test I-2. Strain over the height of the cross-section has been regressed with a linear interpolation for the whole extent of tests, showing how the neutral axis is consistently located at mid-height. Figure 4.50.b shows the linear regression[38] at the center of both plateaus (highlighted in Figure 4.50.a). Results show that the interpolated position of the neutral axis is exactly at mid-height, as expected for a symmetrical cross-section made of an isotropic material.

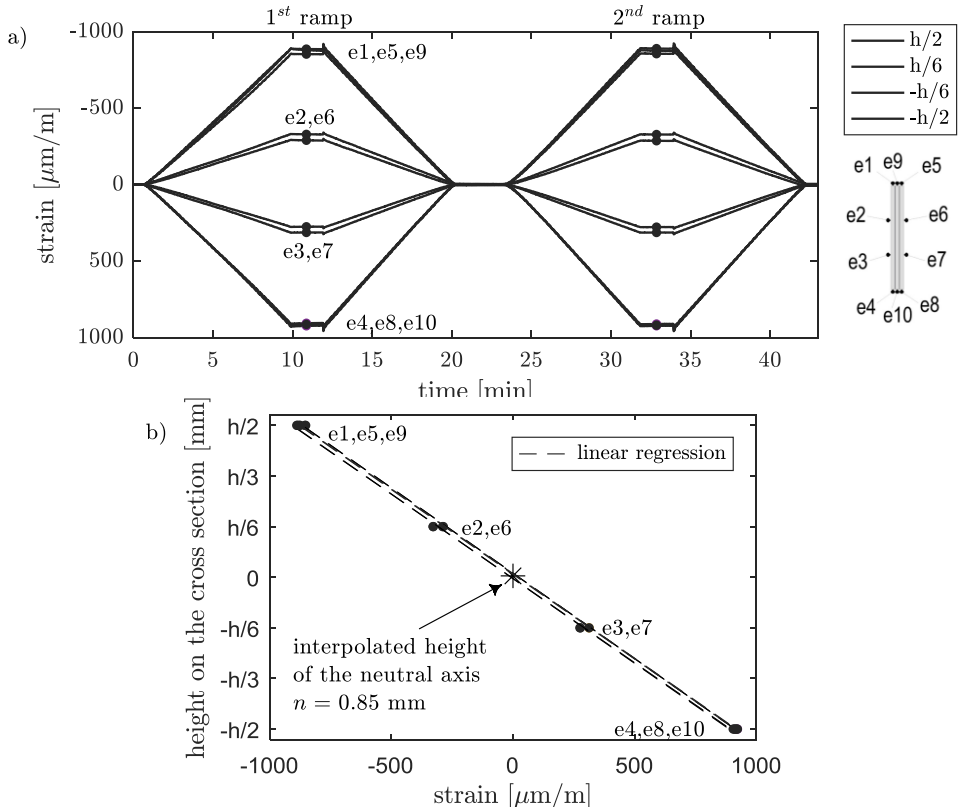

Figure 4.50 – a) measured strain for undamaged specimen B1 in bending test b) interpolated position of the neutral axis computed on the loading plateau

[38] A linear regression is consistent with the Euler–Bernoulli hypothesis that plane sections remain plane.

All undamaged specimens yielded average interpolated positions of the neutral axis close to the cross-section centroid, within 2% of the height.

4.3.3.2 PARTIALLY DAMAGED LG

Bending tests on PDLG specimens were performed under displacement control, up to a fixed maximum load. For stage II the maximum load could be set by design accounting only for ultimate failure calculations, with adequate safety coefficients. On the other hand, the lateral sag induced by asymmetric glass plies failure in stage III compelled to settle upon a much lower maximum design load, to prevent both beam failure and lateral torsional buckling.

The displacement was increased linearly up to its maximum value, maintained constant for two minutes and then decreased to zero. The speed of the actuator was set to 0.5 mm/min, originating a maximum normal stress rate in glass plies of about 4.3 MPa/min for type A specimens and 7.44 MPa/min for Type B&C.

Strain-gauges data on specimens of type B&C was recorded upon failure of the central and lateral glass plies. This procedure was not planned in the campaign on specimens of type A, whose results later hinted to the opportunity to measure the instantaneous strain changes through the transition between increasing levels of damage; a procedure which was implemented for the second campaign.

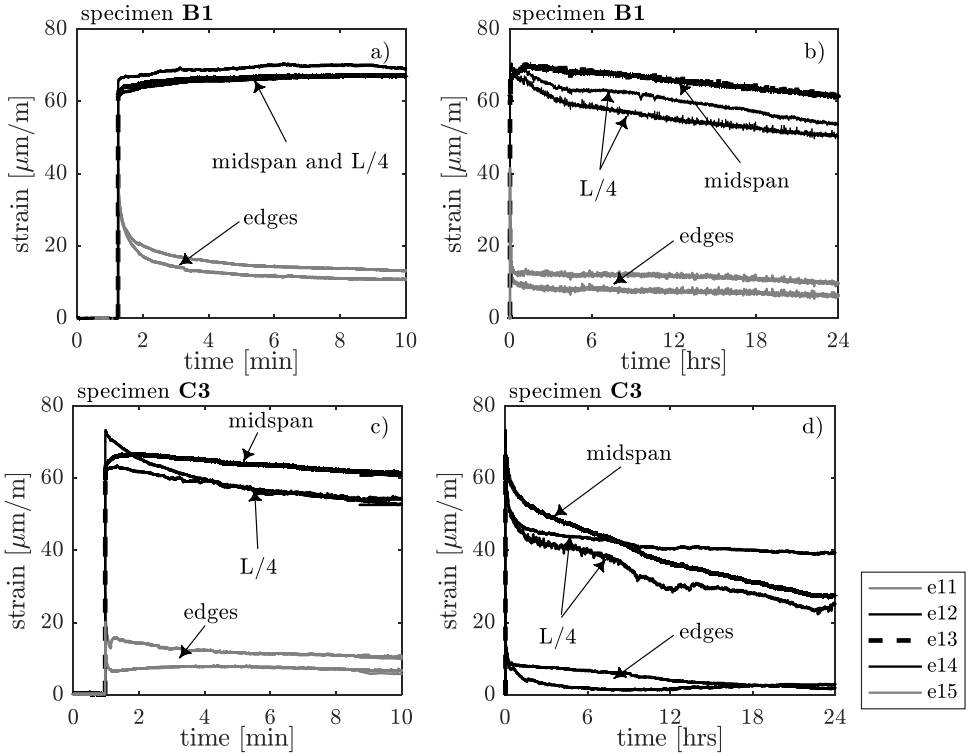

Figure 4.51 - comparison of long- and short-term measured strain on the lateral plies after the failure of the central ply

Results in Figure 4.51 and Figure 4.52 show readings for those instruments which are installed on plies that remain intact after the imposed failures. Strain gauges on shattered glass plies may be affected by local effects which are arguably very difficult to interpret. The maximum extent of induced strains appears to be consistent among the specimen types B&C. Nonetheless, the double interlayer thickness of type C specimens seems to play a role, allowing for a faster stress/strain relaxation in the symmetrical PDLG configuration (Figure 4.51.b and Figure 4.51.d).

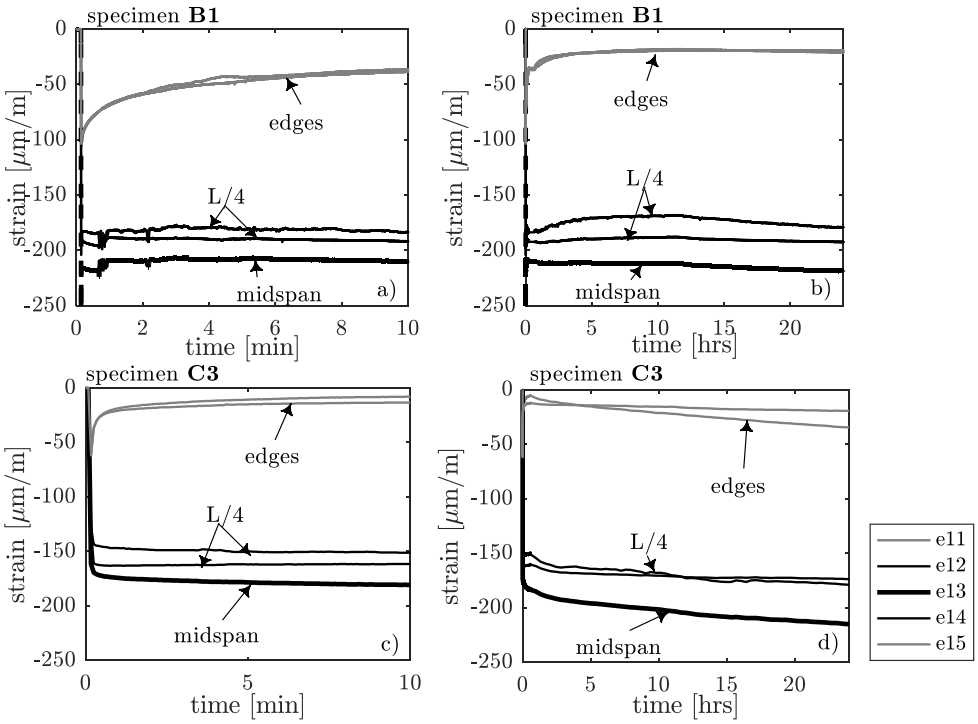

Figure 4.52 - comparison of long- and short-term measured strain on the intact lateral ply after the failure of the opposite lateral ply (the central one is already broken)

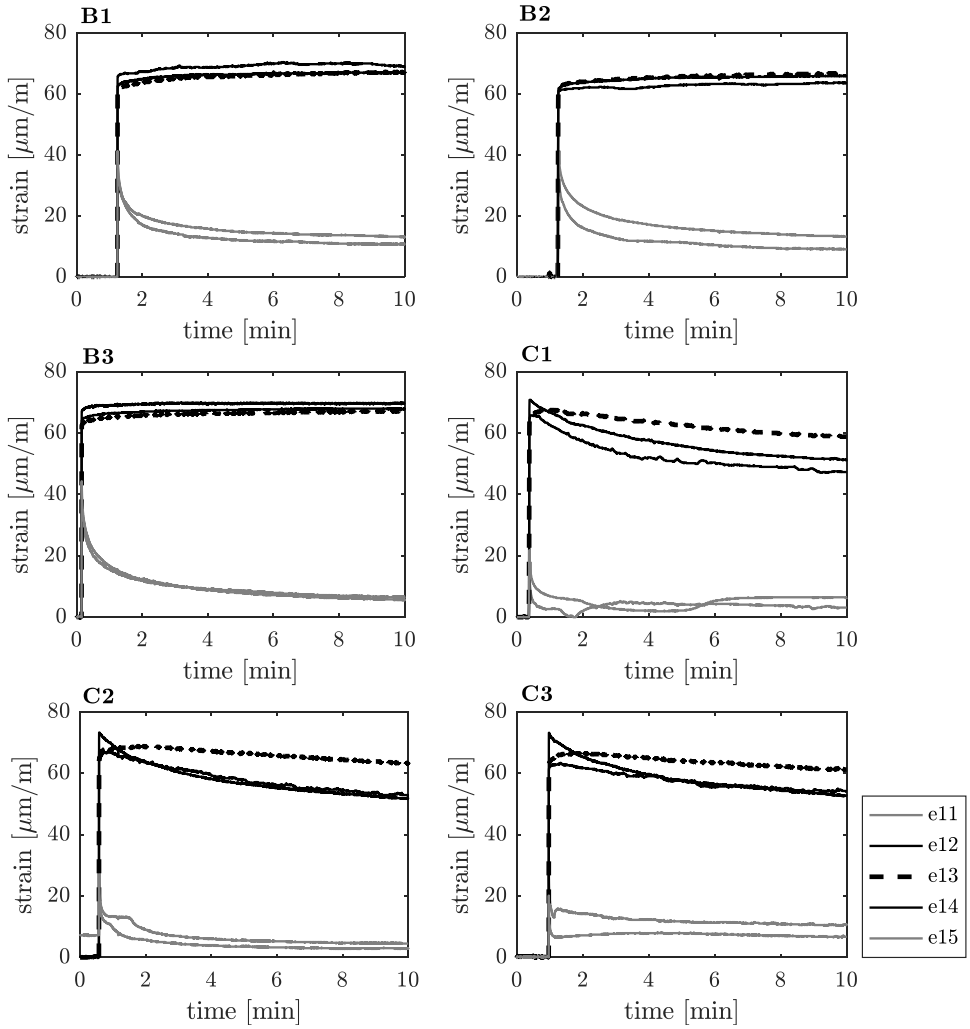

Figure 4.53 - short-term effects after central ply failure on all specimens type B and C

When a lateral ply fails, instruments on specimens of type C with double interlayer thickness indicate that the curvature (hence the stress and strain) slightly increases over time, at least for the first 24 hours. Figure 4.52, for type B specimens with regular interlayer thickness, suggest that instantaneous effects of the lateral glass failure are more consistent over time, except for instruments e11 and e15 installed very close to the edges.

Figure 4.53 provides a graphical comparison of short-term effects of symmetric glass failure for all specimens of type B and C, showing that results are consistent among similar elements.

Dynamic tests have been analyzed similarly to those described in the previous paragraph §4.3.3.1. Figure 4.54 shows spectral density results for accelerometers (this time, on a linear scale, highlighting the spectrum peaks even more compared to Figure 4.49). Results for different specimens do not display substantial differences, a final synthesis of experimental natural frequencies is shown in Table 4.10 (p.113).

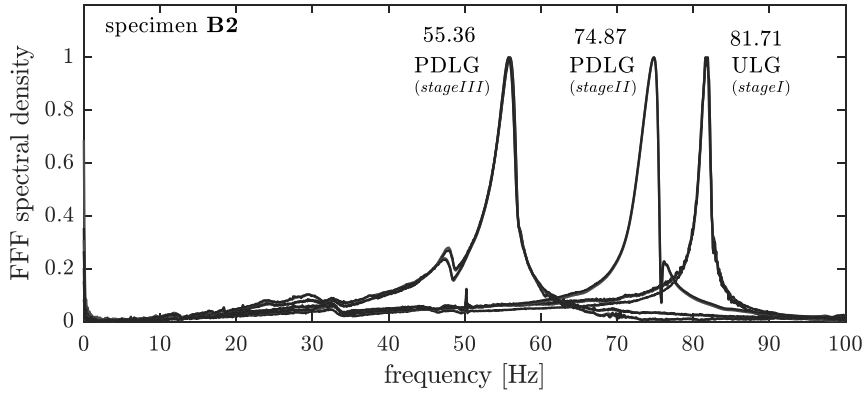

Figure 4.54 – normalized spectral density for specimen B2 PDLG stages

Bending tests II-4 and III-5 on PDLG, continue to showcase a substantial linear elastic response, as did test I-2 on ULG specimens. Figure 4.55 shows curves for applied load over vertical displacement at midspan: evidence suggests that no permanent effects are induced, as the load and unload paths are essentially undistinguishable (plots in Figure 4.55 are displaying both).

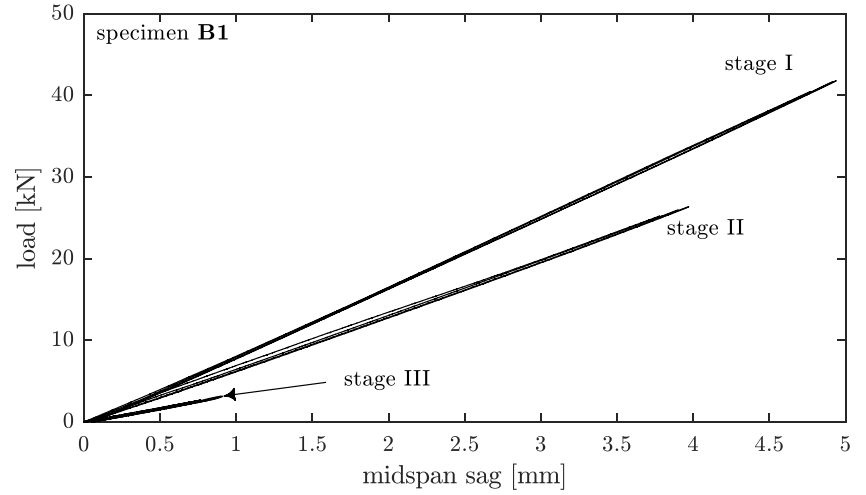

Figure 4.55 - load-displacement curves for PDLG specimen B1

It is worth pointing out that the elastic response of PDLG elements vastly exceeds the one expected only accounting for the undamaged glass plies contribution. As this increased stiffness is ascribable to the collaboration of fractured elements and interlayers, further analyses will be carried out in the following §5.2.

As observations of a rise in the neutral axis position in PDLG bending tests were expected, strain-gauges data from the monitored sections were analyzed similarly the procedure used to verify the isotropic behaviour of ULG specimen (cfr. §4.3.3.1). Figure 4.56. shows how strain measurements gathered in tests II-4 and II-5 (Table 4.7) were linearly regressed to interpolate the likely position of the neutral axis.

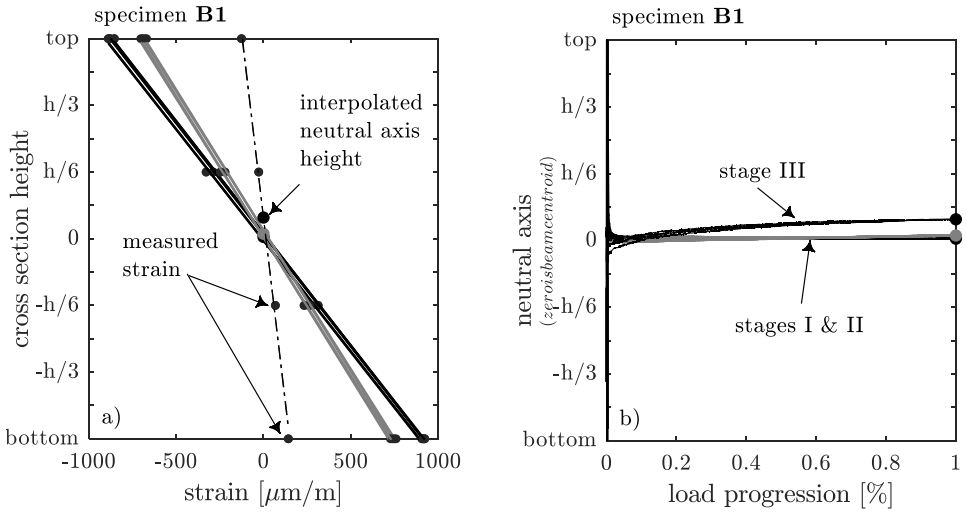

Figure 4.56 - a) snapshot of interpolated strain distribution over the cross-section height at P_{max} and b) progression of the neutral axis position for increasing load

For stage II, when specimens are partially damaged with only the central ply fractured, results show that the neutral axis continues to be steadily consistent with the centroid, as it was previously observed for undamaged specimens in stage I.

Conversely, as damage progresses and one of the lateral plies has failed, evidence from bending tests in stage III shows that the neutral axis rises even so slightly towards the top of the beam, even for moderate loads. The evolution of the neutral axis depth can be understood at best by looking at results of test IV-1, only performed for specimen C2 (cfr. Table 4.7 p.101). Figure 4.57 shows that the neutral axis settles rapidly upon a position slightly above of the centroid and does not move significantly up to the ultimate failure[39].

Table 4.9 lists interpolated positions of the neutral axes for all specimens during bending tests I-2, II-4 and III-5, for the corresponding damage states[40]. Despite

[39] It is worth pointing out that, due to the lateral sag, torsional stress components are induced alongside pure flexural ones. While this effect is not being recorded by the strain gauges installed on section A-A (e5 to e8 in Figure 4.56), as they are designed to monitor strain in the direction of the specimen's axis, the sum of torsional actions to flexural ones may have an effect in anticipating the ultimate failure.

[40] As the bending tests procedure was designed to perform two consecutive load ramps, thus including two loading "plateaus" where the load is held constant, individual values shown in Table 4.9 for specimens A1 to C3 have been computed as the averages between interpolations on both plateaus.

some uniquely unexpected results (e.g. stage III for specimen B2), values of the average rise over the cross-sectional height show remarkable consistency over different specimens.

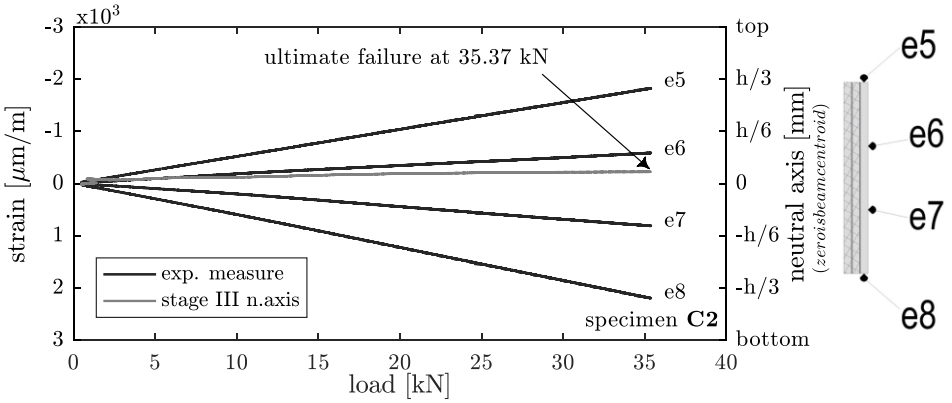

Figure 4.57 - neutral axis evolution for specimen C2 in test IV-1

Table 4.9 - neutral axis rise for bending tests

stage	height of the interpolated neutral axis over the cross-section centroid [mm]								average rise over height [%]		
	A1	A2	B1	B2	B3	C1	C2	C3	A	B	C
I	0,99	0,31	1,24	1,03	1,07	1,50	0,90	1,11	0,36	0,39	0,41
II	3,59	2,00	3,48	3,1	3,38	3,11	3,00	3,32	1,55	1,18	1,12
III	7,54	6,68	14,8	2,81	8,57	10,16	6,91	8,73	3,95	3,11	3,07

4.3.3.3 FULLY DAMAGED LG

Except for specimen B2, which was brought to ultimate failure with a bending test, failure of the last glass ply was always induced with a sharp edge[41]. Also, To avoid major viscous effects and cope with the significantly larger deformations expected, FDLG bending tests were carried out at a higher speed compared to ULG and PDLG tests (0.1 mm/s compared to 0.01 mm/s).

Depending from logistical operations[42], bending tests IV-3 on FDLG specimens were performed about one hour after the failure of the last ply[43].

Experimental evidence shows good consistency among similar specimens, with SG-laminated beams (Type A) substantially stiffer than both DG41- and *reinforced* DG41-laminated ones. The introduction of a thin PC in Type C specimens allowed for significantly higher values of the load bearing capacity, compared to DG41 alone. The vertical axis in Figure 4.58 shows values of the mid-span bending moment $M_{n,m}$, normalized by the total interlayer thickness t and accounting for the dead weight of the specimen:

[41] This choice was motivated by the attempt to test "undisturbed" FDLG specimens in the next phase. Hence, a locally induced failure was preferred to a violent bending one, which was thought to influence the FDLG specimens with different crack patterns and/or a pre-stress in the interlayers.

[42] Operations included the installation of omega transducers, removal of strain-gauges cables and full instruments check.

[43] To prevent self-weight from inducing significant viscous deformations before the start of the data acquisition, specimens were provisionally supported on three points at L/4, L/2 and 3/4L with wooden wedges. Wedges were removed moments before the start of the tests.

$$M_{n,m}(\eta_m) = \frac{1}{t}\left[M_m^{Pm}(\eta_m) + M_m^d\right]$$

$$M_m^{Pm}(\eta_m) = \frac{P_m(\eta_m)L}{4}; \qquad M_{n,m}^d = \frac{MgL}{8}$$

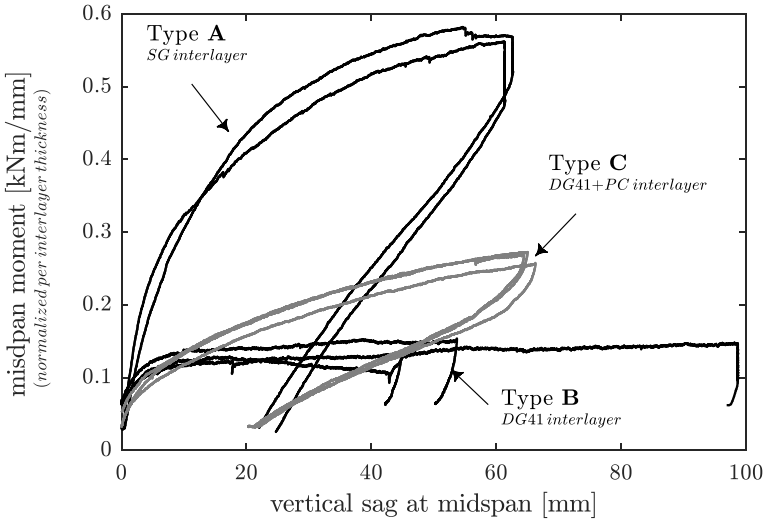

Figure 4.58 - normalized moment over midspan sag for all specimens

where M is the total mass of the specimen (glass plies + interlayers), g is the standard gravity, L is the total span and η_m the measured sag at midspan.

Ageing effects on SG-laminated specimens are shown in Figure 4.59 with a comparison among tests IV-3 and IV-4 (cfr. Table 4.7 p.101). On specimen A1, the IV-3 test has been repeated twice, to assess that the maximum load applied at midspan during the first ramp (2.5 kN) was not yet significantly affecting the mechanical properties of the fractured-glass-interlayer composite. Tests IV-4 were performed on the same specimens, after a five-month storage interval at indoor ambient temperature (20-25 °C) and RH.

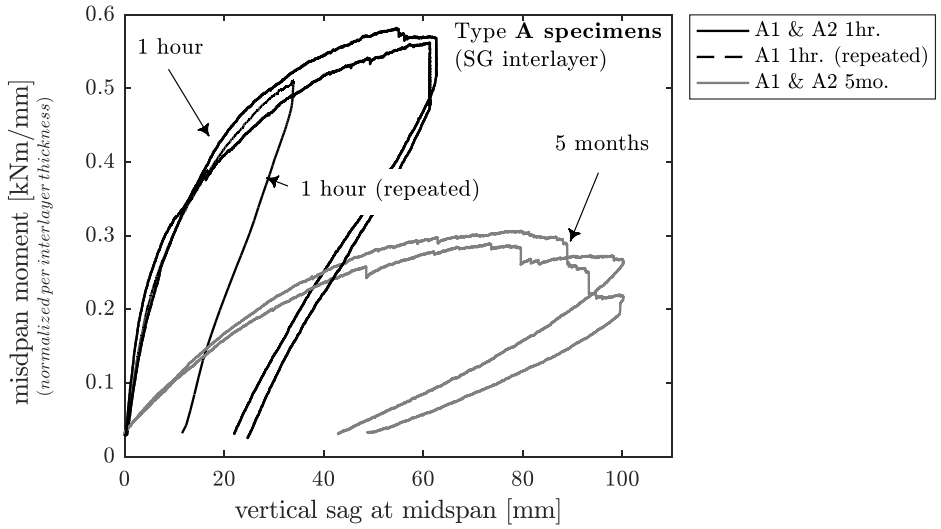

Figure 4.59 - ageing effects for FDLG specimens for bending tests

Omega transducers data were used to compute average strain on top and bottom of the specimens (cfr. Figure 4.44, Figure 4.45 and Figure 4.46 p.99-101). Figure 4.60 shows data for the specimen B2: measured strains on both sides of the mid-span section allow for interpolating the likely position of the neutral axis, with the average value yielding the final best estimate.

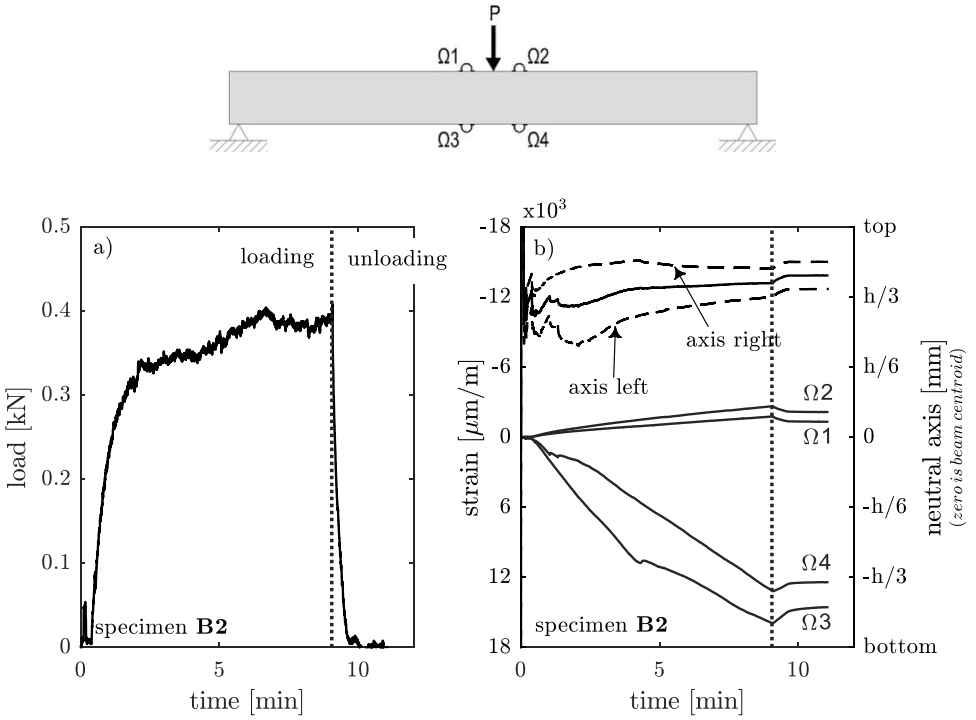

Figure 4.60 - neutral axis interpolation over FDLG bending tests

Figure 4.61 shows final results for all specimens. A clear majority of the cross-section is consistently below the neutral axis, bearing tensile stresses. The translation equilibrium along the direction of the axis is provided through a smaller portion of the cross-section near the top of the beam, whose depth appears to be approximately 10% of the total height.

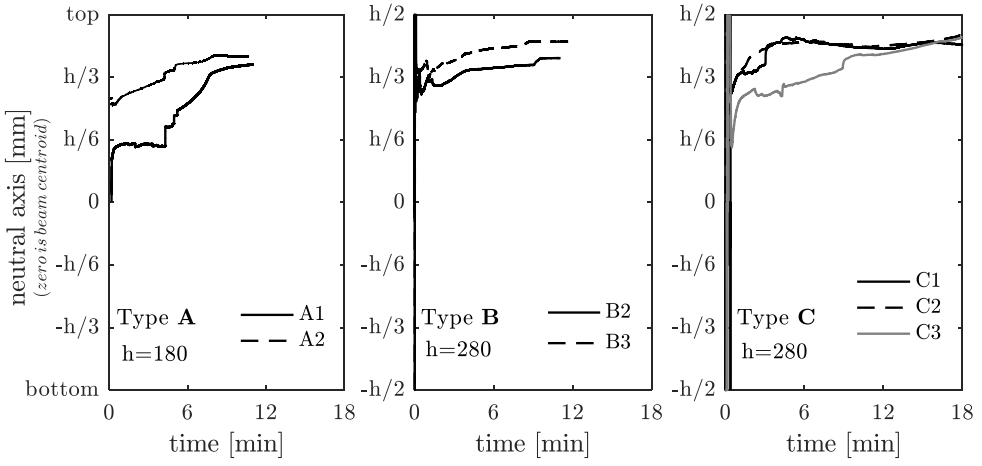

Figure 4.61 - evolution of the depth of the neutral axis in all FDLG specimens[44]

Dynamic response tests IV-2 on FDLG specimens were performed similarly to previously described ones on ULG and PDLG. Table 4.10 presents a conclusive synthesis of all measured peaks in the response spectra, corresponding to the first vertical vibration mode for each specimen.

[44] Data for specimen B1 is not shown, as laboratory observations proved that omega transducers did not work properly during that specific test.

Table 4.10 - experimental natural frequencies [Hz]

specimen	ULG	PDLG		FDLG
	Stage I	Stage II	Stage III	Stage IV
A1	71.92	65.74	50.08	23.53
A2	72.95	66.77	51.33	26.47
B1	77.76	72.95	55.89	18.97
B2	81.71	74.87	55.36	23.27
B3	80.99	74.83	54.41	20.76
C1	80.50	74.15	53.17	16.78
C2	80.69	75.06	50.61	18.55
C3	80.68	74.01	49.13	18.02

After the conclusion of tests, Type A specimens were stored for five months inside the laboratory, in a protected environment, and cut later to extract the smaller material specimens described in §4.3.4. On the other hand, FDLG specimens Type B & C have been stored outside the laboratory after the last bending tests, under natural environmental conditions[45]. After six months, a remarkable difference in the long-term effect was observed (Figure 4.62): all specimens were supported on multiple points with bricks (4 or 5), while Type B laminates had completely lost the original shape, the polycarbonate reinforcements in Type C specimens allowed them to hold their original shape. Moreover, the limited deformation of the latter also reduced penetration of moisture and rainfall inside cracks, allowing for a significantly higher adhesion of fragments[46].

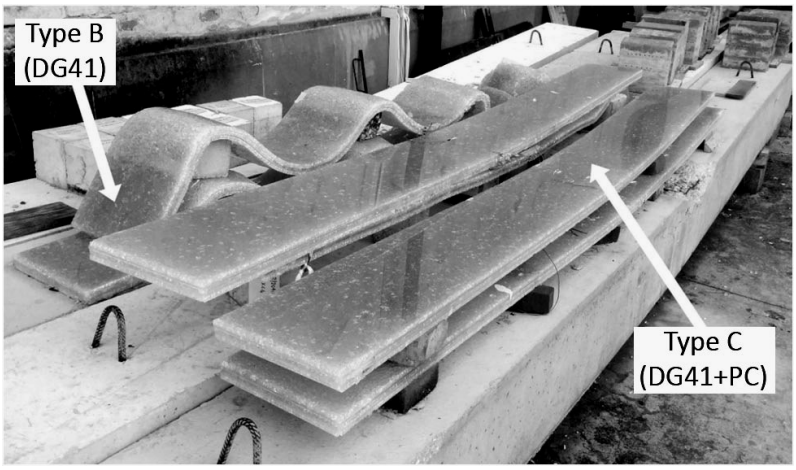

Figure 4.62 - long-term weathering effects on FDLG

4.3.4 UNIAXIAL TESTS ON FULLY DAMAGED LG SPECIMENS

To investigate mechanical properties of the composite material made by interlayers and glass fragments, after tests in Table 4.7, type A specimens portions were cut out from lateral regions of the beams (Figure 4.63). Lateral regions were chosen having been less affected by bending-induced effects in FDLG beam tests. Specimens were prepared for uniaxial tensile and compression tests (Figure 4.64).

[45] About 2-4 hours of sun exposure per day, moderate exposure to wind and moisture, seasonal precipitations and icing, with temperatures ranging approximately between -5 °C and 40 °C.

[46] While fragments of Type B specimens could be removed with little effort, just rubbing a hand over the beams, fragments of Type C beams were still firmly adherent to the interlayer and could not be easily torn apart.

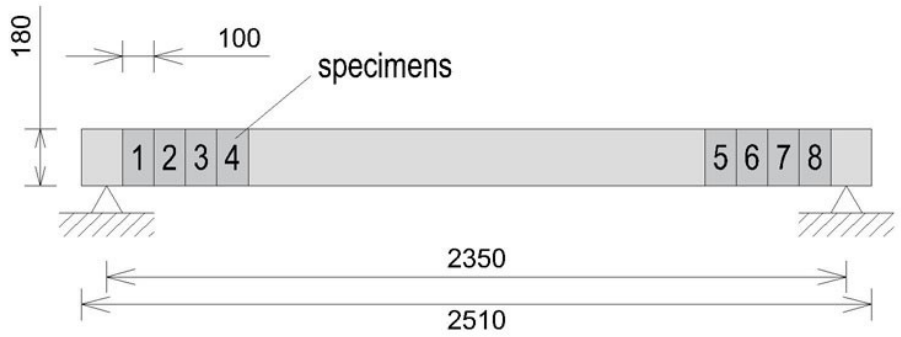

Figure 4.63 - specimens extracted for tensile and compression tests on the fractured-glass-interlayer composite material

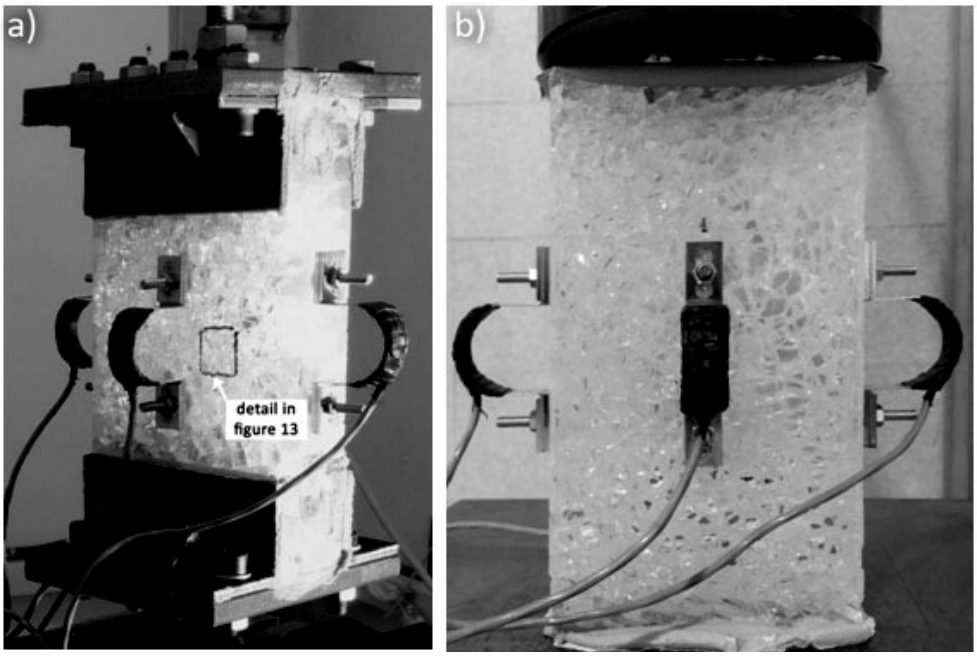

Figure 4.64 - setup for a) tensile and b) compression tests on material specimens

To preserve the integrity of the measuring instruments, tensile tests were initially performed up to relatively small strain extents[47]; this choice allowed for repeated tests on the same specimens, to gradually investigate the damage progression up to slightly higher strain values (~10%). Moreover, two different strain rates were tested: $5 \cdot 10^{-5}\ s^{-1}$ (slow) and $5 \cdot 10^{-4}\ s^{-1}$ (fast), respectively.

Figure 4.65 shows experimental curves of tensile tests on material specimens. Stresses were calculated assuming that the cross-section reduces to only the two ionoplast interlayers. Similarly to observations in §4.1.2, experimental evidence highlighted once again how the loading rate is an important parameter: the faster the strain rate, the higher the stress peak. In addition, for strain cycling multiple times between zero and $\varepsilon = 0.04$ appears not to give a major decay on the stress peak and only a minor one for the elastic modulus, slightly lowering the initial stiffness of this composite material.

[47] about 4%, which is small compared to the full elongation potential of the interlayer material itself, which is about 350% as previously shown in Figure 4.4 §4.1.2.

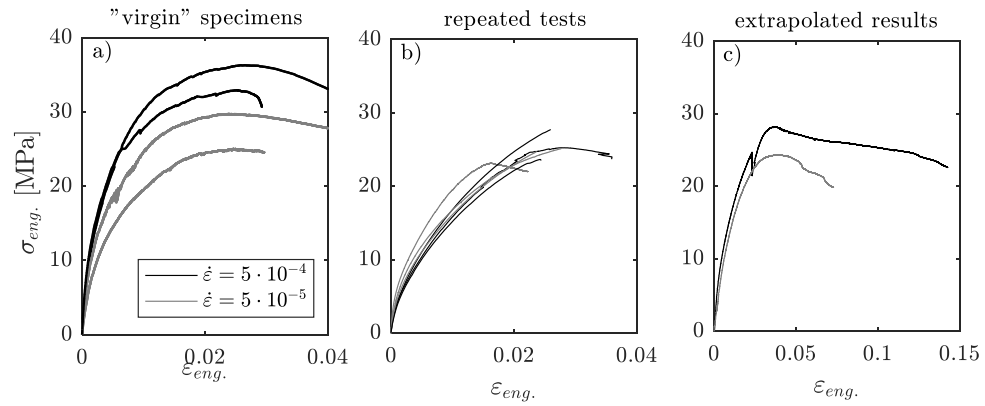

Figure 4.65 - experimental curves of tensile tests on material specimens

When the adhesion bond is compromised, the interface had been observed to produce a slightly different gleam with reduced transparency; a contrast which can been be further incremented with post-processing photography. Aiming to capture the debonding progression of the glass-interlayer interface, a photographic follow-up was performed. The setup was put in place during one of the "slow" tensile tests on the composite FDLG material, similarly to the one described in §4.1.2 for SG interlayers only.

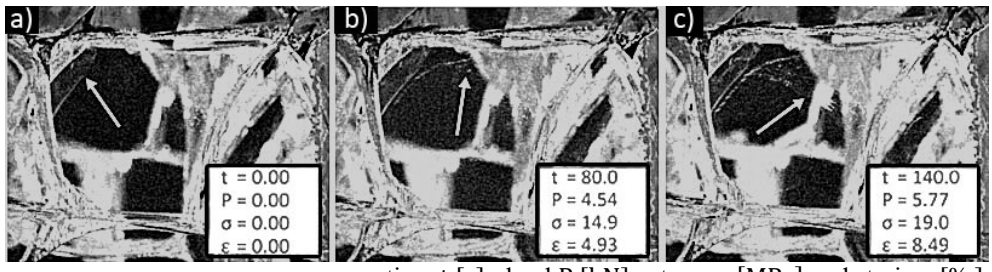

time t [s] , load P [kN] , stress σ [MPa] and strain ε [‰]

Figure 4.66 – delamination observed from tensile tests photographic follow-up

Figure 4.66.a shows that a small initial debonding is already present in the specimen, even before the start of the test. On the specific fragment selected for the analysis, the area interested by the loss of adhesion bond started to expand rapidly even at low strains, about 5‰ as shown in Figure 4.66.b, and affected about 40% of the total interface around $\varepsilon = 8.5‰$. From there on, debonding on the selected fragment was stable up to the end of tests.

Compression tests on FDLG material samples were also performed by imposing a controlled displacement generating a strain rate of $5 \cdot 10^{-5} s^{-1}$. Tests were carried out to the ultimate failure of the samples, resulting in a violent destructive procedure[48] which didn't allow for repeated tests, as it was instead for tensile ones. Figure 4.67 shows the results of experimental compression tests: the mean stress shown in the vertical axis is calculated on the total cross-sectional area, composed by the two layers of SG and adherent glass fragments[49].

[48] Final collapse happened with as a sudden explosion of the FDLG material specimens. The explosion instantly and violently scattered a large number of glass fragments out of the specimens body, reducing the load bearing capacity to a fraction of the one measured before the collapse.

[49] Glass fragments alone are unable to bear any tensile actions. Therefore, assuming that tensile stresses are concentrated in the interlayer seems a rather logical choice. On the other hand, glass

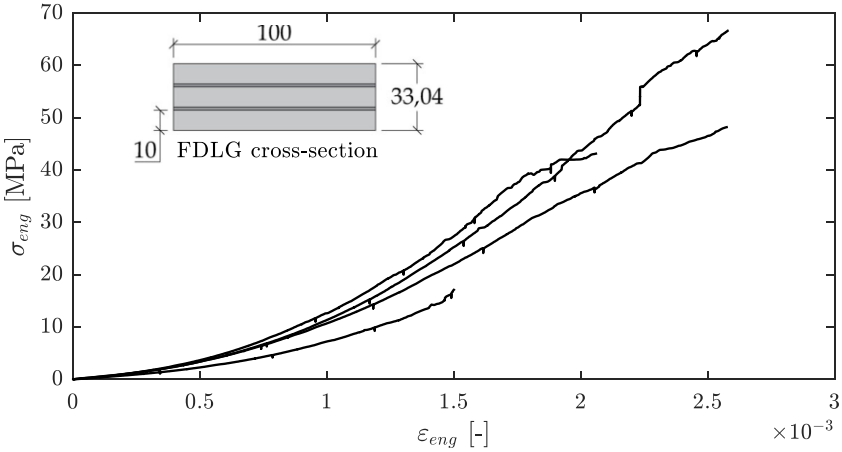

Figure 4.67 - experimental curves of compressive tests on material specimens

This composite FDLG material displayed a remarkable compressive hardening behaviour: experimental curves are characterized by an initial non-linear branch, followed by a distinctively more linear one.

A numerical overview of FDLG properties of in tensile and compressive tests presented in Table 4.11.

Table 4.11 – tensile and compressive properties of FDLG[50]

Tensile tests (calculated on the interlayer cross-section alone)		
Secant modulus at 5 MPa	E_0	$15 \div 18\ GPa$
Yielding stress	σ_y	$25 \div 36\ MPa^{\dagger}$
Yielding strain	ε_y	$0.02 \div 0.03$
Long term stress asymptote	σ_a	$19 \div 22\ MPa$
Compression tests (calculated on the total FDLG cross-section)		
Secant modulus at 2.5 MPa	E_0	$20 \div 27\ GPa$
Ultimate stress	σ_u	$15 \div 70\ MPa$
Ultimate strain	ε_u	$0.002 \div 0.003$

† *higher value for higher strain rate*

fragments are able to bear very significant compressive actions by exchanging contact forces one another. Anyhow, the mechanic response measured during compressive tests on FDLG is greatly influenced by the presence of interlayers to which the fragments adhere to. Without the interlayers contribution, fragments would be unable to provide the same response on their own. With that in mind and for sake of simplicity, an equivalent stress could be calculated on the interlayer surface alone, similarly to tensile rests. Such a radical choice can be motivated by the ultimate goal to provide a simple, macroscopic, overview of this composite material performance. This approach is used in the following to model the stress distribution along the cross section of the beams in the bending tests described in the previous paragraphs.

[50] Experimental values are given for a three-layered LG arrangement, assembled with two 1.52 mm thick SG interlayers and 10 mm thick glass plies. It is likely that different arrangements may yield different experimental values for similar tests, although the order of magnitude is not expected to vary dramatically.

5 CRITICAL ANALYSIS AND DISCUSSION

The scientific community has yet to agree on reliable predicting models for LG. Due to many factors involved, experimental tests and empirical models are to this day the main toolkit at a designing engineer's belt. Results gathered within previous investigations are now examined in depth, aiming to share more light on the subject.

Experimental tests in Chapter 4 have been divided into three parts. From a thematic point of view, long-term viscoelastic properties and short-term tensile response tests deal about interlayer properties alone, with limited interest on the mechanics of LG composites. On the other hand, tests on structural LG beams bypass the investigation on the intrinsic behaviour of interlayer, aiming instead to a better understanding on the full-scale, post-failure performance.

In the following, topics will be conveniently united based on a thematic point of view: a first part is dedicated to interlayer mechanics, merging the results described in paragraphs §4.1 and §4.2, while the last part dedicated to analyses on full-scale LG introduced in §4.3 and post-failure effects.

5.1 INTERLAYER PROPERTIES

Short-term tensile results are more suited to model effects such as impact loading, blasts and generally any effect which takes place over a short amount of time (i.e. seconds, minutes); those interlayer properties are discussed in the following paragraphs. On the other hand, results and models provided for long-term properties of interlayers are the core of the research and essential for the design of LG elements; these are dealt with in §5.1.2.

5.1.1 SHORT-TERM PROPERTIES OF INTERLAYERS

Tests carried in out in §4.1 yielded a vast amount of data on tensile properties of three among the most commonly used interlayer materials: PVB, SG and DG41. Existing standard guidelines have been followed when possible and some early results have already been discussed accordingly (cfr. §4.1 and sub-paragraphs).

In the following, an in-depth analysis of those results is carried out, a discussion articulated around the experimental outcomes, with an eye on the state-of-the-art research and the regulations in force. *True* stress-strain diagrams are produced by interpreting the numerical results and the photographic follow-ups presented (cfr. §4.1.2). Hyperelastic models are then calibrated and discussed for the supposedly reversible network entanglement effects. Together with a novel interpretation of the intermolecular cross-links response, those hyperelastic models are used to yield a final decomposition according to the theory proposed by Haward and Thackeray [76]. Finally, a discussion on the yielding (or "*pseudo-yielding*") point for different thermoplastics is undertaken, concluding with the proposal of a more universal approach to the problem.

5.1.1.1 TRUE STRESS-STRAIN DIAGRAMS

Soft and semi-rigid thermoplastics are known to be quasi-incompressible [280], so much that it is common for FE LG design to disregard *de facto* the compressibility of interlayers [62,185]. The Poisson ratio for soft polymers is very close to its theoretical limit value of 0.5. On the other hand, semi-rigid thermoplastics are yield ratio values as low as 0.44 for short-term actions at temperatures around 0°C[1]. Values of the Poisson ratio for climatic conditions corresponding to those for tensile tests (cfr. §4.1) on the three investigated materials are shown in Table 5.1.

True strain is defined as $\varepsilon = \ln(1 + \varepsilon_{eng.})$ [164]. While for materials with homogeneous deformations[2] such as PVB this equation can be applied in a straightforward way, the onset of significant localized necking in SG and DG41 asks for an in-depth analysis of strain concentrations.

Table 5.1 – 1h Poisson ratio for interlayers at 23°C/50%RH

SG	DG41	PVB
0,465*	0.476†	0,470‡

* 2014, Kuraray, unspecified ASTM standard (www.kuraray.com)

† 2014, Saflex, according to ASTM D638 [66] (www.saflex.com)

‡ 2003, DuPont, unspecified technique at "ambient temperature" (www.dupont.com) confirmed by several researchers [281]

By looking at the time-lapse photographic recordings described in §4.1.2, some insight could be obtained on the influence of necking for SG specimens. Because the width of the reference lines is influenced by the elongation, an automated photogrammetric analysis could not be successfully implemented. Nonetheless, digital images could be manually analysed to extract average longitudinal engineering strain within each segment -*i* in the investigated area (Figure 4.35):

$$\varepsilon_{eng,i} = \frac{L_i - L_{0,i}}{L_{0,i}}$$

where L_i and $L_{0,i}$ are the length of the segment during tests and its initial length respectively. Figure 5.1 compares the strain readings from the testing device, calculated as the average among the measure points in Figure 4.9, to photogrammetric strain measurements resulting from the time-lapse. Results show that the relative error in the early part is (i.e. for small average strain) in very significant, while it seems to be consistently under 5% after the engineering stress curve crosses once again the *pseudo-yielding* threshold (cfr. §). Complete results are in Appendix E.

The maximum strain obtained by photogrammetric measurements is the best estimate of the maximum strain within the body region. Although those measurements still represent a local average, one which could be improved with more tightly-packed marks (cfr. Figure 4.9 p.71), if this local average is a good estimation of the effective punctual elongation, *true* strain has been computed accordingly.

[1] As a general rule of thumb, the value of the Poisson's ratio for polymers is known to be is positively correlated with time and temperature [240] (i.e. the lower the temperature and/or elapsed time, the lower the ratio). Greatest variations are observed across the glass transition temperature.

[2] where it can be assumed that in the narrow area average and maximum strain are consistent.

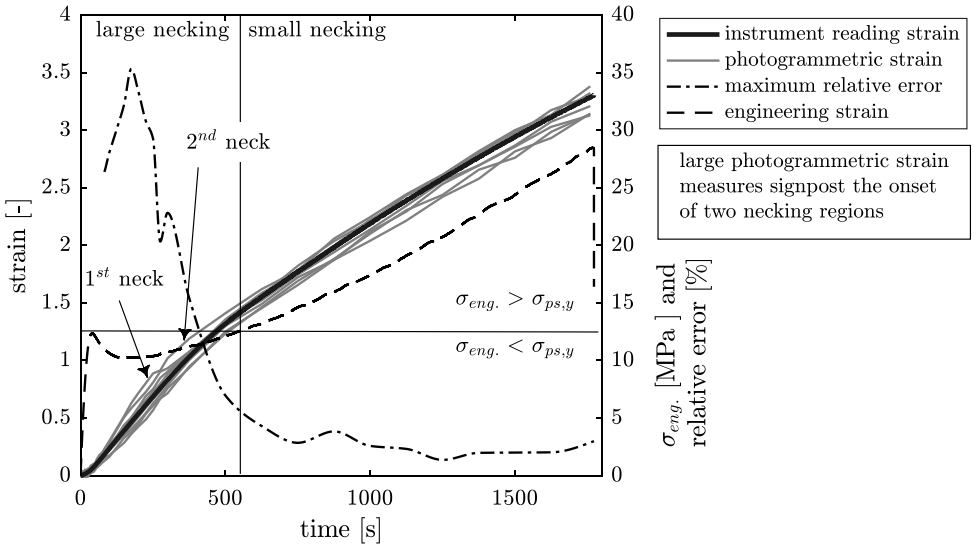

Figure 5.1 – photogrammetric strain analysis (SG at $v = 5mm/min$)

If the Poisson ratio for the three materials is consistent over large deformations [3] with the values given in Table 5.1, knowing the applied load $P(\varepsilon)$ as a function of the *true* strain ε, *true* stress $\sigma(\varepsilon)$ can now be calculated over the reduced cross-sectional area A_r [4].:

$$\sigma(\varepsilon) = \frac{P}{A_r} \quad ; \quad A_r = A_0(1+\varepsilon)^{-2\upsilon}$$

Results in Figure 5.2 show how formerly observed softening regions in SG and DG41 were ascribable to the engineering representation of the curves, while true stress-strain diagrams exhibit a consistent hardening response.

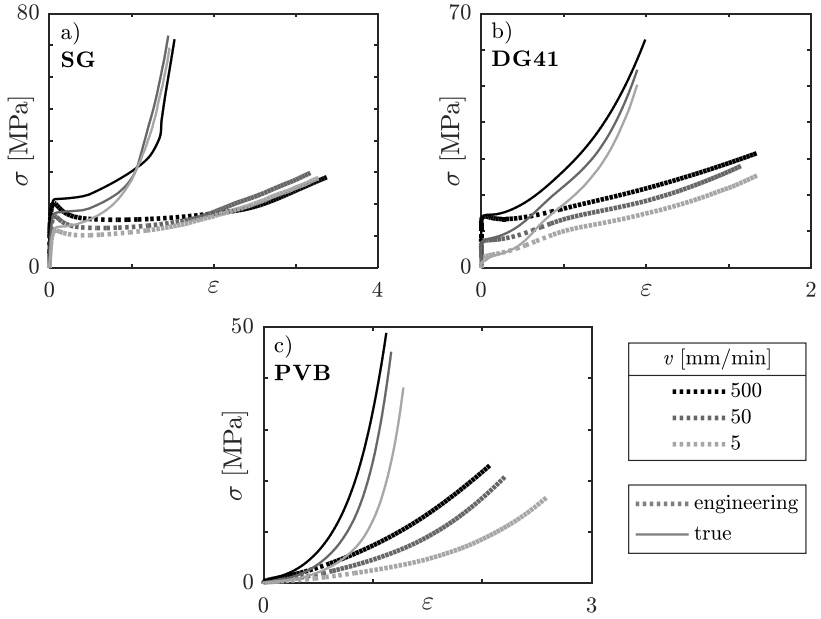

Figure 5.2 - true stress-strain diagrams compared to engineering

[3] cfr. footnote 8 page 86.

[4] If considering interlayers as incompressible materials (i.e. $\upsilon = 0.5$) is an acceptable approximation, the formula simplifies into $A_r(\varepsilon) = A_0/(1+\varepsilon)$.

5.1.1.2 A GENERAL MODEL FOR THE INTRINSIC RESPONSE

The creation of constitutive models for thermoplastics has always presented numerous challenges due to numerous effects involved [114]:

- the quasi-incompressible high deformability,
- onset of viscoelastic decay which principally affects tests carried out at a lower speed rate,
- difficulties in modelling softening effects,
- high dependency from load/strain rate and temperature.

Despite this fundamental complexity, the use of phenomenological hyperelastic models (cfr. §3.1.2) has become common practice for the description of uniaxial tests, with better results obtained for elastomeric or thermoplastics materials which do not exhibit either significant softening behaviour nor a high initial stiffness [16,222,230,282] (cfr. §1.1.2).

The hyperelastic material reaction is believed to be connected to the reversible *network response* of the polymer matrix [7,155]: long and reciprocally entangled chains of molecules, form a deformable network (Figure 1.8.a). When an external action is applied, the network allows the molecules to stretch, but doesn't allow for changes in reciprocal positions. With this interpretation, the higher the strain, the higher the influence of the hyperelastic response [7,78]. On the other hand, the reaction of cross-linked polymers hinges on chemical interactions among molecules: the *intermolecular response* relies on the strength of the chemical bonds, a property which has been shown to be largely dependent on the temperature [283].

The network entanglement effect has been proven to be well represented by a wide array of both compressible and incompressible hyperelastic models[5]. Nonetheless, if the material has a strongly cross-linked structure, these models seem to lack the ability to characterize the initial part of the response [237]. While several theories have been advanced, to this day there seems to be no general agreement for modelling this effect [51,151], which is arguably critical for most engineering applications. Delincé said in [7]:

> *"[…] the non-linear response and the presence of a yield point followed by strain softening in the small strain range are associated to breakage of secondary bonds and segmental movements […], the large strain deformation is rather due to conformational changes of the molecular chains, involving stretching and orientation of the coils and leading to strain hardening."*

The analysis carried out in §5.1.1.1 showed that the "strain softening" mentioned by Delincé can be a deceptive property, only observable when neglecting the true stress-strain path in favour of the engineering one. Rather than actual softening, the flattening of SG and DG41 true stress-strain curves after the "yielding point" in Figure 5.2 shows that the response reaches a sort of transient plateau[6]. Accepting the decomposition by Haward and Thackeray [76] (cfr. §1.1.2), this quasi-constant stress lasts until the network entanglement finally kicks in at higher strain.

---

[5] For instance, a neo-Hookean model has been used in [156] for studying true-stress strain curves of a compressible thermoplastic material, while engineering stress-strain relations on incompressible polymers have been studied by several other authors using various models [222,226,230,234,282].

[6] for approximately $0.1 < \varepsilon < 0.5$ in SG and $0.1 < \varepsilon < 0.3$ in DG41 tests (Figure 5.3).

Experimental tensile tests results[7] (cfr. §4.1.2) have been compared with several known hyperelastic models[8] (cfr. §3.1.2); while most among those could reliably describe the shape of the engineering stress-strain curve for PVB, fitting the results for both DG41 and SG proved to be a more challenging task.

Table 5.2 displays the different accuracy of four among the most commonly used HE models to fit experimental results. The Yeoh model proved to be the simpler among the two most reliable ones. Figure 5.3 shows final results for Yeoh incompressible model with coefficients in Table 5.3.

Table 5.2 – accuracy of hyperelastic models for first and final parts of the curves

Model	Number of coefficients	experimental data fit efficacy					
		SG		DG41		PVB	
		first	final	first	final	first	final
Neo-Hookean	1	C	C	C	C	B	C
Mooney-Rivlin	2	C	B	C	A	B	A
Yeoh	3	C	A	C	A	A	A
Ogden (N=3)	6	C	A	C	A	A	A

A: good (average relative error lower than10%) - B: average (average relative error between 10 and 90%) - C: limited or very limited (average relative error greater than 100%)

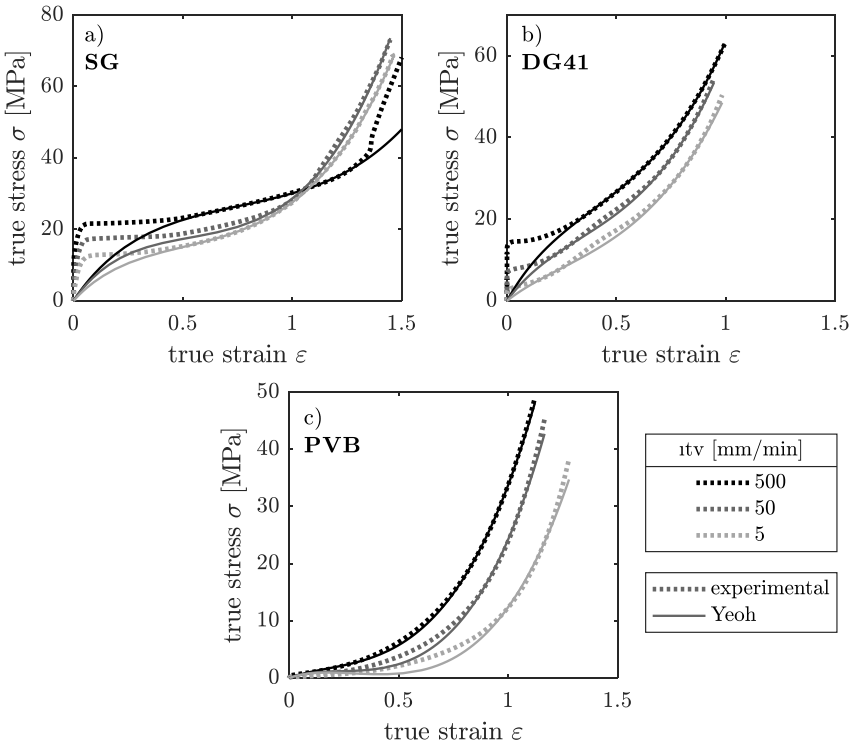

Figure 5.3 - hyperelastic models for a) SG, b) DG41 and c) PVB

[7] Even though the engineering application and modelling are the ultimate focuses of this manuscript, for the following analyses the true stress-strain curves have been preferred to engineering ones (cfr. §5.1.1.1). True response diagrams are believed to be more suited for understanding the microscopical origins of the experimentally measured macroscopic effects. Furthermore, one can always go back easily to the engineering curves knowing the true correlations, while the opposite is generally harder as it requires additional data.

[8] The following models have been used during the analysis: Neo-Hookean (1943) [348], Mooney-Rivlin (1951) [231,235], Ogden (1972) [236] and Yeoh (1990) [349].

Fitting of functions in Figure 4.4 was performed with an iterative least-squares regression, whose base has been chosen according to two principles: the hyperelastic functions must provide a *safe* estimate of the experimental data (i.e. hyperelastic models are only allowed to underestimate the material response) and curves able to reliably describe the final part of the experimental data are preferred to those which can model the initial one[9].

Table 5.3 - coefficients for hyperelastic Yeoh model

material	test speed v $[mm/min]$	Yeoh coefficients		
		C_1	C_2	C_3
SG	500	8.59	-0.12	0.13
	50	8.18	0.89	0.29
	5	7.88	0.84	0.21
DG41	500	18.18	2.50	0.37
	50	17.21	2.91	0.38
	5	14.38	2.46	0.26
PVB	500	9.64	2.47	0.26
	50	6.92	2.28	0.28
	5	3.53	1.41	0.21

Yeoh models results shown in Figure 4.4.c for PVB tested at various strain rates, highlight some of the intrinsic limits this model in fitting any given experimentally determined data (Figure 5.3c). It is worth noting at this point that simpler – and less popular - HE models have been successfully used in the recent past. For instance, Lenci and Clementi in 2014 [284] adopted an incomplete cubic equation such as $\sigma = a\varepsilon + b\varepsilon^3$ for modelling the HE properties of PVB, with coefficients a and b calibrated by Ivanov et al. [285]. In the following analyses, a new calibration of this model will be preferred to the more complex - yet still limited – Yeoh one.

After studying results by Klompen and Delincé [7,156] (cfr. §2.2.1), attempting a wider generalization to all thermoplastic materials, a new empirical decomposition method is proposed. Drawing from the HT decomposition [76] (cfr. §1.1.2), the intrinsic response σ is addictively decomposed in the sum of intermolecular σ_s and network effects σ_r, both dependent on several factors:

$$\sigma(\varepsilon, \dot{\varepsilon}, T, S) = \sigma_s(\varepsilon, \dot{\varepsilon}, T, S) + \sigma_r(\varepsilon, \dot{\varepsilon}, T)$$

with strain and strain rate ε and $\dot{\varepsilon}$, temperature T and thermo-mechanical history parameter S. While the results discussed in this paragraph are obtained in controlled and consistent climatic conditions, for the known dependency of thermoplastics on the temperature T, it seem safe to assume this may be a relevant parameter for both σ_s and σ_r. The dependency on thermomechanically-reversible aging effects is believed to be related to variations in density of intermolecular actions and has not been proven to influence poorly cross-linked polymers [156]. The proposed decomposition aims to separate reversible effects from permanent changes. Consistently with the above-mentioned studies, the following hypotheses are made:

1. large strain effects are governed mostly by the network response and short-range deformations primarily refer to intermolecular effects,
2. conformational changes of the network are fully-reversible,
3. the break of intermolecular bonds is responsible for non-reversible effects.

[9] This choice is consistent with the fundamental interpretation of the hyperelastic effect, expecting a greater influence the network response for high strains [10,14].

Looking at the experimental results of true stress-strain diagrams in Figure 4.3, one can observe that the two significantly cross-linked polymers, SG and DG41, exhibit an initial response step which appears to be dependent on the strain rate. Following both the HT and KD approaches, one can assume that, on a true stress over strain diagram, intermolecular interactions will drive most of the initial material response. Moreover, conclusions and models proposed by KD suggest that intermolecular interactions may produce a steady response over time (the so called *rejuvenated yield stress* $\sigma_{rej,0}$ cfr. Figure 2.5). Having excluded the presence of softening branch in the *true* constitutive response, and considered the shape of the experimental curves, it makes sense trying to model the initial materials reaction with a non-decreasing function which tends to a finite limit. To this end, exponentially asymptotic functions as simple as $\sigma_s = A(-e^{-B\varepsilon} + 1)$ proved to be a powerful and versatile tool: by means of just two coefficients A and B needed to calibrate respectively the *amplitude* and *rate* of stress over strain functions.

Nevertheless, by further investigating the first part of the response curves, experimental results showed that SG displays a very clear and abrupt slope change, in the first part of the stress-strain diagram, as illustrated in Figure 5.4.c[10] (this phenomenon, on a smaller scale, is also visible for DG41). On the other hand, PVB only displays a single initial "load-step" before transitioning to a stress plateau with minor rising slope, as shown in Figure 5.4.b (i.e. there is no point of sudden slope change, but rather a gradual diminishing).

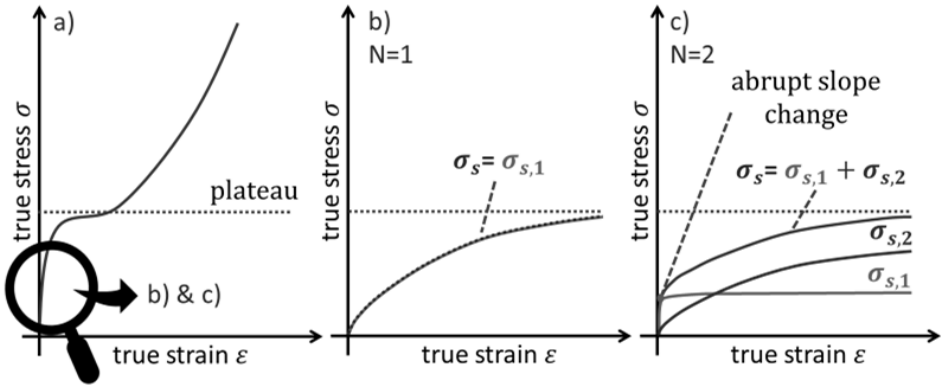

Figure 5.4 - initial response detail for very small strain

While all of this is – knowingly - speculative and still needs deeper investigations, especially on a chemical level, such phenomenon of abrupt response changes in early stages of deformation can be traced back to the presence of different chemical interactions: primary interactions, weaker but very densely packed, may be accountable for the first - very stiff - material response, limited to small stresses. Besides, stronger secondary chemical interactions, able to withstand higher stresses but concurrently scarcely distributed within the polymer matrix, are activated by larger configurational changes. Following these assumptions, the intermolecular response σ_s can be represented by a sum of N terms with $2N$ coefficients A_i, B_i [11]:

[10] It is not excluded that different materials, not included in this campaign, may show not just one but multiple abrupt slope changes along the experimental curves.

[11] Ideally, each element of the series describes the contribution of a specific homogeneous group of intermolecular bonds (cross-links). Nonetheless, the theoretical explanations regarding chemical bonds forming within the three investigated materials within the manuscript are speculative and lack the support of any chemical analysis. Future researches

$$\sigma_s = \sum \sigma_{s,i} = \sum_{i=1}^{N} A_i(-e^{-B_i\varepsilon} + 1)$$

This phenomenological model for small strain will be referred to in the following as the *intermolecular series* (IS) model.

Like in the example of Figure 5.4.b, PVB only showed *one* initial – and very limited – load step, followed by the progressive rise of the response ascribable to the network entanglement effect. While the network effect has been proved to be well represented with an hyperelastic model, the initial response can be modelled by means of one term of the IS model (Figure 5.5.c). On the other hand, the initial phases DG41 and even more so SG showed some abrupt slope change mentioned above of the curves for very small strains, as shown in Figure 5.4.c. With the proposed model, such a slope change can be represented with a larger number of terms in the series. For both materials, with only one slope change, the number of terms needed turned up to be limited to two. Table 5.4 shows coefficients A_i, B_i manually calibrated to model the experimental curves. Overall results and close-ups are shown in Figure 5.5.

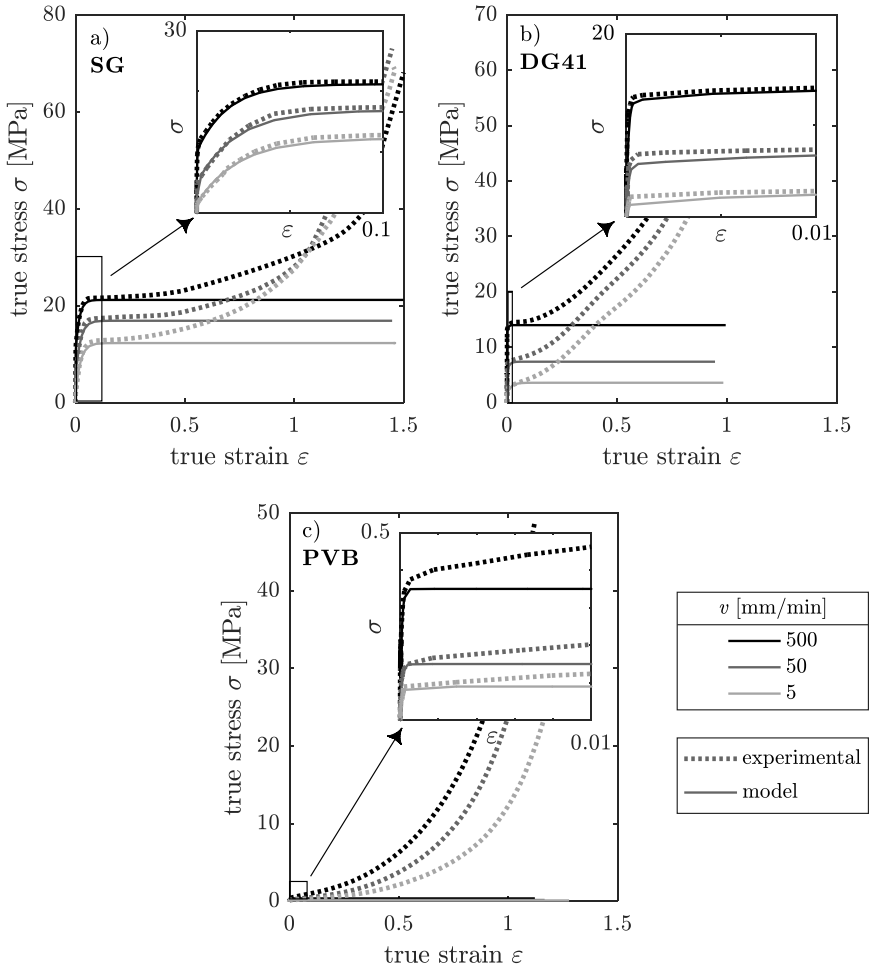

Figure 5.5 - intermolecular series model results

on this matter, either to support or refuse the proposed theories, are deeply encouraged.

With this convenient way for describing the initial response, which is assumed to be ascribable to intermolecular interactions, we are able extract by subtraction the effects of the entanglement of molecules network σ_r (dashed lines in Figure 5.6):

$$\sigma_r = \sigma - \sigma_s$$

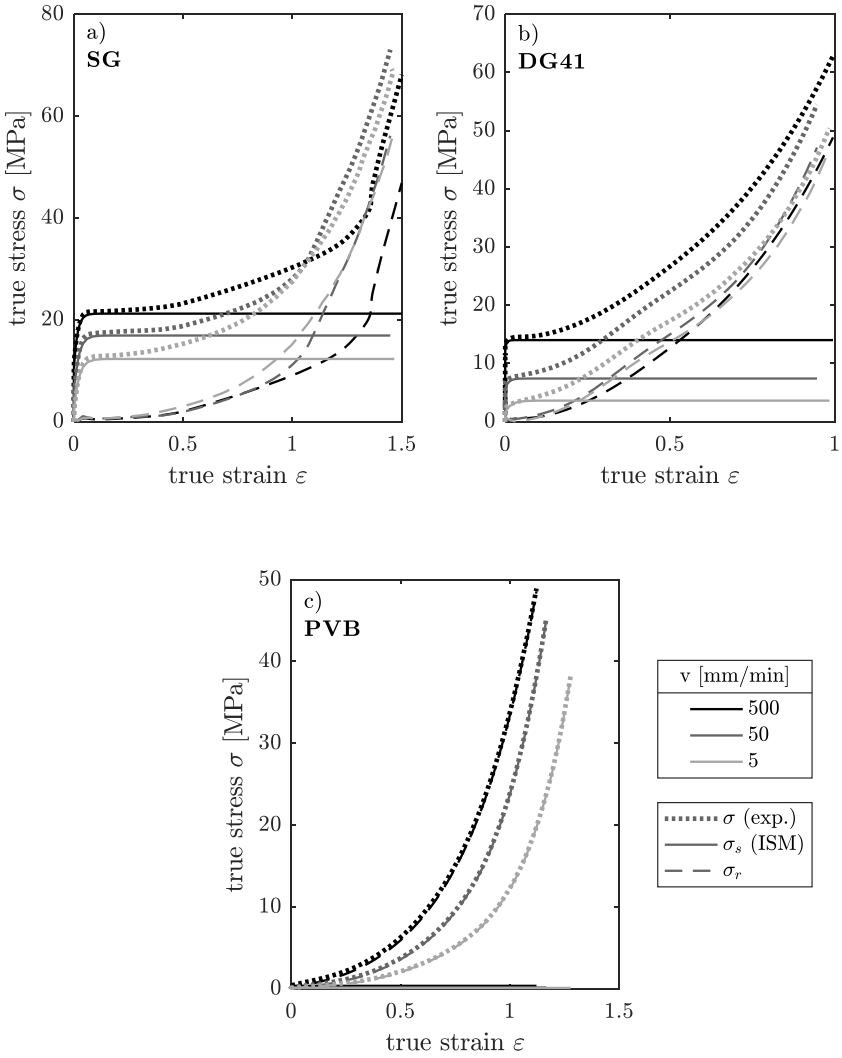

Figure 5.6 - σ_r obtained by subtraction for a) SG, b) DG41 and c) PVB

With IS model takes care of the description of the first part of experimental results, the shape of the remainders $\sigma_r(\varepsilon)$ in Figure 5.6 for the three materials suggest that all can be well represented by numerous hyperelastic models. Among all the well-known and widely used models that can have a fair shot in reproducing the shape of these curves (cfr. Table 5.2), it is worth noting that the aforementioned simple cubic equation $\sigma_r = C\varepsilon^3 + D\varepsilon$, used by Lenci and Clementi in 2014 [284] could be a simple option worth investigating, ultimately yielding to a complete description of the materials response in the form of a *generalized response* (GR) model:

$$\sigma(\varepsilon, \dot{\varepsilon}, T, S) = \sigma_s(\varepsilon, \dot{\varepsilon}, T, S) + \sigma_r(\varepsilon, \dot{\varepsilon}, T)$$

$$\sigma(\varepsilon, \dot{\varepsilon}, T, S) = \overbrace{\sum_{i=1}^{N} A_i(-e^{-B_i\varepsilon} + 1)}^{IS\ model} + \overbrace{C\varepsilon^3 + D\varepsilon}^{hyperelastic\ model}$$

Dependency from the strain rate $\dot{\varepsilon}$, temperature T and thermo-mechanical history S can be accounted for with the calibration of the coefficients A_i, B_i, C and D [12]. Coefficients C and D in Table 5.4 were obtained with a least-square regression on *true* stress-strain curves $\sigma_r(\varepsilon)$.

Table 5.4 - GR model coefficients for true stress-strain

material	test speed v $[mm/min]$	A_1	B_1	A_2	B_2	C	D
SG	500	10.1	$5.0 \cdot 10^3$	11.1	61	11.25	0.0
	50	5.9	$4.1 \cdot 10^3$	12.0	48	16.46	0.0
	5	1.5	$2.5 \cdot 10^3$	10.8	45	17.06	0.0
DG41	500	12.6	$12.6 \cdot 10^3$	1.4	210	32.99	16.42
	50	5.7	$5.7 \cdot 10^3$	1.7	95	30.79	20.59
	5	1.6	$1.6 \cdot 10^3$	2.0	55	27.83	18.69
PVB	500	0.35	$12.0 \cdot 10^3$	-	-	31.19	2.60
	50	0.15	$12.0 \cdot 10^3$	-	-	25.43	0.0
	5	0.09	$12.0 \cdot 10^3$	-	-	15.16	0.0

Inverting the equations in §5.1.1.1 allows to transform the *true* curves back to the original *engineering* representation:

$$\sigma_{eng} = (1+\varepsilon)^{-2\nu} \cdot \sigma \qquad ; \qquad \varepsilon_{eng} = e^{\varepsilon} - 1$$

Figure 5.8 and Figure 5.9 show the results using coefficients in Table 5.4. A schematic recapitulation of the process is provided in Figure 5.7.

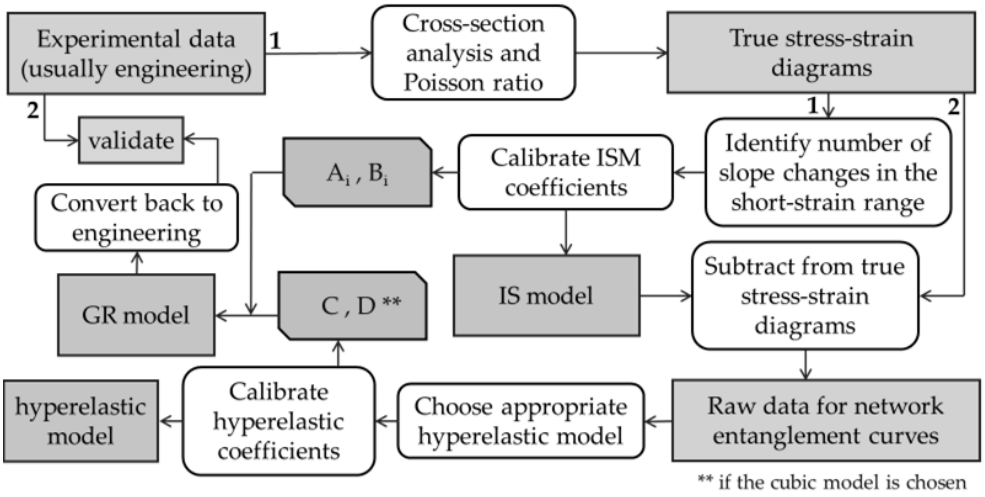

Figure 5.7 - scheme of the process used to produce the final models

[12] Comparing results in Figure 5.36.a/b/c also suggest that the hyperelastic network response may not always be significantly dependent on strain rate $\dot{\varepsilon}$. For instance, DG41 results in Figure 5.36.b show that the remainders $\sigma_r(\varepsilon)$ for different strain rates are very consistent one another. Although this might be a coincidental combination for multiple factors, this fact is worth investigating with future experiments. The only logical deduction at this stage would be not to give for granted the dependency of the model on all supposedly influential parameters.

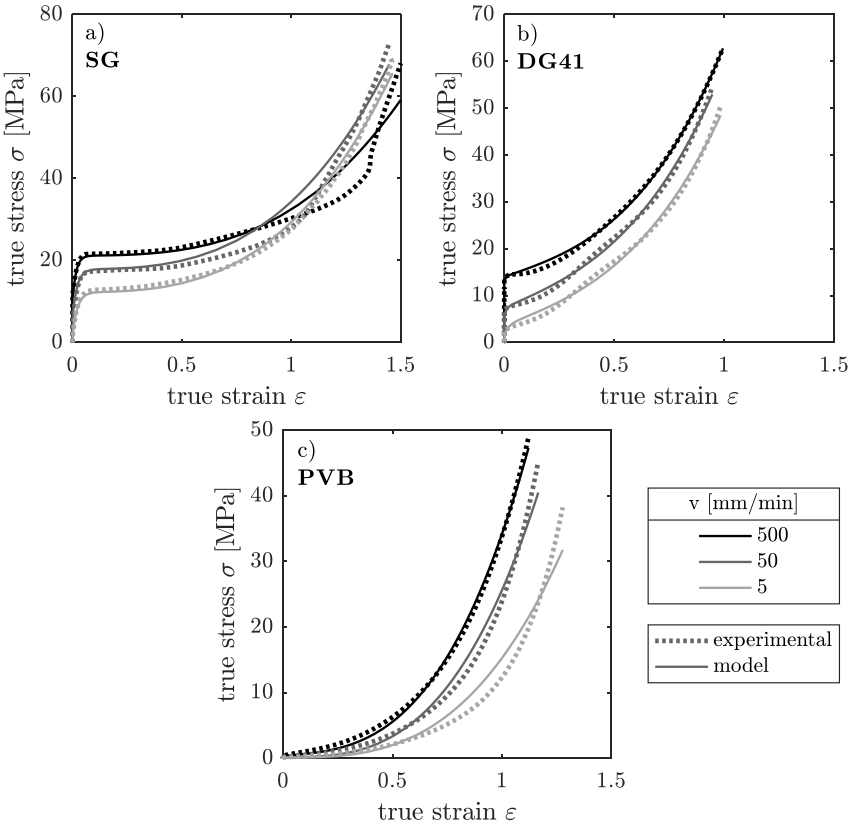

Figure 5.8 - model true stress-strain results for a) SG b) DG41 and c) PVB

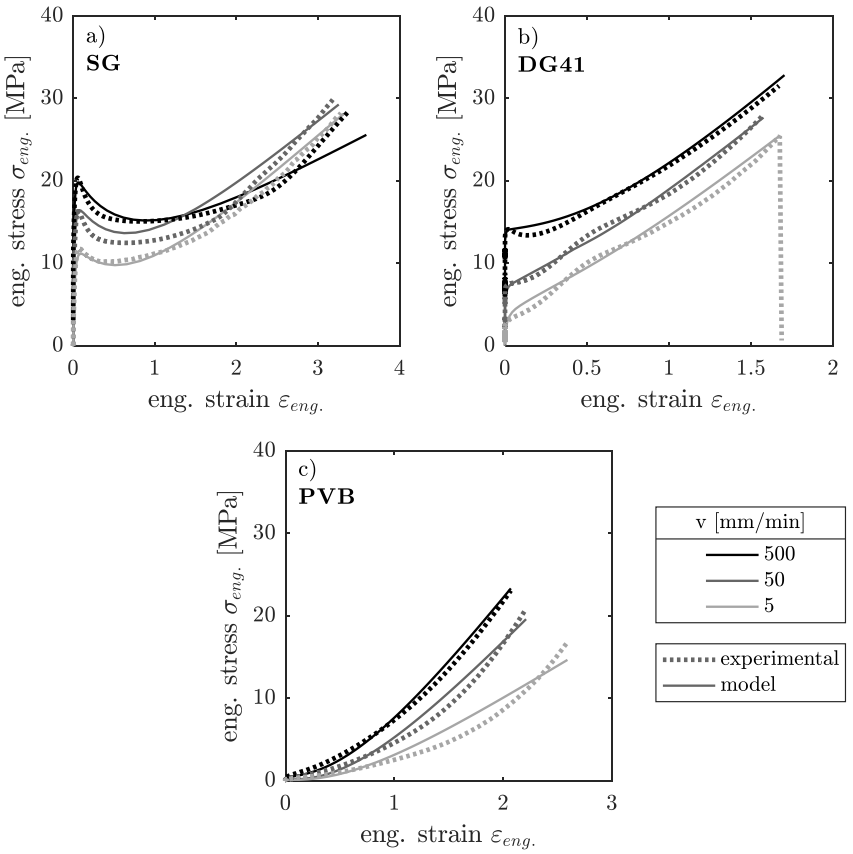

Figure 5.9 - model engineering stress-strain results for a) SG b) DG41 and c) PVB

5.1.1.3 PSEUDO YIELDING

While presenting in §4.1.2 the experimental results on interlayers tensile tests, an early remark on the poor ability of standard-proposed methods [66,264] for the determination of the tensile modulus has been raised. Within this paragraph, a critical analysis of those standardized methods is carried on, together with a few proposals to generalize the traditional approach.

Within the analyses carried out in §5.1.1.2, an observation was made on how, for very small strain ($\varepsilon < 0.5‰$), the initial response of the three investigated materials showed an extremely high stiffness. Although sometimes very brief (i.e. the response changes abruptly for slightly higher strains), this initial response turns out to be several orders of magnitude higher compared to the subsequent tangent modulus[13,14] (Figure 4.6 p.68).

This initial stiffness is likely due to the formation of chemical cross-links among the polymeric chains [59,60,78]. Generally, the higher the strength and density of chemical bonds, the higher the strain at which the material behaviour changes. When the strain is high enough, weaker bonds start to break apart with a domino effect. If no other intermolecular bonds can oppose to the increasing strain, the materials only rely on network entanglement stiffness. The presence of stronger secondary bonds in SG, able to withstand higher stresses in the medium-strain region ($0.5‰ < \varepsilon < 50‰$), can explain the different behaviour compared to PVB and DG41.

Following this interpretation, the strain-rate dependency of the results can be explained accounting for the involvement of the polymer network in distributing the stress among a large number of bonds: if the strain rate is high, molecules have less time to rearrange in a lower entropy state[15] [7], hence a greater number of intermolecular bonds can concurrently compete against the applied strain. With many chemical bonds, the energy required to trigger the domino effect is higher and therefore the macroscopic effect is an observed higher strain at which the material response changes. On the other hand, if the strain rate is small, the molecules network has more time to rearrange according to the direction of the stress: with a new arrangement, fewer bonds will be simultaneously involved in resisting to the applied external force and the stress required to win over the intermolecular interaction will be lower. This interpretation is also consistent with recent researches on adhesives time-temperature dependent tensile properties [286–288].

Moving through increasing engineering strains shown in Figure 4.4 (page 66), a topic worth studying is threshold where stress-strain curves either reach a local maximum point or change abruptly their shape, momentarily flattening along the strain axis. At first glance, this point seems much alike the *yielding point* measured in traditional elasto-plastic materials (i.e. steel and metals in general), but the theoretical extension of the very concept of yielding itself is tricky and should be approached carefully [270].

---

[13] The same phenomenological observation suggested in §5.2.2 the use of a convenient exponentially asymptotic mathematical formulation for the IS model.

[14] For very small strains, engineering and true stress-strain diagrams are almost identical; the engineering representation is chosen to match the approach used in the standards [66,264].

[15] The coil conformation in undisturbed conditions is the state of lower entropy [263].

A "yield point" for plastics is mentioned in the standards [66,264], but its very definition seems only applicable to a small subset of materials, those for whom a *local maximum [is] observed during a tensile test*[16]. This definition can be generally applied to rigid plastics (Figure 5.10.a). Nonetheless, the same standards are very often used to test semi-rigid and thermoplastic materials (cfr. §1.1.2) which to not show a peak in the curve, but only a curvature change (Figure 5.10.b) or a flat and very long plateau (Figure 5.10.c).

For engineering practice and a LG design perspective, the definition of a "yield point" for interlayers must cope with the fact that, for such thermoplastic materials, a distinction between elastic domain and permanent deformation is not only a function of stress (like it is, for instance, for metals), but several other factors come into play such as temperature, time and strain rate; playing a non-negligible role in defining the threshold from which permanent deformations are significant. For instance, permanent deformations can be produced in thermoplastics by minor stresses, in long times [65]. Therefore, the traditional definition of yield seems not straightforwardly applicable[17].

By these remarks, a pseudo-yielding stress limit $\sigma_{ps,y}$ [16,289,290] has been mentioned by several authors in the past, when talking specifically of thermoplastics and elastomers. For instance, the pseudo-yielding limit for PVB has been recently defined by X. Zhang [16] as:

"[the point] where material modulus changes abruptly"

All things considered, a different concept of yielding looks like a necessary introduction in this field. Sadly, a clear definition seems still to be missing.

Many researchers showed that thermoplastic materials can exhibit a wide array of mechanical responses to traditional tensile tests [16,114,153,154,291]. Looking at various experimental outcomes, the case system seems to be ascribable to the three typologies presented in Figure 4.35. Looking for a general tool to define this "abrupt" change in the material response, an arbitrary but simple and generally applicable criterion to identify the pseudo-yielding limit is proposed: on an engineering stress-strain curve, the pseudo-yielding limit may be defined as the point Y where the slope of the tangent line is 10% the secant modulus[18] E_t, calculated for $\varepsilon = 0.5‰$[19].

$$\frac{d}{d\varepsilon}\sigma\left(\varepsilon_{ps,y}\right) = \frac{E_t}{10} \qquad ; \qquad \sigma_{ps,y} = \sigma\left(\varepsilon_{ps,y}\right)$$

[16] [264] §3.6.2 "strength".

[17] For thermoplastic materials, the first part of the stress-strain curves is usually influenced by cross-links strength and density (cfr. §1.1.2). Heavily cross-linked materials have the tendency to exhibit a very stiff behaviour in the initial part of the curves, whereas poorly cross-linked materials must almost immediately rely on the response of the entangled network. This fundamental change in the mechanical, microscopical, response could potentially be used in the future to properly redefine the very concept of yielding for thermoplastic materials. This manuscript will not investigate further this possibility that draws deeply from chemical properties of the material and exceeds the scope of this work.

[18] Both the chord-slope and regression-slope methods can be applied.

[19] The value of 0.5‰ is chosen according to the limits proposed in the ISO standards for calculation of the tensile modulus (cfr. §4.1.2) [264].

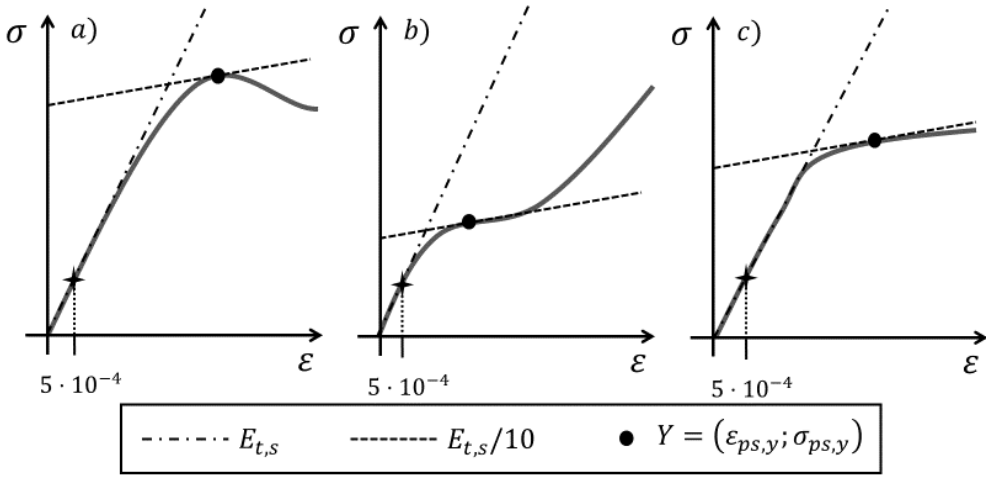

Figure 5.10 – a proposed criterion for defining the pseudo-yielding limit

Results for the performed tests are given according to the proposed method in Table 5.5 and Figure 5.11.

Table 5.5 - pseudo-yielding limit for the performed tests

claw displacement velocity v	**pseudo-strain point**	**SG**	**DG41**	**PVB**
5 mm/min	$\varepsilon_{ps,y}$ [−]	0,060	0,00044	0.0012
	$\sigma_{ps,y}$ $[MPa]$	11,68	2,96	0,10
50 mm/min	$\varepsilon_{ps,y}$ [−]	0,053	0,00038	0.0010
	$\sigma_{ps,y}$ $[MPa]$	16,20	7,02	0,16
500 mm/min	$\varepsilon_{ps,y}$ [−]	0,040	0,00030	0.0007
	$\sigma_{ps,y}$ $[MPa]$	20,04	12,82	0,37

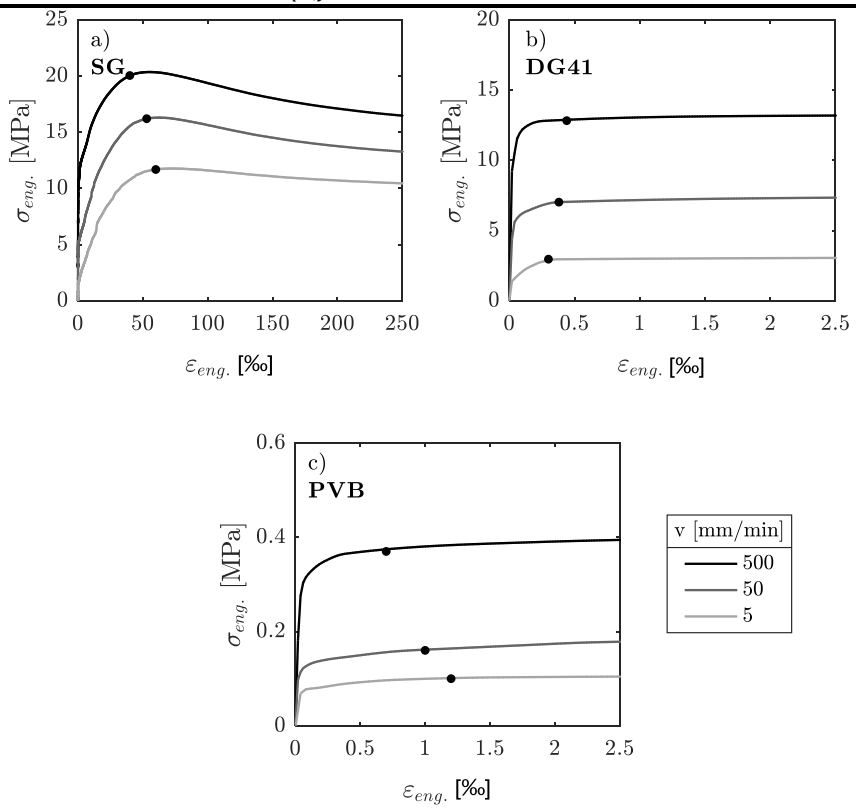

Figure 5.11 - pseudo-yielding limit for the performed tests

5.1.2 VISCOELASTIC PROPERTIES OF INTERLAYERS IN LG

Experimental results gathered throughout the viscoelastic campaign (cfr. §4.2.4.4 p.89) can be straightforwardly used to study effects of imposed loads or displacements for the three interlayers at those temperatures, for similar durations. Nonetheless, experimental results are scattered for temperatures which may not match the exact conditions a specific LG design is facing.

Extending the range of experimental results is useful to gain insight with respect of temperatures and times different than the ones directly investigated. In the following, using a classical model for time-temperature superposition[20] [114,254], results are proposed both in a closed form and simplified tabulations. Limits and scope of the model are discussed, while practical applications are shown in the following chapter.

5.1.2.1 TIME-SHIFT

By correlating properties of a given interlayer at a set temperature to those in a different climatic condition, results can be effectively extended beyond the fixed temperatures investigated in the campaign.

The shape of relaxation and – inverse - creep compliance curves on a *log-log* modulus over time space shown in Figure 4.37 suggest that an horizontal shift of the curves may be used to arrange a single function describing the viscoelastic properties of the materials [114,115].

Choosing a reference temperature T_{ref} for each material (i.e. a segment of the curve that will not be moved from its initial position), linear drifts in an N-base logarithmic time domain for the other i-branches can be performed. The new time scale $t_{i,s}$ for a branch shifted by a dimensionless δ_i factor is:

$$t_{i,s} = t_i \cdot N^{\delta_i}$$

where t_i is the original time of the branch and in our analysis an $N = 10$ base has been chosen (cfr. §3.1.3.5 and §4.2.4.4). An example is presented for $\delta_i = 1,2,3$.

Shift factors for creep and relaxation curves have been iterated to obtain the smoothest functions, a process that will be further clarified in the following. While this procedure may seem highly arbitrary, results from the final mastercurve - the one that is produced from the time-shifted data - are tied by a biunivocal relation to the shift factors used to produce the mastercurve itself (i.e. one cannot be used without the other, and each version of one defines a unique parent of the second among a family of possible curves). To clarify this reasoning, the scheme of the implemented iterative process in this work is shown in Figure 5.13.

The interlocking correlation between WLF and mastercurves implies that the best shift criterion is to produce mastercurves and shift factor distributions which are prone to be well interpolated by the relative functions[21]: a Wiechert-model-based Prony series and WLF equation respectively (cfr. §3.1.3.1 and §3.1.3.5).

[20] Sometimes referred to as the *reduced variables method*.

[21] To evaluate the accuracy of such fitting processes, several methods can be implemented, starting from a purely graphical one to different numerical evaluations. In this work, a least-squares difference minimization criterion was used for both WLF and Prony series fitting curves (for the Prony series mastercurve, the median value of the relaxation or creep modulus of each temperature was used).

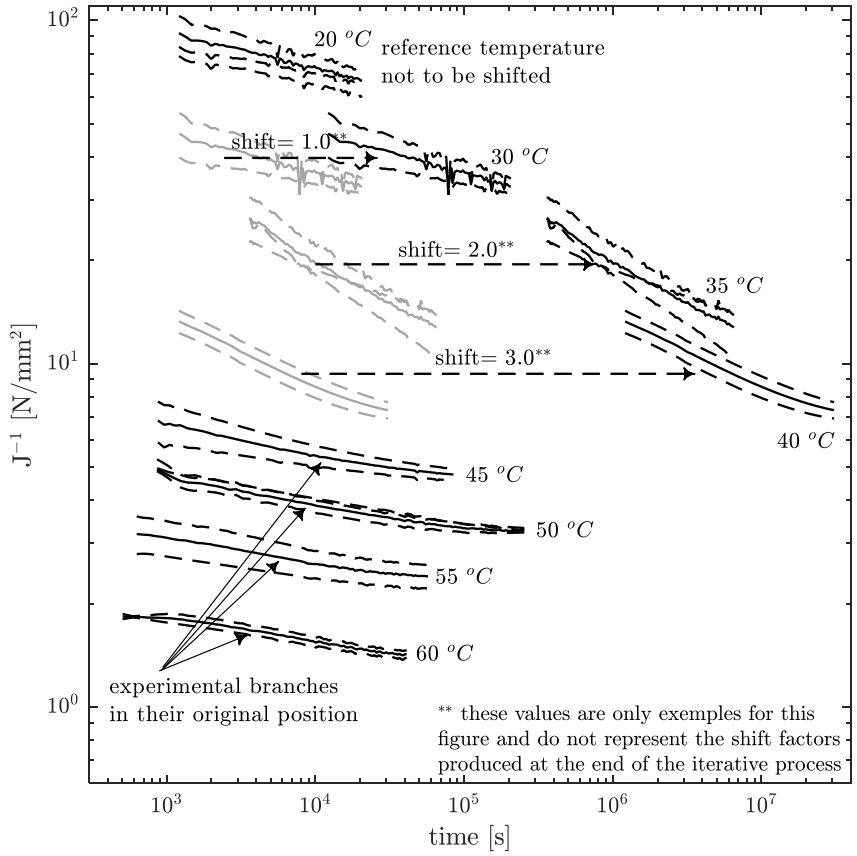

Figure 5.12 - example of shifted experimental branches for SG creep modulus

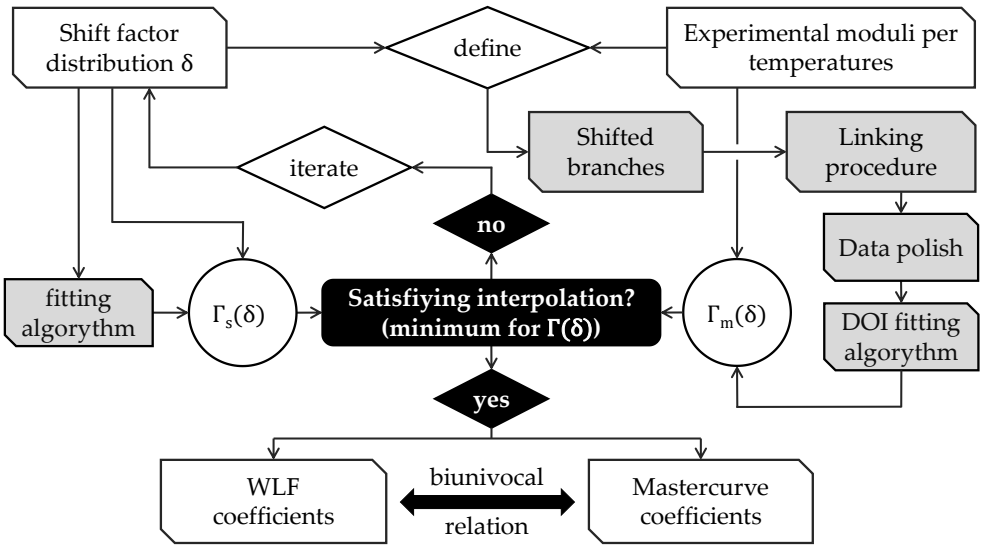

Figure 5.13 –process used to define WLF and mastercurve coefficients

The choice of the reference temperature is arbitrary. For this analysis, a reference temperature of 20°C was chosen, to match the commonly used ambient temperature for architectural design purposes [22] and some of the previously available data and mastercurves for interlayer materials, mostly obtained via dynamic testing techniques (cfr.2.2.1 and Appendix D) [38,65].

[22] By doing so, the curves can be used as presented, without any shift, if the materials response is needed at ambient temperature.

The final choice of the shift factor distributions δ presented in Table 5.6 is made according to the iterative procedure described in Figure 5.13. An algorithm was set up to minimize the sum of square differences between the shift factors distributions and interpolating WLF equations Γ_s[23] and the sum of square differences between the experimental data of shifted branches and interpolating mastercurves Γ_m[24]. The input of the shift factors distribution was done manually and so were the iterations by trial and error. For each attempt, the two sum of square differences were stored recorded and normalized to $\bar{\Gamma}_s$ and $\bar{\Gamma}_m$, with respect of the corresponding number of data points[25]. The final choice of shift factors (answering to the question "satisfying interpolation?" in the scheme of Figure 5.13) was the one that minimized the combined error $\Gamma(\delta) = \bar{\Gamma}_s(\delta) \cdot \bar{\Gamma}_m(\delta)$.

Table 5.6 - shift factors [26]

Temp.	**SG**		**DG41**		**PVB**	
$\boldsymbol{T}$ [°C]	δ_G	$\delta_{J^{-1}}$	δ_G	$\delta_{J^{-1}}$	δ_G	$\delta_{J^{-1}}$
0					-4.524	-7.042
10			-2.434	-7.504	-2.076	-3.365
14			-1.367	-4.278		
17			-0.688	-1.909		
20 (ref.)	0	0	0	0	0	0
23			0.710	1.763		
30	1.848	2.786	2.324	4.633	1.886	3.185
35	2.901	4.349				
40	4.153	6.075	4.328	7.439	3.685	6.171
45	5.532	7.802				
50	7.134	9.813	6.120	9.536	5.281	9.028
55	9.212	12.126				
60	11.911	15.072				

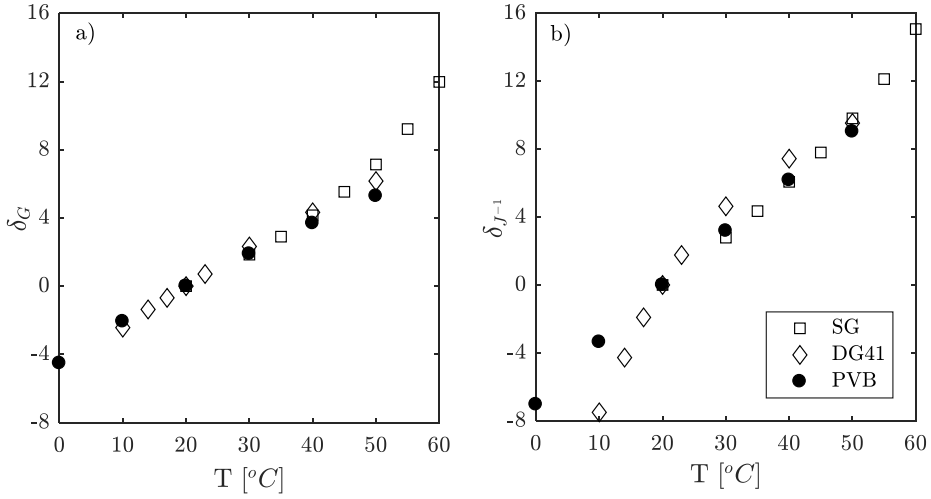

Figure 5.14 - shift factors for a) relaxation and b) creep [26]

[23] Using the proposed interpolating procedure described in §5.1.2.3.

[24] Performed with the DOI method described in §5.1.2.4.

[25] For the WLF, the number of data points is the number of different temperatures of the tests, for the Prony regression the number of data points is the sum of points of the experimental branches.

[26] The choice of the displayed shift factors will be clearer with the following discussions and analyses presented in §5.1.2.3.

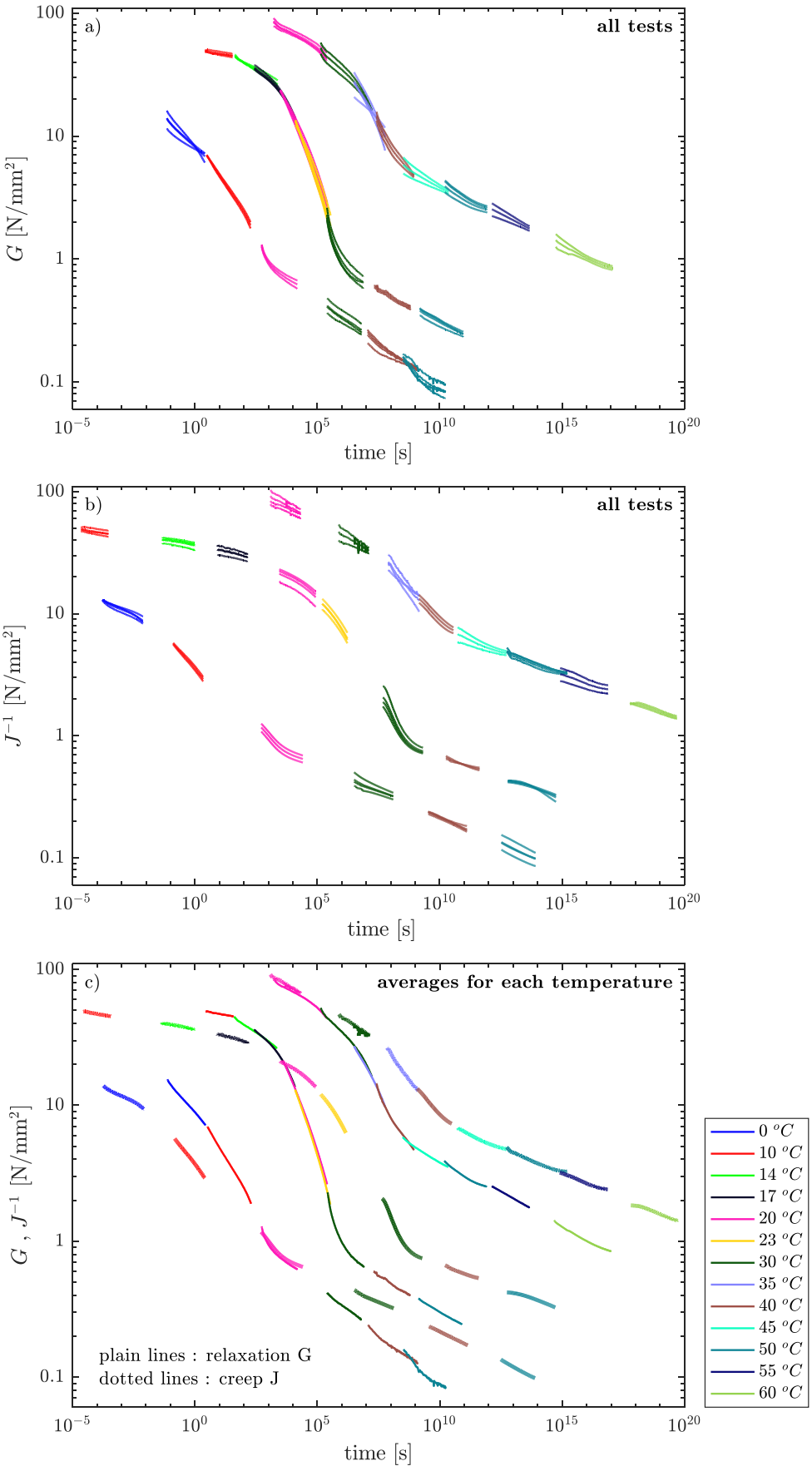

Figure 5.15 - shifted branches for a) exp. relaxation, b) exp. creep and c) averages

Figure 5.15 shows simultaneously average values of shifted branches for both relaxation and creep moduli. Several noteworthy elements can be pointed out:

- pink branches, both for relaxation and creep, are tests performed at the reference temperature T_{ref} (20°C); therefore, all curves remained on the vertical of the same time frame (about $10^4 s$) as only the other branches were shifted back and forward,
- overall, the creep compliance modulus appears to be flatter than the relaxation one (i.e. it is more stretched along the time axis), while values for both moduli at the same temperature do not vary dramatically,
- because of the two previous points, relaxation and creep curves always cross one another at the reference temperature,
- the transition temperature for the three materials, represented by the maximum slope of the function, appears to be close to 20°C for PVB, 23 ÷ 30°C for DG41 and 35 ÷ 40°C for SG,
- to a first approximation, in a *log-log* modulus over time space, the six curves can be roughly interpolated with two or three straight lines, thus in linear scales with three different exponential curves.

5.1.2.2 CONNECTION OF SHIFTED EXPERIMENTAL BRANCHES

Within the optimization algorithm described in §5.1.2.1 and Figure 5.13, three scenarios can occur when juxtaposing consecutive shifted branches (Figure 5.16):

Case 1, shifted branches do not overlap along the time axis and the gap among them is "small", so that $0 < \delta < 0.1$ on a $\log_{10}$ time axis,

Case 2, portions of consecutive branches are superimposed, hence $\delta < 0$,

Case 3, consecutive branches are separated by a non-negligible "gap" whose extent δ is greater than 0.1 on a $\log_{10}$ time axis.

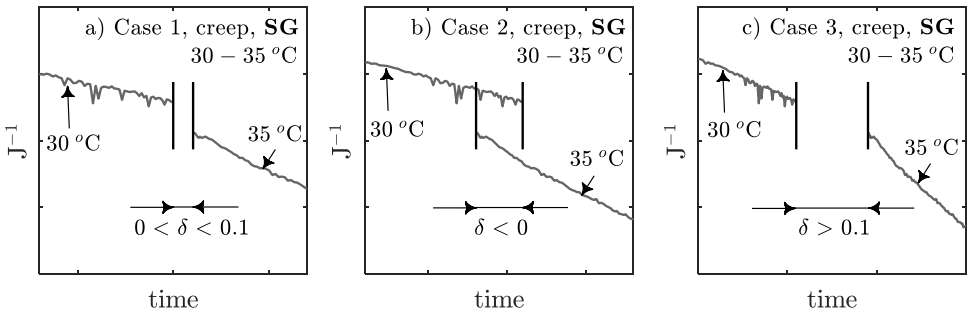

Figure 5.16 - three possible arrangements for consecutive experimental branches

The overlapping or spacing of consecutive branches is a function of the distribution of shift factor fed to the algorithm. Depending on the input, the algorithm was given instructions to deal with the different scenarios in three ways, described in the following.

Case 1 procedure: simply concatenate the consecutive branches, the last point of the previous and the first point of the following become subsequent elements in the merged array,

Case 2 procedure: start by creating a new distribution t_{olp} of uniformly log-spaced point along the time axis, between the limits of the overlapping segments. The number of points in this array is set as the average of the number of points in the overlapping areas of the branches consecutive. Compute the average values of the modulus M_{olp} among the two branches in the overlapping areas at the points

t_{olp}. The final merged array is composed by the point of the first branch before the overlapping area, then the average points where the experimental results are superimposed, followed by the remaining points of the second branch (Figure 5.17).

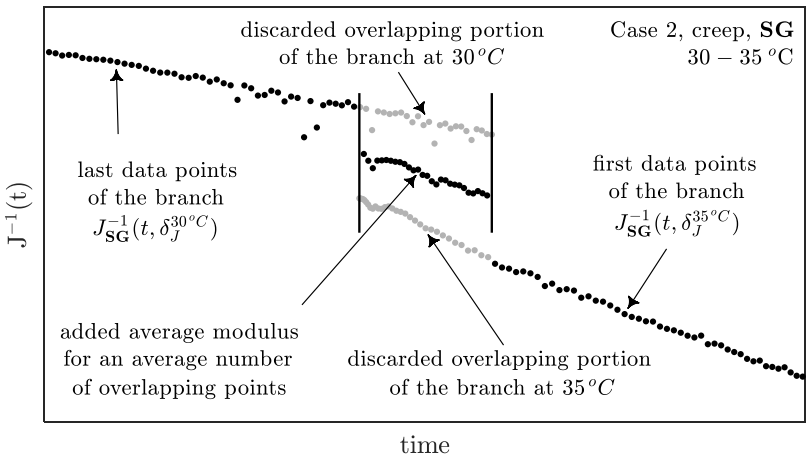

Figure 5.17 - procedure for overlapping areas

Case 3 procedure: concatenate consecutive branches by means of a linking function, the creation of which is described in the following.

As a general rule, large gaps have been observed to be more frequent in the creep curves than in relaxation ones; this is due to two factors: first, creep branches are flatter compared to the relaxation ones (cfr. §5.1.2.1), this amplifies the distance among shifted branches, second, for many tests the viscous recovery testing time was lower, producing shorter branches (cfr. Table 4.5 and Figure 4.24). To address this, a procedure was set up to fill gaps with linking branches, providing a smooth curve which was later used for Prony series interpolation [243,248].

Experimental data in a $\log_N \div \log_N$ time over moduli space (cfr. Figure 5.15) have suggested that exponential linking branches based on a third-degree polynomial are helpful for fill the gaps with a smooth curve. Such functions $G(t)$ and $J^{-1}(t)$ are belong to the family:

$$G(t), J^{-1}(t) = N\wedge\left(\frac{a\ln^3 t}{\ln^3 N}+\frac{b\ln^2 t}{\ln^2 N}+\frac{c\ln t}{\ln N}+d\right)$$

With four constants a, b, c and d to be defined according to boundary conditions, given by the end segments of the branches to be connected. Assuming $N = 10$ (cfr. §5.1.2.1), this non-linear problem can be converted to a linear one using:

$$t' = \log_{10}(t) \quad , \quad G' = \log_{10}(G) \quad , \quad J^{-1\prime} = \log_{10}(J^{-1})$$

The linking function and boundary conditions can hence be expressed in a linear time over moduli transformed environment, where the linking function is a third-degree polynomial curve:

$$G'(t'), J^{-1\prime}(t') = at'^3 + bt'^2 + ct' + d$$

Boundary conditions are chosen to guarantee tangency and congruence among adjacent branches.

A complete example of the procedure is herein presented for the link of two experimental branches, belonging to the creep compliance mastercurve for the SG interlayer. The median value of experimental results for tests carried at 30°C and 35°C are used. The procedure is similar for the other moduli and branches.

After the above-mentioned transformations, target points A and B were manually defined given two target abscissa t'_A and t'_B, respectively close to the end of the first curve and the beginning of the second one. Figure 5.18 shows a close-up of the investigated area, the initial and final target points, along with two set of automatically generated dots defining neighbourhoods around the target points. The width (i.e. the size) of the neighbourhoods was redefined for each linked branch, to allow for a locally satisfying approximation of the curve[27]. For each set of points, a linear regression was carried out with a linear least squares method, henceforth generating the dotted lines in the figure.

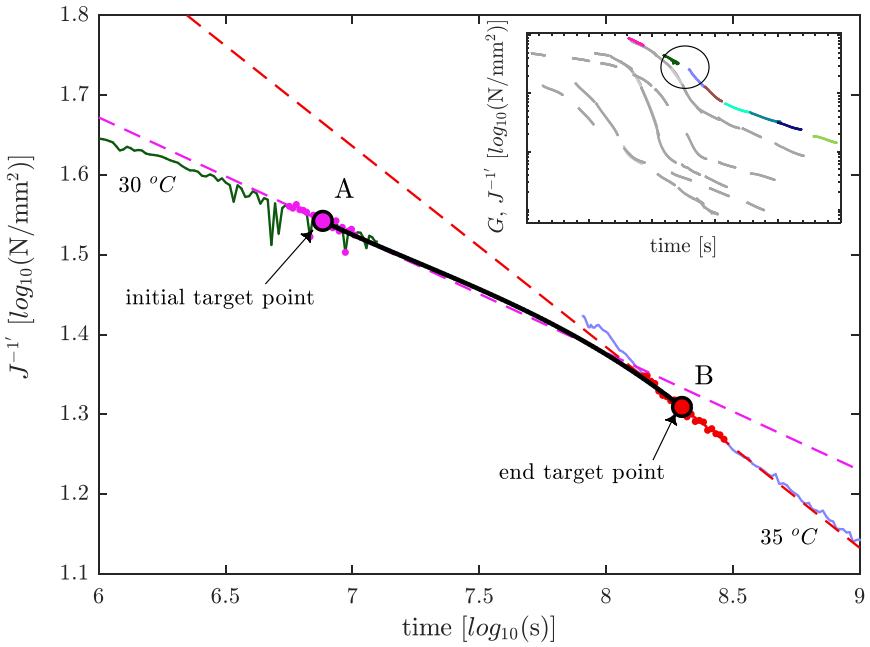

Figure 5.18 - scheme of the linking procedure27

From the linear regression, ordinates ${J^{-1}}'_A$ and ${J^{-1}}'_B$ of the target points and slopes of the curves m_A and m_B were worked out, to be then used as boundary conditions for the polynomial interpolation. Given:

$$A\left(t'_A; {J^{-1}}'_A\right) \quad ; \quad B\left(t'_B; {J^{-1}}'_B\right) \quad ; \quad m_A = \frac{d}{dt'}{J^{-1}}'_A(t') \quad ; \quad m_B = \frac{d}{dt'}{J^{-1}}'_B(t')$$

Coefficients a, b, c and d were found by solving the linear system granting the observance of the established boundary conditions. Numerical results in this example are given to be later implemented in the general equation:

$$\begin{bmatrix} {t'_A}^3 & {t'_A}^2 & t'_A & 1 \\ {t'_B}^3 & {t'_B}^2 & t'_B & 1 \\ 3{t'_A}^2 & 2t'_A & 1 & 0 \\ 3{t'_B}^2 & 2t'_B & 1 & 0 \end{bmatrix} \begin{Bmatrix} a \\ b \\ c \\ d \end{Bmatrix} = \begin{Bmatrix} {J^{-1}}'_A \\ {J^{-1}}'_B \\ m_A \\ m_B \end{Bmatrix} \xrightarrow{yields} \begin{matrix} a = -0.03474 \\ b = +0.7547 \\ c = -5.599 \\ d = +15.65 \end{matrix}$$

[27] Note that, for explanatory reasons, the representation in Figure 5.18 has been intentionally simplified by scattering the and expanding the neighbourhoods around the target points for which the sets are defined. Actual sets generally consisted in thousands of elements, increasingly dense in the ending parts of the curves, an effect due to the applied transformations.

The plain black curve in Figure 5.18 is the polynomial solution ${J^{-1}}'_L(t')\big|_A^B$ for the gap between target points A and B in the transformed variables t', ${J^{-1}}'$, where the subscript L is used to indicate a linking function. The solution $J_L^{-1}(t)$ in the original $\log_{10} J^{-1}$ over $\log_{10} t$ environment can be found by applying the following inverse transformations:

$$t_L = 10^{t'} \quad , \quad J_L^{-1} = 10^{J'}$$

Substituting the general equation yields the final function $J_L^{-1}(t)$:

$$J_L^{-1}(t) = 10\text{^}\,(-2.84 \cdot 10^{-3} \ln^3 t + 0.142 \ln^2 t - 2.42 \ln t + 15.6)$$

for $t \in [t_A, t_B]$.

The same procedure has been applied in an analogous manner for all the gaps in all moduli for the three materials in different $[A_i, B_i]$ intervals.

Dealing with experimental data, inherently prone to a variety of possible approximations and errors, a critical approach in the selection of the target points was preferred to a blind implementation of the procedure. Consequently, target points yielding an overall smoother interpolation of the general trend of the mastercurve were chosen, rather than slavishly connecting the terminal parts of all the connected experimental branches. This approach also took into consideration that the terminal parts of the experimental curves generally have a higher regularity than the initial ones. This phenomenon is also discussed in §4.2.2 and further highlighted in Figure 5.15 by the juxtaposition of branches which do not strictly require a linking function (e.g. $G^{SG}_{45°C}$ and $G^{SG}_{50°C}$, where the initial part of the $G^{SG}_{50°C}$ curves prove to be less regular than the following trend). With this approach, target points and linking functions are presented in Figure 5.19.

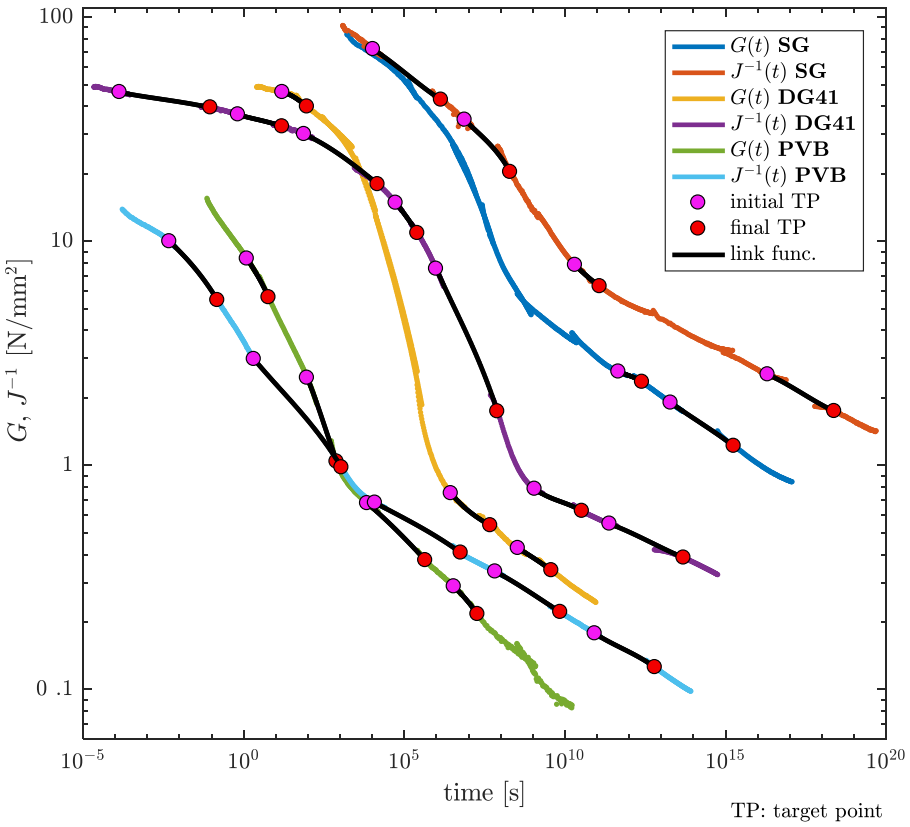

Figure 5.19 - target points for linking branches

Portions of the linking branches have later been cut, to avoid unnecessary superposition with the experimental data, in the - small - portions where the curves were overlapping (experimental data were always preferred to points of the linking functions).

The final operation on the data at this stage, to enhance both reliability and computational load of Prony series interpolations, was to re-sample the data sets among a fixed number of equally distributed points in logarithmic time scales. Provided with a large distribution of points $P_i(t_i; M_i)$ (where M_i stands for either G_i or J_i^{-1}), dense in some areas and sparser in others, a new time array $t_{i,R}$ is defined to uniformly distribute the points along the curve:

$$t_{i,R} = \text{logspace}_{10}(\max(t_i), \min(t_i))$$

Accordingly, re-sampled values of the moduli $M_i(t_i)$ were calculated as the average of the nearest ten points to the re-sampled abscissa $t_{i,R}$ in the original data set. An example of re-sampled data is presented in the following figure for 30 points only, whereas two thousand points were used in the actual data analysis.

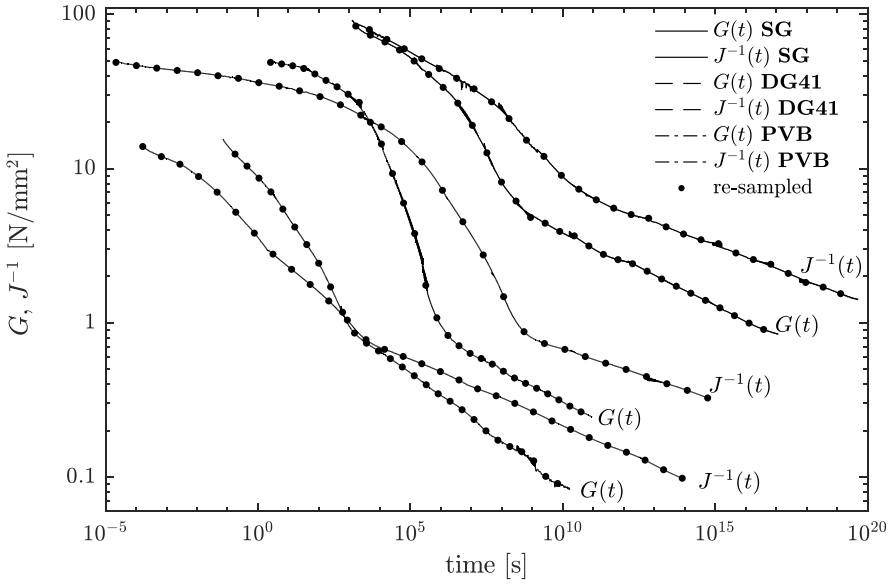

Figure 5.20 - example of a thirty-points re-sampling

5.1.2.3 WLF REGRESSION (A PROPOSED FITTING PROCEDURE)

Mastercurves, produced and perfected in previous paragraphs (cfr. §5.1.2.1, Table 5.6 and Figure 5.14), are inherently tied to the set of shift factors. Within the iterative procedure described in Figure 5.13, to allow for the use of experimental results in terms of relaxation and creep moduli for arbitrary temperatures within the investigated range, a generalization of the punctual temperature-shift correlations needs to be provided.

A now popular formulation for time-temperature superposition was proposed in 1980 by Williams, Landel and Ferry [114], in the form of an equation with two coefficients C_1 and C_2 (cfr. §3.1.3.5).

$$-\log_N a_T = \alpha = \frac{-C_1(T - T_{ref})}{C_2 + (T - T_{ref})}$$

A regression procedure is herein proposed for shift-factor distributions and corresponding test temperatures. The procedure is based on the WLF equation and aims to find the best fitting coefficients C_1 and C_2. The outcome allows to compute the normalized sum of square differences $\bar{\Gamma}_s$ of the WLF regression (cfr. §5.1.2.1).

First, a three-dimensional array of values $\mathbb{C}^{k=1} \in \mathbb{R}^{\boldsymbol{m\times n\times 2}}$ was created, where k designates the progression in the iteration. The space $\mathbb{C}^1$ can be presented as a two-dimensional matrix[28] $\boldsymbol{C}^1$ in $\mathbb{R}^{\boldsymbol{m\times n}}$, in which each element holds a pair of values for $C_{1,i}$ and $C_{2,j}$ for $i = 1, \dots, m$ and $j = 1, \dots, m$. For $k = 1$, values for the two constants in each element of the matrix are set to be linearly ranging among predefined arbitrary limits, so that $C_{1,i} \in [C_{1,\min}, C_{1,\max}]$ and $C_{2,j} \in [C_{2,\min}, C_{2,\max}]$ are spaces centred around initial best-guess values $C_{1,0}$ and $C_{1,0}$:

$$C_{1,\min} = C_{1,0} - a \qquad C_{1,\max} = C_{1,0} + a$$

$$C_{2,\min} = C_{1,0} - b \qquad C_{2,\max} = C_{1,0} + b$$

For a given set of shift factors δ_u and temperatures T_u, the regression base $\boldsymbol{p} \in \mathbb{R}^{\boldsymbol{U}}$ is described as:

$$\boldsymbol{p} = (T_u; \delta_u)$$

For each i, j element in $\boldsymbol{C}^1$ (i.e. for each pair of constants C_1, C_2), the value of the right part of the WLF function is calculated for all temperatures T_u, yielding $\alpha_{ij,u} \in \mathbb{R}^{\boldsymbol{m\times m\times U}}$. The sum of square differences for all u elements was then arranged in $\boldsymbol{D} \in \mathbb{R}^{\boldsymbol{m\times m}}$.

$$\boldsymbol{D} = D_{ij} = \sum_{u=1}^{U} \left(\alpha_{ij,u} - \delta_u\right)^2 \quad \text{with} \quad \alpha_{ij,u} = \frac{-C_{1,i}\left(T_u - T_{ref}\right)}{C_{2,j} + T_u - T_{ref}}$$

For each iteration k, the pair (i^*, j^*) yielding minimum value of $\boldsymbol{D}^k$ is found and associated to a specific couple of constants C_{1,i^*}^k and C_{2,j^*}^k in $\boldsymbol{C}^k$.

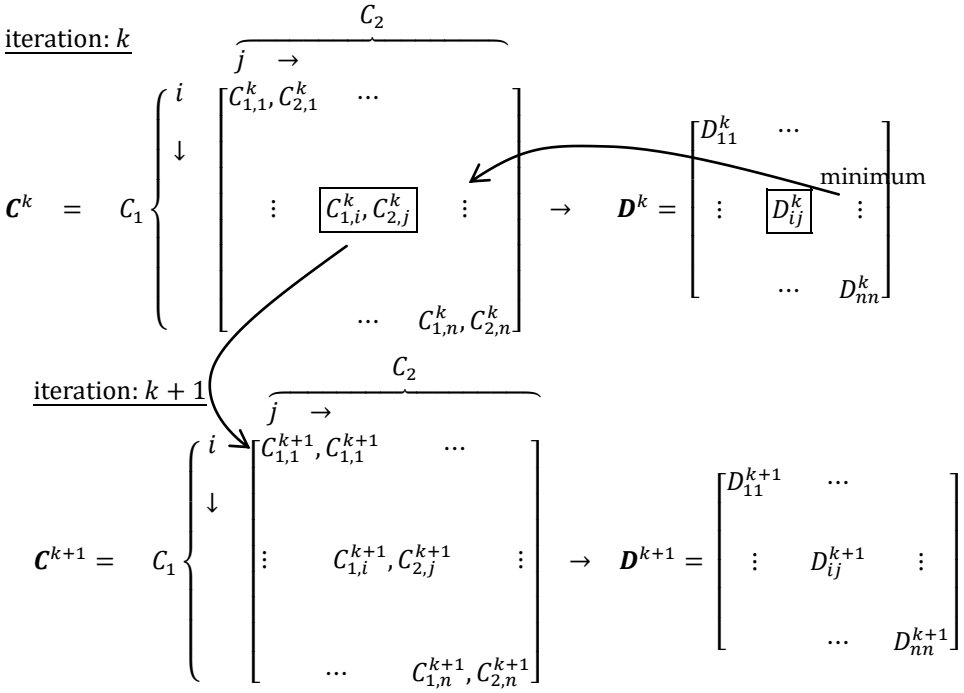

For the iteration $k+1$ of $\mathbb{C}^{k+1}$, limit of $C_{1,i}^{k+1}$ and $C_{2,i}^{k+1}$ are re-centred around the new best estimation C_{1,i^*}^k and C_{2,j^*}^k of the WLF constants. New limits are set as:

[28] The shape of the matrix arbitrary: any different $\mathbb{R}^{\boldsymbol{m\times n}}$ space can have been adopted, without jeopardizing the discussed procedure but possibly affecting its accuracy. In the following, $m = n$ will be assumed, a choice motivated by the fact that there is no a-priori insight on the best fitting values of any of the two constants.

$$C_{1,\min}^{k+1} = C_{1,i^*}^{k} - \frac{a}{2^{k-1}} \qquad C_{1,\max}^{k+1} = C_{1,i^*}^{k} + \frac{a}{2^{k-1}}$$

$$C_{2,\min}^{k+1} = C_{2,i^*}^{k} - \frac{b}{2^{k-1}} \qquad C_{2,\max}^{k+1} = C_{2,i^*}^{k} + \frac{b}{2^{k-1}}$$

Such procedure is repeated until convergence is deemed satisfactory. The scheme of the algorithm advancement is:

1. *(preliminary)*, take the regression base $\boldsymbol{p}$ and set $k = 1$,
2. arbitrarily define m, n, a, b, $C_{1,0}$ and $C_{2,0}$, along with a maximum number of iterations $k_{\max}$,
3. define the initial limits $C_{1,\min}^{k}$, $C_{1,\max}^{k}$, $C_{2,\min}^{k}$ and $C_{2,\max}^{k}$,
4. *(start the iteration)*, set $k = (k + 1)$ and compute the values of $\mathbb{C}^k$,
5. for $i = 1, \dots, m$ and $j = 1, \dots, m$ calculate the sum of square differences D_{ij} using the right part of the WLF equation,
6. find the minimum value of $\boldsymbol{D}^k$ associated to indexes (i^*, j^*),
7. take C_{1,i^*}^{k} and C_{2,j^*}^{k} in $\mathbb{C}^k$,
8. define the new limits $C_{1,\min}^{k+1}$, $C_{1,\max}^{k+1}$, $C_{2,\min}^{k+1}$ and $C_{2,\max}^{k+1}$ and repeat from point 4 until $k = k_{\max}$.

Although the absolute convergence of the method has not been demonstrated with mathematical proof, the convergence has been verified within the general algorithm described in Figure 5.13, for all the shift-factor distributions tested within our analyses. The procedure has proven to be always swiftly convergent, provided that the best-fitting values are simply enclosed within the initial limits.

Choosing $m = n = 100$, $a = b = 10^5$, $C_{1,0} = C_{2,0} = 0$, and a maximum number of 20 iterations, the procedure returns the final values for the WLF coefficients displayed in Table 5.7.

Graphical results, displaying that the defined WLF functions are a good regression of the experimental shift values, are presented in Figure 5.21, whereas Figure 5.22 provides insight on the convergence of the procedure for the six functions in terms of the minimum value in $\boldsymbol{D}^k$ per iteration k.

Table 5.7 - WLF coefficients

	SG		**DG41**		**PVB**	
	relax.	**creep**	**relax.**	**creep**	**relax.**	**creep**
C_1	12.91	29.46	-53.36	-21.96	-40.12	-103.82
C_2	-83.46	-118.95	228.43	38.70	198.31	315.54

Curves in Figure 5.22 for the final shift-factor distributions show that the functions are not all convergent to the same value. This ought to be expected, for the inherent differences among the six regression bases $\boldsymbol{p}$: distributions which are more prone to be fitted by a curve belonging to the WLF family will yield lower final values of $\min(\boldsymbol{D}^k)$. Prior to the acquisition of final values for C_1 and C_2 two checks were performed: all error curves must be asymptotic to a final value and the WLF equations must be graphically fitting the trend of each regression base.

Due to the nature of the algorithm, notably due to the progressively increasing density of the inquired mesh of points in $\mathbb{C}^k$. If C_1^* and C_2^* are the best possible values of C_1 and C_2 respectively, the accuracy of the results at the end of the iteration ($k = 20$) is:

$$C_1^* = C_1^k \pm \frac{2a}{m2^k} = C_1^k \pm 0.002 \qquad \text{and} \qquad C_2^* = C_2^k \pm \frac{2b}{n2^k} = C_2^k \pm 0.002$$

Therefore, coefficients in Table 5.7 are accurate up to the second decimal.

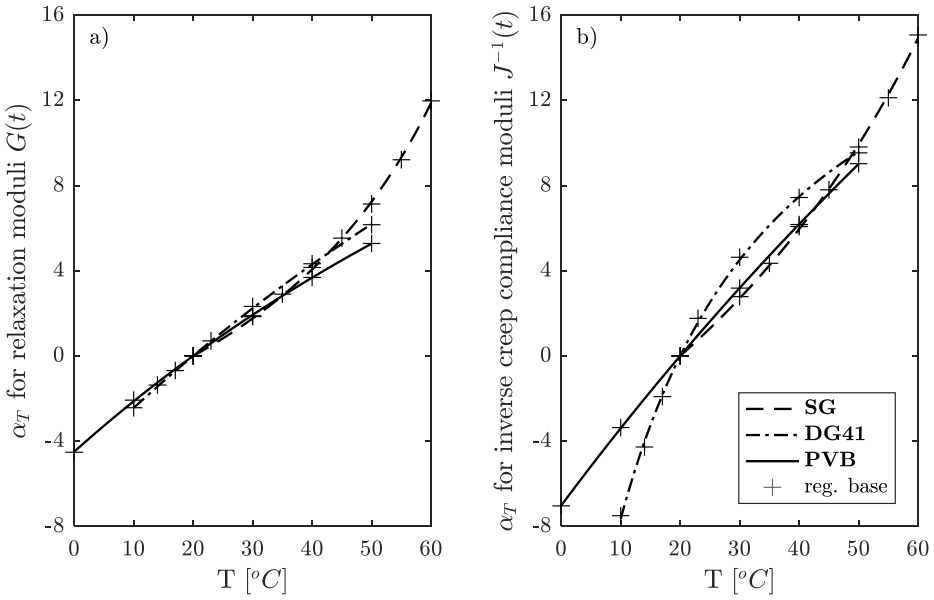

Figure 5.21 - WLF functions for a) relaxation and b) creep mastercurves

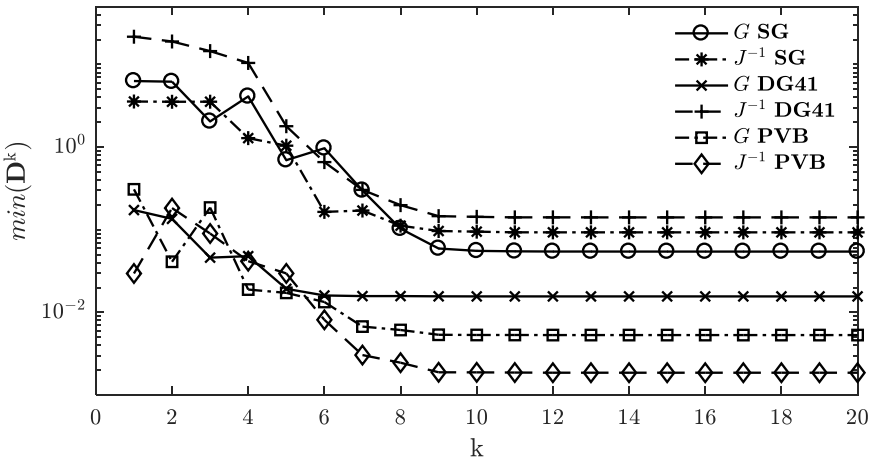

Figure 5.22 - convergence of the WLF regression algorithm

5.1.2.4 PRONY SERIES CORFFICIENTS FOR MASTERCURVES

Experimental mastercurves, produced and discussed in § 5.1.2.1, have to be conveniently fitted with appropriate functions, to be implemented in analytical or numerical laminated glass design problems.

Several models, techniques and functions can be used to adequately fit exponentially decaying data sets, the kind of those obtained with the experimental campaign; some have been previously mentioned and discussed in §3.1.3. All things considered, the choice of a Wiechert model, associated with a Prony series regression, have been deemed to be the optimum choice for the presented fitting problem. The series are therefore searched in the form:

$$M(t) = M_0 + \sum_{i=1}^{N} M_i \exp\left(\frac{t}{\tau_i}\right)$$

where $M(t)$ is either the relaxation modulus $G(t)$ or the inverse compliance $J^{-1}(t)$, and M_0 , M_i, τ_i are the $2N + 1$ constants to be found.

An effective and versatile technique, capable of performing the Prony series regression on experimental data, has been articulated in 1997 in a research paper by Gant and Bower as the "*domain of influence method (DOI)*" [243]. The paper extensively provides instructions to implement the method in a regression algorithm; as neither the series themselves nor the regression method are innovative contributions to this work, the content of the method will not be hereby further discussed. Nonetheless, original remarks are listed underneath, regarding properties and limits of the procedure emerged throughout the analyses (details on the algorithm are provided in Appendix I):

1. the regression algorithm requires to be fed a monotonic descending array of data, therefore experimental results may be required a refinement procedure, adding some level of arbitrariness,
2. in the arbitrary selection of the value of $\delta \log(t)$ (cfr. Figure 5.24), a verification criterion is needed, to ensure that each exponential term always operates upon a meaningful amount of points,
3. the method being based on a natural exponentials sum (a choice which has arguably several mathematical advantages), the number of terms required to perform an accurate fit depends on the shape of the function to be regressed,
4. experimental data on long time spans generally require large number of coefficients, regardless the regularity of the curve,
5. due to the presence of a final, constant, "steady state" term within the series, resulting curves may be soon unfit to extrapolate data after the last experimental time point,
6. the first point of the regression is always equal to the first experimental point, this may affect significantly the accuracy.

For the experimental nature of data and data analysis processes described in previous paragraphs, average experimental mastercurves, produced in §5.1.2.1 and displayed in Figure 5.20, did not always present a strictly monotonic descending trend. Therefore, a preliminary polishing procedure was needed to allow for the implementation of the DOI method. Starting from the first data point and proceeding in ascending time order, the procedure simply removed any data point which, for higher time values, had a higher modulus than any of the previous points. Similarly to the procedure for linking branches, the polish procedure is also an integral component of the general algorithm described in Figure 5.13.

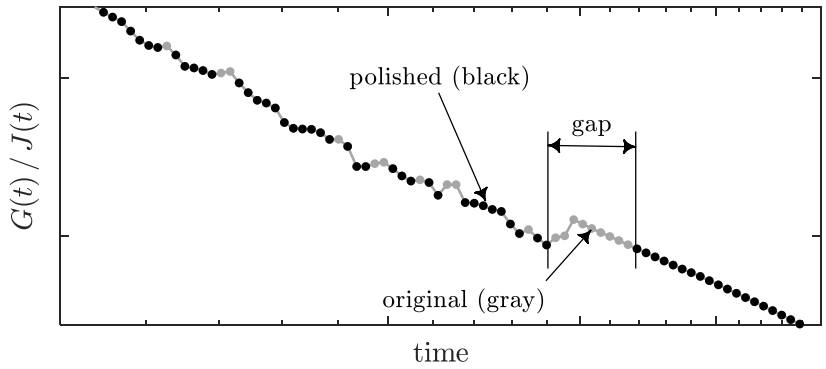

Figure 5.23 – detail of data polish procedure outcome

An illustration of the polish procedure is shown in Figure 5.23, highlighting how this method occasionally causes the data sets to encompass a few gaps among subsequent points.

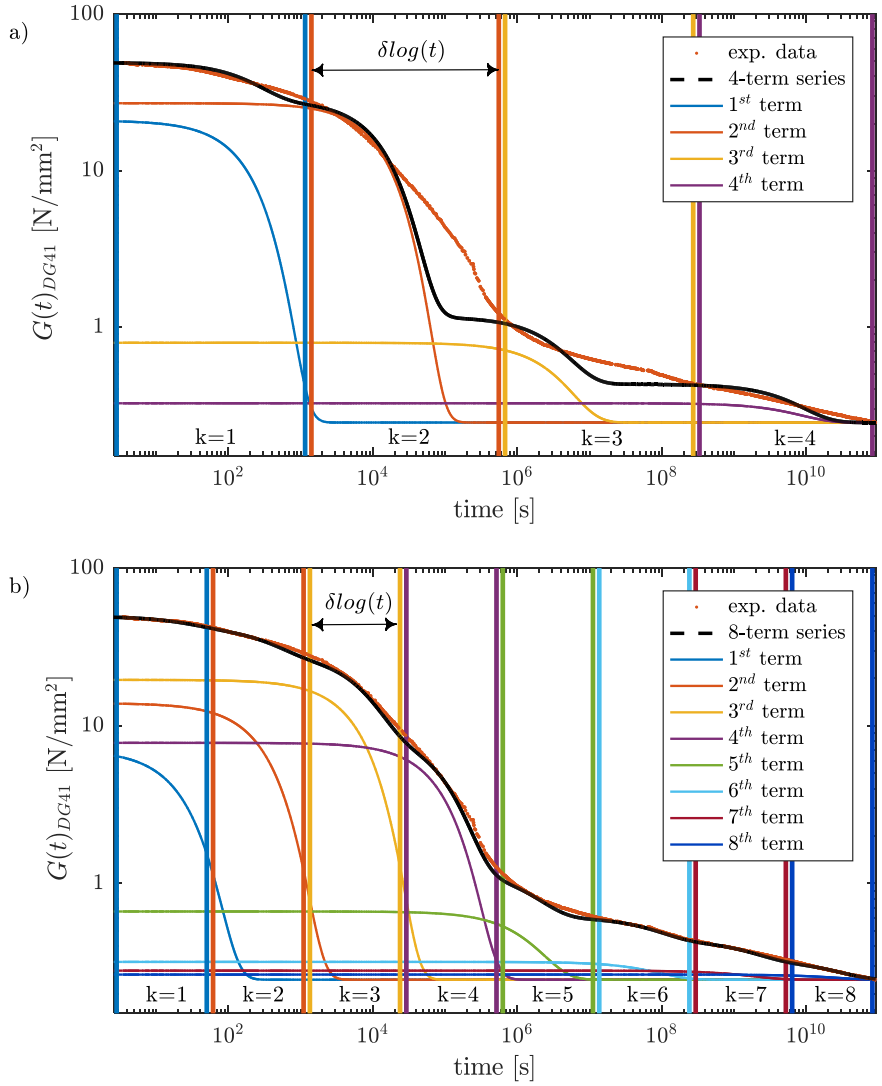

Figure 5.24 –final mastercurve and elements of the series with a) 4-terms or b) 8-terms

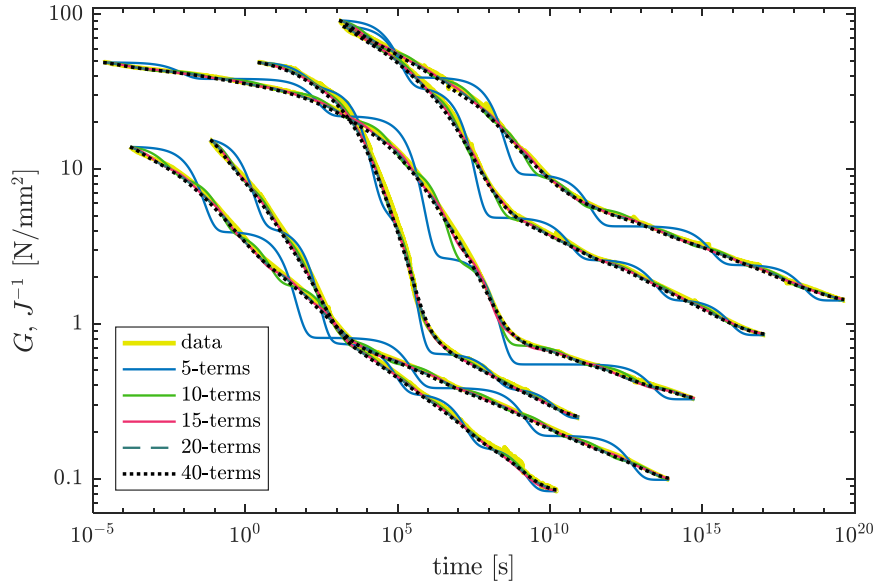

Figure 5.25 - Prony fit comparison with different term series

Gaps are meaningful to the DOI method, to the extent that the higher the number of terms in the series, the smaller are the domains among which the constants τ_i and M_i are computed. If the domains are small enough and encompass one or several wide gaps, the number of points in that specific domain may drop dramatically, therefore severely affecting the accuracy of the regression in that portion of the curve. For each interpolation, a limit to the minimum width of each domain $\delta \log(t)$ has been imposed as follow:

$$\delta \log(t) \geq 3 \cdot \max(\log(t_i) - \log(t_{i+1}), \forall i \in [1, \text{size}(t)])$$

Figure 5.24 shows an example of the regression of DG41 relaxation mastercurve with 4-terms and 8-terms series, highlighting the effects on the number of terms on the accuracy. The number of terms in increased by reducing the value of $\delta \log(t)$, connected to the width of each DOI.

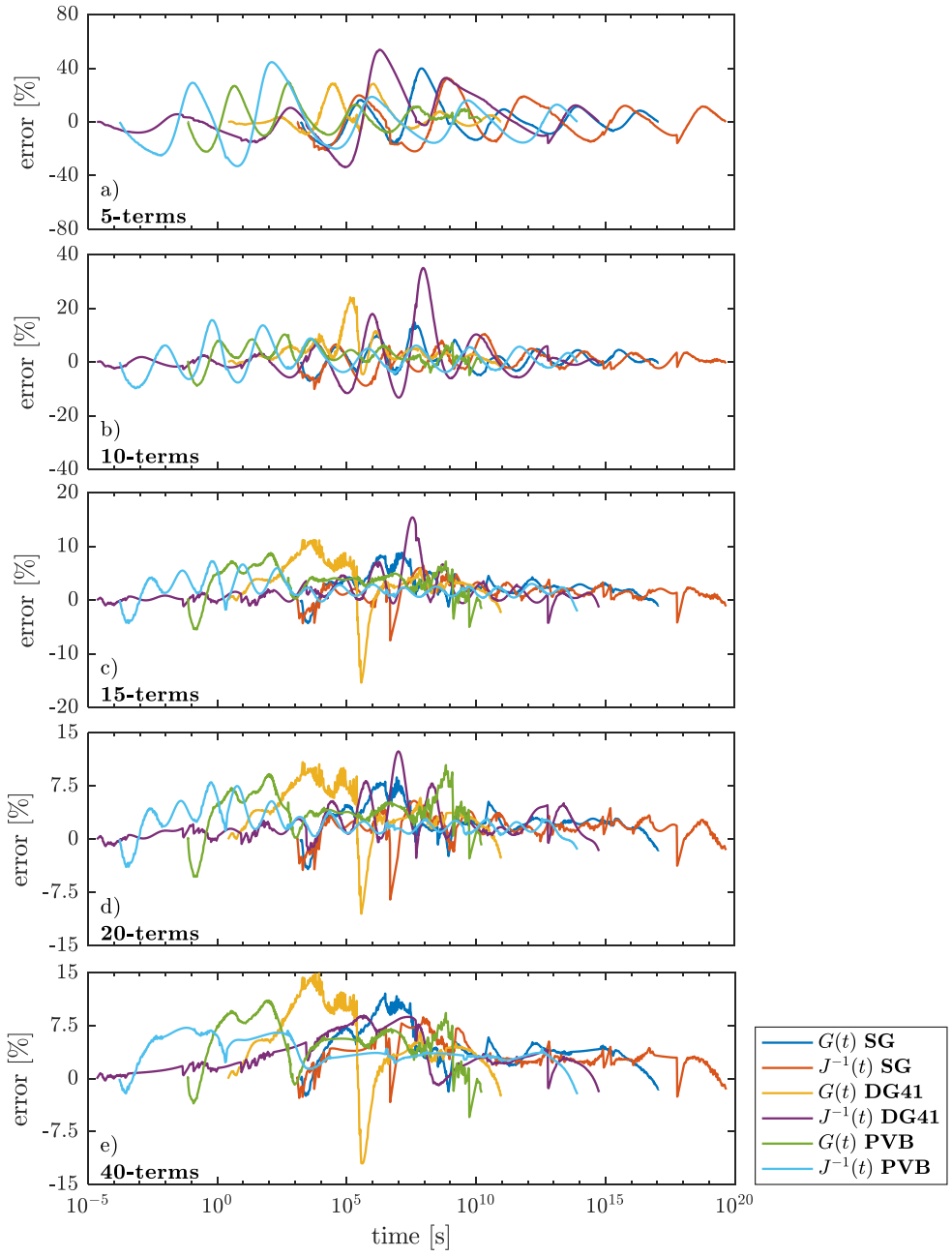

Figure 5.26 - error for a) 5- , b) 10- , c) 15 -, d) 20- and e) 40-term series

For internal consistency among final results produced in this work, it was decided to provide Prony series with equal number of terms for all moduli of all materials. The number was then chosen to successfully fit all the curves with appropriate accuracy and also avoid inappropriate "jiggling" (a technical term used in [243] and visible in Figure 5.24) around the mean value.

For increasing number of terms, the accuracy was first estimated as the percental error between experimental data[29] and the generated Prony series, along the entire time span of each mastercurve. For increasing number of terms, curves are shown in Figure 5.25 and percental errors in Figure 5.26.

Error curves show that the accuracy initially increases if the number of terms also increases: the maximum error between 5- and 15-terms series diminishes from about $40 - 50\%$ to mere $10 \div 12\%$ (cfr. Figure 5.26.a, b & c); nonetheless, data also suggest that the error does not monotonically decrease with increasing number of terms (cfr. Figure 5.26.d e).

To evaluate the accuracy of the Prony series fit to experimental data, a slightly refined criterion may be used to knowingly choose the final number of terms for the series. The normalized average of square root of square differences $\bar{\Gamma}_m$, can be defined as:

$$\bar{\Gamma}_m = \frac{\mu}{\max(\mu)} \qquad \text{where} \qquad \Gamma_{\mathrm{m}} = \frac{\sqrt{\sum_{i=1}^{n}(M_{\mathrm{P}}(t_i) - M_i)^2}}{n}$$

n being the number of elements i in each data set (t_i, M_{i}) and M_{P} the value of the modulus at time t_i , calculated using the appropriate Prony series.

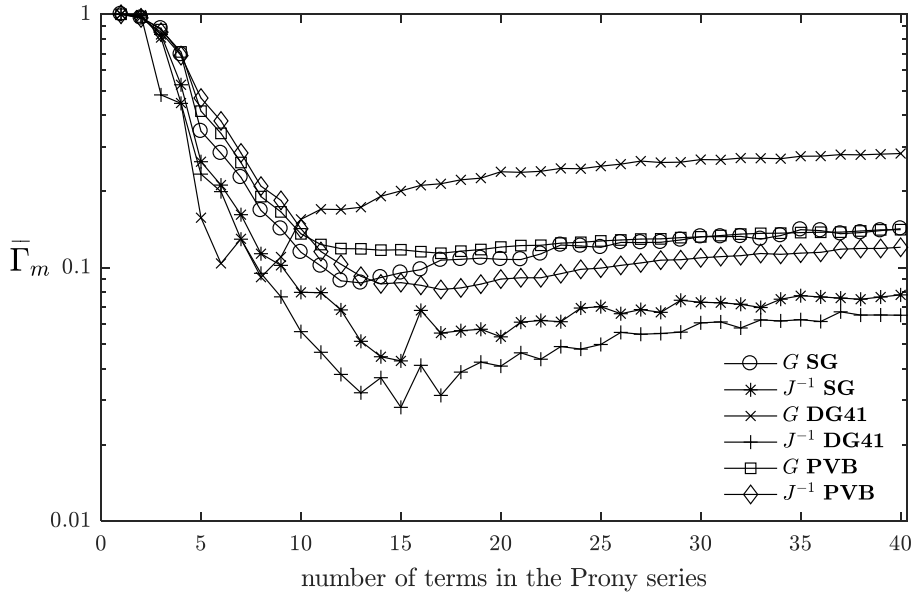

Figure 5.27 - error evaluation for Prony series with increasing number of terms

Figure 5.27 shows that a very high number of terms is not suited, if the purpose is to maximise the accuracy of the fit.

All things considered, the choice of the conclusive number N of elements for the series has been chosen mediating among the three different criteria:

[29] The data as they are collected prior to the polish procedure, which has been used to the sole purpose of running the fitting DOI algorithm and generate the series.

- series must be accurate over the entire time span,
- significant "jiggling" around experimental values must be avoided,
- the number of elements should be as low as possible.

A reasoned choice among several options finally led to the choice:

$$N = 20$$

This criterion was implemented in the general algorithm shown in Figure 5.13. With the final mastercurves coefficients, the normalized sum of square differences between the experimental data of shifted branches and interpolating Prony mastercurves $\bar{\Gamma}_m$ was found, allowing to find and compare the overall measure Γ of shift-factors accuracy among various distributions.

The shape of the 20-terms Prony series functions is displayed in Figure 5.28, compared to experimental data and coefficients are shown in Table 5.8.

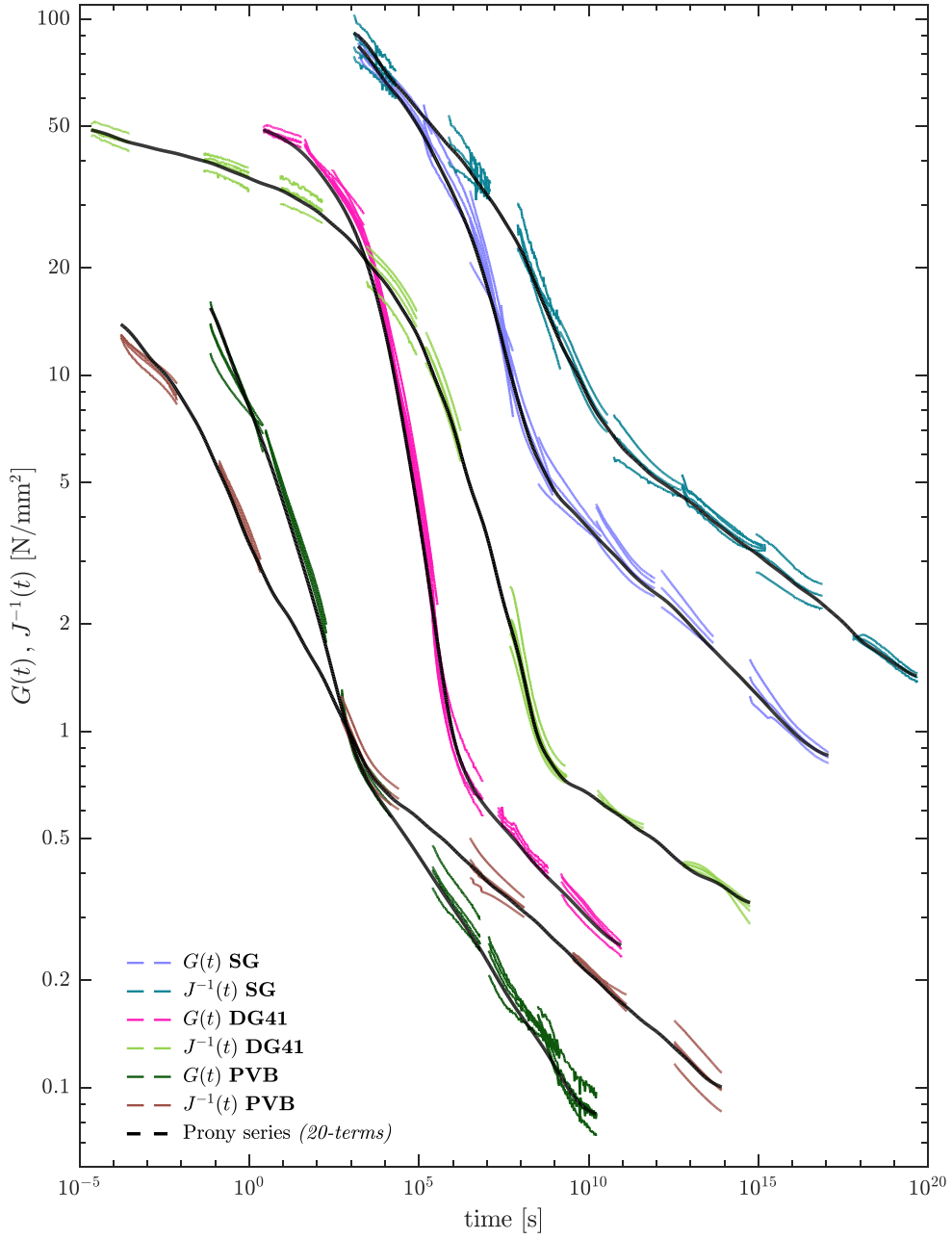

Figure 5.28 – final 20-terms Prony series mastercurves

Table 5.8 - mastercurves coefficients, $T_{ref} = 20℃$, time in seconds, moduli in MPa

	SG				DG41				PVB			
i	G_i	τ_i	J_i^{-1}	τ_i	G_i	τ_i	J_i^{-1}	τ_i	G_i	τ_i	J_i^{-1}	τ_i
0	0,845		1,415		0,245		0,325		0,083		0,098	
1	21,90	3,50E+03	24,46	4,08E+03	2,570	5,06E+00	4,027	9,35E-05	6,609	1,47E-01	3,553	4,81E-04
2	11,52	2,22E+04	13,11	2,83E+04	2,719	2,12E+01	2,287	8,32E-04	2,929	6,01E-01	2,505	5,44E-03
3	13,56	1,15E+05	11,85	1,76E+05	5,437	6,60E+01	2,112	8,29E-03	2,439	2,31E+00	2,741	3,94E-02
4	10,98	5,13E+05	9,119	1,18E+06	5,282	2,11E+02	2,703	7,01E-02	2,119	8,21E+00	2,301	2,78E-01
5	11,13	2,94E+06	8,660	4,73E+06	5,686	7,57E+02	3,148	6,91E-01	1,385	3,10E+01	1,379	1,85E+00
6	9,531	1,27E+07	8,004	5,90E+07	7,320	2,50E+03	3,282	8,30E+00	1,101	1,22E+02	0,720	1,87E+01
7	6,650	5,24E+07	8,698	3,53E+08	8,562	8,66E+03	3,533	7,88E+01	0,807	4,29E+02	0,565	1,55E+02
8	2,488	2,89E+08	4,398	2,78E+09	5,780	2,56E+04	5,220	6,50E+02	0,279	1,43E+03	0,452	1,15E+03
9	0,881	1,58E+09	2,791	1,47E+10	3,701	8,88E+04	5,224	5,04E+03	0,118	6,20E+03	0,154	7,56E+03
10	0,687	7,53E+09	1,378	1,10E+11	2,104	2,79E+05	5,506	5,77E+04	0,104	2,44E+04	0,097	8,09E+04
11	0,523	4,40E+10	0,811	7,44E+11	0,445	9,25E+05	5,544	5,15E+05	0,093	9,11E+04	0,089	6,71E+05
12	0,495	1,66E+11	0,570	7,10E+12	0,154	3,38E+06	3,521	4,04E+06	0,082	3,40E+05	0,083	5,07E+06
13	0,234	8,99E+11	0,657	3,72E+13	0,088	1,17E+07	2,040	4,00E+07	0,057	1,29E+06	0,054	4,15E+07
14	0,356	4,66E+12	0,454	2,32E+14	0,056	3,91E+07	0,754	2,46E+08	0,053	4,96E+06	0,054	3,43E+08
15	0,315	2,20E+13	0,454	1,67E+15	0,083	1,31E+08	0,117	3,02E+09	0,055	1,79E+07	0,048	2,63E+09
16	0,247	1,12E+14	0,397	1,10E+16	0,045	4,54E+08	0,095	3,68E+10	0,035	6,90E+07	0,038	2,07E+10
17	0,219	5,55E+14	0,338	8,52E+16	0,044	1,69E+09	0,074	3,40E+11	0,024	2,88E+08	0,030	1,57E+11
18	0,203	2,75E+15	0,338	5,56E+17	0,043	5,39E+09	0,093	4,70E+12	0,033	1,22E+09	0,023	1,44E+12
19	0,157	1,30E+16	0,224	4,00E+18	0,038	1,74E+10	0,041	3,77E+13	0,021	4,28E+09	0,025	1,08E+13
20	0,091	5,92E+16	0,189	2,14E+19	0,029	5,94E+10	0,053	2,63E+14	0,003	1,45E+10	0,011	5,02E+13

5.1.2.5 ANALYTICAL AND TABULATED RESULTS

With the experimental outcomes presented in the previous paragraphs, results for both relaxation $G(t,T)$ and creep compliance $J^{-1}(t,T)$ can be given as a function of time at an arbitrary temperature for any of tested materials.

A case study is shown on the procedure for extracting from mastercurves and WLF equations the solution for a specific material, time, temperature and action (i.e. imposed stress or strain). For a DG41 interlayer, whose relaxation modulus G is needed after 10 minutes of imposed strain at a temperature $T = 25$°C, the WLF coefficients $C_1 = -53{,}36$ and $C_2 = 228{,}43$ can be retrieved from Table 5.7 p.141, and the shift factor a_T can be computed by rearranging the WLF equation as follows:

$$a_T\left(T, T_{ref}\right) = 10^A \qquad \text{with} \qquad A = \frac{C_1\left(T - T_{ref}\right)}{C_2 + \left(T - T_{ref}\right)}$$

yielding $a_T = 0{,}072$. The coefficients G_0, G_i and τ_i for the DG41 relaxation mastercurve are in Table 5.8 p.148, while the time-shifted Prony series is:

$$G(t,T) = G_0 + \sum_{i=1}^{20} G_i \exp\left(-\frac{t}{a_T\left(T, T_{ref}\right) \cdot \tau_i}\right)$$

As mastercurve coefficients are given with τ_i in $seconds$ and G_i in N/mm^2, converting to the appropriate dimensions ultimately yields:

$$G_{DG41}(600\ s, 25\text{°C}) = 14.31\ MPa$$

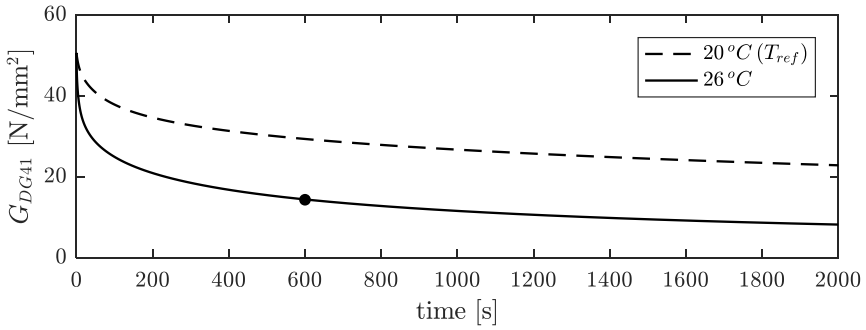

Figure 5.29 - DG41 relaxation modulus over time for $T = 26°C$

The analytical solution is arguably not always an optimal tool from a LG design perspective. In preliminary design phases, to envisage general design choices, an order of magnitude for interlayer modulus is usually plenty just to grasp the properties of laminated elements. Simplified tabulated results[30] are in Appendix G.

Values for short-term actions at low temperature and for long-term ones at high temperatures have not been shown in the tables for two different reasons, related either to the range of the experimental analyses or the nature of the analytical model used to build the mastercurves.

Limits of both analytical and tabulated results will be further discussed in §5.1.2.6, along with suggested safety factors that should be considered for a safe LG design.

5.1.2.6 LIMITS AND RELIABILITY OF RESULTS

Results gathered using Prony series mastercurves should always be looked at with a critical eye to the whole range of materials properties. As the original theory for time-temperature superposition has been developed for dynamic tests (cfr.

[30] Tabulated times have been chosen according to the design instructions for load durations described in prEN16612-2013 and used in CNR-DT 210/2013.

§3.1.3.5) [114,291], application to direct shear tests as those performed in this work must account for the actual testing conditions.

In chapter 4, it was discussed how experimental curves for relaxation and creep (cfr. Figure 4.35 to 4.37) start to be reliable after a finite time interval. While short-term effects for high and intermediate temperatures can be drawn through the mastercurve gathering from experimental results at lower temperatures, the same cannot be said for the lowest temperatures (i.e. 20°C for SG, 10°C for DG41 and 0°C for PVB). Lowest temperatures must account for their own reliability, so short-term properties cannot not be extrapolated from the series prior the reliability limit (this justifies blank values in the top-left corner of Tables in Appendix G).

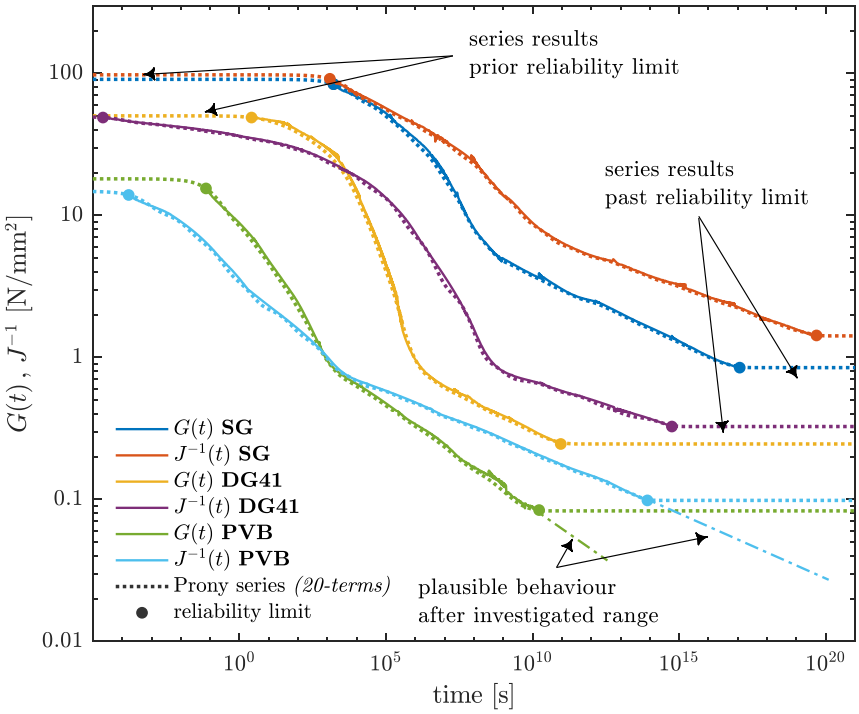

Figure 5.30 - reliability limits for mastercurves Prony series

Besides, for long term effects on the right side of the curves, a limit to the reliability of Prony series results must also be provided. The Wiechert model (cfr. §3.1.3.1) on which the Prony series are based, implies the presence of a finite value of each modulus upon which the material settles for an infinite amount of time[31] [243]. Nonetheless, the shape of experimental mastercurves suggest that, if tests had been performed for higher temperatures or if the same tests had been carried out for longer times, the shape of the curves may have continued a descending trend, rather than reaching a steady value (Figure 5.30). To avoid extracting inaccurate value from the series, reliability limits for which values are reliable are given as a function of time t and temperature T:

$$10\text{^}\left[\log_{10} t_1 - \frac{-C_1(T-T_{ref})}{C_2+(T-T_{ref})}\right] \leq t \leq 10\text{^}\left[\log_{10} t_2 - \frac{-C_1(T-T_{ref})}{C_2+(T-T_{ref})}\right]$$

where t_1 and t_2 are the maximum and minimum reliability times for the mastercurve at the reference temperature T_{ref} (Figure 5.30 and Table 5.9) and C_1 , C_2 are the WLF coefficients.

[31] Coefficients G_0 and J_0 in Table 5.8 stand for this infinite modulus value (cfr. §3.1.3.1), for relaxation and creep functions respectively.

Table 5.9 – reliability times in seconds

	SG		DG41		PVB	
	relax.	**creep**	**relax.**	**creep**	**relax.**	**creep**
t_1	$1.63 \cdot 10^{3}$	$1.23 \cdot 10^{3}$	$2.67 \cdot 10^{0}$	$2.19 \cdot 10^{-5}$	$7.18 \cdot 10^{-2}$	$1.65 \cdot 10^{-4}$
t_2	$1.16 \cdot 10^{17}$	$4.85 \cdot 10^{19}$	$9.02 \cdot 10^{10}$	$5.64 \cdot 10^{14}$	$1.62 \cdot 10^{10}$	$8.27 \cdot 10^{13}$

Note how the shape of the reliability limits is closely correlated to the shape of the WLF equation; in fact, the same technique used to define the reliability limits can be applied to plot the results on simple graphs, correlating time, temperature and materials moduli. These graphical results are also shown in Appendix G.

An important aspect to evaluate concerns short-term properties of tested materials, namely their known load/strain rate dependent properties (cfr. §3.2 and §4.2). Analyses performed with LG specimens are dedicated to study viscous effects, which are increasingly important with passing of time. Hence, the goal of proposed viscoelastic models is to reliably replicate the effects of long-term constant actions, while the rate at which these actions are applied has a limited influence on the test outcome. Conversely, analyses described in §5.1.1 for the tensile response of thermoplastic interlayers showed that the stiffness of such materials for short-term effects is highly non-linear and influenced by the rate at which actions are applied.

Instantaneous elastic properties are always superimposed to the viscoelastic effects [114,282,291,292], therefore outcomes of viscoelastic analyses should always be looked at with a critical eye. Results given in terms of Prony series mastercurves and WLF coefficients are not meant to describe short-term properties of the materials (indicatively, not much shorter than 5-10 minutes). Therefore, short-term relaxation and creep moduli found with a linear viscoelastic approach should be considered as conservative lower bound values of both creep and relaxation, as if actions were applied at an infinitesimal stress or strain rate. In reality, the stiffness of the materials for short-term effects is influenced by the strain-rate hardening response described with the GR model in 5.1.1.2. In fact, the actual short-term response of LG elements can possibly be better anticipated using the results of short-term tensile tests on interlayer specimens, neglecting all viscous effects.

5.1.3 TEMPERATURE-DEPENTENT ADHESIVE PROPERTIES

Adhesive properties of interlayers in glass lamination are usually investigated with TCT tests[32]: the ends of two-layered LG specimens, whose glass has been artificially cracked on both sides, are pulled with a constant displacement rate. The peak load measured during these tests can be correlated to the adhesion among the materials. Nonetheless, this interpretation is intrinsically correlated to the geometry of specimens and is not prone to be easily generalized [125,293]. While adhesion is represented in many ways, what is measured is really the "practical adhesion" which is defined as the force or the work required to detach a film or coating from its substrate [294]. K. L. Mittal wrote [295]:

> *"A frequently asked question is: What is the best method for measuring adhesion? The answer is: the best, rather most appropriate, method is one that simulates usage stress conditions."*

[32] Through Crack Tensile test

To my knowledge, full loss of adhesion of glass-interlayers interface has never been reported as an issue in the LG market. In most cases, a partial debonding (i.e. a loss of adhesion which only affects a potion of the interface) is enough to deem that the element has essentially failed its purpose: aesthetics and transparency, trait features of LG, are henceforth compromised. Also, the perception of security of the structural element is compromised from the end-user point of view, even though the mechanical properties may not have been deeply affected. Therefore, a study is shown on the conditions under which the adhesion has been observed to be undermined in LG safety glass.

Interlayer materials are known to have crucial temperature-dependent properties (cfr. §1.1.2), which are yet to be effectively correlated with the strength of the adhesion bond with glass. Even though tests on LG specimens described in §4.2 were not purposely aimed to this analysis, results discussed in §4.2.4.5 and described in Appendix C allow for some considerations. Far from attempting to a detailed dissertation on this very articulate and complex topic, contents of this paragraph can be looked at as a first step for the design a specific investigation, should the circumstances demand for a better understanding of LG delamination. Recent researches highlighted that the strain rate (i.e. the instant power distribution over which the strain energy builds up) is a relevant factor in the onset and progression of delamination [293]:

> *"Using the TCT test, we have shown that steady state delamination can be obtained only in a limited range of temperature and applied velocity."*

Alas, for specimens where delamination was measured at the end of tests, there is no reliable data indicating the exact time frame when delamination process has started, and how it has evolved over time. Nonetheless, in some tests the climatic chamber was open for very brief periods after the end of the loading phase (i.e. when presses are loaded by fastening of the loading bolt Figure 4.11 p.73) to perform small operations and to check the setup. Observations during those operations showed that some delamination had already occurred shortly after the end of the loading phase (about 10 minutes to one hour). While the extent of the delamination could not be measured accurately in those phases, neither compared to the final delamination described in Appendix C, the simple observation that some had occurred allows to ascribe to the loading phase itself a role in setting the conditions for the surpass of the fracture toughness threshold. With this consideration, an estimate of adhesion thoughtless can be given in terms of supplied energy throughout the loading phase, similarly to more traditional tensile tests [125]. An analysis in that direction has been performed for all specimens with numerical integration of recorded force F and displacement δ data. Figure 5.31 presents a graphical interpretation of this analysis for one of the specimens[33].

$$E_{ext} = \int_{\delta_0}^{\delta_1} F(\delta)d\delta \cong \frac{1}{2}\sum_{i=1}^{N-1}[(\delta_{i+1} - \delta_i)(F_{i+1} + F_i)] \quad ; \quad P = \frac{d}{dt}E_{ext}$$

[33] To help correlating these results to other parts of this manuscript, data is shown for specimen S12 (one of the SG-laminates), one among those that had been previously chosen as a case study for the data analysis in §4.2.2 and respective subparagraphs.

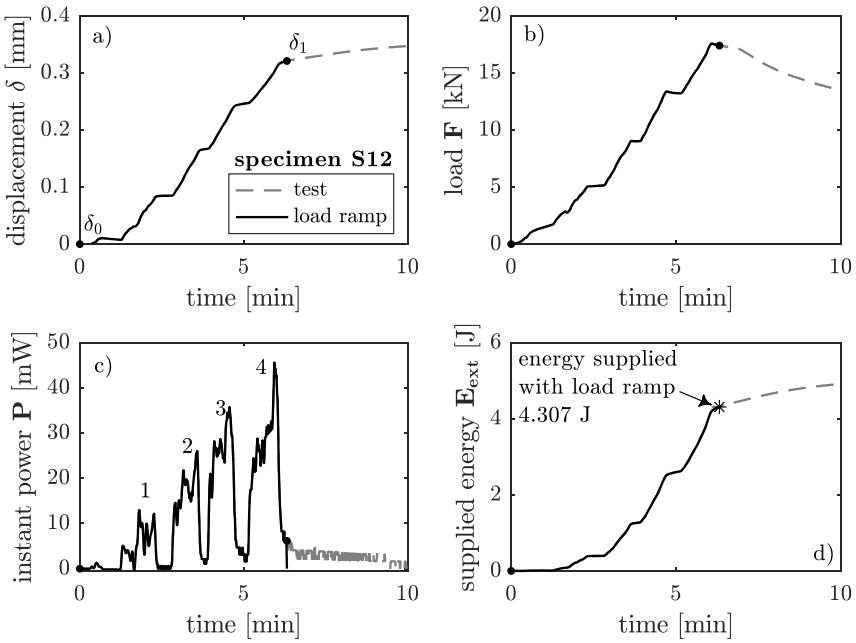

Figure 5.31 - a) displacement and b) load over time for specimen S12 (55°C), c) instantaneous power and d) supplied energy by numerical integration

Figure 5.31.a shows the progression of the loading phase with the four imposed displacement steps performed by design, to progressively load the specimens; Figure 5.31.c highlights that the energy is supplied in the same number of "chunks" corresponding to the manual bolts tightening.

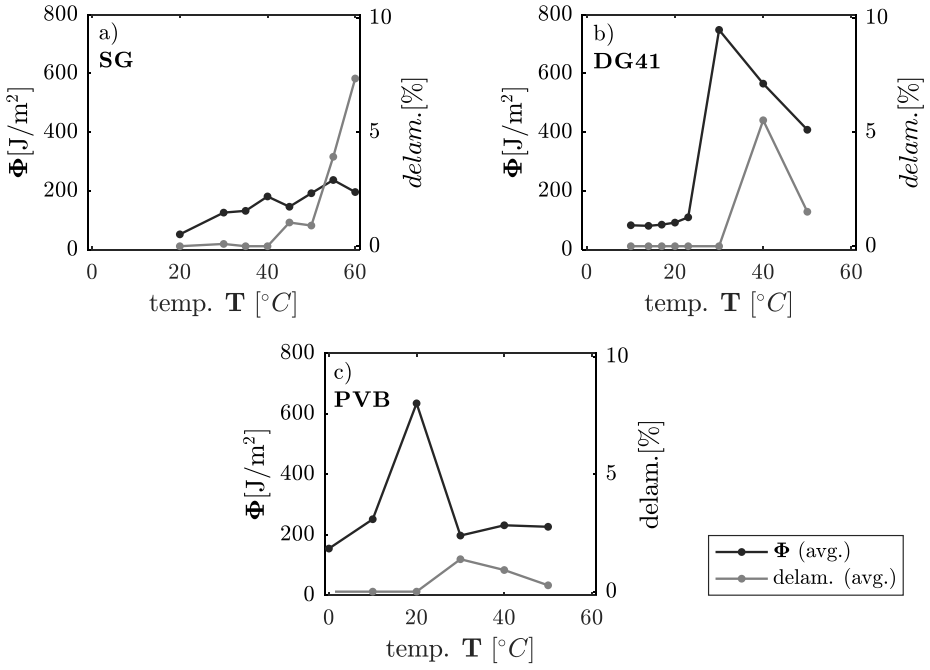

Figure 5.32 - average delamination correlated with average loading energy density

Results show that most of the energy is supplied in the loading phase. The energy density of the glass-interlayer interfaces Φ can be computed dividing the supplied energy for the area of the interlayers[34]. Details are in Appendix H.

[34] approximately 2000 mm^2, varying from one specimen to another for manufacturing tolerances.

Figure 5.32 condenses average data from the delamination analysis (Appendix C) and outcomes of load energy density calculations (Appendix H); the resulting correlation helps to draw some general conclusion on the fracture toughness of the glass-interlayer interface. The maximum imposed shear stress τ in the loading phase to the average extent of delamination for each material.

Table 5.10 – glass-interlayer fracture toughness estimate for varying temperatures

Temp.	**fracture toughness** $[J/m^2]$		
[°C]	**PVB**	**DG41**	**SG**
0	>165	*n/d*	*n/d*
10	>264	>100	*n/d*
14	*n/d*	>100	*n/d*
17	*n/d*	>97	*n/d*
20	>639	>106	>55
23	*n/d*	>118	*n/d*
30	170÷196	>788	>126
35	*n/d*	*n/d*	>148
40	<274	<518	>185
45	*n/d*	*n/d*	<115
50	<199	<333	160÷190
55	*n/d*	*n/d*	<215
60	*n/d*	*n/d*	<161

Results agree with outcomes of other researches on PVB interlayers: about $> 5\ kJ/m^2$ at 20°C for $\dot{\delta} = 1\ mm/s$ (Elzière, 2017 [293]), stressing how temperature plays a key role in defining the fracture toughness of the interface. Information on the energy density alone seems to be insufficient to assess whether delamination will arise: the interface in able to take in significant energy at lower temperatures without compromising the integrity of the adhesion, on the other hand, while temperature rises, lower energy levels are capable to onset partial delamination.

5.2 POST-FAILURE PROPERTIES OF LG

Experimental evidence discussed in §4.3 shows that both the increased stiffness provided by damaged glass plies in PDLG and residual stiffness of FDLG beams is significant. For given climatic conditions, because of the higher short-term stiffness of new interlayer materials (cfr. §4.2 and §4.1), post-failure performance of LG elements can be substantially enhanced compared to more traditional structures, laminated with PVB interlayers.

5.2.1 ANALYSIS OF THE TENSION-STIFFENING EFFECT

A lower bound prediction of PDLG bending stiffness can be obtained by fully neglecting the mechanical contribution of broken plies. Nonetheless, experimental evidence suggests that after tempered glass shatters, it is still able to give a contribution to the overall bending stiffness, through its adhesion to the interlayers. Comparing experimental results to the minimum stiffness expected can provide useful insight for understanding this *tension stiffening* (TS) effect, quantifying the mechanical contribution of damaged glass plies.

This calculation requires once again the hypothesis that, glass being order of magnitudes stiffer than interlayers, it can be considered relatively undeformable (cfr. §4.2.1). This hypothesis implies that interlayer shear stress and strain can be approximated with uniform distributions.

In PDLG specimens, a fictitious equivalent elastic modulus for fractured glass plies $E_{fg,eq}$ can be estimated under two hypotheses: first, that fractured plies confined by adherent interlayers can still be looked at as an isotropic material, able to bear tensile and compressive stresses; the second, that the moment of inertia along the strong axis of damaged and undamaged plies is the same. The validity the first hypothesis is confirmed by experimental outcomes on the position of the neutral axis in PDLG, at least when quasi-static imposed loads are modest (cfr. §4.3.3.2, Table 4.9 p.110). For a simply supported LG beam having span L, assembled with three glass plies of thickness t_g and inertia $J_{1,g} = h^3 t_g/12$ about the strongest axis, with a concentrated load P_m at mid-span, the equivalent modulus for one ($E_{fg,eq,1}$) or two ($E_{fg,eq,2}$) shattered plies is:

$$E_{fg,eq,1} = \frac{P_m L^3}{48 J_{1,g} \eta_m} - 2E_g$$

$$E_{fg,eq,2} = \frac{a P_m L^3}{96 J_{1,g} \eta_m} - \frac{E_g}{2}$$

Table 5.11 - fictitious equivalent Young modulus [GPa] of damaged glass plies

	unit	A1	A2	B1	B2	B3	C1	C2	C3
stage I									
E_g †	GPa	66.3	67.8	66.4	65.8	68.5	66.7	67.1	69.1
stage II									
$E_{fg,eq,1}$	GPa	29.9	28.8	18.2	16.3	22.3	16.3	22.9	14.3
stiffness increase	%	22.5	21.2	13.7	12.4	16.3	12.2	17.1	10.3
stage III									
$E_{fg,eq,2}$	GPa	16.3	16.9	16.7	15.3	13.6	9.09	10.7	11.0
stiffness increase	%	49.2	50.0	50.3	46.5	39.7	27.3	31.9	31.8

† cfr. Table 4.8

where a is a correction factor accounting for torsional effects. With two broken plies, PDLG beams are bent laterally because of the asymmetric glass failure. As a result, applying a vertical force at midspan generates non-negligible torsional effects along with flexural ones. Throughout tests III-5 (Table 4.7), torsional restraints[35] (cfr. Figure 4.42 p98) were used to keep specimens in vertical position. Accounting for the exact position of the restraints and the extent of the lateral sag, the correction factor a has been calibrated with a 3D FE linear elastic model.

5.2.2 DYNAMIC TESTS

With the same simplified approach used for the analysis of three-point bending tests, the lower bound of expected frequencies for specimens in PDLG conditions can be anticipated, by neglecting the mechanical contribution of broken glass plies and interlayer while accounting for both of their masses[36]. An analytical

[35] which have been installed as close as possible to midspan for those tests.

[36] The exact weight of glass and interlayers has been determined experimentally with density tests performed after of all the analyses described in §4.3. Density results are: glass $2.489\ g/cm^3 \pm 0.2\%$, SG $0.987\ g/cm^3 \pm 1{,}2\%$ and DG41 $1.098\ g/cm^3 \pm 0.46\%$. The density of PC could not be assessed experimentally, the literature value of $1.21\ g/cm^3$ was used [350] (although, for this specific case study the volume of PC is so small that it could have been assimilated to DG41 interlayer with very limited consequences).

formulation is known for the frequency of the first modal form of a uniform beam of span L and modulus E_g, simply supported at both ends with uniform weight per unit length $\overline{w}$ (or mass per unit length $\rho = w/g$) with $a = 1.0$ [37] [107,296]:

$$f_1 = \frac{9.87a}{2\pi}\sqrt{\frac{E_g J g}{\overline{w} L^4}}$$

The expected natural frequency of specimens can be calculated in Table 5.12, using experimental values of the glass elastic modulus from quasi-static three-point bending tests (Table 4.8), along with material properties[36] and geometries described in §4.3.2. Such values have been compared to experimental data from bending tests. An analysis of the influence of boundary conditions is performed in Appendix F.

Table 5.12 - expected frequencies based on ULG three-point bending tests stiffness

	$E^{\dagger}$ x10^3 N/mm^2	J x10^7 mm^4	A_g x10^3 mm^2	A_{int} x10^3 mm^2	w_g x10^{-5} N/mm^3	w_{int} x10^{-6} N/mm^3	$\bar{w}$ N/mm	L x10^7 mm	freq Hz
A1	66,3	1,71	6,48	0,55	2,44	9,68	0,164	2,35	74,3
A2	67,8								75,1
B1	66,4								86,9
B2	65,8	5,35	8,40	0,85	2,44	1,08	0,212	2,7	86,5
B3	68,5								88,3
C1	66,7								85,1
C2	67,1	5,35	8,40	1,83*	2,44	1,08	0,225	2,7	85,3
C3	69,1								86,6

† *cfr. Table 4.8.*
* *an equivalent area of homogeneous DG41 interlayer is used, to account for the different density of PC embedded within the interlayer matrix.*

The approach used to compute the expected natural frequency in the ULG state can be tweaked, using additional hypotheses, and applied for both PDLG states (Stages II&III).

The minimum frequency expected, shown in Figure 5.33, can be computed by neglecting the mechanical contribution of damaged plies and interlayers (i.e. neglecting the TS effect), while accounting for all masses.

A better estimate of the experimental PDLG natural frequencies can be produced, based on data from three-point bending tests elaborated in §5.2.1, which quantify the TS effect. With an equivalent Young modulus for damaged plies (Table 5.11), an equivalent modulus E_{eq} can be computed for the entire cross section by homogenising material properties according to proportions shown below. Using E_{eq} instead of E_g in the previous formulation for f_1 yields results of the Equivalent Stiffness Model (ESM) for stages II & III shown in Figure 5.33.

$$E_{eq} = E_g\left(\frac{2}{3} + \frac{E_{fg,eq,1}}{E_g}\right) \qquad \text{for PDLG stage II (1 broken ply)}$$

$$E_{eq} = E_g\left(\frac{1}{3} + \frac{2E_{fg,eq,2}}{3E_g}\right) \qquad \text{for PDLG stage III (2 broken plies)}$$

[37] Validation of this analytical formulation, with calibration of the correction factor a for this case study is provided in Appendix F.

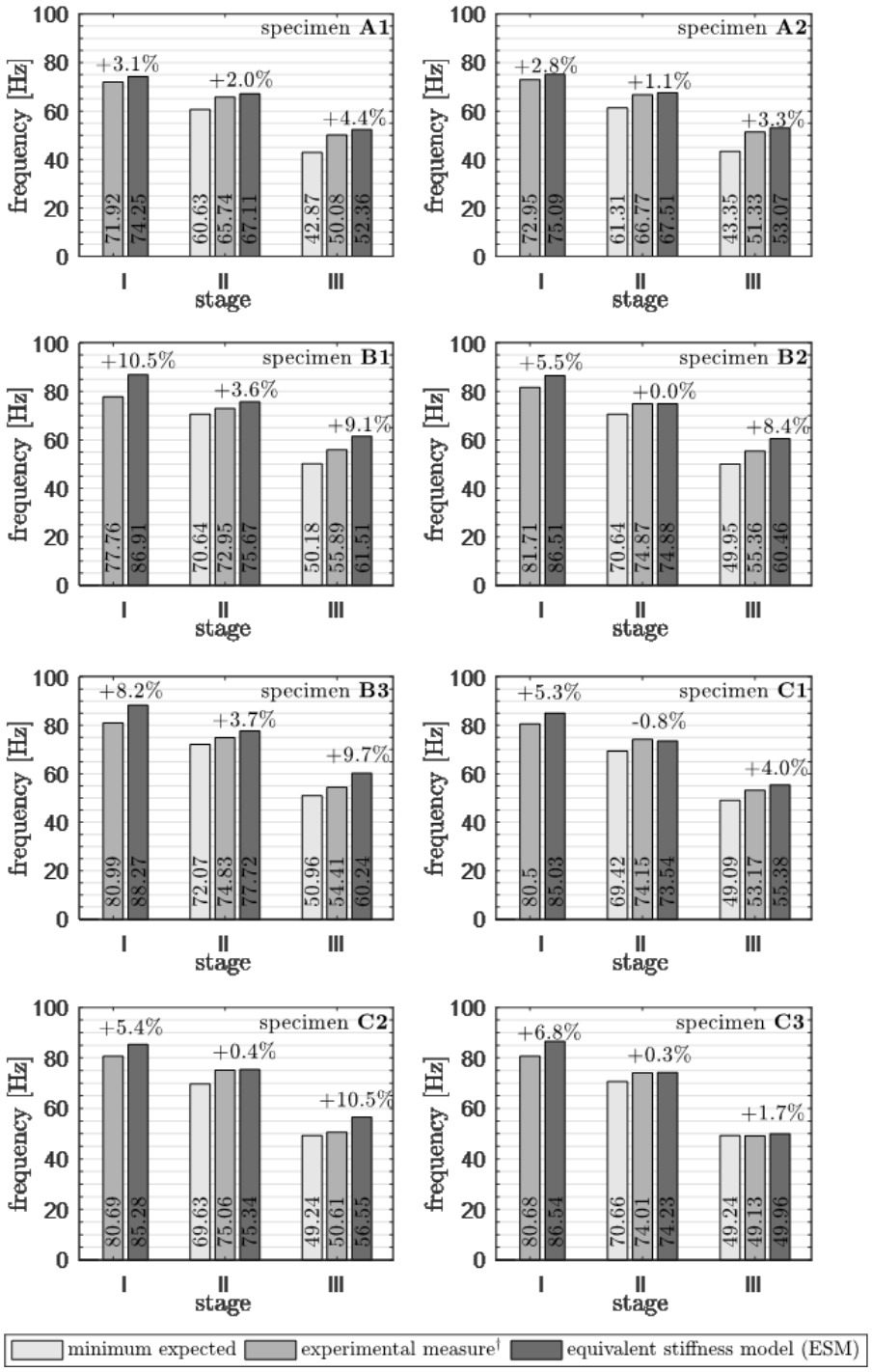

† *cfr. Table 4.10*

Figure 5.33 - experimental and model frequencies comparison

Although based on a small number of specimens and lacking statistical accuracy, results of the comparison shown in Figure 5.33 exhibit several consistent patterns, prompting to wide-ranging considerations.

Stage I – Undamaged Laminated Glass (ULG)

- The experimental natural frequency of undamaged LG specimens (Stage I) is consistently lower than expected, based on the ESM with glass properties descending from experimental three-point bending tests. Causes of this phenomenon were investigated thoroughly, but the fundamental reason for the discrepancy among the two measurements could not be tracked down.

Recorded data and instruments were double-checked multiple times showing no evidence of acquisition errors or unintended setup response.

- Dynamic test frequencies are always lower than the ESM ones.
- Comparison of dynamic and ESM for undamaged SG-laminated (Type A) seem to be closer one another, with a difference of about 3%. On the other hand, results for DG41-laminates (Type B & C), display a greater average difference, around 7%, regardless the presence of the PC foil and interlayer thickness.

Stage II & III– Partially Damaged Laminated Glass (PDLG)

- With the only exception of specimen C1, whose ESM frequency in Stage II is slightly lower compared to experimentally measured one (-0.8%), dynamic tests experimental results can be consistently found within the minimum expected frequency and equivalent stiffness model predictions.
- ESM model is more accurate for Stage II than for any other damage state, with predictions consistently within 4% relative error.
- Results for specimens B & C in Stage III are consistently close to the average of the ESM and minimum expected frequencies (e.g. for specimen B2 $55.36 \sim 55.21 = [49.95 + 60.46]/2$)

5.2.3 EQUIVALENT THERMAL EXPANSION MODEL

Tempered glass has strong compressive stresses on outer surfaces and tensile stresses inside. For undamaged tempered glass, compressive and tensile stresses are in equilibrium (cfr. §1.1.1); the outer surface of glass is plane and each portion exchanges equal and opposite actions with all neighboring ones. Due to the elastic behaviour of glass, when the glass fails, fragments release part of the stored mechanical energy by expanding at the edges, releasing compressive stresses, and contracting in the central part, releasing tensile stresses. A graphical interpretation of this phenomenon on a small scale is shown in Figure 5.34.

If a system, like an interlayer with good adhesion, can keep fragments from scattering away, the observed macroscopic behaviour of the fractured glass ply is its tendency to expand in its own plane.

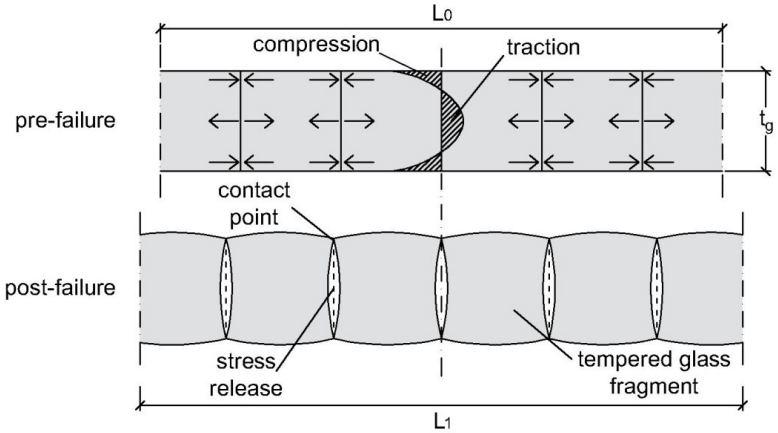

Figure 5.34 - fragmentation of broken tempered glass plies

An expansion originated by glass failure, such as the one illustrated in Figure 5.35, is arguably not easy to model starting from a microscopic point of view. Repulsion mechanisms originating the expansion are dependent on a variety of factors such as the strength and depth of the tempering process, thickness of glass plies, crack density and distribution, shape of the fragments, size of contact points between fragments, etc.

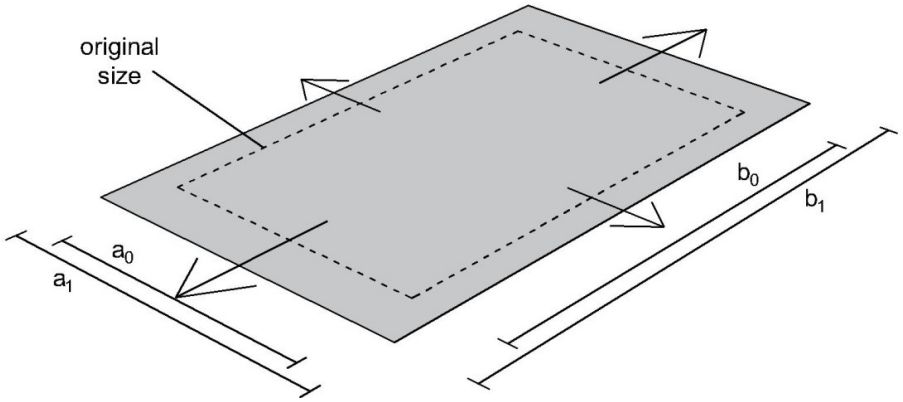

Figure 5.35 - expansion of a confined tempered glass ply upon failure

To model the mutual effects of broken tempered glass plies on undamaged ones, a simple model was put to the test for PDLG specimens, reproducing the effects measured with the onset of cracks using an Equivalent Thermal Expansion Model (ETEM)[38]. One can postulate that for the transition between Stage I and Stage II, if the interlayer shear stiffness was zero, the fractured glass size would increase freely, not involving the adjacent plies (Figure 5.36.a). Besides, if the hypothesis that plane sections remain plane still holds [164], a solution can be found with the flexibility method[39], as presented in Figure 5.36.

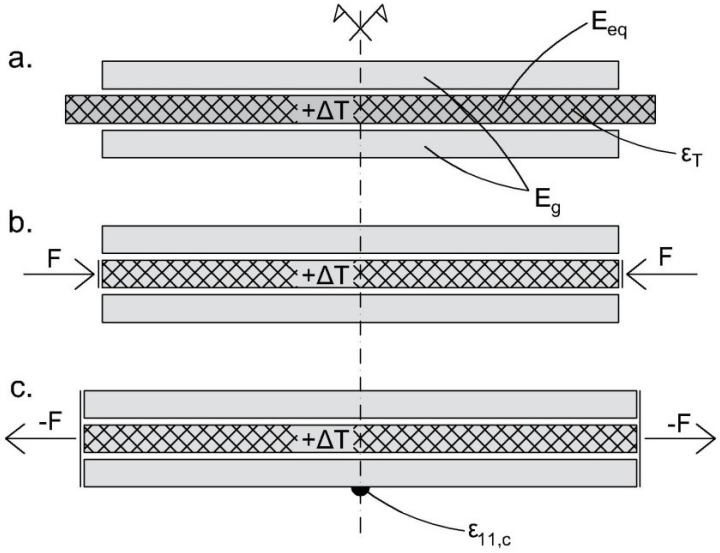

Figure 5.36 - flexibility method model for an expanding central fractured glass ply

An equivalent temperature variation ΔT_{eq} can be defined as a function of the previously defined fictitious equivalent modulus $E_{fg,eq}$ (cfr. §5.2.1) of the fractured glass ply. If the stiffness of interlayers is negligible compared with glass, fractured or not, and provided with the experimental measure of the axial strain on one lateral – undamaged - glass ply[40], it follows that:

[38] The FE model was built using an equivalent non-isotropic temperature gradient: a numerical gradient only applied in the two main dimensions of the specimen, but not across the thickness.

[39] Also known as method of consistent deformations.

[40] cfr. strain gauges $e13$ for specimens Type B & C shown in Figure 4.45 p.104.

$$\Delta T_{eq}(E_{fg,eq}) = \frac{1}{\alpha_g}\left(\frac{A_g}{A_{fg}}\frac{E_g}{E_{fg,eq}} + 1\right)\varepsilon_{11,c}$$

where A_g and A_{fg} are cross-sectional areas of undamaged and fractured plies respectively, $\alpha_g = 90 \cdot 10^{-7} K^{-1}$ is glass thermal expansion coefficient [5,19,38] and $\varepsilon_{11,c}$ is the longitudinal measured strain at mid-span on the outer undamaged plies upon failure of the central ply[41].

ΔT values have been calculated using results for $E_{fg,eq}$ of PDLG specimens with one or two broken plies (Table 5.11)[42].

Table 5.13 - equivalent modulus and gradient for PDLG models

	unit	B1	B2	B3	C1	C2	C3
E_g †	GPa	66.4	65.8	68.5	66.7	67.1	69.1
$\varepsilon_{11,c}$ (30s) ‡	$\mu m/m$	63.1	63.5	64.9	67.4	68.6	66.5
$E_{fg,eq,1}$ †	GPa	18.2	16.3	22.3	16.3	22.9	14.3
$E_{fg,eq,2}$ †	GPa	16.7	15.3	13.6	9.09	10.7	11.0
ΔT_{eq} stage II	K	58	64	52	69	52	79
ΔT_{eq} stage III	K	63	68	80	117	103	100

† *cfr. Table 5.11* ‡ *cfr. Figure 4.53*

With ETEM, a prediction of effects transferred trough the interlayers from shattered glass plies on undamaged ones is possible. With the calibrated thermal expansion described above for Stage II, Figure 5.37 shows results of different strain patterns on the outer surface of the external glass ply (Figure 5.37.a) and within the interlayer (Figure 5.37.b), varying the stiffness of the interlayer itself.

Numerical results allow to study shear stresses transfer mechanism through the interlayers. Regardless the stiffness of the material, the shear transfer zone from the expanding central ply to the outer undamaged plies shows a peak between 50-100mm from the edge ((Figure 5.37.b) This peak shrink over time, while the transfer zone progressively expands towards the inner regions, for diminishing interlayer shear modulus. The steady value of strain at midspan proves that the total shear transfer is consistent over time (i.e. for a relaxing interlayer).

Numerical results have been validated in Figure 5.38 with experimental measurements gathered with tests II-1 (cfr. Table 4.7 p.101) for Type B specimens. Results of this comparison are consistent with a swiftly relaxing material: strain gauges $e11$ and $e15$, at 50mm distance from the lateral edges of the beams, show considerably high strains at failure, rapidly dropping in the a few minutes. This entails that on the outer edges the interlayer material rapidly loses the ability to transfer a significant amount of stress from the central fractured ply to the lateral ones. On the other hand, instruments $e12$, $e13$ and $e14$ are noticeably steady, an observation in full agreement with results presented in Figure 5.37.a.

Numerical model results for the positions corresponding to instruments $e12$, $e13$ and $e14$ are in perfect agreement with experimental results around 30 s after the

[41] Conventionally, the strain measured by instrument $e13$ after thirty seconds from the failure of the central ply was used. Figure 4.53 p.115 shows the progression of $e13(t)$.

[42] With the aforementioned hypotheses, such procedure is only rigorous for Stage II, a symmetrical damage state. The same procedure is an approximation for the asymmetric Stage III, the curvature-induced effects as with two broken plies are neglected.

failure of the class ply. This should come to no surprise, as the ETEM with whom the numerical analysis was carried was calibrated with experimental readings at 30 *s* after failure of the glass ply.

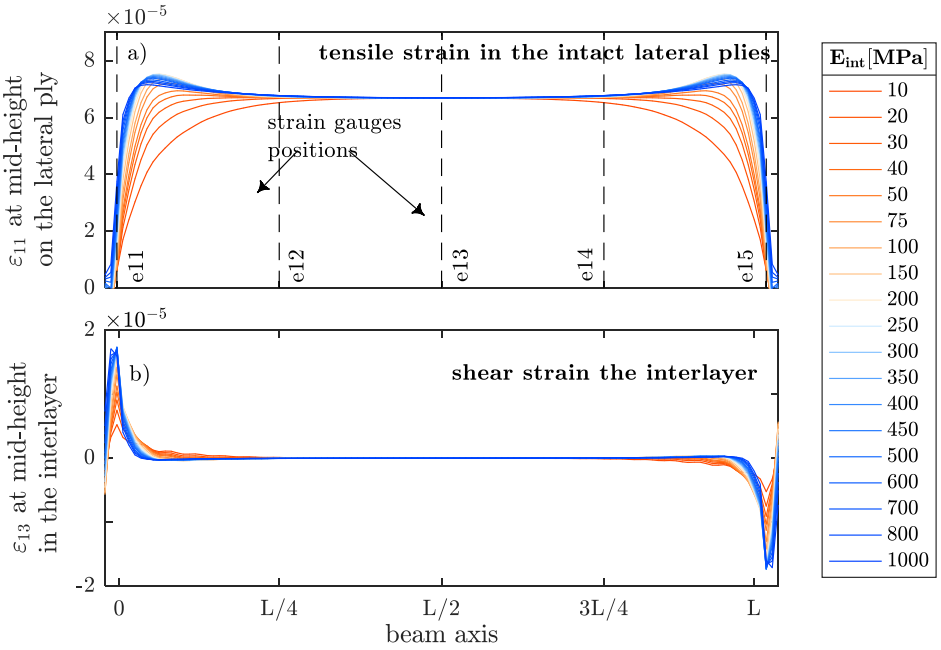

Figure 5.37 - Stage II linear elastic finite element results using ETEM

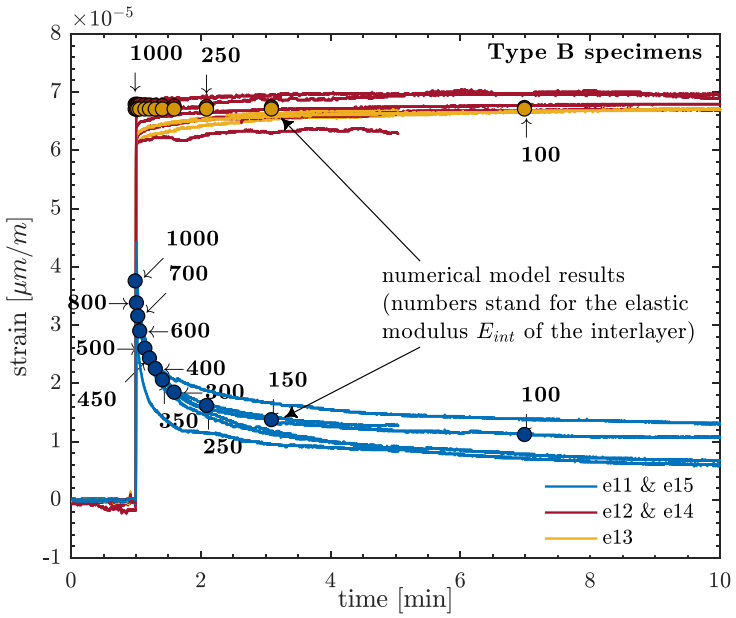

Figure 5.38 - numerical model compared to experimental strain measures

The slightly rising trend of those three instruments in the first minutes has to be ascribed to the delay in the formation of some of the cracks: once tempered ply fails, most cracks are generated almost instantly; however, experimental observations showed that the number and density of cracks grew slightly over a few hours. In point of fact, this agrees with the idea that interlayers exhibit a stronger action in immediately after failure, meaning that they are more effective in holding back the fragments. As the time passes, viscous deformations originate a progressive drop in their ability to clasp the fragments and contain partially-formed cracks from expanding further. Consequently, a few new cracks form over time, contributing to the overall expansion of the fractured ply. From a

macroscopic point of view, this behaviour results in a delayed expansion, a phenomenon which was not taken into account in our model. Finally, the gradual reduction of recorded strain over time, which was recorded after the first hour up to 24 hours in Figure 4.51 p.106, can be instead ascribed to the relaxation of the shear modulus of interlayer materials, due to viscous effects.

Consistently with results for creep and relaxation discussed in §5.1.2, this comparison proves once again that DG41 interlayer modulus at room temperature is very high for short and impulsive actions (about 1 to 2 GPa), but rapidly diminishes for its inclination to viscous relaxation.

Furthermore, the ETEM can be used to analyze non-symmetrical damage states, like Stage III specimens with central and one of lateral plies broken (cfr. Table 4.7 p.101). With data in Table 5.13, insight on the lateral deflection can be obtained and compared with experimental measurements (Test III-2) Figure 5.39.

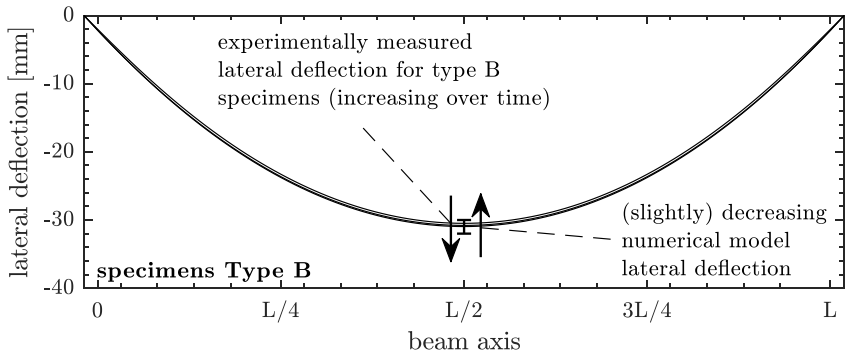

Figure 5.39 – Stage III lateral deflection comparison (view from above)

Results from the numerical model highlight that a decrease of the interlayer's stiffness[43], does not translate in a significant variation of the lateral deflection, which is mainly affected by geometrical properties (i.e. the numerical model showed that the thickness of the plies and the length of the specimens are the main factors affecting the lateral deflection). Nonetheless, while the numerical model shows a progressively diminishing sag for diminishing interlayer stiffness, experimental measurements show instead a slight sag increase. This inconsistency may be explained by pointing out that the ETEM model doesn't account for the delayed increase in the number of cracks, which in fact contributes to expanding the lateral and central broken plies, thus inducing a further sag increase.

5.2.4 FULLY DAMAGED LG MODELS

Uniaxial tests performed on SG-laminated samples (cfr. §4.3.4 p.113), cut out of Type A specimens after all tests had been performed, allow for a better understanding of both TS effect and compressive response of glass fragments.

Experimental results described in Figure 4.65 can be compared with simple models known in literature [38,55,63] and experimental outcomes on interlayer specimens analysed in §4.1, whose results can be seen in Figure 4.4 p.66. The latter comparison is shown in Figure 5.40. While interlayer results are shown for a strain rate which is almost double the strain rate for FDLG[44] (i.e. results of dotted curves

[43] Either for conspicuous viscous relaxation or a choice of a different, softer, interlayer material.

[44] The strain rate of $\dot{\varepsilon} = 87 \cdot 10^{-4} s^{-1}$ has been calculated knowing the speed rate ($v = 5mm/min$) and the span of dog-bone specimens between the clamps ($95mm$, cfr. §4.1.1).

are overestimating the response one would record for the same specimens at $50 \cdot 10^{-4} s^{-1}$), a very significant TS effect is measured, due to the presence of adherent glass fragments. While tests on FDLG could not be carried out up to very high strain to preserve the instruments (cfr. §4.3.4), plausible forecasts can be hypothesized, if glass fragments adhesion is eventually lost and FDLG ultimately deteriorates to the interlayer only.

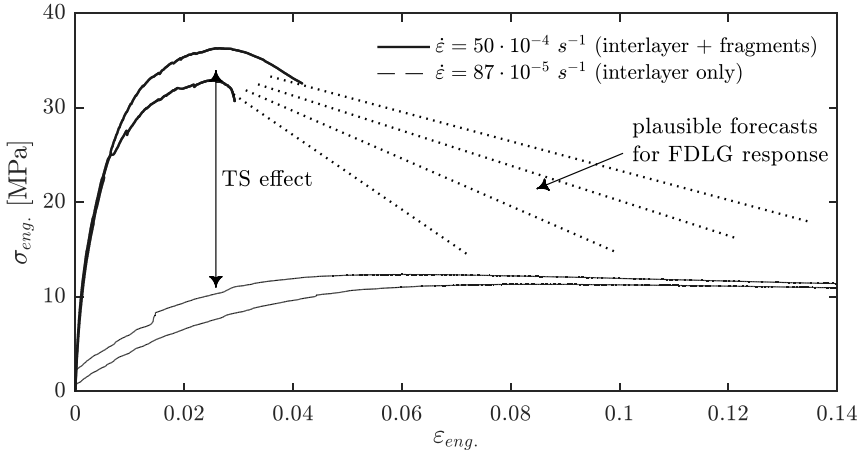

Figure 5.40 - Experimental results of tensile tests on FDLG specimens

A different comparison can be performed using the effective modulus formula [63,104], allowing to estimate the proportionality coefficient k for the maximum load bearing capacity of SG-laminated fractured glass at room temperature:

$$E_{eff} = k \frac{l^*}{\lambda^*} E_p$$

Table 5.14 – effective modulus E_{eff} in FDLG with SG interlayer [MPa]

E_{eff} as a function of total elapsed time					
	strain rate $[s^{-1}]$	*5 s*	*10 s*	*30 s*	*60 s*
slow test	$5 \cdot 10^{-5}$	9300	8110	5864	4283
fast test	$5 \cdot 10^{-4}$	6320	4464	2153	1133
E_{eff} as a function of total accumulated strain					
	strain rate $[s^{-1}]$	*0.0025*	*0.005*	*0.015*	*0.03*
slow test	$5 \cdot 10^{-5}$	4662	3292	1686	899
fast test	$5 \cdot 10^{-4}$	6320	4464	2153	1133

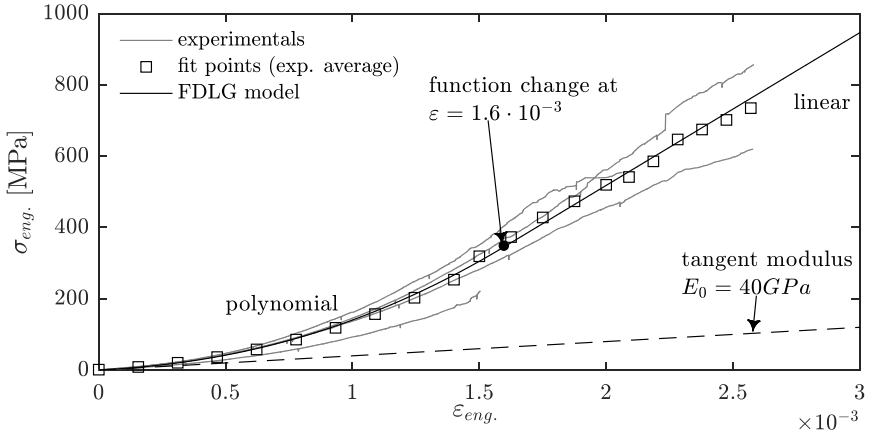

Figure 5.41 – FDLG compression tests and proposed constitutive law

The size of a typical $10mm$-thick tempered glass ply fragment was measured between $l^* = 6 - 10\ mm$ on average. Up to the maximum stress (around 0.025

strain), the effective modulus appears to be higher than SG interlayer alone; comparing numerical data on tensile tests for FDLG with the photographic follow-up carried in §4.3.4, one can estimate the depth of the delaminated surface λ^* around $18-39\%$ the size of the glass fragments, yielding $0.45 < k < 0.6$. Table 5.14 lists values of the modulus E_{eff} for SG-laminated FDLG.

Compression tests performed on FDLG specimens are also described in §4.3.4, showing a remarkable hardening behaviour. As experimental curves presented an initial nonlinear branch, followed by a linear one (cfr. Figure 4.67 p.116), it was observed that such stress-strain correlations could be well approximated through a hardening polynomial up to $\varepsilon\sim1.6‰$, followed by a linear function for higher strains, up to the ultimate failure.

The hardening behaviour, represented by the progressive change of slope of the curves, is arguably due to closing of cracks and subsequent transmission of compressive stresses through direct contact between glass fragments. Table 5.15 lists main mechanical parameters obtained from tensile and compression tests on FDLG specimens for tensile and compressive actions.

Table 5.15 – mechanical parameters for SG-FDLG made with tempered plies

Tensile tests		
Secant modulus at $5MPa$	E_0	$9 \div 21\ GPa$
Yielding stress	σ_y	$25 \div 36^{\dagger}\ MPa$
Yielding strain	ε_y	$0.02 \div 0.03$
Long term stress asymptote	σ_a	$19 \div 22\ MPa$
Compression tests		
Secant modulus at $30MPa$	E_0	$60 \div 360\ GPa$
Ultimate stress	σ_u	$200 \div 900\ MPa$
Ultimate strain	ε_u	$0.002 \div 0.003$

† *The higher value refers to higher strain rate.*

Stage IV tests (cfr. Table 4.7 p.101) highlighted that the load-bearing capacity of FDLG beams is not entirely lost. Significant detrimental effects of time have been observed, as they triggered a drastic reduction of both the stiffness and ultimate strength in SG-laminated specimens (Type A) and total loss of shape and load-carrying capacity for DG41-laminated ones (Type B). Reinforced DG41-laminates (Type C) showed an intermediate behaviour.

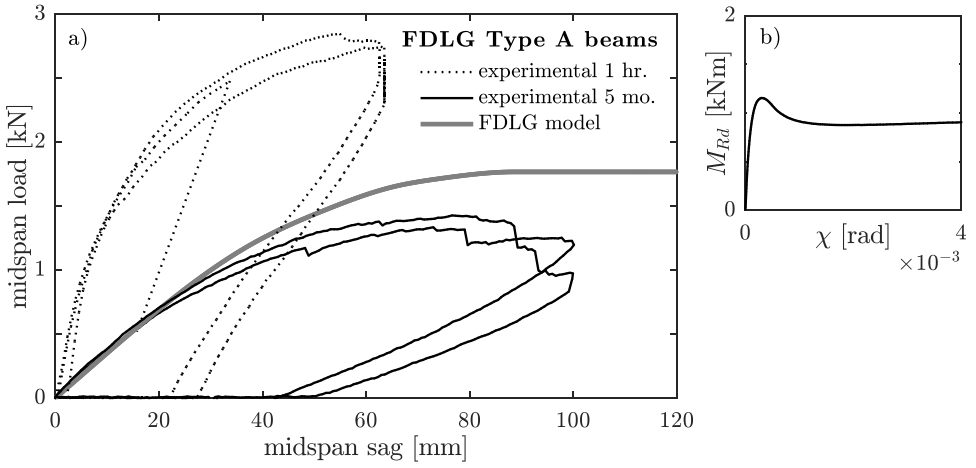

Figure 5.42 - FDLG bending tests comparison to analytical model

For Type A specimens, both initial stiffness and ultimate strength decreased with storage time: mechanical properties of FDLG beams appeared to have substantially changed after five-month storage, compared to properties of observed a few hours

after the failure of the last glass ply. The decrease in stiffness and strength can be explained by considering that glass cracks allowed for a widespread exposition of the interlayer to moisture during the storage interval, triggering a decay in the chemical bonds between glass and interlayers around each glass fragment [45].

A simple FDLG analytical beam model was defined using stress-strain curves drawn from tensile and compression tests. For tensile stresses, "slow tests" were used (cfr. Figure 4.65.a p.115), as the strain rate of three-point tests on FDLG beams was the same imposed in those tests. The FDLG model curve in Figure 5.42.a was obtained by computing the moment-curvature diagram $M = M(\chi)$ with experimental constitutive equations for tensile and compressive actions (Figure 5.42.b), then integrating the curvature twice over the beam axis. Boundary conditions of a simply supported three-point bending test were considered.

Figure 5.42 shows how the analytical model can accurately predict the response of five-month old FLDG beams (which ought to be expected, as the material specimens used to perform tensile and compressive tests and draw the experimental stress-strain correlations were extracted from those LG beams and tested a few days after). On the other hand, the analytical model seems to overestimate the ultimate load-bearing capacity and stiffness after the initial part of the curves.

Differences between the model and 5-month experimental results can be explained by comparing the experimentally recorded strain at the bottom and at the top of beams (through "omega" transducers in Figure 4.44 p.99) with those of "material specimens" in tension and compression tests (Figure 5.43).

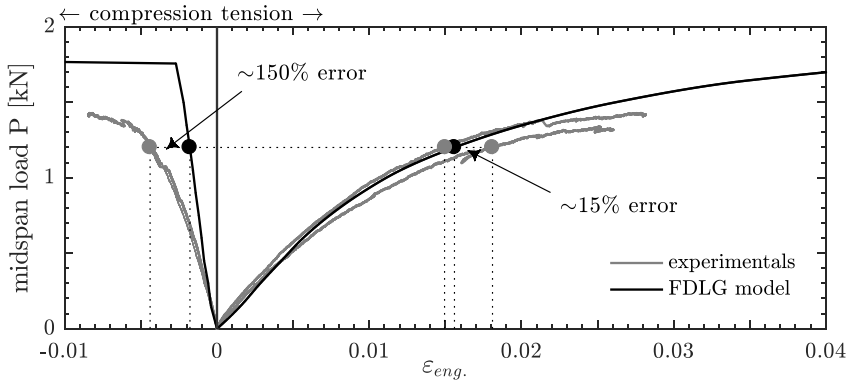

Figure 5.43 – experimental compressive and tensile strain on top and bottom of the beam at midspan, compared to FDLG analytical model results

In the tensile region (to the right in Figure 5.43), the model quite accurately predicts the strain pattern in 5-month old FDLG beams. On the contrary, the model is only accurate in the initial part of the compressed region (to the left in Figure 5.43), for loads approximately on third the ultimate capacity, while it vastly underestimates the strain at top fibres for higher loads. As an example, at a load of 1.2 kN (85% of the ultimate capacity) the error is around 15% in the tensile region, but is about one order of magnitude higher in the compressed region.

Very high differences in the compressed region can be explained considering the greater confinement of glass fragments in uniaxial compression tests, rather than in the compressed region on top of the FDLG beams in three-point tests. In the latter case, a progressive expulsion of shards and fragments was observed from top of the beams, which can explain both the lower stiffness and the reduced value of the ultimate load capacity with respect to the model.

5.2.5 DELAMINATION AND TS EFFECT

As the depth of the delamination grows, the tensile stiffness of the composite material (glass fragments + interlayer) tends to the stiffness of the interlayer alone. On the other hand, the interlayer exhibits an increased stiffness because of the migration of stresses between glass fragments and the interlayer. This pattern creates stress concentrations at the edge of the delamination surface, inducing more delamination over time. To simulate the effect of the loss of bond adhesion on the TS effect, an elastic FE model was developed. The width of glass fragments in tested specimens has been observed to be comparable with the thickness of glass plies, so fragments have been imagined as perfect cubes of side length 10 mm for modelling purposes. Numerical simulations have been performed considering two simplified cracking patterns. Figure 5.44 shows symmetric layout and maximum offset between cracks of the two glass plies.

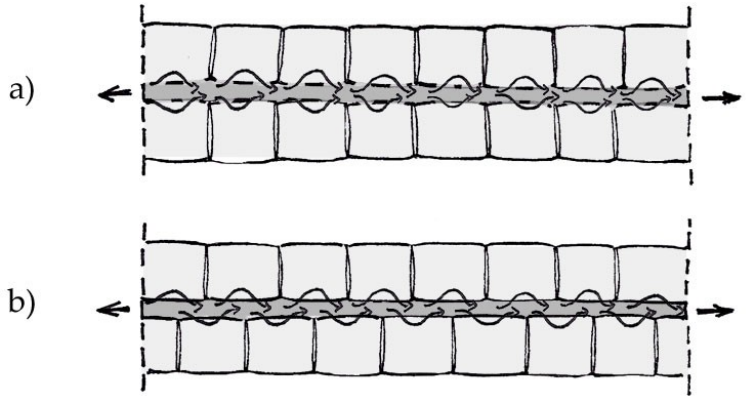

Figure 5.44 - Schematic crack patterns: a) symmetric layout, b) maximum offset

Figure 5.45 shows results of FE analyses, where it can be observed that mean TS effect may be approximated using an exponential interpolation.

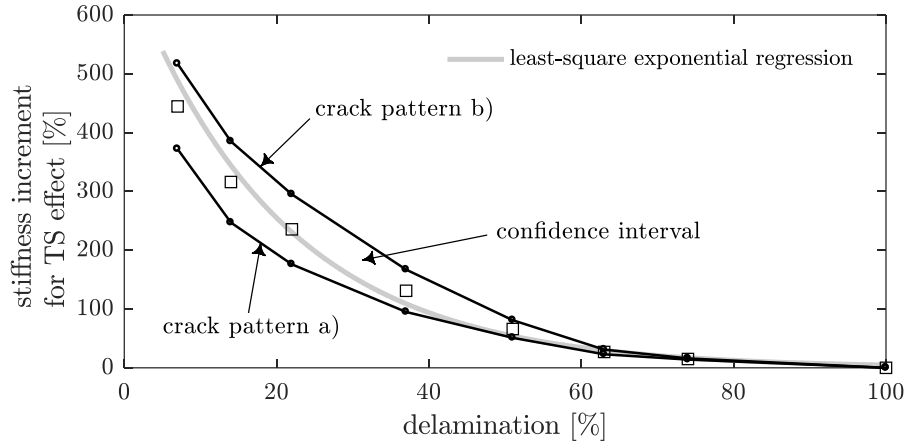

Figure 5.45 - increment in SG stiffness vs. delamination ratio from FE elastic analyses

For each delamination ratio, the figure shows the upper and lower values of the stiffness increase of the interlayer due to TS, corresponding to the two cracking patterns of Figure 5.44. For instance, the stiffness of the interlayer is about twice as big for debonded surface ratios of ~40% and four times as big for ratios of ~15%. It can be observed that at increasing debonded surface ratio the two limit values of the stiffness increment approach one another and for high delamination ratios (more than 80%) they are almost zero.

5.2.6 SYNTHESIS OF POST FAILURE LG PROPERTIES

Table 5.16 presents general information which can be useful from a designer point of view to understand and compare effects of progressive damage on LG elements.

Table 5.16 - noteworthy effects of progressive damage on LG beams

	Type A (2x1.52 SG)	**Type B** (2x1.52 DG41)	**Type C** (2x3.04 DG41 +2x0.2PC)
ULG			
Interlayer role for in-plane bending	negligible	negligible	negligible
Symmetrical PDLG (Stage II)			
Longitudinal expansion	limited†	limited†	limited†
Lateral deflection	none	none	none
Effect on undamaged plies	unk.	non-negligible	non-negligible
In-plane bending interlayer influence	negligible	negligible	negligible
Tensile stresses relaxation rate	unk.	very slow	slow
Asymmetrical PDLG (Stage III)			
Longitudinal expansion	limited/null‡	limited/null‡	Limited/null‡
Lateral deflection	non-negligible	non-negligible	non-negligible
Effect on undamaged plies	unk.	negligible	negligible
Rotation at the end supports	non-negligible	non-negligible	non-negligible
In-plane bending interlayer influence	small	negligible	small
Tensile stresses relaxation rate	unk.	very slow	slow
FDLG (Stage IV)			
In-plane bending interlayer influence*	high	limited	considerable
Long-term shape-preserving ability*	good	very limited	good
Long-term fragments adhesion*	good	very limited	good

† *generally negligible, provided there are no stiff constraints to elongation at both ends of the beam,*
‡ *because of the significant lateral deflection, the longitudinal relative displacement of beam ends can result in a net contraction rather than an elongation.*
***** *grades are assigned by comparison among the three specimen types.*

6 APPLICATIONS

To highlight and clarify some of the results discussed within this manuscript, some examples are provided, showing how experimental findings can be used to improve LG design. The following studies will try to focus on the main aspects of novelty, whereas standard and well-established procedures may be referenced and summarized but not dealt with extensively.

In the following paragraphs, two case-studies are shown: the first, dealing with a cold-bending application of large glazing panes, the second with the post-failure safety assessment of a compressed LG strut.

6.1 COLD-BENT GLAZING

A recent concept design for a museum in Parma, Italy is taken as a case study. A ramp which contains part of an historical automotive exhibition grants access from the ground floor to the 1st floor of the building. This part of the structure is designed around two semi-circles: one for the external profile and one for an internal court which serves as a light well (Figure 6.1).

Figure 6.1 - external rendering and sketch of the semi-circular ramp

The original design proposed the use of hot-bent LG panes (cfr. §1.1.1) to cover both the internal and external glazing surfaces. The hot-bending-process being very expensive and detrimental to the optical properties of glass, the aim of the following analysis is to propose solutions for alternative cold-bent LG solution.

The geometry of both glazing elements is presented in Figure 6.2, Figure 6.3 and Table 6.1.

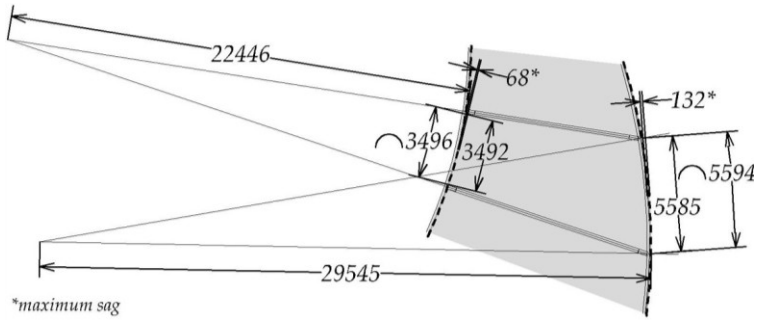

Figure 6.2 - layout of the case study with details on LG plates sizes and curvatures

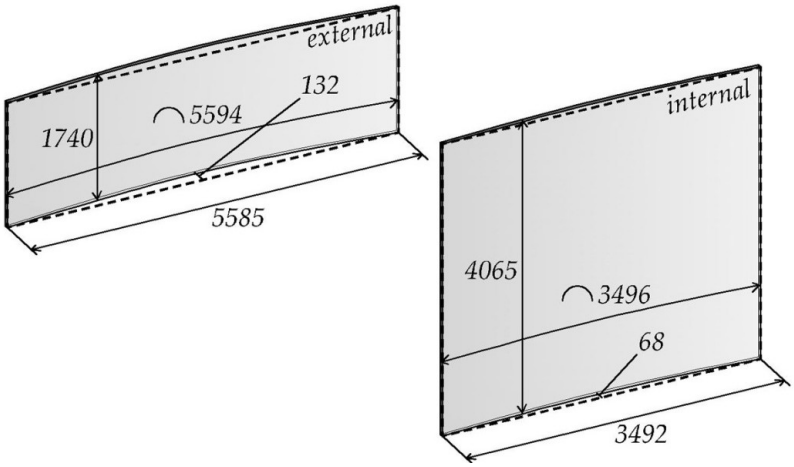

Figure 6.3 - geometry of LG panes for the internal and external glazing

Table 6.1 - median axis geometry for the cold-bent laminated elements

		external glazing	**internal glazing**
height	*H*	1740 mm	4065 mm
arc length	*B*	5594 mm	3496 mm
vertical supports distance		5585 mm	3492 mm
maximum sag		132 mm	68 mm
radius	*R*	29545 mm	22446 mm
arc		0.1557 rad	0.1893 rad

6.1.1 DESIGN HYPOTHESES AND MATERIAL PROPERTIES

Some hypotheses are made to perform an analytical verification of both elements and reliably apply the experimental results discussed in the previous chapters:

- LG panes are simply supported in the vertical direction, with supports placed at the top and bottom edges, bending is induced by pulling the LG elements towards the supports on the vertical edges (cfr. Figure 6.4.a),
- to evaluate the effects of horizontal actions, vertical portions of the cold-bent element LG panes are extracted and studied as an infinitely long simply supported pane[1] (Figure 6.4.b),
- LG elements are made with tempered glass which is polished, has triangular finishing on the edges and is thicker than 5 mm (UNI-EN-12150 [297]),
- the duration of the cold-bending phase is supposed to be higher than 30

[1] The additional boundary effects on vertical edges and the bi-dimensional structure of the LG plates are neglected for these analyses, both assumptions going towards safety.

minutes and performed at ambient temperature higher than 25°C[2],

- installation must be performed before the end of June and the opening to the public must not be allowed earlier than September or it must be checked that over 200 hours above 30°C elapse between installation and use[3,4],
- the building is a category C3 according to Eurocode 1, BSI 6399-1 and CNR-DT210/2013, so that the horizontal design loads are: a uniformly distributed $q_{k1} = 1.5\ kN/m^2$ and a linear load $q_{k2} = 3.0\ kN/m$ at a height $h_q = 1200\ mm$,
- distributed loads of wind, including safety factors and dynamic effects, account for a total of $0.87\ kN/m^2$ according to Italian standards [298,299],
- the self-weight only induces a minor in-plane compression, whose effects will be neglected for a safer design (slightly diminishing the tensile stress in glass).

The design maximum tensile stress in the glass plies is [38,300]:

$$f_{g,d} = \frac{k_{mod}\ k_{ed}\ k_{sf}\ \lambda_{gA}\ \lambda_{gl}\ f_{g,k}}{R_M\ \gamma_M} + \frac{k'_{ed}\ k_v\ \left(f_{b,k} - f_{g,k}\right)}{R_{M;v}\ \gamma_{M;v}}$$

with fixed $f_{g,k} = 45\ MPa$, $f_{b,k} = 120\ MPa$, $R_M = 0.70$, $R_{M;v} = 0.90$, $\gamma_M = 2.5$, $\gamma_{M;v} = 1.35$, $k_{sf} = k_v = 1$ and $\lambda_{gl} = 1.0$; other coefficients may vary for different load durations and are shown in Table 6.2 along with the final result for $f_{g,d}$.

Table 6.2 – coefficients and values for the design tensile stress of tempered glass plies $f_{g,d}$

	service (50 yrs)	**bending (30′)***	**crowd (30″)***	**wind gust (5″)**
k_{mod}	0.26†	0.65†	0.78†	0.88†
k_{ed} , k'_{ed}	0.80	0.80	1.00	1.00
λ_{gA}	0.89‡	0.89‡	0.89‡	0.89‡
$\boldsymbol{f_{g,d}}$	**52 MPa**	**58 MPa**	**79 MPa**	**82 MPa**

* *a nominal duration of 30" is used for the crowd actions on balustrades in* [38]
† *results from Linear Elastic Fracture Model (LEFM) are preferred to prEN16612*
‡ *values are different for the internal and external glazing; with a precautionary approach, the lowest value is considered*

[2] This prescription as a design choice, to work with known values of the relaxation modulus.

[3] This prescription in terms of months is intended to guarantee a minimum amount of time above 30°C between installation and opening to public. To this end, a comparison of weather station LIMP (Parma Airport, N44°49.33' / E10°17.72', elevation 49.1 m MSL) data over the years 2015, 2016 and 2017 was performed. Daily logs for 2017 are shown:

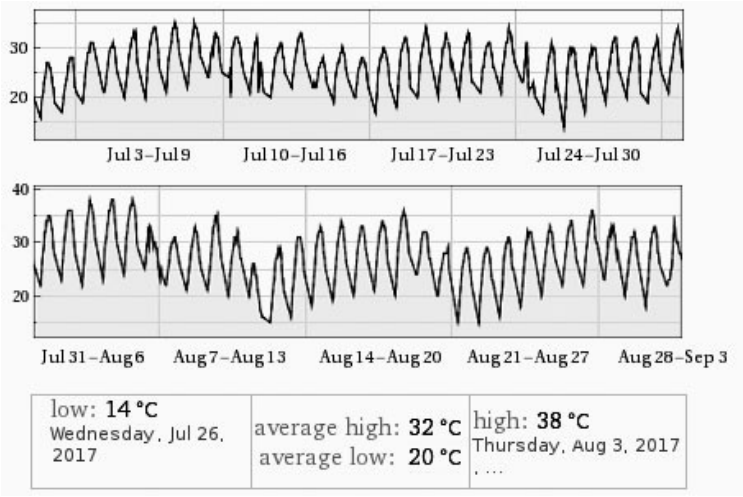

[4] For external glazing elements that are exposed to direct sunlight, this hypothesis is highly conservative, considering that surface temperatures are likely to rise above ambient temperature.

As an original contribution to the design, the shear modulus G_{int} of the three interlayer materials can now be calculated using the experimental results described in §0, verifying the compliance to the limits in §5.1.2.6. Table 6.3 shows analytical results compared to tabulated results provided in Appendix G of this manuscript.

Table 6.3 – interlayer relaxation modulus G_{int} and tabulated results (in brackets) in [MPa]

phase/verification	time & temperature	SG	DG41	PVB
installation	30 min. at 25°C	65.38 (75.6)	8.65 (14.3)	0.57 (0.66)
serviceability	200 hrs. at 30°C	10.79 (11.5)	0.46 (0.47)	0.17 (0.18)
crowd push	30 sec. at 35°C	61.5 (61.5)	5.47 (5.47)	0.57 (0.57)
wind gust	5 sec. at 35°C	77.3 (77.3)	13.5 (13.5)	0.72 (0.72)

The design values of the interlayer shear modulus $G_{\text{int},d}$ have been calculated as:

$$\mathrm{G}_{\text{int},d} = \frac{\mathrm{G}_{\text{int}}}{\gamma_G}$$

where the safety coefficient γ_G was defined as:

$$\begin{cases} \gamma_G = 2 & \text{if a stiffer interlayer goes towards safety} \\ \gamma_G = 0.5 & \text{if a softer interlayer goes towards safety} \end{cases}$$

6.1.2 DESIGN PROCEDURE AND VERIFICATIONS

Verifications are made in terms of maximum tensile stress in the glass plies of the LG elements. Four cases are considered:

Case 1: installation (progressive cold-bending in 30 minutes),

Case 2: linear distribution of forces simulating the push of a crowd (pushing outwards at 1.2m from the level of the floor plating, applied for 30" and accounting for cold-bending effects after 2 months),

Case 3: distributed pressure simulating the push of a crowd (pushing outwards, applied for 30" and accounting for cold-bending effects after 2 months),

Case 4: distributed pressure simulating the effects of wind (pushing inwards, applied for 5" and accounting for cold-bending effects after 2 months).

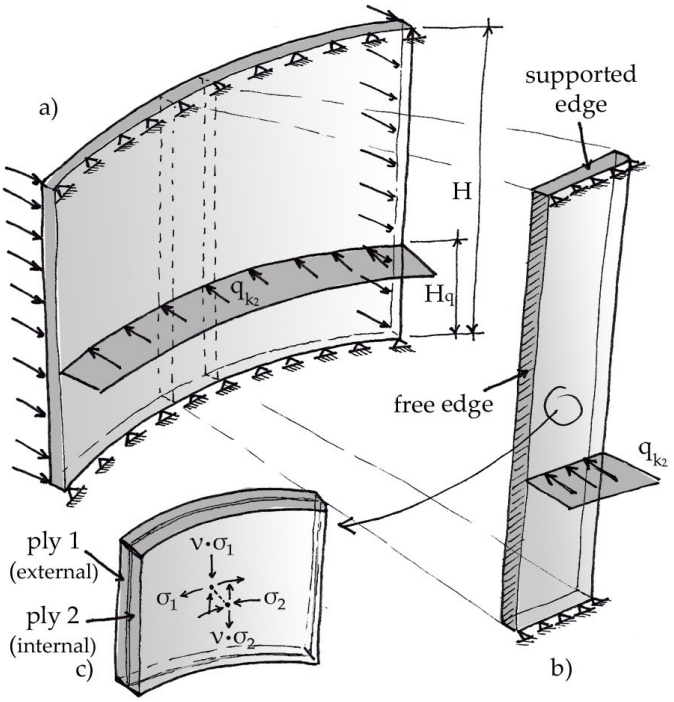

Figure 6.4 - a) scheme of cold-bent LG and b) an extracted vertical stripe "beam", used to compute the effects of horizontal loads accounting for c) cold-bending pre-existing stresses

For the Poisson effect, cold-bending generates compressive and tensile stresses in perpendicular directions (σ_1 and σ_2 in Figure 6.4c). Such stresses diminish over time as an effect of the decaying shear modulus and coupling abilities of all interlayers.

For load cases 2, 3 and 4, cold bending effects are accounted for as pre-stress: tensile effects induced by cold-bending add up with those produced by the live loads. On the other hand, to further increase safety, compressive stresses induced by cold-bending will not be accounted for.

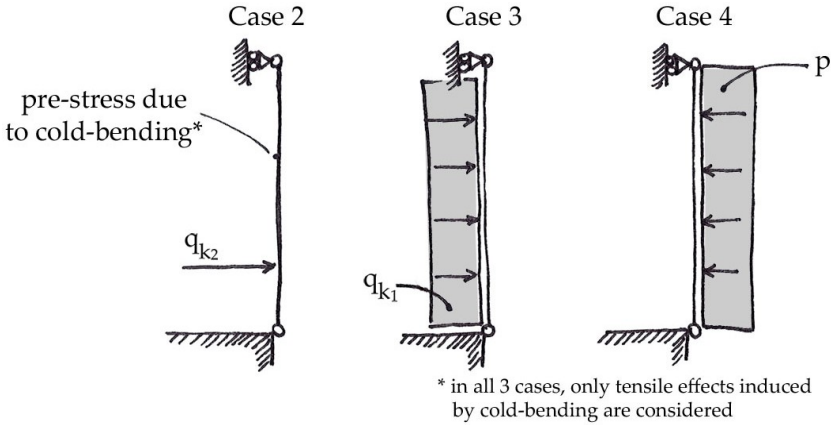

Figure 6.5 - schemes for studying the effects of live-loads in Cases 2, 3 & 4

Cases 2, 3 and 4 contain both actions of cold-bending and live loads on glass, two effects which refer to different times. In accordance with the CNR standard [38], a procedure analogous to the Palmer-Miner linear damage hypothesis for fatigue is adopted [301,302]. Therefore, verifications are satisfied when:

$$\sum_{i=1}^{N} \frac{\sigma^i}{f_{g,d}^i} < 1$$

where σ^i and $f_{g,d}^i$ are the i-th imposed and resistant stresses respectively.

The Enhanced Effective Thickness (EET) method is used to calculate the equivalent thickness of the LG sandwich structure [113] (cfr. §2.2.2).

An example of the procedure for cases 1 and 2 of the external LG plate is described, all other cases and the internal glazing can be dealt with in an analogous manner.

Case 1

The LG plate is made with two glass plies of the same thickness $h_1 = h_2 = 8\,mm$, bonded with a $h_{int} = 1.52\,mm$ thick SG interlayer. For cold-bending, a soft interlayer goes towards safety, hence $\gamma_G = 0.5$ and $G_{int,d} = 130.76\,MPa$. Considering a stripe of LG of unitary amplitude and the glass elastic modulus $E = 70\,GPa$, the coupling coefficient η can be calculated as:

$$\eta = \frac{1}{1 + \frac{E\,h_{int}}{G_{int}\,b}\frac{J_{abs}}{J_{full}}A^*\Psi} = 0.9998$$

where:

$$J_{abs} = \frac{h_1^3}{12} + \frac{h_1^3}{12} \quad ; \quad J_{full} = \frac{(h_1 + h_2 + h_{int})^3}{12} \quad ; \quad A^* = \frac{h_1 h_2}{h_1 + h_2} \quad ; \quad \Psi = \frac{168}{17B^2}$$

Such value of η very close to 1, hints that the behaviour of the plate is very close to the monolithic limit. The equivalent thickness $\hat{h}_w$ which can be used to model the bending stiffness of the plate is therefore:

$$\hat{h}_w = \sqrt[3]{\frac{1}{\frac{\eta}{h_1^3 + h_2^3 + 12(h_1 d_1^2 + h_2 d_2^2)} + \frac{1-\eta}{2s^3}}} = 17.51\ mm$$

where:

$$d_1 = U - \frac{h_1}{2} \quad ; \quad U - \frac{h_2}{2} \quad ; \quad U = \frac{h_1 + h_2 + h_{int}}{2}$$

The equivalent thickness $\hat{h}_{i,\sigma}$ for calculating the stresses in the i-th glass ply is:

$$\hat{h}_{i,\sigma} = \sqrt{\frac{1}{\frac{2\eta|d_i|}{h_1^3 + h_2^3 + 12(h_1 d_1^2 + h_2 d_2^2)} + \frac{h_i}{\hat{h}_w^3}}} = 17.51\ mm$$

The curvature imposed with the cold-bending is $\kappa = 1/R = 3.38 \cdot 10^{-5} mm^{-1}$, hence the –constant- bending moment induced is:

$$M_{cb} = \kappa E J_{eq} = \kappa E \left(\frac{\hat{h}_w^3}{12}\right) = 1.06 \cdot 10^5\ Nmm$$

The horizontal stress $\sigma_{i,\mathrm{h}}$ and vertical stress $\sigma_{i,\mathrm{v}}$ for the i-th ply in Case 1 are:

$$\sigma_{i,\mathrm{h},1} = \pm \frac{6|M_{cb}|}{\hat{h}_{i,\sigma}^2} \qquad \sigma_{i,\mathrm{v},1} = \mp \nu \cdot \sigma_{i,\mathrm{h},1}$$

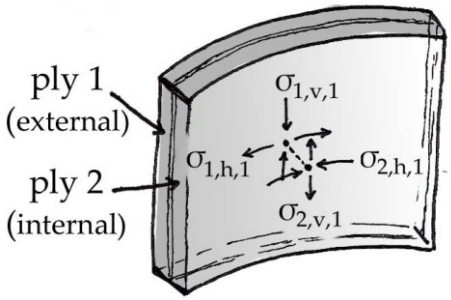

$$\sigma_{1,\mathrm{h},1} = +20.74\ MPa$$
$$\sigma_{1,\mathrm{v},1} = -4.36\ MPa$$
$$\sigma_{2,\mathrm{h},1} = -20.74\ MPa$$
$$\sigma_{2,\mathrm{v},1} = +4.36\ MPa$$

The verification in this case is possible by simple comparison of stresses $\sigma_{1,\mathrm{v},1}$ and $\sigma_{2,\mathrm{h},1}$ with the design maximum tensile stress of 58 MPa.

Case 2

Effects of cold-bending after the design relaxation period are calculated with the same procedure described for Case 1, the only difference is the diminished shear relaxation modulus which is now:

$$\mathrm{G}_{\mathrm{int},d} = \frac{\mathrm{G}_{\mathrm{int},d}}{\gamma_{\mathrm{G}}} = 21.58\ MPa$$

Yielding the new –slightly lower- values for cold-bending induced stresses σ':

$$\sigma'_{1,\mathrm{h},1} = -20.68\ MPa \ ; \ \sigma'_{1,\mathrm{v},1} = +4.34\ MPa$$
$$\sigma'_{2,\mathrm{h},1} = +20.68\ MPa \ ; \ \sigma'_{2,\mathrm{v},1} = -4.34\ MPa$$

The procedure for calculating the stresses induced by the horizontal live loads of the crowd are also computed similarly. The coupling coefficient η for the extracted vertical stripe in Figure 6.4b is calculated with the appropriate value of Ψ:

$$\Psi = \frac{10}{H^2}$$

$\hat{h}_w$ and $\hat{h}_{i,\sigma}$ are calculated with the same formulae, while the maximum bending moment, which is reached at a height H_q (cfr. Figure 6.4b) is:

$$M_{q_{k2}} = \frac{q_{k2}(H - H_q)H_q}{H} = 2.51 \cdot 10^5\ Nmm$$

Vertical and horizontal stresses can be now calculated as:

$$\sigma_{i,v,1} = \pm \frac{6|M_{q_{k2}}|}{\hat{h}_{i,\sigma}^2} \qquad \sigma_{i,h,1} = \mp \nu \cdot \sigma_{i,v,1}$$

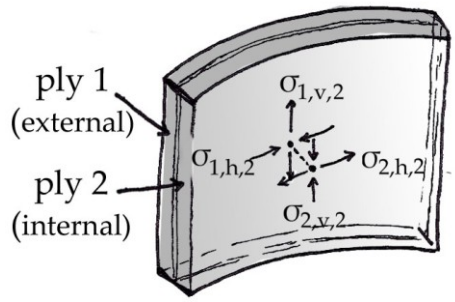

$$\sigma_{1,v,2} = +49.80\ MPa$$
$$\sigma_{1,h,2} = -10.50\ MPa$$
$$\sigma_{2,v,2} = -49.80\ MPa$$
$$\sigma_{2,h,2} = +10.50\ MPa$$

The verification must now account for the pre-existing stresses due to the cold-bending process, hence the Palmer-Miner criterion must be satisfied for the four stresses $\sigma_{1,v}$, $\sigma_{1,h}$, $\sigma_{2,v}$ and $\sigma_{2,h}$:

$$\text{for } \sigma_{1,v} = 0 \times \left(\frac{-4.34\ MPa}{52\ MPa}\right) + 1 \times \left(\frac{49.80\ MPa}{79\ MPa}\right) = 0.62 < 1$$

$$\text{for } \sigma_{1,h} = 1 \times \left(\frac{+20.68\ MPa}{52\ MPa}\right) + 0 \times \left(\frac{-10.50\ MPa}{79\ MPa}\right) = 0.39 < 1$$

$$\text{for } \sigma_{2,v} = 1 \times \left(\frac{+4.34\ MPa}{52\ MPa}\right) + 0 \times \left(\frac{-49.80\ MPa}{79\ MPa}\right) = 0.08 < 1$$

$$\text{for } \sigma_{2,h} = 0 \times \left(\frac{-20.74\ MPa}{52\ MPa}\right) + 1 \times \left(\frac{+10.50\ MPa}{79\ MPa}\right) = 0.13 < 1$$

Multiplications per zero are the result of the procedure of neglecting the beneficial effects of compressive stresses in the glass plies[5]. Altogether, verifications for Case 2 are successfully checked with a maximum 62% use of the design resistance of glass (for the outer ply in the vertical direction).

Other cases

Checks for the other two cases and for all other interlayer materials are not reported in full, as the procedures are alike those shown above. Nonetheless, while tensile effects of cold-bending and live loads were not addictive in case 2 for the external glazing, it must be pointed out that those can in fact induce addictive effects, depending on the direction of the bending and live loads.

6.1.3 RESULTS, DESIGN OPTIONS AND INTERLAYERS COMPARISON

Table 6.4 shows the results of verifications were carried out for several combinations of glass plies and interlayer thicknesses. Numbers under the verification columns V represent the percentage of use of the tensile glass mechanical resources according to the Palmer-Miner superposition criterion, which was generally observed either for case 2 (0 is no stress, 100 is failure). Results are found to be dependent on the mechanical properties and thickness of the interlayer materials. The following statements can be made:

[5] With the exception for those induced by the tempering process.

- when dealing with combinations of cold-bending effects and live loads, stiffer interlayers are not always beneficial (e.g. SG-laminated glazing with 15+15 mm plies cannot be used, while softer interlayers allow for multiple solutions)
- varying the interlayer thickness may or may not be beneficial (cfr. Table 6.4, 10+8 mm combinations using DG41 and PVB for external glazing: for DG41 stiffer is better, for PVB thinner is better).

Table 6.4 – analysis of glass/interlayer thickness (verifications are satisfied for $V < 100\%$)

internal glazing					**external glazing**				
$h_1 + h_2$ [mm]	h_{int} [mm]	V [%] SG	DG41	PVB	$h_1 + h_2$	h_{int}	V [%] SG	DG41	PVB
	3,04	97	97	*fail*		3,04	**87**	*fail*	*fail*
10+10	1,52	*fail*	*fail*	*fail*	6+6	1,52	*fail*	*fail*	*fail*
	0,76	*fail*	*fail*	*fail*		0,76	*fail*	*fail*	*fail*
	3,04	88	86	*fail*		3,04	68	77	*fail*
10+12	1,52	93	94	*fail*	6+8	1,52	80	**86**	*fail*
	0,76	98	98	*fail*		0,76	88	91	*fail*
	3,04	88	84	*fail*		3,04	68	83	*fail*
12+10	1,52	93	**93**	*fail*	8+6	1,52	81	90	*fail*
	0,76	98	98	*fail*		0,76	88	94	*fail*
	3,04	92	76	99		3,04	54	66	*fail*
12+12	1,52	90	82	**96**	8+8	1,52	63	70	*fail*
	0,76	89	86	94		0,76	68	72	96
	3,04	98	71	89		3,04	49	52	80
12+15	1,52	95	78	84	8+10	1,52	51	56	**77**
	0,76	94	84	81		0,76	55	57	72
	3,04	98	76	78		3,04	49	56 ↑	96 ↓
15+12	1,52	96	82	77	10+8	1,52	51	58	90
	0,76	95	86	80		0,76	55	59	82
	3,04	*fail*	77	74		3,04	53	46	76
15+15	1,52	*fail*	84	74	10+10	1,52	50	47	71
	0,76	*fail*	90	81		0,76	48	48	65

With such a vast array of design options, the final design can rely on different criteria such as the economic edge or availability of interlayers; the most valuable options have been circled in Table 6.4 [6]. Final options are then:

for internal glazing

- 12+10/1.52DG41 minimizes overall thickness and glass cost,
- 12+12/1.52 PVB minimizes interlayer cost,

[6] Even if not always beneficial from a mechanical or economical standpoint, 1.52 mm interlayers are most reliable, matching the thicknesses tested within the experimental campaigns described in this work, and because scaling effects regarding interlayer thickness were not investigated. Besides, this choice is made for most structural LG applications and has proven to be reliable.

for external glazing

- 6+6/3.04 SG minimizes overall thickness and glass cost,
- 6+8/1.52 DG41 balances thickness/cost,
- 10+8/1.52 PVB minimizes interlayer cost.

A comparison with a much simpler design, one that neglects the viscous properties of interlayers, is useful to understand the relevance of the experimental results provided in this work.

If reliable data on interlayer properties weren't available, one could still attempt a safe cold-bent LG design: the detrimental mechanical effects of cold-bending could be studied using a *monolithic* cross section, a limit case which treats the interlayer as being as stiff as the glass elements ($E_{\mathrm{int},d} = E$); conversely, the effects of horizontal live loads on glazing could be studied with the opposite *layered* limit case, where the glass plies are considered juxtaposed and non-collaborating, as if the interlayers had no stiffness ($E_{\mathrm{int},d} = 0$). Results of such analysis yield:

for internal glazing

- there is no combination of glass plies that successfully passes all checks,

for external glazing

- a combination of 10+10 mm glass plies satisfies the ULS verifications with any interlayer thinness up to 3.04 mm.

6.2 POST-FAILURE ANALYSIS OF A LG ELEMENT

Results of the post-failure experimental results and models are applied to enhance the design of LG struts, forming part of the structural backbone of a pedestrian bridge[7].

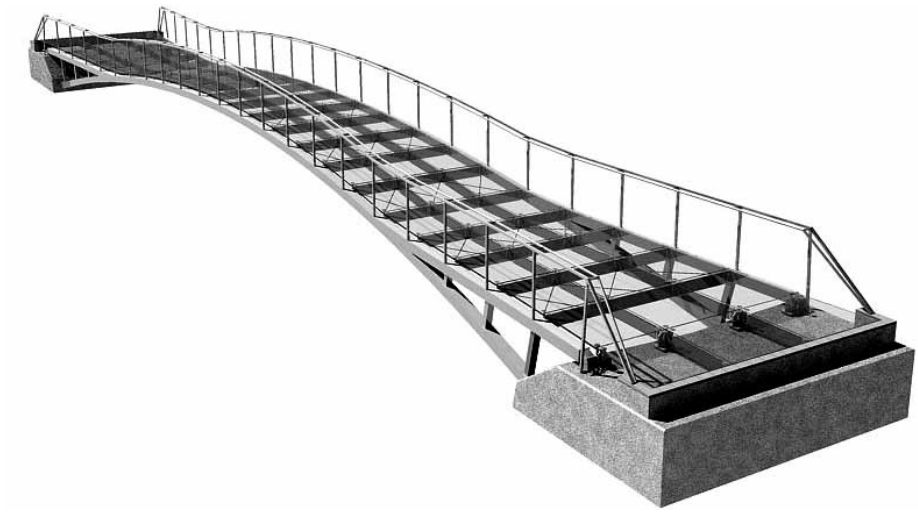

Figure 6.6 - rendering of the pedestrian bridge

The deck of the bridge is upheld by two double-curvature steel arches; a portion of the structure close to midspan is shown in Figure 6.7. Not all portions of the deck are provided with wind bracing trusses; nevertheless, to establish a pleasing structural continuity, LG struts have been inserted from the beginning to the end of the structure, even if some have no binding structural responsibility.

[7] This structure of the bridge was studied in 2013 with Prof. S. G. Morano at University of Florence. The first analysis of the LG struts, which serves as reference for the following analyses, was performed in my master thesis, supervised by Prof. M. Orlando and Ph.D. E. Cagnacci [110].

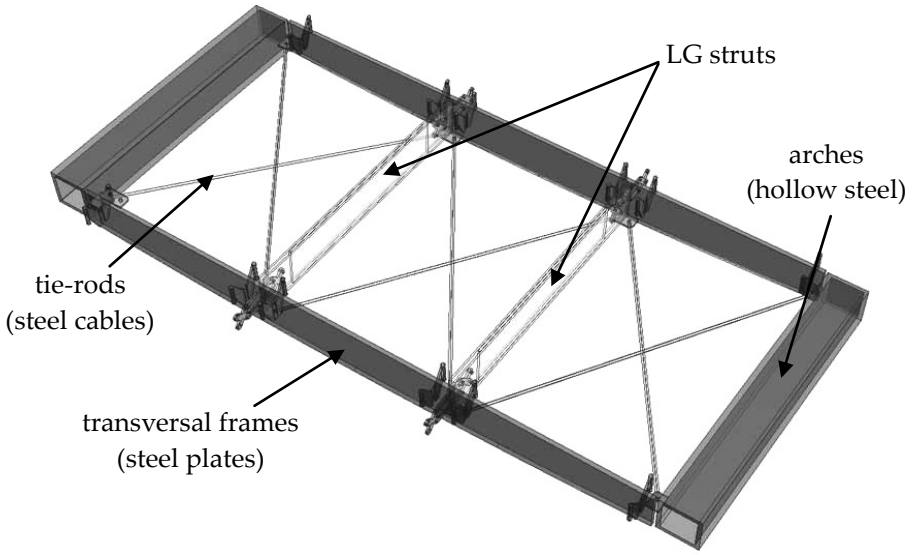

Figure 6.7 - portion of the deck showing the wind bracing made with LG struts and tie-rods

The object of this second case-study is the design of LG struts forming part of the wind bracing trusses in the deck of the bridge. The design will account for the event of accidental failure of any of the glass pies included in those elements.

The bridge is designed to be built in five phases, schematically illustrated in Figure 6.8. LG struts first, then LG plates for the causeway, are both designed to be installed in the final part of the assembly. Therefore, the only actions on those elements needing verification are referred to SLS and ULS of the finished structure.

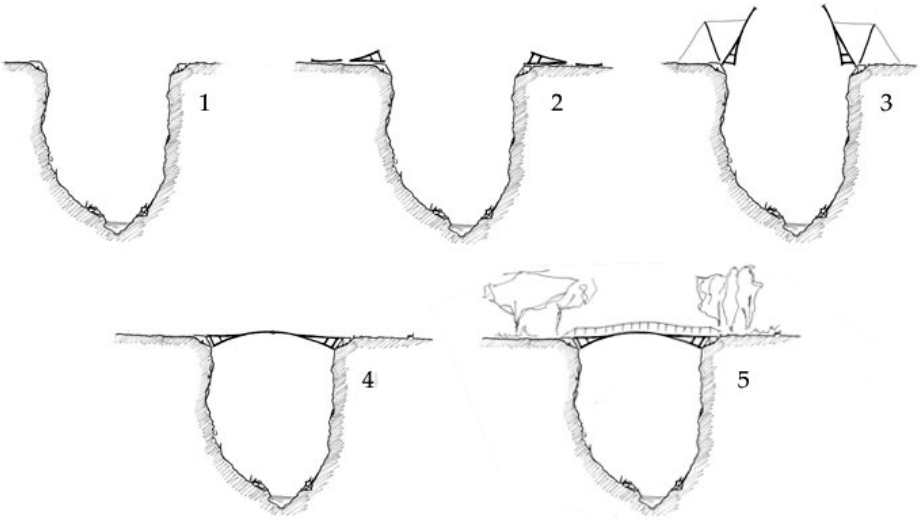

Figure 6.8 –phase 1) groundwork and banks 2) assembly of main steel elements 3) positioning by rotation 4) completion of the steel structure 5) LG elements installation

6.2.1 DATA, CONSTRAINTS AND PARAMETERS

The structural analysis of the bridge was performed with an analytically validated SAP2000® LE FEM model with 17 different load cases for either SLS and ULS including: temperature effects (2), wind pressure including the dynamic effect of wind gusts (6) pedestrian distributions including dynamic effects (7), self-weight and permanent loads (2). Within the global model, LG struts were modelled using frame elements.

Table 6.5 - design loads for LG struts verification

action type	ULS (undamaged)		SLS (partially damaged)	
	axial force [kN]	duration	axial force [kN]	duration
tensile	+1,90	12 hrs	+1,20	12 hrs
	+0,12	50 yrs	+0,10	50 yrs
compressive	-27,0	30 sec	-18,0	30 sec
	-2,80	12 hrs	-1,80	12 hrs
	-0,12	50 yrs	-0,10	5 yrs

The design maximum tensile stress in the glass plies is calculated as previously shown in §6.1, yielding the results shown in Table 6.6.

with $f_{g,k} = 45\ MPa$, $f_{b,k} = 120\ MPa$, $R_M = 0.70$, $R_{M;v} = 0.90$, $\gamma_M = 2.5$, $\gamma_{M;v} = 1.35$, $k_{sf} = k_v = 1$ and $\lambda_{gl} = 1.0$. Remaining coefficients may vary and are reported in Table 6.2, along with the result for $f_{g,d}$.

Table 6.6 –design tensile resistance of the glass plies $f_{g,d}$ in MPa used for the LG struts

glass	30 seconds	12 hours	50 years
tempered	81,7	74,5	68,4
float annealed	20,0	12,8	6,68

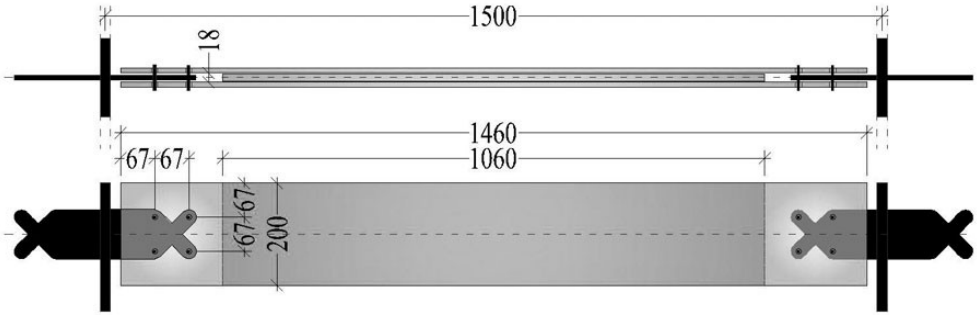

Figure 6.9 - view general scheme of the strut a) from above and b) in a lateral view

DG41 interlayer of thicknesses $h_{int} = 1.52\ mm$ will be used, to allow for a reliable application of the equivalent thermal expansion model which has been developed for specimens of type B (cfr. §4.3 and §5.2).

The element was initially designed to be composed by three glass plies, a central 15 mm thick and two lateral 10 mm thick ones. It was pointed out that the choice of inserting portions of non-laminated glass on the two sides (lateral regions of the strut shown in Figure 6.9) is not optimal from a post-failure safety point of view, as glass fragments will be expelled in the event of accidental failure. Instead, the two lateral plies will be replaced with two 5+5 millimetres thick tempered plies bonded with DG41 interlayer.

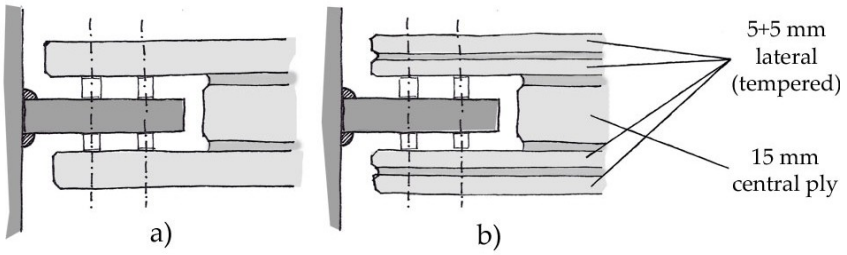

Figure 6.10 - a) old 3-plies design with PVB and b) new 5-plies design using DG41

6.2.2 VALIDATION OF THE NUMERICAL MODEL

The EET method [38] doesn't provide a solution for multi-laminates with more than three plies with arbitrary thicknesses. Therefore, a validated SAP2000® LE FE model will be used to work out the stress in the glass plies (Figure 6.11).

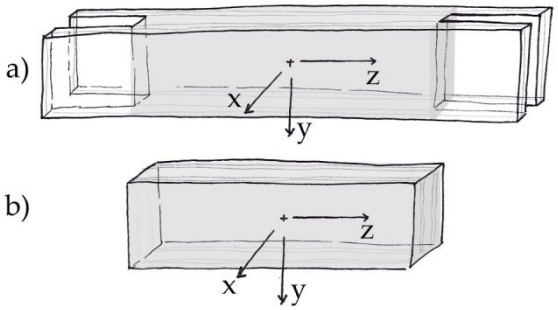

Figure 6.11 - a) scheme of the strut and conventional axes b) partition used for validation

The model is validated by studying the case of failure of the two external plies (Figure 6.10b). For this validation, analytical calculations are carried out under the hypothesis of perfect coupling among the glass plies ($\eta = 1$). This assumption implies that $J_{eq} \cong J_{full}$, which has been shown to be here a reasonable hypothesis: a parametric analysis for a multi-layered LG of similar total thickness (composed by five 7-mm thick glass plies and four 1.52-mm thick interlayers) was performed with the EET method. Results show that a relative error between layered and monolithic models of 5% for $G_{int} = 312\ MPa$ (Figure 6.12).

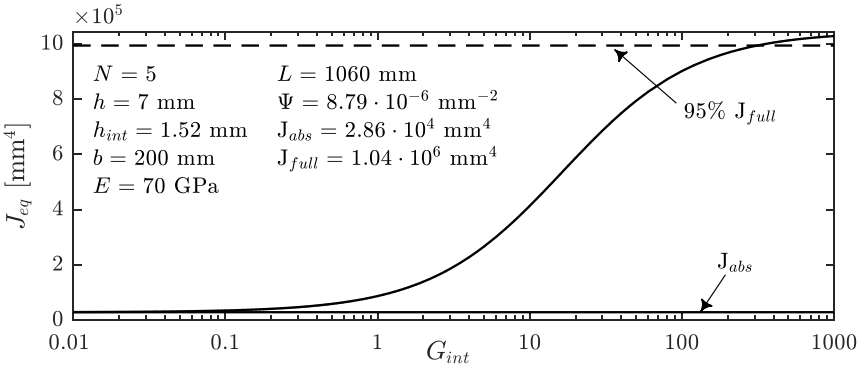

Figure 6.12 - effect of interlayer stiffness on the equivalent moment of inertia

The action N in Figure 6.13a, which annuls the expansion of the broken glass plies, can be calculated using the equivalent thermal expansion model (cfr. §5.2.3). With the average values of $E_{fg,eq,2}$ for type B specimens and corresponding average ΔT_{eq} for stage III (cfr. Table 5.13), one finds:

$$N = \alpha \cdot \Delta T_{\mathrm{eq}} \cdot \bar{E}_{\mathrm{fg,eq,i}} \cdot A_{\mathrm{i}} = 1.97 \cdot 10^4\ N \quad \text{and} \quad M = N \cdot d = 4.2 \cdot 10^5\ Nmm$$

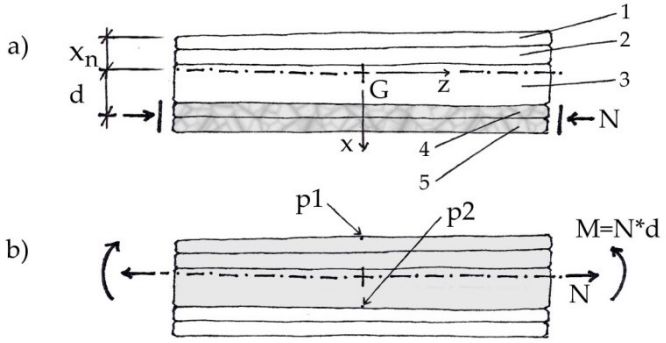

Figure 6.13 - external action equilibrating the expansion b) effects on the undamaged plies

The centroid of the homogenised cross-section is found in $x_n = 18.07\,mm$, accounting for the equivalent stiffness of the broken plies. The monolithic moment of inertia with respect of the axis y is then $J_{full,hom} = 3.46 \cdot 10^5\,mm^4$.

To study effects of glass fragments expansion, stresses are calculated at points $p1$ and $p2$ in Figure 6.13b. With respect of the centroid G, N is applied at a distance $d = 17.25\,mm$ inducing a moment $M = Nd$. For equilibrium along z, N results in a compressive action for the broken plies 4 & 5 and a tensile one for the undamaged 1, 2 & 3 of total cross-sectional area $A_{ud} = 5000\,mm^2$. Distances x_{P1} and x_{p2} of points $p1$ and $p2$ from the centroid along x allow for calculating:

$$\sigma_{zz}^{p1} = -\frac{|M \cdot x_{P1}|}{J_{full,hom}} + \frac{N}{A_{ud}} = -7.51\,MPa \quad \text{and} \quad \sigma_{zz}^{p2} = +\frac{|M \cdot x_{P2}|}{J_{full,hom}} + \frac{N}{A_{ud}} = +10.3\,MPa$$

The numerical model is assembled using the same properties for the glass plies and an elastic modulus of $E_{int} = 936\,MPa$, corresponding to $G_{int} = 312\,MPa$ with $\nu = 0.5$. Results are shown in Figure 6.14, yielding:

$$\sigma_{zz}^{p1} = -8.10\,MPa \quad \text{and} \quad \sigma_{zz}^{p2} = 12.11\,MPa$$

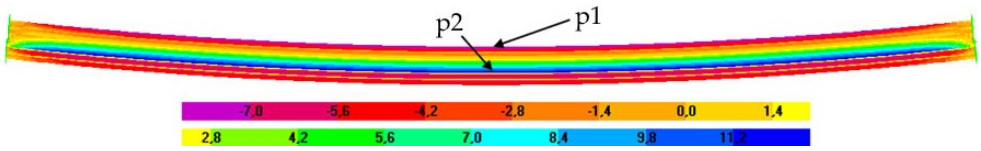

Figure 6.14 - numerical model used for validation

Accounting for a known discrepancy around 5% for having considered a monolithic analytical model, results of the numerical model seem to be still 2% off for σ_{zz}^{p1} and 10% off for σ_{zz}^{p2}. This result comes with no surprise for two reasons: first, mechanical contributions of interlayers themselves are not accounted for in the EET model (it only considers coupling effects), second, the equivalent thickness for stress calculation $\hat{h}_{i,\sigma}$ [38,113] is proportional to the plies thickness, hence larger plies will be more affected than thin ones when comparing monolithic and layered responses. Both observations being consistent with the validation comparison, the numerical model is considered acceptable for the following analyses.

6.2.3 VERIFICATIONS AND DESIGN

With the addition to the numerical model of the protruding parts of the external plies and the steel frames of the anchorages, post-failure effects are investigated on the actual geometry of the LG struts. Verifications are carried out for:

- maximum stress in the intact plies after partial failure,
- maximum stress in the intact plies after partial failure with external loads,

Maximum stress in the intact plies after partial failure

Figure 6.15 displays a scheme and a graphical model output for the failure of the external tempered plies, one of the three-post-failure scenarios considered.

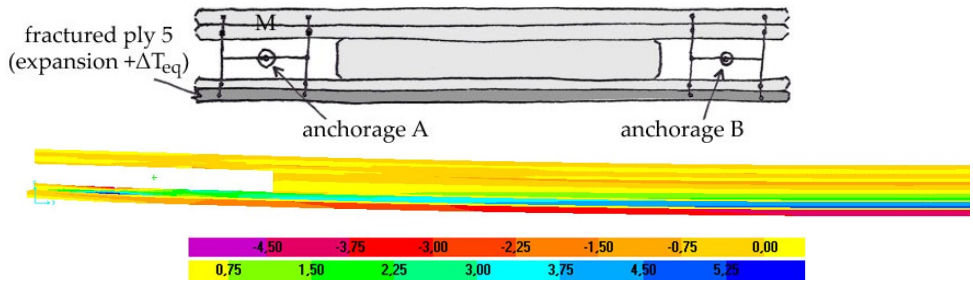

Figure 6.15 – stresses σ_{zz} after 50 yrs in half beam model in the event of failure of ply 5

Table 6.7 and Figure 6.16 show the results at midspan[8] for stresses σ_{zz} in the undamaged plies, because of the failure of one or both external plies.

Table 6.7 - maximum and minimum stresses σ_{zz} at midspan in [MPa] and lateral sag

case		ply 5 fails			ply 4 fails			plies 4 & 5 fail		
time		30″	12h	50y	30″	12h	50y	30″	12h	50y
1	*min*	-3.69	-1.88	-0.75	-1.16	-0.75	-1.07	-8.05	-4.63	-2.39
	max	-2.22	-0.26	+0.34	-0.41	+0.14	+0.47	-4.32	-0.12	+1.02
2	*min*	-1.81	-1.44	-0.94	-0.26	+0.47	+0.58	-3.44	-1.75	-0.52
	max	-0.34	+0.17	+0.15	+0.49	+1.38	+2.13	+0.27	+2.74	+2.90
3	*min*	+0.04	-1.79	-0.54	+0.60	-0.41	-1.77	+1.06	-3.84	-4.19
	max	+4.42	+3.03	+1.72	+2.86	+2.27	+2.83	**+12.1**	+9.56	+6.00
4	*min*	+4.81	+5.86	+3.69						
	max	+6.28	+7.49	+4.78						
5	*min*				+4.18	+4.67	+2.58			
	max				+4.94	**+5.57**	+4.13			
sag [mm]		0.817	0.824	0.533	0.420	0.650	1.27	2.18	2.55	2.35

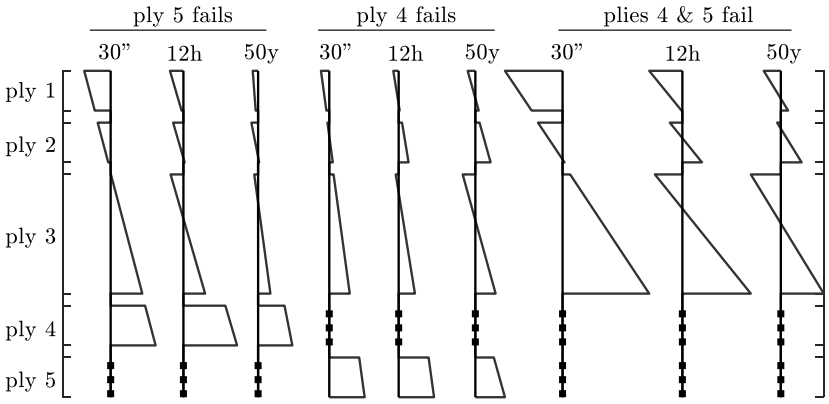

Figure 6.16 – graphical representation of the evolution of stresses σ_{zz} over time in the intact glass plies (dotted lines are placed to signpost the position of damaged plies)

Verification of maximum tensile stresses in plies 1, 2, 4 and 5 (when intact) are fulfilled with a large margin: stresses are always lower than 5.57 MPa, which is more than one order of magnitude lower than the lowest design tensile stress of tempered glass (cfr. Table 6.6). For the central ply, maximum tensile stresses are found in the case of failure of plies 4 & 5: either for 30 seconds, 12 hours and 50 years effects. For these three times, tensile stresses consistent with the maximum allowable in annealed glass.

Maximum stress in the intact plies after partial failure with external loads

All checks of the strut in the post-failure phases with external compressive actions can be met with the verification of the worst-case scenario: the failure of plies 4 & 5

[8] It has been observed that different geometries and mechanical properties of the anchorages can produce high concentrated stresses (e.g. Figure 6.15, left part of the model). While these may be significant, the analysis of local effects is deeply connected to the specific anchoring technology, the study of which goes beyond the purpose of both this work and this specific example.

combined with a compressive action of $-27.0\ kN$ or a tensile one of $+1.90\ kN$ (cfr. Table 6.5).

To account for second order effects, a bending moment M has been applied at both ends on the anchorages (Figure 6.17).

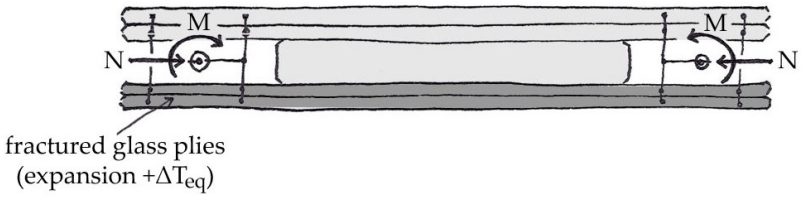

Figure 6.17 - scheme for maximum stresses verification in a loaded strut after partial failure

The resulting bending moment at midspan $M(f_1, N)$ has been calculated with a step by step analysis, whose results are shown in the figure below. Increments of the compressive action δN_i are applied on a deformed configuration, which transitions from a configuration C_1 to an equilibrium configuration C_2. For the final FE analysis the final midspan moment $M = N \cdot f_2$ is then applied at both anchorages as shown in Figure 6.17, which is a choice on the side of safety.

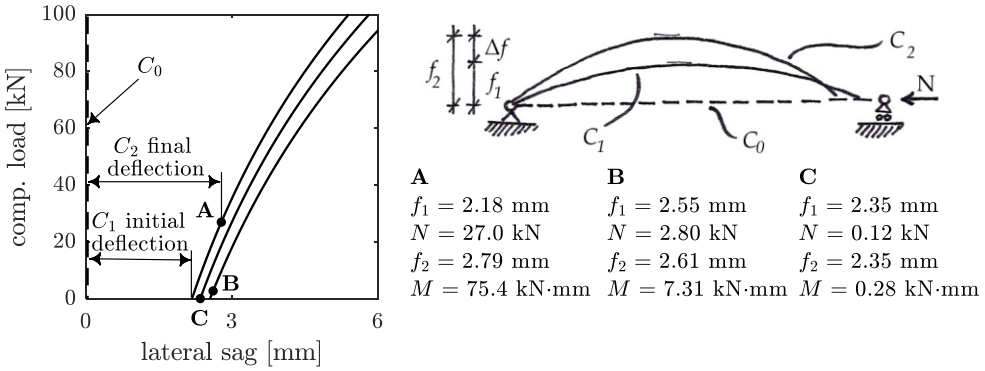

A	B	C
$f_1 = 2.18$ mm	$f_1 = 2.55$ mm	$f_1 = 2.35$ mm
$N = 27.0$ kN	$N = 2.80$ kN	$N = 0.12$ kN
$f_2 = 2.79$ mm	$f_2 = 2.61$ mm	$f_2 = 2.35$ mm
$M = 75.4$ kN·mm	$M = 7.31$ kN·mm	$M = 0.28$ kN·mm

Figure 6.18 - result of the step-by-step non-linear analysis on the compressed strut

Despite the -small- bending moment, compressive actions are beneficial in this case from the point of view of tensile stresses in the intact plies. On the other side, the tensile force $N = +1.90\ kN$, induces stresses so small that the final effects are almost indistinguishable from those found after the fractured glass expansion alone. In light of these considerations, all verifications are met for loaded elements in post-failure conditions.

For a bent strut such as the damaged LG element, a compressive action on doesn't lead to the risk of loss of stability, as the element is already in a deformed configuration $C_1 \neq C_0$. Therefore, the compressive action will progressively magnify the existing sag with no sudden changes of conformation. Nevertheless, as the sag produced by failure of the external plies is indeed very small (cfr. Table 6.7), a verification with respect of the Euler's critical load was performed accounting for the three intact plies in the worst post-failure case scenario. The equivalent stiffness was calculated using both the EET method and the FE model using a safety coefficient of two for the interlayer modulus G_{int} at 30", with similar results for both models: $\hat{J}_{\text{min,EET}} = 3.15 \cdot 10^5\ mm^4$ and $\hat{J}_{\text{min,FE}} = 2.79 \cdot 10^5\ mm^4$. The critical load is therefore $121 \div 137\ kN$, much higher than any design load envisaged for these elements.

This analysis concluded that effects of failure of any of the lateral tempered glass plies are not a threat to the safety for both ULS and SLS. Provided that failure only occurs on one side of the LG strut, replacement of damaged elements can be scheduled with no urgency from the point of view of structural safety.

7 THESIS AND DEVELOPMENTS

Performance of laminated glass and post-failure safety assessments both address various issues, related to material properties and peculiar mechanics. Therefore, such investigations inevitably involve different research fields: from material science to standardization techniques, industrial development and structural engineering. After critical analyses and discussions, this conclusive thesis tries to share more light on some of the aspects which were deemed to be the most wanting, keeping in mind that results are directed to an area of research which is very diverse interdisciplinary in nature.

7.1 CONCLUSIONS OF THE RESEARCH

The experimental analyses and forthcoming discussions carried on throughout this manuscript yielded several results, models and consideration, carrying elements of novelty. The initial goals of the research were to investigate and model the viscoelastic properties of some of the most common interlayer materials, together with the assessment of post-failure performance of structural LG elements. Results concerning these two broad topics constitute the key elements of this conclusive *thesis*, and are described in the following at points 3, 5 and 6. Nevertheless, analyses on a large body of experimental outcomes allowed to produce unanticipated and results of interest for this field of research, despite not being the primary focus of this work. Namely, studies on tensile tests, delamination and ageing of LG provided several elements of novelty in this field of research.

Short-term tensile response of interlayers and standardization

1. A *generalized response* model was proposed, to provide a better description of thermoplastic materials behaviour in uniaxial tensile tests. Through a mathematical formulation inspired by the work of Haward and Thackray [76], this model allows to separate the contribution of intermolecular cross-links and network entanglement of molecules. The proposed solution has proven to be able to fit a wide range experimental results, from heavily to poorly cross-linked materials, with a small number of coefficients. A simple hyperelastic model was used to study the network entanglement response in the three investigated interlayer materials, but the procedure allows to include more complex and well-established hyperelastic models, should different experimental data suggest doing so (cfr. §5.1.1.2 p.120). Conversion of experimental data on tensile tests from the *engineering* stress-strain curves to their *true* counterpart has proved to be a useful tool, to provide a more rigorous interpretation of the tensile tests. This translation also opened for a simpler decomposition in terms of *intermolecular* and *network entanglement* effects, compared to previously suggested techniques. From an engineering point of view, when dealing with thermoplastics for LG design, engineering correlations can be chosen, being far easier to obtain and close to the true response for the whole range of strains which is meaningful for the overwhelming majority of practical LG applications.
   From a LG design standpoint, tensile properties of interlayers may be relevant

especially for fully-damaged elements; in fact, the results of tensile tests were used later in the experimental analyses[1]. While this part of the research may seem less connected with practical LG applications, the study of tensile properties and models is relevant as key draft standards propose a subdivision of interlayers in "stiffness families", based uniquely on the results of similar tests (prEN 16613:2013 [303] and FprEN 16613:2016 [303]).
To some extent, results based on short-term tensile properties could be used for LG design if loads have a duration comparable to the duration of the tests. However, studies on viscous properties of interlayers allow to compare short-term to long-term effects, suggesting that it would be unadvisable to extend tensile test results to extrapolate the long-time response. In fact, such choice would involve overlooking some of the most relevant mechanics governing the interlayers response, possibly overestimating their properties.

2. A simple method for defining the *pseudo-yielding* limit of thermoplastics is discussed, a definition providing an alternative to the one proposed in standards such as "ISO 527:2012 *Plastics - Determination of tensile properties*" [264] and "ASTM D638-14 *Standard Test Method for Tensile Properties of Plastics*" [66]. The proposed criterion allows to define a point on the engineering stress-strain curves where the properties change abruptly, and can be applied even to those materials which do not show a peak in the measured stress with a subsequent softening branch (§5.1.1.3 p.128).
Converging on a definition for the pseudo-yielding criterion would allow to identify limits in terms of stress and strain under which tensile results on interlayers can be used in LG design using LE models.

Viscoelastic, long-term and adhesive properties of interlayers

3. Most applications and designs of LG involve actions and effects which take place over a large amount of time. Thermoplastic materials are known to build up conspicuous viscous effects which are in turn greatly dependent on the operating temperatures. Tensile tests on interlayers are unfit to study the long-term response of such materials within the layered structure of LG. Therefore, the long-term viscoelastic properties have been studied with small specimens of LG using three of the most widespread interlayers within the LG industry: PVB, SG and DG41. The analyses ultimately provided analytical results in the form of Prony series mastercurves and time-temperature superposition functions, allowing to predict the effects of viscoelastic flow within well-defined reliability limits. Results were provided in terms of both stress relaxation and creep compliance moduli as a function of time and temperature. This double formulation is needed for the design of structural LG elements: while these quantities are often confused one another, they represent in fact two different physical effects. As rigorous procedures for converting relaxation to creep functions (and vice-versa) involve the introduction of Laplace transforms, which are arguably not suited for practical engineering, separate formulations based on empirical measurements have been deemed to be the most reliable and effective way of proceeding.
The direct the method used within this work to derive viscoelastic properties of interlayers[2] can be compared with a few other researches which used dynamic

[1] To study the *tension stiffening* effect in fully-damaged LG specimens (cfr. §5.2.4 p.181).

[2] A direct approach to this problem was called for by D. Delincé in his work [7], and by a handful

techniques instead. While new results roughly agree with the –limited- previously available data, the proposed approach is believed to be more reliable and consistent with operating conditions of interlayers in LG elements (cfr. §0 p.148 and §5.1.2.6 p.149).
Experimental results gathered within the analyses of viscoelastic properties of interlayers have been used in a case study for a cold-bending LG design application, allowing for a comparison of the advantages and disadvantages of different materials (cfr. §6.1 p.169).
Some researchers suggested that a high glass transition temperature for interlayers is be desirable, to take advantage of a full range of applications in the architectural industry [69]: "*a higher glass transition temperature is suitable for more demanding architectural applications*". While this belief has been observed to be quite common throughout the pertinent literature, this research has shown that one can hardly rely on this parameter alone to anticipate the effectiveness of the coupling abilities of interlayers. For instance, the glass transition temperature of DG41 is much closer to SG rather than it is to traditional PVB; nevertheless, for medium- to long-time applied actions, the response of DG41 is much closer to PVB than it is to SG for a wide range of temperatures.

4. The loss of adhesion between glass and interlayers, also known as *delamination*, is a factor of major concern for LG, affecting durability, mechanical properties and aesthetics. Within this work, a correlation between the strain energy and the glass-interlayer interface fracture toughness is provided, based on phenomenological observations. The correlation allows to assess the risk of delamination between glass and different interlayer materials at varying temperatures (cfr. §5.1.3 p.151).
   Additional analyses on adhesive properties have been carried out for fully damaged LG specimens, to provide a correlation between the loss of adhesion which comes with the tension stiffening effect using numerical models.

Post-failure properties of LG elements

5. The response of three-ply, progressively damaged LG beams was investigated with static and dynamic in-plane experimental analyses. Results showed that the choice of interlayers does not have a significant influence for the in-plane response in the pre-failure phase. On the other hand, the post-failure response depends on the coupling ability of interlayers and glass fragments. In partial damage conditions, the beams stiffness did not reduce to the stiffness of intact glass plies alone; likewise, for fully damaged elements, the glass stiffness did not vanish completely, but the small tempered glass fragments of were able to effectively contribute to the stiffens and residual load-bearing capacity. This behaviour was ascribed to the coupling of glass fragments and interlayers, a phenomenon called *tension stiffening* effect, which has been observed to suffer a reduction with the progression of the debonding. Experimental results highlighted that SG and DG41 provide a similarly remarkable contribution to the overall stiffness in partial damage conditions, while for fully damaged conditions the ionoplast SG interlayer is vastly superior. Static and dynamic tests have been compared in terms of in-plane bending stiffness, allowing to validate an *equivalent stiffness model* for partially damaged LG beams.

---

of other researchers which also have tackled this problem in the past; such suggestion has been firmly embraced and followed through in this work.

6. Experimental measurements which allowed to interpolate the position of the neutral axis in bending tests, showed that its depth is consistently close to mid-height in all partially damaged conditions. This finding resulted in the proposal and validation of an e*quivalent thermal expansion model*, which uses previous results on equivalent stiffness, to reproduce the macroscopic effect of shattered tempered glass plies (cfr. §5.2.3 p.158). The post-failure tempered glass expansion results in an internal state of stress which affects the intact plies in partially damaged conditions.
   As a case-study, the equivalent thermal expansion model is used to assess the post-failure safety of a LG strut within the deck of a pedestrian bridge (cfr. §6.2 p.177).
7. Studies on *ageing* of fully damaged LG were performed by comparison of bending tests after five months, showing a drastic reduction on the tension stiffening effect. This is due to the combined effects of interlayer relaxation diminishing the internal state of compression of the glass fragments and to the progression of delamination. Due to the adhesion decay moisture can reach the interlayer-glass interface diffusely through cracks. The ageing process has been observed to be much more pronounced on beams stored in natural external weathering conditions (cfr. §5.2.4 p.162).

7.2 OPEN TOPICS FOR FUTURE INVESTIGATIONS

Relying on the combination of tests at different scales, the conclusions provided in this work -°summarized in the previous paragraph°- expand the knowledge on several issues regarding LG structural elements. Nevertheless, aside from these main outcomes, several other interesting pathways emerged from the analyses such a vast body of experimental evidence. Consequently, elements of doubt and unresolved issues remain or have not yet been properly considered; either for not being the primary focus of this work, either for having emerged late throughout the research and thus requiring the planning of additional experimental analyses.

An overview of the topics deemed to be of greater interest for future analyses is presented and discussed in the following. Hopefully, some of those matters will be addressed soon in upcoming researches, conveying increased confidence on the results of this work.

The "dream" of a unified model

The ultimate goal in polymer science applied to LG design is arguably to provide a unified mechanical model, capable of describing all properties of thermoplastics emerging from their microscopic nature:

microscopic properties		*emerging properties*
network entanglement, cross-link interactions	→	elasticity, plasticity, viscosity, ultimate strength and adhesion (to glass)

For practical LG design, this would lead to defining cases under which certain properties can be neglected or when these are more relevant. For instance, the response of thermoplastics far below their glass transition temperature is known to be often similar to brittle materials. Conversely, at higher temperatures, the same material could behave as a very viscous fluid. Therefore, it is unsurprising that equations allowing to model the response of such materials change dramatically for varying boundary conditions. Ultimately, the macroscopic behaviour has to do with the nature of microscopic interactions among these long molecules.

While this vision still seems to be out of reach, new researches should always go in the direction of bridging the gap between different fields of inquiry. With a unified model, simplified equations could also be brought up to quantify one specific aspect of the polymer response that is of interest for one specific application, while knowingly disregarding others.

In this work, a few wide-ranging conclusions can be given in the direction of a unified model, with some advices for future developments.

Decomposition of intermolecular and network effects

Aside from the different hyperelastic models, two approaches have been follower in material science for plastics and rubbers, to replicate the short-term correlations between stress and strain: one is a statistical approach[3], in which elastic constraints are linked to the distribution of interactions between polymer chains (i.e. crosslinks density and chains length), the second is an empirical one, where experimental data is used as a regression base for fitting functions that are exclusively based on experience and intuition [304,305].

Arguments can be made to support the adoption of a mixed model, which empirically accounts for the statistical distribution of cross-links within polymer molecules. In that direction, the GR model provides an option for dividing in two parts the response of thermoplastic materials, which are only supposedly ascribed to intermolecular forces and network entanglement of molecules. While our results fit perfectly within a the framework of such theory, there is currently no clear evidence on whether or not such speculations are an accurate representation of these micromechanical interactions. As such, it is useful to remind that our calibrations are not yet meant to divide the materials response in that sense, but only aim to a faithful reconstruction of the intrinsic response.

If it is proven that the reversible part of deformation can be ascribed to the network effects and the plastic ones to the rupture of intermolecular cross-links, a calibration of the decomposition could be achieved using cyclic load/hold/unload tests at various speed rates and temperatures, using a pattern similar the one shown in Figure 7.1.

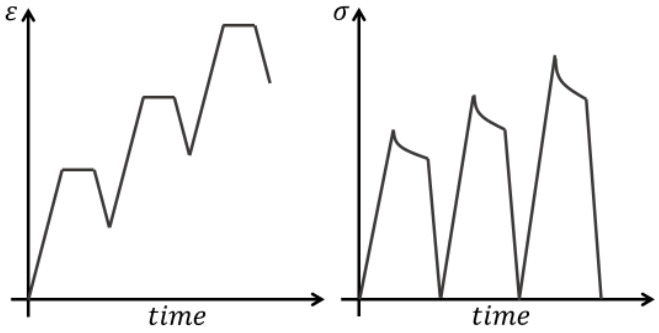

Figure 7.1 - cyclic tests for determination of plastic deformations[4]

Calibration of the generalized response model

The procedure to build the GR model (cfr. §5.1.1.2) has proven to be versatile and capable to mimic the response of very different materials. Nevertheless, a few

[3] Also referred to as the "Gaussian" or "molecular" approach.

[4] Applicable Standards are ASTM D638 [66] and ISO 527 [264].

parameters have been observed to be poorly dependent from some conditions investigated within our analyses. For instance, the hyperelastic part of the response of DG41 is almost independent from the strain rate, similarly to the short-range intermolecular interactions for PVB (Table 5.4 and Figure 5.9). A more in-depth analysis on such correlations will lead to better understanding the fundamental causes of different materials response.

A comparison with the results of our analyses can be made using the work of Kott and Vogel [306], which also investigated the response of PVB at different temperatures and strain rates (Figure 7.2). Their study showed that below 0°C PVB exhibits a behaviour which is very similar compared to our results for DG41 and more even so SG at room temperature (23.5°C in the temperature-controlled room). This outcome is consistent with the evidence provided within this manuscript for the part concerning viscoelastic properties at different temperatures (i.e. "softer" materials behave similarly to "harder" ones, only at lower temperatures).

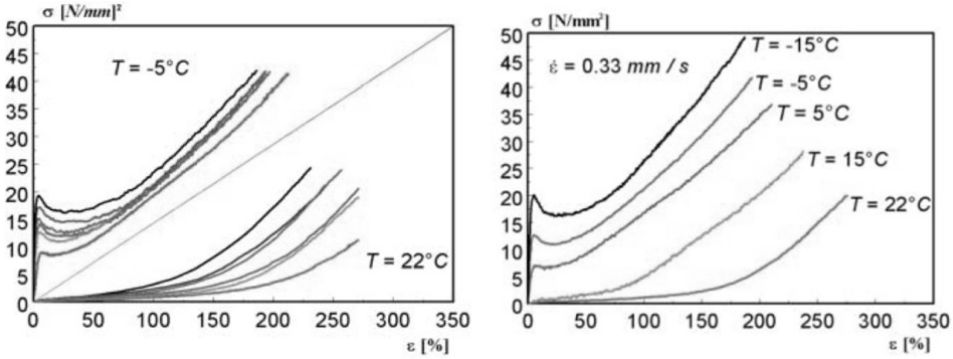

Figure 7.2 - uniaxial tests on PVB for a) at various displacement rates (0.037 to 5.000 mm/s) and b) 0.33 mm/s for temperatures between -15 and +22°C (Kott and Vogel 2003)

These observations hints that the coefficients of the newly introduced GR model may be in turn conveniently described as functions of strain rate, temperature and possibly other parameters, to consistently replicate the outcome of tensile tests with the same mathematical formulation.

$$\sigma(\varepsilon, \dot{\varepsilon}, T, S) = \sum_{i=1}^{N} \left\{ \boldsymbol{A_i}(\dot{\varepsilon}, T) \cdot \left[-e^{-\boldsymbol{B_i}(\dot{\varepsilon}, T) \cdot \varepsilon} + 1 \right] \right\} + \boldsymbol{C}(\dot{\varepsilon}, T) \cdot \varepsilon^3 + \boldsymbol{D}(\dot{\varepsilon}, T) \cdot \varepsilon$$

Varying properties of patented interlayer materials

Tensile tests on SG[5] referred by I. Belis et al. in 2009 [307] show a similar behaviour at higher strain rates compared to tests performed with our experimental analyses (Figure 7.3). On the other hand, lower strain rates do not exhibit the same peak stress drop, making it worth investigating if the composition of the product has changed within the last decade, or if other factors may affect its properties (e.g. production method, storage time or conditions, etc.).

It is known that interlayer materials can be affected by changes in their chemical composition over time, namely for the direct contact of air and moisture on the edges of LG elements and solar radiation on surfaces exposed to direct sunlight. Results provided in this work in terms of Prony series and WLF coefficients (cfr. §5.1.2.5), regarding the viscoelastic properties of PVB, SG and DG41, could potentially be used to forecast the mechanical response of such materials over a

[5] At the time, the commercial acronym was SGP, rather than today's SG (-P for "Plus").

very long amount of time. Nevertheless, predictions should always keep in mind that properties of the materials are likely to change over the course of many years. Therefore, predictions for $10 \div 50$ years should be looked at with a critical eye, acknowledging that changes in the chemical compositions of the materials could lead to inaccurate predictions of the mechanical response.

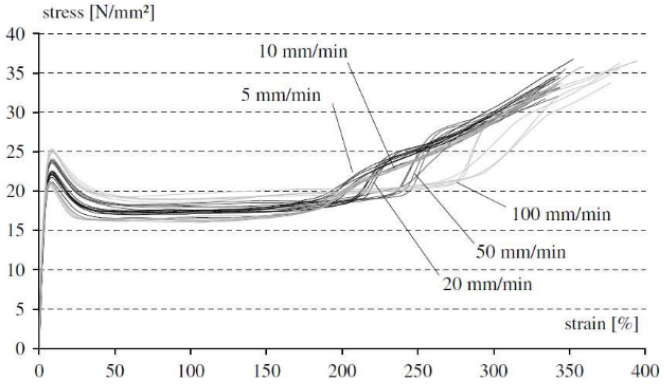

Figure 7.3 - tensile tests on SG at room temperature (engineering curves) [307]

Comparison of dynamic tests and shear tests

The direct shear testing procedure, which has been followed through within this work to study the viscoelastic properties of interlayers, represents an element of novelty for this field of research. Traditionally, viscoelastic parameters are given by manufacturers as a result of dynamic testing techniques, like as those described in §3.1.3.4. It has been pointed out, both in this work and by other researchers, that such tests are not optimal when trying to extend the results for LG design, as the uncoiling of the polymer chains and the modification of cross-link network are effects that inherently requires time to develop [240]. The high strain-rate response of thermoplastics (i.e. high frequencies) is believed to be mostly governed by short-range intermolecular actions, a belief strengthened by the fact that a different response is observed for tensile tests at different strain rates. As intermolecular effects are less relevant upon longer time spans, this may ultimately lead the dynamic procedures to overestimate the long-term response of thermoplastic materials [7,10,237,240].

A comparative experimental campaign direct using both direct and dynamic tests would share more light on this open question. To be effective, both analyses must separately aim to assess the same viscoelastic properties of identical materials using the two methodologies. A final cross-examination of the outcomes will lead to a better understanding of the limits under which both procedures are reliable for LG design purposes.

Defining yielding (pseudo-yielding) for thermoplastics

A universally accepted definition of the pseudo-yielding limit is believed to be an essential step in research advancement regarding structural applications plastic materials. Trying to encompass most response typologies, an original – simple - proposal for this definition was made within this paper. Nonetheless, while contemplating the outcomes of numerous other researches, the current proposition is based on a limited number of tests and materials.

A study on the point where the properties of the material change dramatically could end up in defining the limits under which linear theories are acceptable, both for linear elasticity and linear viscoelasticity.

Convergence and uniqueness for WLF regression method

The convergence of the proposed WLF regression procedure has been only verified for the six distributions of shift factors that were of interest for our analyses. Proving mathematical proof of the convergence of this method, along with the uniqueness of the solution, will allow to implement the procedure in a straightforward way, without *a posteriori* verifications.

A genetic algorithm for WLF-mastercurve optimization

An iterative procedure has been proposed to provide the coefficients of the experimental mastercurves and the corresponding time-temperature superposition coefficients. The analyses carried out in this work between §5.1.2.1 and §5.1.2.4 involve inevitably a degree of arbitrariness in what is considered an "acceptable" fit of the mastercurves and the WLF equations; to generalise this procedure in an efficient routine, a genetic algorithm could be set up to optimize the iteration:

Feed: load the experimental branches for all investigated temperatures (3 minimum), define the desired number of terms for the mastercurves, the maximum number of generations and the survival ratio.

Step 1 create a pre-determined number N of random distributions of shift factors δ_i. Shift the branches accordingly for each distribution.

Step 2 find mastercurve coefficients using the DOI method, then compute the sum of square differences ϵ_{MST} for each for each of the distributions.

Step 3 use the WLF regression procedure on the random distributions of shift factors and store final sum of least squares ϵ_{WLF} for each one.

Step 4 Arrange the distributions for increasing values of $\epsilon = \epsilon_{MST} \cdot \epsilon_{WLF}$ and save the best ones for the next generation according to the survival ratio.

Step 5 Produce small random variations of the saved distributions to fill the population of the next generation with new shift factors distributions and repeat from step 2 until the last generation is complete.

Contribution of damaged plies to ultimate failure of partially damaged LG

The research has presented advances with respect of the enhanced response of in-plane loaded structural LG elements after partial failure, due to the stiffening effect provided by adherent tempered glass fragments. The progressive failure being artificially induced on non-loaded conditions, our analyses covered the topic of "stiffening" rather than the "reinforcing". Little is yet known regarding the effect of glass fragments on the ultimate failure of partially damaged elements.

Does the presence of glass fragments increase the load-bearing capacity? To what extent? These two questions are yet without satisfying answers. Of all bending tests carried during the analyses in §4.3, only one was extended up to the ultimate failure of the beam (specimen C2, cfr. Table 4.7). That test, which recorded the ultimate failure at $35.37\ kN$, can be compared to the expected strength of a single undamaged ply which turns out to be approximately $26\ kN$[6]. Far from having any statistical ambition, this single result hints that the contribution of glass fragments to the ultimate strength can be almost as significant as the contribution to stiffness.

[6] Calculated using the characteristic strength for glass $f_{g,k} = 133.67\ MPa$.

Numerical models for partially-damaged LG

Non-linear Discrete Element Models (DEMs) have been used with good results by other researchers for fully-damaged LG [215]. The outcomes of our research, namely the parts regarding the observed macroscopic expansion induced by failure of tempered glass, could be implemented in such numerical analyses for partial levels of damage to assess the intermediate damage state compliance of fail-safe requirements.

The successful implementation of similar numerical models ultimately depend on the dependable representation the mutual interactions among tempered glass fragments, which arise from the discharge of internal stresses.

Out-of plane properties of partially-damaged LG

Both for static and dynamic properties of partially damaged LG elements have been extensively investigated in this work with respect of in-plane actions. Therefore, damaged plies were always imposed both compressive actions (on top) and tensile ones (at the bottom) during our analyses. Except for the lateral sag produced upon failure (cfr. §4.3.3.2 and §5.2.3), this procedure implies that the order with which the plies fail has a limited effect on the global response. Namely, the in-plane bending properties are not expected to vary whether the left or right ply fails.

On the other hand, the stiffness and residual load-bearing capacity of damaged LG to which out-of-plane loads are assigned, is likely to be largely influenced by the circumstances governing the damage progression. For the anisotropic nature of the response of glass fragments, which was highlighted by uniaxial tests in §4.3.4, there is reason to believe that the mechanical properties of partially damaged LG may vary significantly, according to which ply fails first: regardless the number of plies and assuming to deal with simply supported LG elements with vertical loads, if the ply on top fails first, an increasing load will induce compressive effects among fragments and reduce the amplitude of cracks. Vice-versa, if the bottom ply fails, increasing vertical loads will tend to open the cracks. The different contribution of damaged plies in both scenarios deserves an in-depth investigation, both from an experimental and numerical point of view.

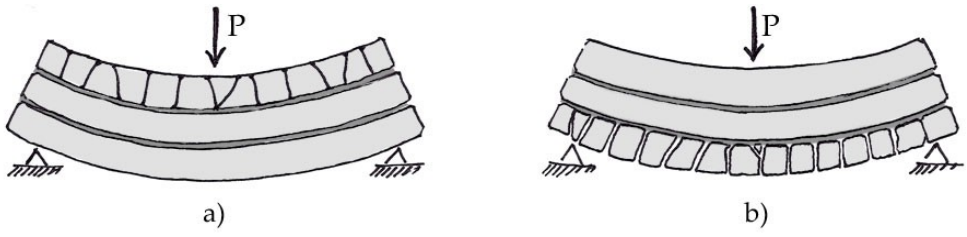

Figure 7.4 - different scenarios for out-of plane bending of partially damaged LG: a) top ply fractured and b) bottom ply fractured

Cold-bent insulated glazing

An application for cold-bent glazing has been shown using LG elements with different thickness of the glass plies and different interlayers (cfr. §6.1). Issues regarding the mechanical properties of LG in such conditions have been examined

and solutions have been proposed. Yet, in many architectural applications, glazing used for the envelope of buildings are made with insulated glass[7] rather than single blocks of LG. In turn, the inner and outer panes comprising the insulated element can be made with LG.

To my knowledge, cold-bent insulated glazing has not yet been studied nor tested. The extension of results brought in this work to such applications call for an analysis of the mechanical properties of edge seal spacers used for insulated glass units. A first analysis in that direction has been performed by A. Hagl [308], but the focus of that research was put to relative rotations of the edges, rather than the shear displacements that can be induced by cold-bending (Figure 7.5).

Provided that the mechanical properties of the sealing unit can be correctly understood, the mutual effects among LG panes can be modelled and added to the cold-bending effects on the single panes.

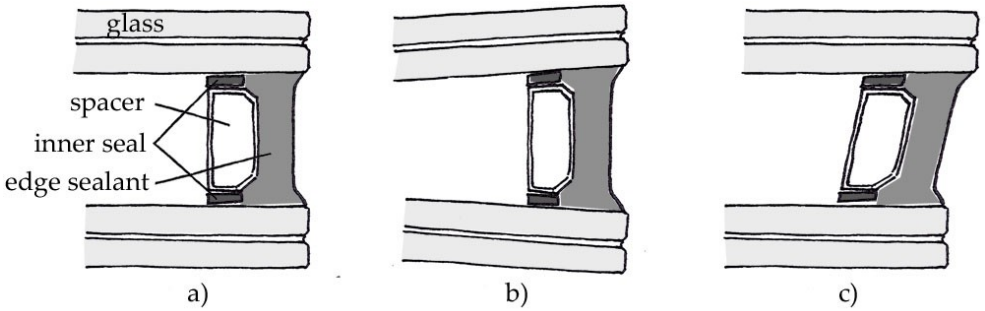

Figure 7.5 - a) insulated glass components, b) analyses by A. Hagl [308], c) case-study of interest for cold-bending applications

[7] Typicallt two glass panes separated by a vacuum or gas filled space, to reduce heat transfer.

APPENDIX A

A theoretical approach is proposed for modelling the readings of the load recording device during the opening of the climatic chamber. The problem is related to thermal deformations of parts composing the device: dynamometric ring, aluminium pads and LVDT transducer, which is itself composed by several elements (external case, shaft, inner core, etc.). Parts are presented in Figure A.1.

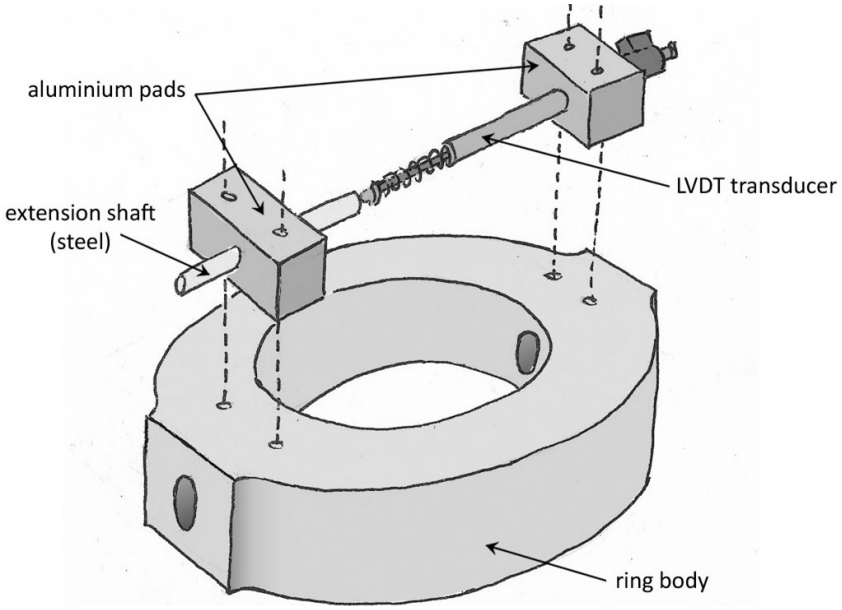

Figure A.1 - layout of the elements in the load-measuring devices

Effects of temperature can then be studied with general thermodynamic model:

$$\Phi = -mc_v \frac{dT}{dt}$$

where Φ is the heat loss function, m and c_v are the mass of the object and the specific heat capacity of the material and T is the varying temperature over time t.

In the case Newton's law for convective heat transfer applies, one can assume:

$$\Phi(\mathrm{T}) = \frac{dQ}{dt} = hA(T - T_{amb.})$$

The loss heat function Φ is defined as the rate of transferred heat Q. On the right side of the equation, h is the heat transfer coefficient, A the external surface of the object generating the convective flow and $T_{amb.}$ the ambient temperature. With the applied convention the heat flow is positive when directed from the object to the surrounding fluid (in our situation, an infinite volume of freely convective air). Solving the differential equation with assigned boundary condition $T(0) = T_{test}$ and rearranging for T yields:

$$T^{(1)} = (T_{test} - T_{amb.}) \cdot \exp\left(-\frac{hA}{mc_v}t\right) + T_{amb.}$$

where T_{test} is the original temperature of the object at time $t = t_0$.

The equation describes the temperature variation of an object at temperature T_{test} in a convective surrounding fluid at temperature $T_{amb.}$ (the superscript on the temperature on the left side of the equation has been added only to differentiate it

with respect of symbols used in the following). If the surrounding ambient temperature is abruptly brought back to the original temperature (in our case the temperature T_{test}) at a given time $t_1 > t_0$, one can calculate the effect which previous temperature change would have induced starting at t_1 for $t > t_1$:

$$T^{(2)} = (T_{test} - T_{amb.}) \cdot \exp\left(-\frac{hA}{mc_v}(t - t_1)\right) + T_{amb.}$$

By subtracting this effect to the previous, one finds the cumulative effect for an object subject to and temperature cycle between T_{test} and $T_{amb.}$ between t_0 and t_1:

$$T = T^{(1)} - T^{(2)} = (T_{test} - T_{amb.}) \cdot \left[\exp\left(-\frac{hA}{mc_v}t\right) - \exp\left(-\frac{hA}{mc_v}(t - t_1)\right)\right]$$

The analysis of the thermodynamic properties of the elements accountable for varying readings in the dynamometric ring system ought to consider two key elements with very different properties: the steel ring itself and the LVDT transducer. Some assumptions are made on the properties of the system:

- constant heat transfer coefficient,
- purely convective heat transfer in still air,
- instantaneous (fast) temperature changes in the climatic chamber,
- aluminium pads thermal deformations are negligible,
- extension shaft and LVDT transducer are in thermal equilibrium,
- parts inside the transducer are always in thermal equilibrium,
- different elements do not exchange a significant amount of heat.

Table A.1 - thermal properties for the parts of the system

	Sym.	Unit	Ring	LVDT
mass	m	kg	2.35	$2.74 \cdot 10^2$
specific heat capacity	c_v	$J/(kg \cdot K)$	490	490
heat transfer coefficient	h	$W/(m^2 \cdot K)$	30	30
external surface area	A	m^2	$4.52 \cdot 10^{-2}$	$3.61 \cdot 10^{-3}$ †

† considering the presence of the protrusions of various elements to the actual steel case

To calibrate a model for the readings of the load recording devices in the effective test situation, we can consider a conditioned test which has reached a steady temperature of $T_{test} = 50°C$ (i.e. the temperature of all the parts of the device, of the chamber internal wall surface and the air contained inside the chamber itself have all reached the set-point temperature for tests, therefore all parts are in thermal equilibrium). The temperature of the air surrounding the metal parts at the instant of the chamber opening is considered to be immediately dropping from $T_{test} = 50°C$ to $T_{amb.} = 21°C$ [1]. The temperature at the closing of the chamber is considered to rise back rapidly to the previous $T_{test} = 50°C$ [2].

[1] This is not an unreasonable hypothesis, given that the hot air flow is free to leave the volume of the climatic chamber and spread into the surrounding room. The surrounding ambient being extremely large, it will be considered uninfluenced by the mixture of the hot air coming from the open chamber, in such a way that its temperature can be considered constant at all times.

[2] This hypothesis may seem less rigorous than the previous, as the chamber needs time to build up the climatic condition defined by the set-point. Nonetheless, readings of the in-built sensors of the chamber suggest that the time needed to bring back the temperature to the set-point for a previously conditioned chamber is very limited, in the range of $10\ s$ to $40\ s$ seconds, depending on the temperature difference between the set-point and the ambient temperature.

Assuming $t_0 = 0$ and $t_1 = 7\,\text{min}\ 20\ s$ (time interval intended to match the opening time of the chamber corresponding to the loading phase of the specimens), together with all the data presented above, the solution of the equations for $T(t)$ are presented in Figure A.2. For each part in the load-measuring device, the dotted lined line represents temperature variation $T^{(1)}(t)$ of the objects (i.e. the temperature variation upon opening, if the chamber is not closed back).

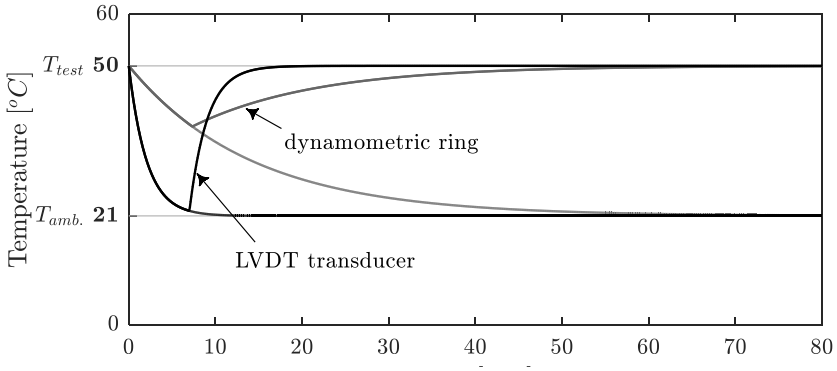

Figure A.2 - temperature variation for test at 50°C

Results show that the thermal inertia of the ring is higher compared to the transducer. Hence, the temperature variation of the transducer is greater, but this elemental is also faster in coming back to the temperature T_{test} and the effects of the chamber opening are negligible approximately 10 minutes after it is closed.

Based on the separate temperature variations of the parts, we investigated whether load readings were affected with positive or negative correlations between temperature variations and load measurements. Starting from the dynamometric ring itself, the correlation is clearly negative: if the temperature of the ring diminishes, the structure contracts simulating a compression load, yielding a positive value. However, this point of view alone may be misleading, as the dynamometric ring and the transducer share one fixed point (on the upper side of the ring). From the reference system originated from the shared fixed point: as temperature lowers, the ring contracts, but because the transducer cools faster it contracts even more. From the point of view of the measuring device this phenomenon is perceived as an actual expansion, rather than a contraction (the same logic applies in reverse if the elements are heating rather than cooling). Therefore, it is safe to say that the load readings of the system ring-transducer r_{t-r} are affected by a negative correlation. This may be presented in the form of:

$$r_{t-r} = k_1 \cdot (T_t - T_r)$$

Where k_1 is the (negative) correlation factor between the relative temperature effects of transducer and ring with load readings.

The second correlation to be understood is the internal correlation between the moving parts of the transducer: the steel case, the metallic shaft and the moveable core. Although the accurate description of the mutual effects and heat transfers inside the transducer are a very complex problem (they may probably be the subject of a separate research on their own), we are lucky enough to have at our disposal data which is only related to the global effects of the thermal interaction of elements inside the transducer: the ones set to measure the displacement at the base of the specimens. Data shows that a rapid cooling of the instrument results in a - virtual - measured expansion of the shaft. Therefore, for the mere purpose of finding the correlation inside the load measurement device, this also results in

knowing this is a negative correlation: the diminishing temperature of the instrument results in an increasing virtual load recorded. If k_2 is the correlation coefficient between the transducer temperature and the load readings:

$$r_t = k_2 \cdot T_t$$

The last step of the calibration procedure is finding the correlation among coefficients k_1 and k_2 using the experimental data. Readings of the "virtual" load registered upon chamber opening may be written as:

$$r(t) = r_{t-r} + r_t = k_1 \cdot [T_t(t) - T_r(t)] + k_2 \cdot T_t(t)$$

Hence, the calibration of the coefficients with experimental data yields $k_1 = -0.11$ and $k_2 = -0.09$. Figure A.3 shows the validation of the model results compared to experimental data. The meaning of those coefficients is to yield the proportion between a given temperature variation and the corresponding load reading. To better illustrate how those have been calibrated, values for t_1 and $T_{amb.}$ are also presented in Table A.2, for each temperature tests have been ran at. As shown in Table A.2, ambient temperature may vary significantly among tests, but this is not surprising: some chamber openings were performed during early morning hours, when temperatures were generally lower, whereas most were performed in the afternoon, when temperatures reached peaks of 24 to 25°C.

Table A.2 - ambient temperature and duration of the opening for tests

T_{test} [°C]	60	55	50	45	40	35	30	23	20	17	10	0
T_{amb}[°C]	21.5	21.0	21.0	23.5	23.0	22.0	22.5	24.0	19.0	20.5	17.5	17.0
t_2 [s]	357	390	440	246	332	345	327	430	301	459	399	607

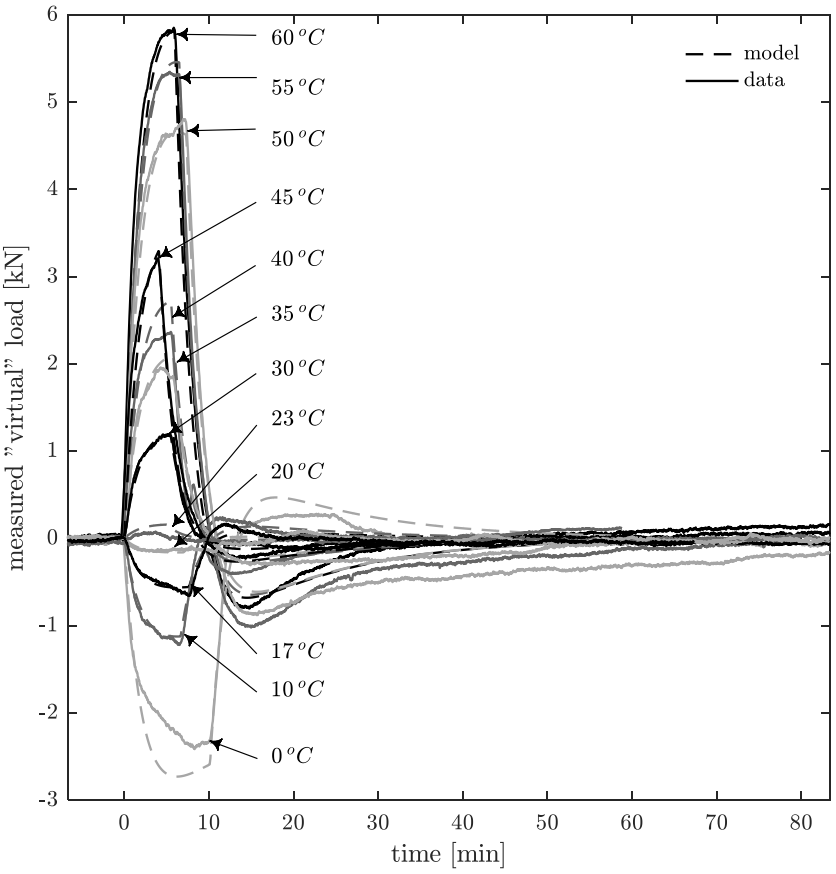

Figure A.3 - validation of the thermodynamic model for the load-recording devices

APPENDIX B

A few criteria have been evaluated to model the response of testing devices used for the campaign on long-term viscoelastic properties of interlayer materials (cfr. §4.2). The problem is defined in terms of finding suitable mathematical models for reproducing the response of the base contrast elements shown in Figure 4.22 in terms of load over displacement curves. The final result of the analyses described in the following in shown in Figure 4.23.

Many attempts for modelling the response of the setup did not immediately yield satisfactory results, either for being poorly able to represent the shape of experimental results shown in or for creating numerical glitches. Among others, the following were evaluated:

- polynomial order < 8 (vastly inaccurate fit),
- polynomial order 9-11 (oscillating results around data points),
- polynomial order > 12 (badly conditioned problem
- exponential order 1 (unable to model the first part of the curve),
- exponential order 2 (different shapes for different devices, poorly able to model the first part of the curves, no reliability outside the interpolation span).

In the light of these results, a combined polynomial-exponential equation was deemed to be the best solution, combining the best features of both models while working around their limits. The fitting function was chosen to be in the form of:

$$P(\delta) = \mathrm{A}e^{\mathrm{B}\delta} + \mathrm{C}\delta^2 + \mathrm{D}\delta + \mathrm{E}$$

Where P and δ are the loads and displacements, while A, B, C, D and E are five coefficients to be found to minimize the least-squares problem for assigned δ_i , P_i:

$$\min\left(\sum\left[P_i - \left(\mathrm{A}e^{\mathrm{B}\delta_\mathrm{i}} + \mathrm{C}\delta_\mathrm{i}{}^2 + \mathrm{D}\delta_\mathrm{i} + \mathrm{E}\right)\right]^2\right) = \min\left(\sum f(P_i, \delta_i)\right)$$

This can be also be expressed as the root finding problem of the partial derivatives of the function with respects of the coefficients A to E:

$$\frac{\partial}{\partial K}\sum\left[P_i - \left(\mathrm{A}e^{\mathrm{B}\delta_\mathrm{i}} + \mathrm{C}\delta_\mathrm{i}{}^2 + \mathrm{D}\delta_\mathrm{i} + \mathrm{E}\right)\right]^2 = 0 \qquad K = A, \dots, E$$

$$\begin{cases} \sum\left[2e^{B\delta_i}\left(Ae^{B\delta_i} + C\delta_i^2 + D\delta_i + E - P_i\right)\right] = 0 \\ \sum\left[2A\delta_i e^{B\delta_i}\left(Ae^{B\delta_i} + C\delta_i^2 + D\delta_i + E - P_i\right)\right] = 0 \\ \sum\left[2\delta_i^2\left(Ae^{B\delta_i} + C\delta_i^2 + D\delta_i + E - P_i\right)\right] = 0 \\ \sum\left[2\delta_i\left(Ae^{B\delta_i} + C\delta_i^2 + D\delta_i + E - P_i\right)\right] = 0 \\ \sum\left[2\left(Ae^{B\delta_i} + C\delta_i^2 + D\delta_i + E - P_i\right)\right] = 0 \end{cases}$$

Presented in this form, the problem is partially non-linear and cannot be solved straightforwardly. To work around this issue, a slightly different approach has been undertaken.

Data in the first part of the experimental curves was more suited for a polynomial fit, while an exponential model is more appropriate in the final part. A polynomial interpolation was performed on the initial part alone from the entire data set. After several attempts, the boundaries for this - arbitrarily fixed - reduced data set have

been set from zero to a maximum displacement equal to 60% of the average displacement measured at 35 kN for each device. The value of 35 kN has been chosen according to the actual use of this interpolation procedure in the following data analysis, as the tests on LG specimens never went above 30 kN by design, so any model only requires to be well calibrated up to that value. Nonetheless, to gain full insight on the behaviour of the base contrast steel elements, a slightly higher value of 35 kN was chosen. A 2nd degree polynomial least-squares interpolation was performed on the reduced data set. In the following figure B1, black dots represent the reduced dataset $\left(P_{i,\mathrm{poly}}, \delta_{i,\mathrm{poly}}\right)$ for the initial part of the curves, which are interpolated by the polynomial best fit (red line in the following figures).

The polynomial fit is intended as the solution of the linear problem issued by:

$$\min\left(\sum\left[P_{i,\mathrm{poly}} - \left(C{\delta_{i,\mathrm{poly}}}^2 + D\delta_{i,\mathrm{poly}} + E\right)\right]^2\right) = \min\left(\sum g\left(P_{i,\mathrm{poly}}, \delta_{i,\mathrm{poly}}\right)\right)$$

Yielding the values of the variables C, D and E and thus the function:

$$P_{\mathrm{poly}}(\delta) = \mathrm{C}\delta^2 + \mathrm{D}\delta + \mathrm{E}$$

With this part of the interpolation, values calculated with the function $P_{\mathrm{poly}}(\delta)$ have been subtracted from the original dataset, producing a new dataset $\left(P_{i,\mathrm{exp}}, \delta_{i,\mathrm{exp}}\right)$ which was used to interpolate the exponential part of the curves:

$$\left(P_{i,\mathrm{exp}}, \delta_{i,\mathrm{exp}}\right) = \left(P_i, \delta_i\right) - \left(P_{\mathrm{poly}}(\delta_i), 0\right)$$

The $\left(P_{i,\mathrm{exp}}, \delta_{i,\mathrm{exp}}\right)$ is presented in the following figures by the gray dot clouds. The remaining part of the procedure was to interpolate the new set of data with the exponential function using a - now possible - least square interpolation:

$$P(\delta) = \mathrm{A}\mathrm{e}^{\mathrm{B}\delta}$$

The problem can be made linear by recognizing that one can take the natural logarithm of both sides of the equation, so that various methods of polynomial fit approaches can be used:

$$\ln P_{i,\mathrm{exp}} = \ln \mathrm{A} + \mathrm{B}\delta_{i,\mathrm{exp}}$$

Taking $A' = \ln \mathrm{A}$ and $P_i' = \ln P_{i,\mathrm{exp}}$:

$$P_i' = \mathrm{A}' + \mathrm{B}\delta_{i,\mathrm{exp}}$$

The least-square interpolation problem is given as a minimum-finding problem:

$$\min\left(\sum\left[{P_i}' - \left(\mathrm{A}' + \mathrm{B}\delta_{i,\mathrm{exp}}\right)\right]^2\right) = \min\left(\sum h\left({P_i}', \delta_{i,\mathrm{exp}}\right)\right)$$

Solving this system yields the values of the constants A and B. Values of the constants have been calculated for the three devices used.

Table B.1 - constants for best fitting curves of testing devices

	A	**B**	**C**	**D**	**E**
device 048	3.776e-06	116.4	194.2	25.72	0.1364
device 054	2.712e-06	83.23	72.32	30.75	0.1894
device 052	2.509e-04	74.75	244.0	19.76	0.0948

The final curves for modeling the response of the setup are shown in Figure B.2 for the three devices.

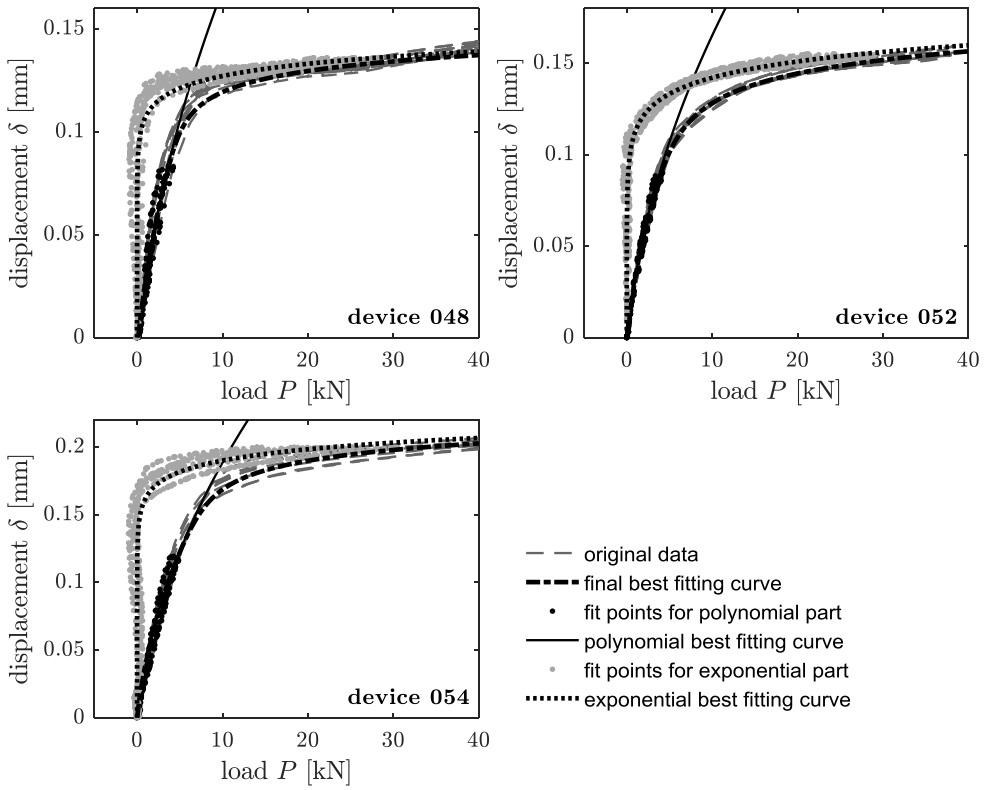

Figure B.1 - calibration of the nonlinear elastic correlation for device 048

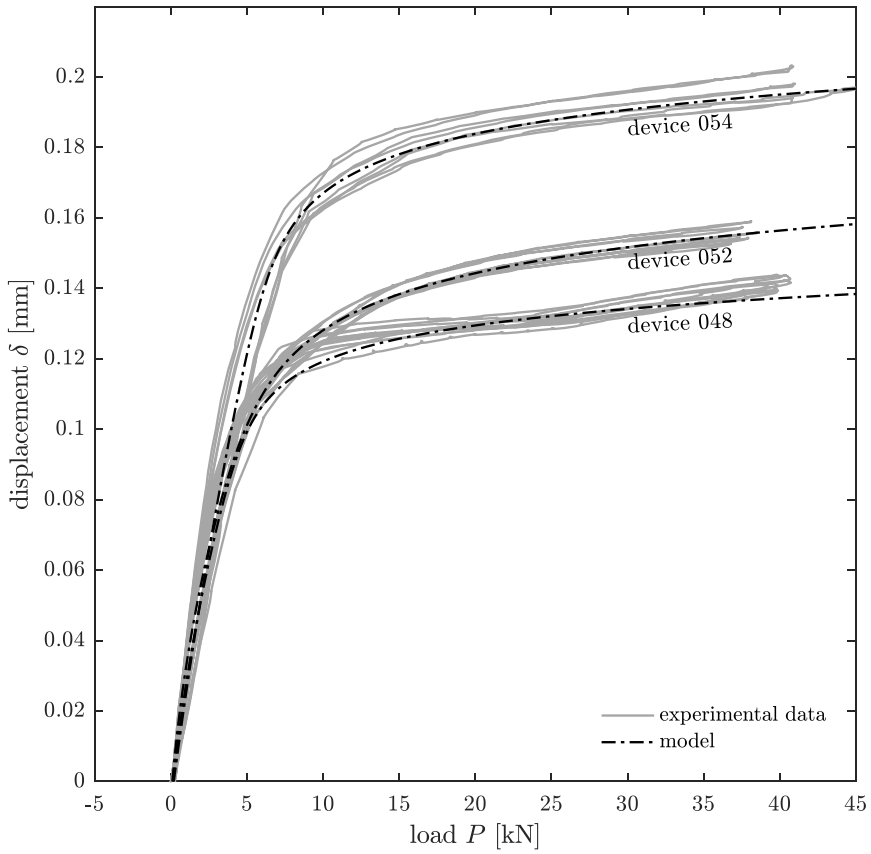

Figure B.2 - calibration of the nonlinear elastic correlation all testing devices

APPENDIX C

While specimens delamination was visible to the naked eye, photographing it properly proved to be a very challenging task. Several techniques were put to the test varying lighting, backgrounds and angles. Taking pictures from a square angle proved to be an impractical solution, as there seems to be no way to avoid having a disturbing camera reflection on the final image. A solution was found with the setup in Figure C.1, using a dark blue cloth background, which helps the delamination reflections to stand out, and a white paper sheet to intercept the reflection from the glass surface.

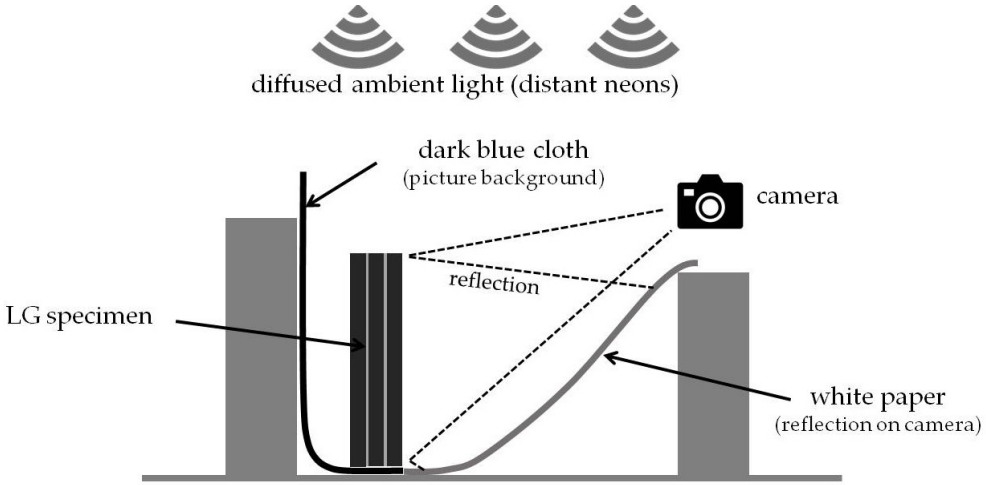

Figure C.1 - setup for imaging delamination

Pictures were straightend up correcting for perspective with an image processing software (Figure C.2.a) and the result then manually analysed using AutoCAD to recreate the delamination patterns (Figure C.2.b).

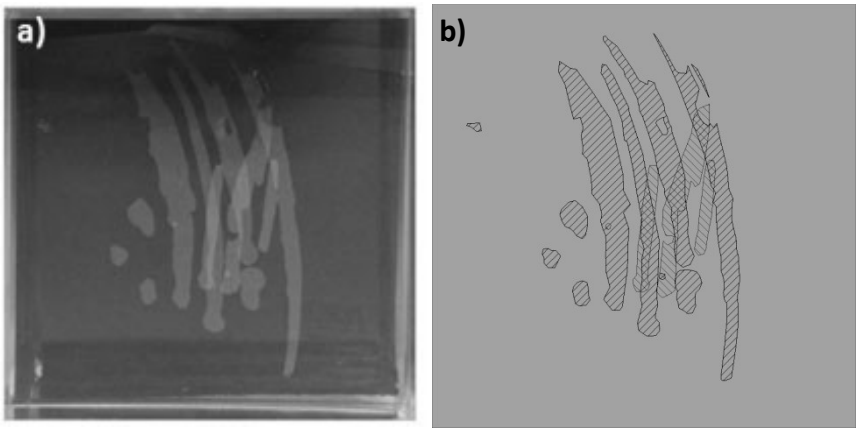

Figure C.2 - delamination analysis for specimen S09

PVB	Temp.	Specimen	Delaminated area [mm² / %]
	0°C	P03	0,0 / 0,00
		P04	0,0 / 0,00
		P05	0,0 / 0,00
	10°C	P14	0,0 / 0,00
		P15	0,0 / 0,00
	20°C	P16	0,0 / 0,00
		P17	0,0 / 0,00
	30°C	P11	0,0 / 0,00
		P12	235,5 / 1,18
		P13	593,3 / 2,97
	40°C	P08	270,2 / 1,35
		P09	263,6 / 1,32
		P10	20,9 / 0,10
	50°C	P06	0,0 / 0,00
		P07	107,6 / 0,54
		P02	56,7 / 0,28

30°C	40°C	50°C
	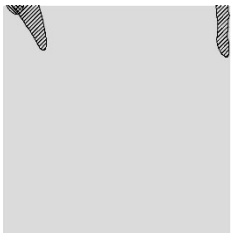	
P11 - 0.00%	P08 - 1.35%	P06 - 0.00%
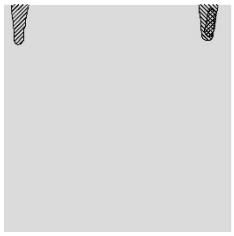	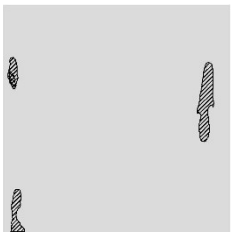	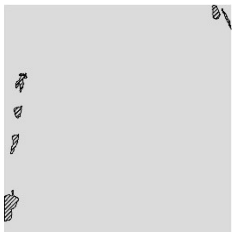
P12 - 1.18%	P09 – 1.32%	P07 – 0.54%
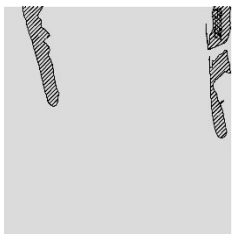		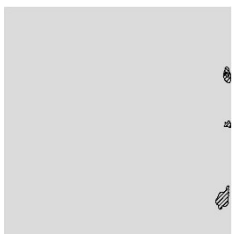
P13 - 2.97%	P10 - 0.10%	P08 – 0.28%

DG41	Temp.	Specimen	Delaminated area [mm² / %]
	10°C	D13	0,0 / 0,00
		D14	0,0 / 0,00
		D15	0,0 / 0,00
	14°C	D19	0,0 / 0,00
		D20	0,0 / 0,00
		D22	0,0 / 0,00
	17°C	D23	0,0 / 0,00
		D25	0,0 / 0,00
		D26	0,0 / 0,00
	20°C	D16	0,0 / 0,00
		D17	0,0 / 0,00
		D18	0,0 / 0,00
	23°C	D10	0,0 / 0,00
		D11	0,0 / 0,00
		D12	0,0 / 0,00
	30°C	D06	0,0 / 0,00
		D07	0,0 / 0,00
		D08	0,0 / 0,00
	40°C	D01	750,2 / 3,75
		D02	1458,8 / 7,29
	50°C	D03	304,9 / 1,52
		D04	345,7 / 1,73
		D05	255,5 / 1,28

40°C	**50°C**
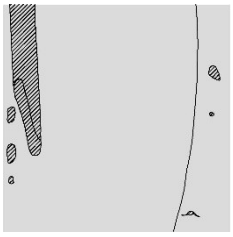	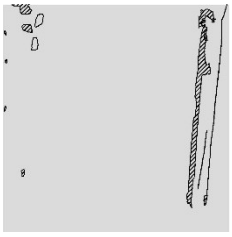
D01 – 3.75%	D03 – 1.52%
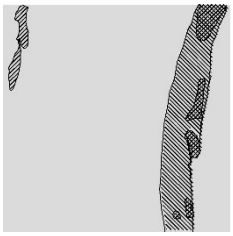	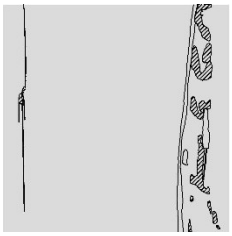
D02 – 7.29%	D04 – 1.73%
	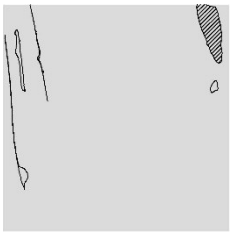
	D05 – 1.28%

SG	Temp.	Specimen	Delaminated area [mm² / %]
	20°C	S27	0,0 / 0,00
		S28	0,0 / 0,00
		S29	0,0 / 0,00
	30°C	S24	4,3 / 0,02
		S25	0,0 / 0,00
	35°C	S17	0,0 / 0,00
		S18	0,0 / 0,00
		S19	0,0 / 0,00
	40°C	S23	0,0 / 0,00
		S26	0,0 / 0,00
	45°C	S13	193,0 / 0,97
		S15	224,0 / 1,12
	50°C	S20	499,8 / 2,50
		S21	0,0 / 0,00
		S22	43,1 / 0,22
	55°C	S09	1529,0 / 7,65
		S12	38,0 / 0,19
	60°C	S14	1212,0 / 6,06
		S16	1727,3 / 8,64

45°C	50°C	55°C	60°C
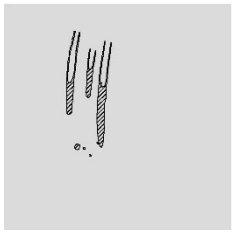		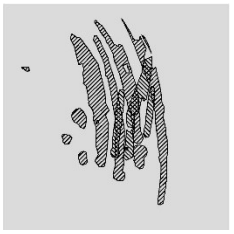	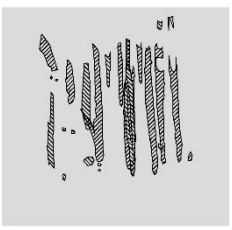
S13 – 0,97%	S20 – 2,50%	S09 – 7,65%	S14 – 6,06%
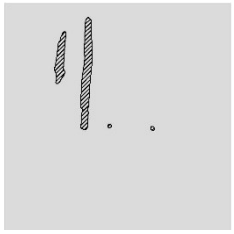		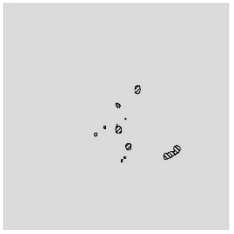	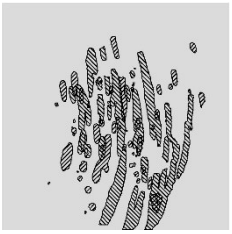
S15 – 1,12%	S21 – 0,00%	S12 – 0,19%	S16 – 8,64%
	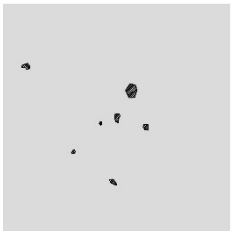		
	S22 – 0,22%		

APPENDIX D

Saflex®DG41 Young Modulus (www.saflex.com)

Load Duration	Temp								
	20°C	25°C	30°C	35°C	40°C	45°C	50°C	55°C	60°C
	MPa								
1 sec	1101	782	449	154	27	6.8	3.2	2.4	2.1
3 sec	1007	700	319	80	11	3.8	2.4	2.1	1.8
30 sec	812	466	115	13	3.0	2.4	1.8	1.8	1.5
1 min	735	387	74	8.3	2.7	2.1	1.8	1.5	1.5
5 min	596	213	20	3.5	2.1	1.8	1.5	1.5	1.2
30 min	413	83	5.6	2.4	1.8	1.5	1.2	1.2	0.9
1 hour	316	47	4.1	2.1	1.8	1.5	1.2	0.9	0.6
1 day	65	5.0	2.1	1.5	1.2	0.9	0.6	0.3	0.3
5 days	19	2.7	1.8	1.5	0.9	0.6	0.3	0.3	--
1 week	14	2.7	1.8	1.5	0.9	0.6	0.3	--	--
3 weeks	6.8	2.1	1.5	1.2	0.9	0.6	0.3	--	--
1 month	5.3	2.1	1.5	1.2	0.6	0.3	0.3	--	--
1 year	2.4	1.7	1.2	0.6	0.3	--	--	--	--
10 years	1.9	1.4	0.8	0.3	--	--	--	--	--
15 years	1.9	1.3	0.7	0.3	--	--	--	--	--
50 years	1.8	1.2	0.6	--	--	--	--	--	--

Young's modulus E' is calculated using formula E'= 2G'(1+v) where v = Poisson's ratio of approximately 0.476 for isotropic polymeric material as measured in accordance with ASTM D638.

Kuraray SentryGlas® (SG) Shear Modulus(www.kuraray.com)

Shear Modulus G MPa (psi)		Load Duration						
		1 s	3 s	1 min	1 h	1 day	1 mo	10 yrs
Temperature	10 °C (50 °F)	240. (34800)	236. (34220)	225. (32625)	206. (29870)	190. (27550)	171. (24795)	153. (22185)
	20 °C (68 °F)	217. (31465)	211. (30595)	195. (28275)	169. (24505)	146. (21170)	112. (16240)	86.6 (12557)
	24 °C (75 °F)	200. (29000)	193. (27985)	173. (25085)	142. (20590)	111. (16095)	73.2 (10614)	43.3 (6279)
	30 °C (86 °F)	151. (21895)	141. (20445)	110. (15950)	59.9 (8686)	49.7 (7207)	11.6 (1682)	5.31 (770)
	40 °C (104 °F)	77.0 (11165)	63.0 (9135)	30.7 (4452)	9.28 (1346)	4.54 (658.3)	3.29 (477.1)	2.95 (427.8)
	50 °C (122 °F)	36.2 (5249)	26.4 (3828)	11.3 (1639)	4.20 (609)	2.82 (408.9)	2.18 (316.1)	2.00 (290)
	60 °C (140 °F)	11.8 (1711)	8.18 (1186)	3.64 (527.6)	1.70 (246.5)	1.29 (187.1)	1.08 (156.6)	0.97 (140.7)
	70 °C (158 °F)	3.77 (546.7)	2.93 (424.9)	1.88 (272.6)	0.84 (121.8)	0.59 (85.6)	0.48 (69.6)	0.45 (69.6)
	80 °C (176 °F)	1.55 (224.8)	1.32 (191.4)	0.83 (120.4)	0.32 (46.4)	0.25 (36.3)	0.21 (30.5)	0.18 (26.1)

APPENDIX E

Photogrammetric strain analysis for SG interlayer, compared to instrument readings for three different testing speeds (cfr. §5.1.1.1 page 118).

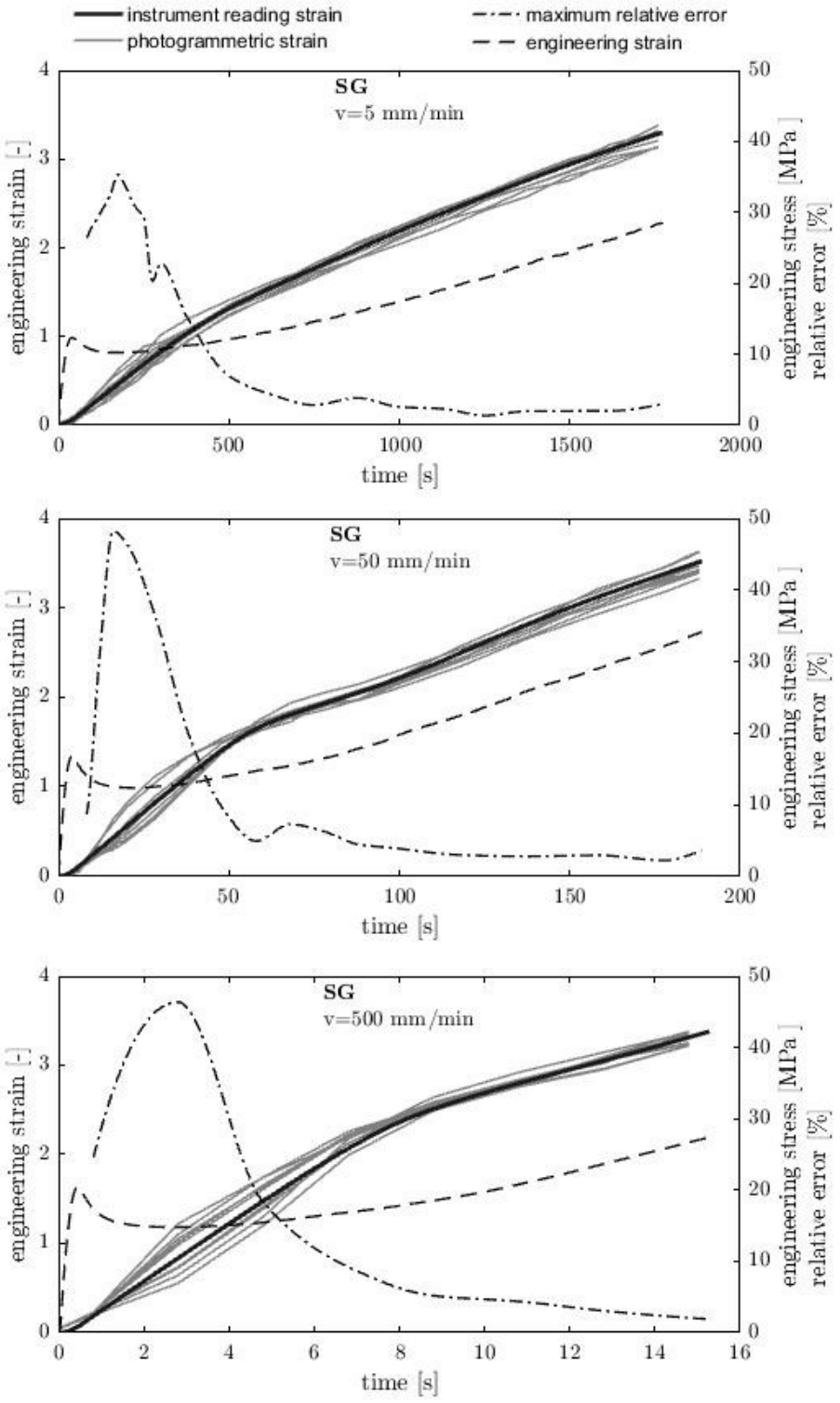

APPENDIX F

Hypothesis for the analytical formulation provided by W. Young and R. Budynas [296], whose results were used for the modal analysis in §5.2.1, are not an exact match of experimental conditions. Namely, supports at the ends of the specimen are not located along the axis, but are supporting the bottom edge instead. Moreover, a thin aluminium pad is attached do the glass plies, to serve as an interface with the steel rollers and protect the specimen from the risk of local stress concentrations. Moreover, the proposed analytical formulation neglects the presence of – small – lateral protrusions of the specimens beyond the supports at both ends.

Two LE numerical models were built: one to replicate the conditions under the theoretical hypotheses and one that corresponds to the setup configurations. The models were identical in every single aspect with the exception of the insertion of the aluminium pads (the central mass was calibrated to replicate the mass of the accelerometers).

A comparison of the results concluded that the differences between the two models response in terms of natural frequencies are very limited.

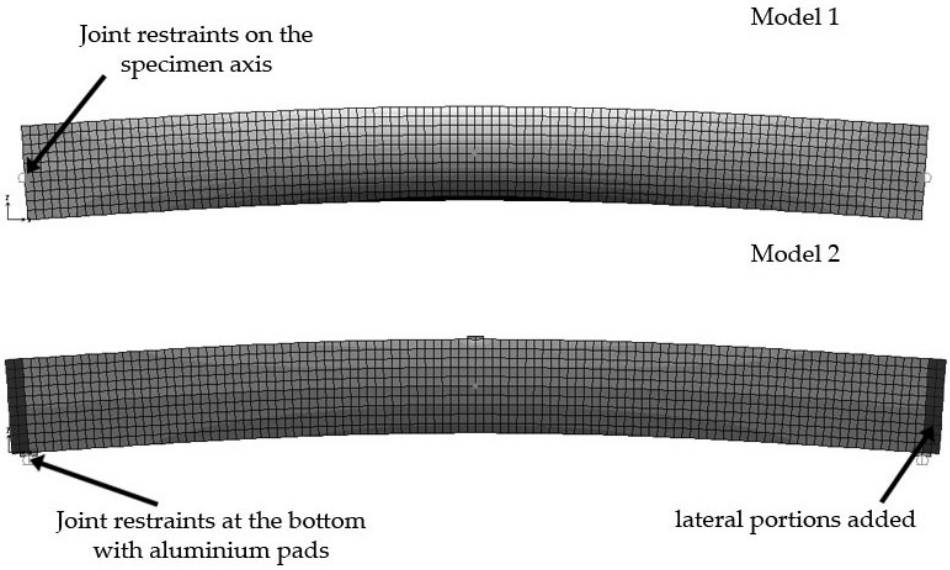

Type	A	B	C
calibrated using specimen data	A1	B1	C1
Model 1 frequency [Hz]	75.03	88.01	86.15
Model 2 frequency [Hz]	74.97	87.97	86.08
correction factor a	0.9992	0.9995	0.9991

APPENDIX G

Part1 : tabulated results

Table G.1 - SG relaxation modulus G

Temp°C	5s	30s	10m	11h	1w	3mo.	6mo.	50yrs.
20			**83,1***	56,5	35,9	19,2	15,3	4,56
25			75,6	41,8	23,6	9,90	7,82	3,71
30		83,0†	57,6	27,3	11,5	5,51	4,89	2,99
35	77,3†	61,5†	38,6	12,6	5,62	3,98	3,71	2,42
40	53,5†	39,6†	20,0	5,48	3,86	2,98	2,78	1,86
45	29,3†	17,8†	6,53	3,63	2,76	2,25	2,11	1,34
50	8,29†	5,35†	3,71	2,49	1,97	1,53	1,43	0,92
55	3,71†	3,11†	2,39	1,60	1,23	0,96	0,91	**0,86***
60	2,18†	1,82†	1,36	0,92				

Table G.2 - SG inverse creep compliance modulus J^{-1}

Temp°C	5s	30s	10m	11h	1w	3mo.	6mo.	50yrs.
20			**91,4***	61,2	44,4	31,5	29,1	12,3
25		91,3†	69,8	43,2	30,0	20,3	17,5	7,19
30	85,7†	67,8†	48,3	28,4	17,5	10,3	8,99	5,24
35	55,7†	45,1†	30,4	14,4	8,52	6,08	5,67	4,07
40	33,9†	27,5†	15,4	7,05	5,38	4,54	4,30	3,04
45	17,1†	11,7†	6,91	4,82	3,93	3,25	3,10	2,19
50	6,88†	5,71†	4,64	3,36	2,75	2,27	2,15	1,52
55	4,44†	3,83†	3,09	2,26	1,80	1,51	**1,45***	
60	2,79†	2,44†	1,93	**1,45***				

Table G.3 - DG41 relaxation modulus G

Temp°C	5s	30s	10m	11h	1w	3mo.	6mo.	50yrs.
10			**48,6***	36,1	22,3	8,07	5,55	0,65
15		48,5†	41,8	21,4	6,85	1,41	0,98	0,47
20	47,6†	42,7†	29,3	6,77	1,27	0,63	0,58	0,36
25	39,4†	31,1†	14,3	1,34	0,62	0,47	0,43	0,28
30	27,4†	17,1†	3,92	0,64	0,47	0,36	0,34	0,26
35	13,5†	5,47†	0,93	0,49	0,37	0,29	0,27	**0,25***
40	4,03†	1,28†	0,60	0,38	0,29	0,26	**0,25***	
45	1,02†	0,66†	0,47	0,31	0,26	**0,25***		
50	0,63†	0,51†	0,38	0,26	**0,25***			

† Numbers shown for $5s$ and $30s$ should always be looked at as lower conservative values, as actual moduli are possibly significantly higher (cfr. §5.1.2.6)

* Higher and lower moduli that should be extracted from the mastercurve (cfr. §5.1.2.6).

Table G.4 - DG41 inverse creep compliance modulus J^{-1}

Temp°C	5s	30s	10m	11h	1w	3mo.	6mo.	50yrs.
10			**49,1***	43,9	41,1	38,0	37,1	30,6
15		40,9†	37,2	31,3	26,1	19,9	18,22	7,41
20	33,6†	30,8†	24,8	14,9	8,30	3,70	2,95	0,75
25	22,2†	17,9†	10,9	3,14	1,14	0,72	0,69	0,52
30	11,3†	7,16†	2,78	0,76	0,64	0,54	0,52	0,38
35	3,90†	2,17†	0,80	0,60	0,50	0,42	0,40	**0,33***
40	1,25†	0,78†	0,64	0,49	0,40	0,35	**0,33***	
45	0,73†	0,65†	0,54	0,40	0,35	**0,33***		
50	0,64†	0,57†	0,47	0,36	**0,33***			

Table G.5 - PVB relaxation modulus G

Temp°C	5s	30s	10m	11h	1w	3mo.	6mo.	50yrs.
0			**17,5***	7,87	3,70	1,58	1,22	0,50
5		17,5†	11,0	3,62	1,45	0,70	0,63	0,33
10	16,7†	12,1†	5,69	1,49	0,69	0,49	0,44	0,23
15	9,97†	6,47†	2,68	0,71	0,49	0,34	0,31	0,15
20	5,50†	3,23†	1,14	0,52	0,35	0,24	0,22	0,11
25	2,79†	1,49†	0,66	0,37	0,25	0,17	0,15	0,09
30	1,30†	0,76†	0,50	0,27	0,18	0,13	0,11	**0,08***
35	0,72†	0,57†	0,37	0,20	0,13	0,09	0,09	
40	0,55†	0,43†	0,28	0,15	0,10	**0,08***		
45	0,42†	0,33†	0,21	0,11	**0,08***			
50	0,33†	0,25†	0,16	**0,08***				

Table G.6 - PVB inverse creep compliance modulus J^{-1}

Temp°C	5s	30s	10m	11h	1w	3mo.	6mo.	50yrs.
0			14,6*	9,94	6,40	3,59	3,11	1,42
5		13,7†	9,88	4,63	2,55	1,69	1,51	0,68
10	10,6†	8,41†	4,72	2,07	1,29	0,78	0,71	0,49
15	5,59†	3,72†	2,14	1,01	0,66	0,54	0,51	0,35
20	2,45†	1,86†	1,07	0,61	0,49	0,39	0,37	0,25
25	1,33†	0,93†	0,63	0,45	0,35	0,29	0,27	0,18
30	0,70†	0,60†	0,47	0,33	0,26	0,21	0,19	0,13
35	0,53†	0,45†	0,35	0,24	0,19	0,15	0,15	
40	0,39†	0,34†	0,26	0,18	0,14	0,12		
45	0,30†	0,25†	0,19	0,14	0,11			
50	0,22†	0,19†	0,15	0,10*				

† Numbers shown for $5s$ and $30s$ should always be looked at as lower conservative values, as actual moduli are possibly significantly higher (cfr. §5.1.2.6)

* Higher and lower moduli that should be extracted from the mastercurve (cfr. §5.1.2.6).

Part2 : graphical results

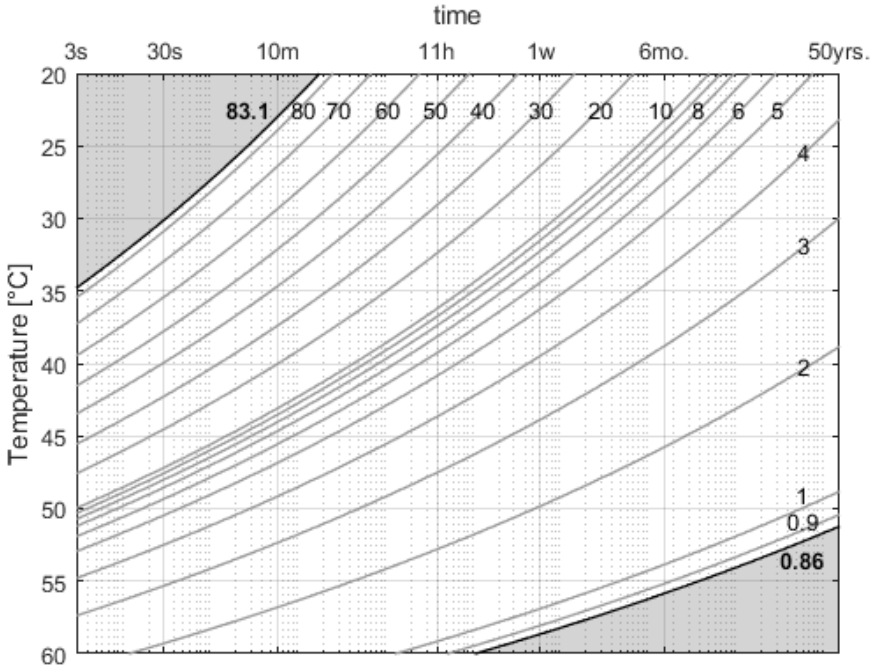

Figure G.1 - SG relaxation modulus G in MPa

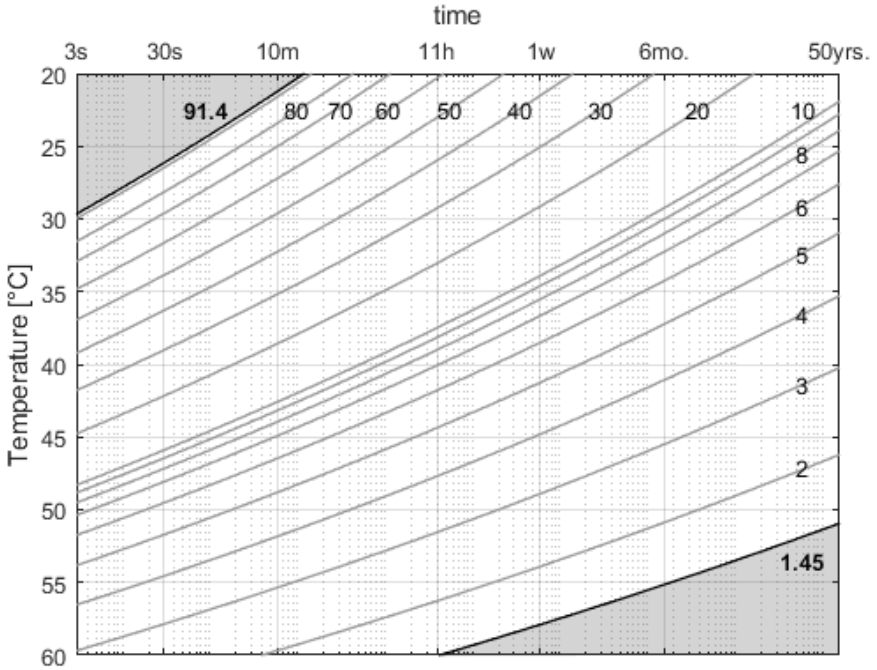

Figure G.2 - SG inverse creep compliance modulus J^{-1} in MPa

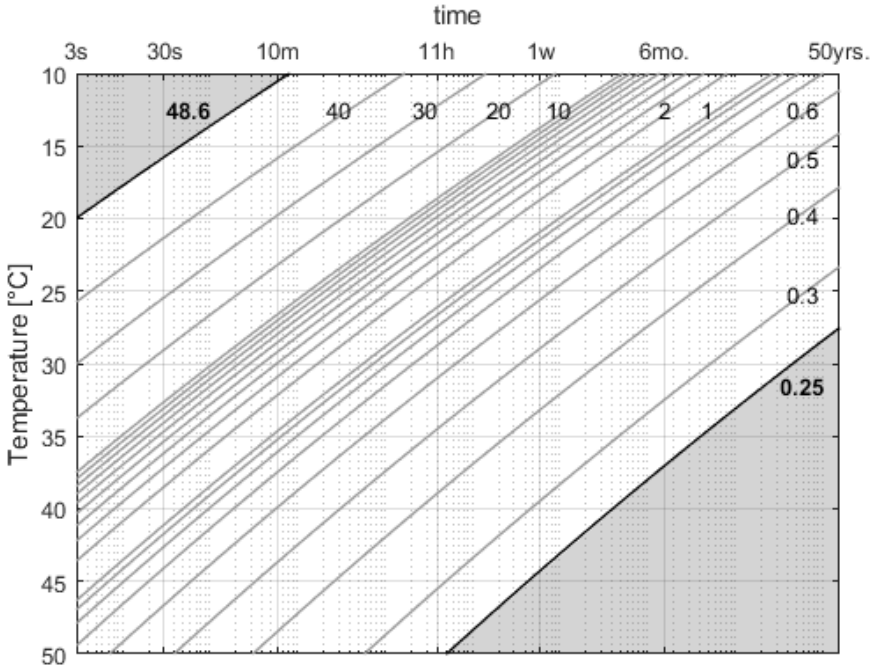

Figure G.3 - DG41 relaxation modulus G in MPa

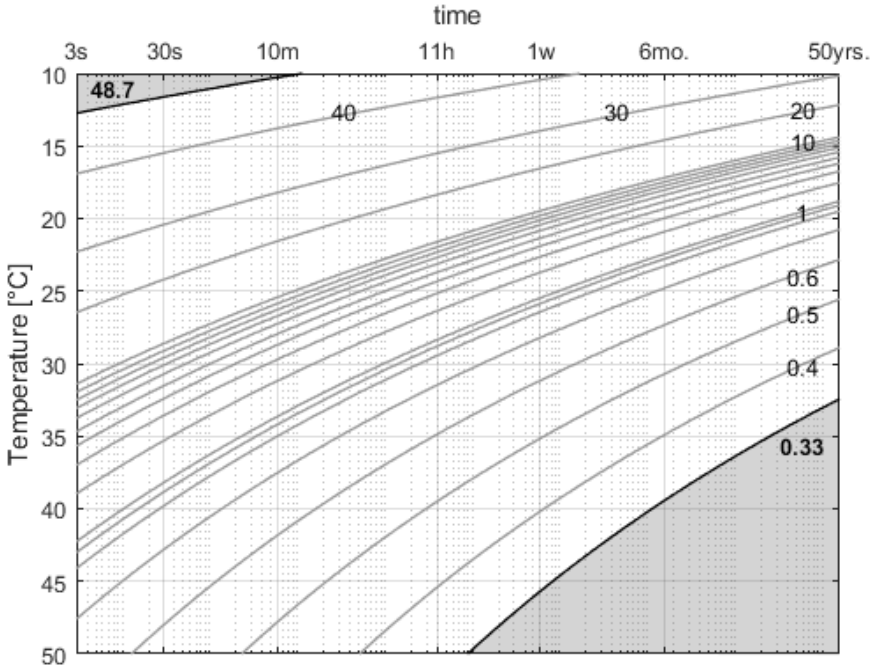

Figure G.4 - DG41 inverse creep compliance modulus J^{-1} in MPa

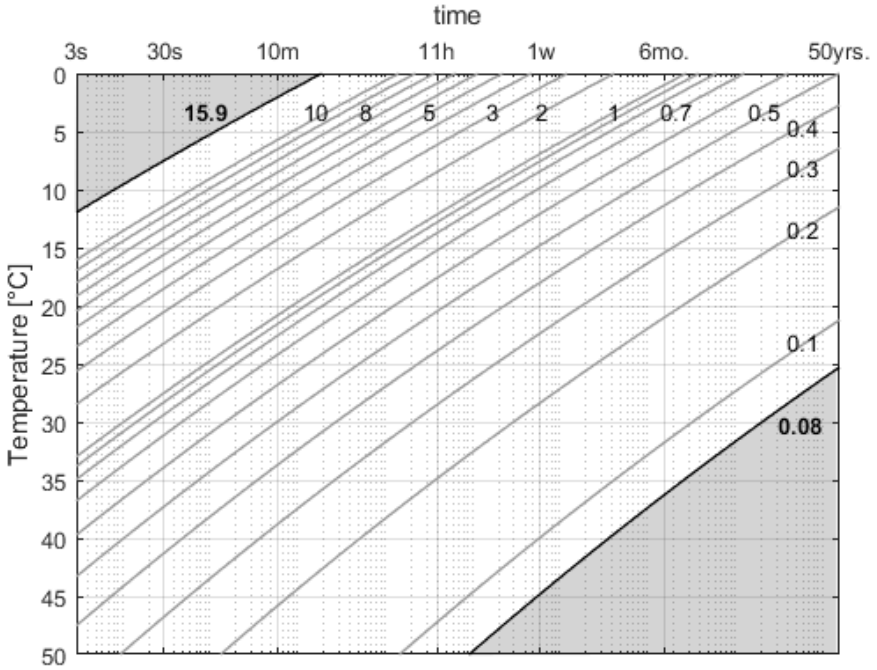

Figure G.5 - PVB relaxation modulus G in MPa

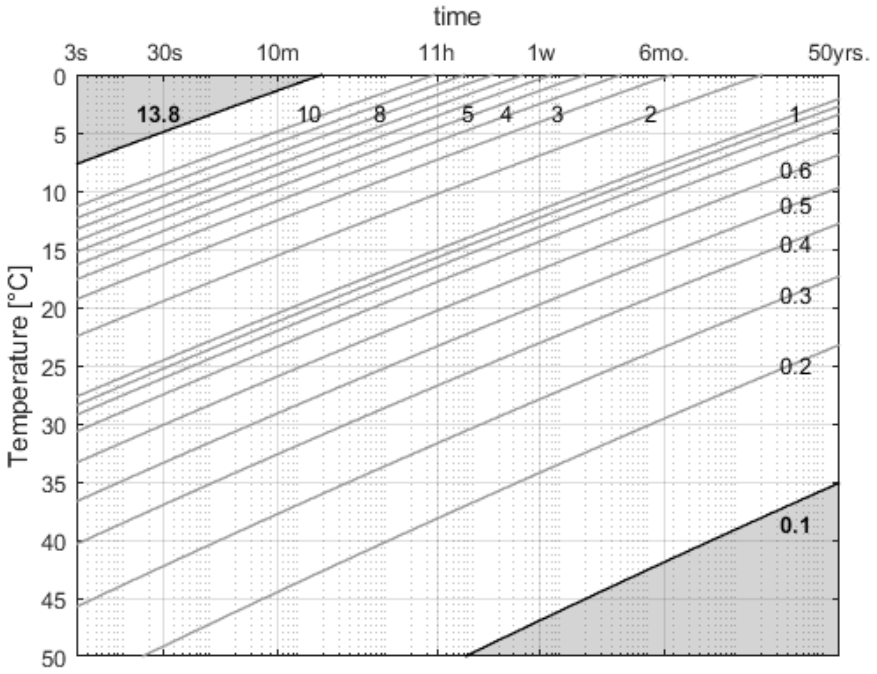

Figure G.6 - PVB inverse creep compliance modulus J^{-1} in MPa

APPENDIX H

Average energy density for PVB, DG41 and SG specimens (continues to next page)

mat.	temp.	spec.	delaminated area* [%]	energy density [J/m^2]	average [J/m^2]
PVB	0°C	P03	-	165	**154**
		P04	-	154	
		P05	-	141	
	10°C	P14	-	264	**251**
		P15	-	239	
	20°C	P16	-	639	**634**
		P17	-	630	
	30°C	P11	-	170	**197**
		P12	1,18	196	
		P13	2,97	226	
	40°C	P08	1,35	175	**231**
		P09	1,32	243	
		P10	0,10	274	
	50°C	P06	-	251	**226**
		P07	0,54	199	
		P02	0,28	229	
DG41	10°C	D13	-	66	**83**
		D14	-	84	
		D15	-	100	
	14°C	D19	-	100	**81**
		D20	-	78	
		D22	-	66	
	17°C	D23	-	97	**85**
		D25	-	88	
		D26	-	70	
	20°C	D16	-	76	**92**
		D17	-	95	
		D18	-	106	
	23°C	D10	-	109	**110**
		D11	-	118	
		D12	-	102	
	30°C	D06	-	696	**748**
		D07	-	760	
		D08	-	788	
	40°C	D01	3,75	612	**565**
		D02	7,29	518	
	50°C	D03	1,52	510	**408**
		D04	1,73	333	
		D05	1,28	382	
SG	20°C	S27	-	48	**52**
		S28	-	55	
		S29	-	53	
	30°C	S24	0,02	125	**126**
		S25	-	126	
	35°C	S17	-	118	**132**
		S18	-	130	
		S19	-	148	
	40°C	S23	-	185	**181**
		S26	-	178	
	45°C	S13	0,97	115	**146**
		S15	1,12	178	
	50°C	S20	2,50	227	**192**
		S21	-	160	
		S22	0,22	190	
	55°C	S09	7,65	260	**237**
		S12	0,19	215	
	60°C	S14	6,06	161	**196**
		S16	8,64	232	

**cfr. Appendix C*

APPENDIX I

Step-by-step DOI method for building a Prony series, given experimental data set $E_i(t_i)$, monotonous, decreasing, with an horizontal asymptote for $t \to \infty$.

Step 1

Define the interval within which the single exponential terms operate in terms of $\delta \log(t)$ (the greater this value, the fewer elements are in the series).

Step 2

For each experimental data point compute the base-10 logarithm of time $\log_{10}(t)$.

Step 3

Compute the differences:

$$\delta\log(t_i) = \log(t_i) - \log(t_1)$$

Step 4

Divide the array of data after point n, in such a way that for each group j:

$$\delta\log\left(t_k^{\mathrm{j}}\right) = \log\left(t_k^{\mathrm{j}}\right) - \log\left(t_1^{\mathrm{j}}\right) < \delta \log(t)$$

where t_k^{j} is the k-th point of the j-th group.

Step 5

Repeat points 3 and 4 until the data array is divided in N groups, taking the $(n+1)$-th point as the first point of the j-th group (The final result will me a division in groups such that the $\log_{10}$-time distance between the first and last point is always lower than $\delta \log(t)$).

Step 6

Compute the absolute variation of data among each group:

$$\delta E_k^j = E_k^j - E_1^{j+1}$$

Step 7

For each group, normalize the variation δE_k^j as:

$$\delta \bar{E}_k^j = Norm\left(\delta E_k^j\right) = \delta E_k^j / \delta E_1^j$$

Step 8

Find the characteristic time τ_j of the j-th group with linear interpolation among the two consecutive $\log_{10}$-time values t_k^j and t_{k+1}^j which encompass the value of e^{-1} (~0,37):

$$\tau_j = \left(e^{-1} - \delta \bar{E}_k^j\right) \frac{t_{k+1}^j - t_k^j}{\delta \bar{E}_{k+1}^j - \delta \bar{E}_k^j} + t_k^j$$

Step 9

Identify the value of total data variation $\tilde{\varepsilon}_j = \delta E_1^j$ for each group j.

Step 10

The infinite modulus can be interpreted as the average of the last a terms of the data array (a~$3 \div 10$ usually yealds good results):

$$\varepsilon_0 = \frac{\sum_{s=0}^{a} E_{M-s}}{a}$$

Step 11

Scale the values $\tilde{\varepsilon}_j$ using the exponential function and the characteristic time for each group:

$$\varepsilon_j = \frac{\tilde{\varepsilon}_j}{\exp\left(-\frac{t_1}{\tau_j}\right)}$$

Step 12

The N values of ε_j and τ_j define the terms in the Prony series sum, the constant term (infinite time modulus) is given by ε_0:

$$\varepsilon(t) = \varepsilon_0 + \sum_{j=1}^{N} \varepsilon_j \exp\left(-t/\tau_j\right)$$

INDEX OF FIGURES

INDEX OF TABLES

REFERENCES

[1] Barnes S. The design of caring environments and the quality of life of older people. Ageing Soc 2002;22:775–89. doi:10.1017/S0144686X02008899.

[2] Sorensen S, Brunnstrom G. Quality of light and quality of life: An intervention study among older people. Light Res Technol 1995;27:113–8. doi:10.1177/14771535950270020501.

[3] Boyce PR, Veitch JA, Newsham GR, Jones CC, Heerwagen J, Myer M, et al. Lighting quality and office work: two field simulation experiments. Light Res Technol 2006;38:191–223. doi:10.1191/1365782806lrt161oa.

[4] Krewinkel HW. Glass Buildings: Material, Structure, and Detail. Princeton Architectural Press; 1998.

[5] Cagnacci E, Orlando M, Spinelli P. Il vetro come materiale strutturale. Polistampa [Italian]; 2010.

[6] Ledbetter SR, Walker AR, Keiller AP. Structural use of glass. J Archit Eng 2006;12:137–49. doi:10.1061/(ASCE)1076-0431(2006)12:3(137).

[7] Delincé D. Experimental Approaches for Assessing Time and Temperature Dependent Performances of Fractured Laminated Safety Glass. Gent University, 2014.

[8] Transparency Market Research. Construction Glass Market - Global Industry Analysis, Size, Share, Trends and Forecast. 2016.

[9] Blascone M. Facciate in vetro strutturale: analisi tipologica e progettazione di una facciata con pinne verticali in vetro. Univertità Degli Studi di Firenze, 2017.

[10] Carraher C. Polymer Chemistry. Polym Chem 2003:36–44. doi:10.1039/c4py01415d.

[11] Duser A Van, Jagota A, Bennison SJ. Analysis of Glass/Polyvinyl Butyral Laminates Subjected to Uniform Pressure. J Eng Mech 1999;125:435–42. doi:10.1061/(ASCE)0733-9399(1999)125:4(435).

[12] Preston DL, Tonks DL, Wallace DC. Model of plastic deformation for extreme loading conditions. J Appl Phys 2003;93:211–20. doi:10.1063/1.1524706.

[13] Pelfrene J, Kuntsche J, Van Dam S, Van Paepegem W, Schneider J. Critical assessment of the post-breakage performance of blast loaded laminated glazing: Experiments and simulations. Int J Impact Eng 2016;88:61–71. doi:10.1016/j.ijimpeng.2015.09.008.

[14] Larcher M, Arrigoni M, Bedon C, van Doormaal JCAM, Haberacker C, Hüsken G, et al. Design of Blast-Loaded Glazing Windows and Facades: A Review of Essential Requirements towards Standardization. Adv Civ Eng 2016;2016:1–14. doi:10.1155/2016/2604232.

[15] Zhang X, Hao H, Wang Z. Experimental study of laminated glass window responses under impulsive and blast loading. Int J Impact Eng 2015;78:1–19. doi:10.1016/j.ijimpeng.2014.11.020.

[16] Zhang X, Hao H, Shi Y, Cui J. The mechanical properties of Polyvinyl Butyral (PVB) at high strain rates. Constr Build Mater 2015;93:404–15. doi:10.1016/j.conbuildmat.2015.04.057.

[17] Tilley RJD. Understanding Solids: The Science of Materials. John Wiley & Sons; 2013.

[18] Mihir J, Prabodh P, Shaan K. Flat Glass Industry At A Glance. 2015.

[19] Bansal NP, Doremus RH. Handbook of Glass Properties. Elsevier Science; 2013.

[20] Larsen AW, Merrild H, Christensen TH. Recycling of glass: accounting of greenhouse gases and global warming contributions. Waste Manag Res 2009;27:754–62. doi:10.1177/0734242X09342148.

[21] Ozer C, Boysan F, Cırık S. Technical Note, Recycling of Glass Waste - An Application for the Esentepe Campus of Sakarya University. Procedia Earth Planet Sci 2015;15:602–6. doi:10.1016/j.proeps.2015.08.111.

[22] Ward PD, Brownlee D. Rare Earth – why complex life is uncommon in the universe. Int J Astrobiol 2003. doi:10.1017/S1473550404261924.

[23] Editor-in-Chief Haimei Zhang. Building Materials in Civil Engineering, 1st Edition. Woodhead Publishing; 2011.

[24] Fanderlick I. Optical properties of glass. United States: Elsevier Science Pub.,New York, NY; 1983.

[25] Vogel W, editor. Glass Chemistry. Berlin, Heidelberg: Springer Berlin Heidelberg; 1994. doi:10.1007/978-3-642-78723-2.

[26] Brodsley L, Frank C, Steeds JW. Prince Rupert's Drops. Notes Rec R Soc 1986;41:1–26. doi:10.1098/rsnr.1986.0001.

[27] Saint Gobain Glass. Manuale del Vetro 2006.

[28] BS EN 572-1:2012 Glass in building. Basic soda lime silicate glass products. Float glass 2012.

[29] Pilkington NSG Group Flat Glass Bussines. Pilkington Glass Handbook 2010 2010:200.

[30] Varshneya AK. Fundamentals of Inorganic Glasses 1st Edition. New York: Academic Press, Inc. An Imprint of Elsevier; 2013.

[31] Creyke WE, Sainsbury IE, Morrell R. Design with Non-Ductile Materials. Springer Netherlands; 1982.

[32] Barsom JM. Fracture of Tempered Glass. J Am Ceram Soc 1968;51:75–8. doi:10.1111/j.1151-2916.1968.tb11840.x.

[33] Varshneya AK. Chemical Strengthening of Glass: Lessons Learned and Yet To Be Learned. Int J Appl Glas Sci 2010;1:131–42. doi:10.1111/j.2041-1294.2010.00010.x.

[34] Anderson TL. Fracture mechanics: fundamentals and applications. CRC press; 2017.

[35] Michalske TA, Bunker BC. The fracturing of glass. Sci Am 1987;257:122–9.

[36] Broek D. Elementary engineering fracture mechanics. Springer Science & Business Media; 2012.

[37] Soules TF, Busbey RF, Rekhson SM, Markovsky A, Burke MA. Finite-Element Calculation of Stresses in Glass Parts Undergoing Viscous Relaxation. J Am Ceram Soc 1987;70:90–5. doi:10.1111/j.1151-2916.1987.tb04935.x.

[38] CNR-DT 210/2013. n.d.

[39] Overend M, De Gaetano S, Haldimann M. Diagnostic Interpretation of Glass Failure. Struct Eng Int 2007;17:151–8. doi:10.2749/101686607780680790.

[40] Bennison SJ, Hayes RA, Pesek SC, Shaffer WA, Smith CA. Laminates comprising ionomer interlayers with low haze and high moisture resistance 2013.

[41] Behr RA, Minor JE, Linden MP, Vallabhan CVG. Laminated Glass Units Under Uniform Lateral Pressure. J Struct Eng 1985;111:1037–50. doi:10.1061/(ASCE)0733-9445(1985)111:5(1037).

[42] Foraboschi P. Hybrid laminated-glass plate: Design and assessment. Compos Struct 2013;106:250–63. doi:10.1016/j.compstruct.2013.05.041.

[43] Hooper JA. On the bending of architectural laminated glass. Int J Mech Sci 1973;15:309–23. doi:10.1016/0020-7403(73)90012-X.

[44] Xu J, Li Y, Liu B, Zhu M, Ge D. Experimental study on mechanical behavior of PVB laminated glass under quasi-static and dynamic loadings. Compos Part B Eng 2011;42:302–8. doi:10.1016/j.compositesb.2010.10.009.

[45] Louter C, Belis J, Veer F, Lebet J-P. Durability of SG-laminated reinforced glass beams: Effects of temperature, thermal cycling, humidity and load-duration. Constr. Build. Mater., vol. 27, 2012, p. 280–92. doi:10.1016/j.conbuildmat.2011.07.046.

[46] Stevanovic D, Kalyanasundaramb S, Lowe A, Jar P-Y. Mode I and mode II delamination properties of glass/vinyl-ester composite toughened by particulate modified interlayers. Compos Sci Technol 2003;63:1949–64. doi:10.1016/S0266-3538(03)00162-3.

[47] Serafinavius T, Lebet JP, Louter C, Lenkimas T, Kuranovas A. Long-term laminated

glass four point bending test with PVB, EVA and SG interlayers at different temperatures. Procedia Eng 2013;57:996–1004. doi:10.1016/j.proeng.2013.04.126.

[48] Teotia M, Soni RK. Polymer Interlayers for Glass Lamination-A Review. Int J Sci Res 2014;3:1264–70.

[49] Walley SM, Field JE, Blair PW, Milford AJ. The effect of temperature on the impact behaviour of glass/polycarbonate laminates. Int J Impact Eng 2004;30:31–53. doi:10.1016/S0734-743X(03)00046-0.

[50] Govaert LE, Timmermans PHM, Brekelmans WAM. The Influence of Intrinsic Strain Softening on Strain Localization in Polycarbonate: Modeling and Experimental Validation. J Eng Mater Technol 2000;122:177. doi:10.1115/1.482784.

[51] Tervoort TA, Smit RJM, Brekelmans WAM, Govaert LE. A Constitutive Equation for the Elasto-Viscoplastic Deformation of Glassy Polymers. Mech Time-Dependent Mater 1997;1:269–91. doi:10.1023/A:1009720708029.

[52] Royer-Carfagni G, Silvestri M. Fail-safe point fixing of structural glass. New advances. Eng Struct 2009;31:1661–76. doi:10.1016/j.engstruct.2009.02.050.

[53] Biolzi L, Orlando M, Piscitelli LR, Spinelli P. Static and dynamic response of progressively damaged ionoplast laminated glass beams. Compos Struct 2016;157. doi:10.1016/j.compstruct.2016.09.004.

[54] Bennison SJ, Qin MHX, Davies PS. High-performance laminated glass for structurally efficient glazing. Innov. Light. Struct. Sustain. Facades, Hong Kong: 2008, p. 1–12.

[55] Bennison SJ, Stelzer I, Davies PS, Sloan JG, Xiaokun H, Liu G. Calculation Methods for the Structural Behavior of Laminated Glass. Glas Perform Days 2009 2009:433–4.

[56] Kennar GA. Interlayer for laminated safety glass 1977.

[57] Sharpe WN, editor. Springer Handbook of Experimental Solid Mechanics. Boston, MA: Springer US; 2008. doi:10.1007/978-0-387-30877-7.

[58] Staudinger H. Über Polymerisation. Berichte Der Dtsch Chem Gesellschaft (A B Ser 1920;53:1073–85. doi:10.1002/cber.19200530627.

[59] Vegt a K Van Der, van der Vegt AK. From Polymers to Plastics. VSSD 2002:268. doi:10.1017/CBO9781107415324.004.

[60] Fried JR. Polymer Science and Technology, 3rd Edition. Prentice Hall; 2014.

[61] Gilbert GK. The Moon's Face: A Study of the Origin of Its Features. Philosophical Society of Washington; 1893.

[62] Ivanov I V. Analysis, modelling, and optimization of laminated glasses as plane beam. Int J Solids Struct 2006;43:6887–907. doi:10.1016/j.ijsolstr.2006.02.014.

[63] Bennison SJ. Structural Properties of Laminated Glass, Short Course. Glas. Process. Days, Tampere (Fi): 2009.

[64] Galuppi L, Royer-Carfagni G. Laminated beams with viscoelastic interlayer. Int J Solids Struct 2012;49:2637–45. doi:10.1016/j.ijsolstr.2012.05.028.

[65] Biolzi L, Cagnacci E, Orlando M, Piscitelli L, Rosati G. Long term response of glass-PVB double-lap joints. Compos Part B Eng 2014;63:41–9. doi:10.1016/j.compositesb.2014.03.016.

[66] International ASTM. ASTM D638-14, Standard Test Method for Tensile Properties of Plastics. West Conshohocken, PA: 2014. doi:10.1520/D0638-14.

[67] Harper CA. Handbook of Plastics, Elastomers, and Composites, Fourth Edition. New York, NY: McGraw-Hill; 2002.

[68] Askadskiĭ AA. Computational materials science of polymers. Cambridge Int Science Publishing; 2003.

[69] Karagiannis A, Szlosek ML, Farhoudi Y. Multilayer interlayers having high Tg and high modulus 2016.

[70] Meitzner R, Schulze SH. Method for determination of parameters for moisture simulations in photovoltaic modules and laminated glass. Sol Energy Mater Sol Cells 2016;144:23–8. doi:10.1016/j.solmat.2015.08.014.

[71] Dhaliwal AK, Hay JN. The characterization of polyvinyl butyral by thermal analysis. Thermochim Acta 2002;391:245–55.

[72] Miller DC, Kempe MD, Glick SH, Kurtz SR. Creep in photovoltaic modules: Examining the stability of polymeric materials and components. Conf Rec IEEE Photovolt Spec Conf 2010:262–8. doi:10.1109/PVSC.2010.5615832.

[73] Cuddihy EF, Coulbert CD, Liang RH, Gupta a., Willis P, Baum B. Applications of ethylene vinyl acetate as an encapsulation material for terrestrial photovoltaic modules. NASA STI/Recon Tech Rep N 1983;83:29809.

[74] Agroui K, Collins G, Farenc J. Measurement of glass transition temperature of crosslinked EVA encapsulant by thermal analysis for photovoltaic application. Renew Energy 2012;43:218–23. doi:10.1016/j.renene.2011.11.015.

[75] Chen Z, Fang P, Wang H, Zhang S, Wang S. Property of ethylene vinyl acetate copolymer in melting processing. J Appl Polym Sci 2006;101:2022–6. doi:10.1002/app.23767.

[76] Haward RN, Thackray G. The Use of a Mathematical Model to Describe Isothermal Stress-Strain Curves in Glassy Thermoplastics. Proc R Soc A Math Phys Eng Sci 1968;302:453–72. doi:10.1098/rspa.1968.0029.

[77] Delincé D, Callewaert D, Belis J, Van Impe R. Post-breakage behaviour of laminated glass in structural applications. Proc Challenging Glas Pg 2008:459–67.

[78] Meijer HEH, Govaert LE. Mechanical performance of polymer systems: The relation between structure and properties. Prog Polym Sci 2005;30:915–38. doi:10.1016/j.progpolymsci.2005.06.009.

[79] Keller U, Mortelmans H. Adhesion in Laminated Safety Glass – What makes it work? Glas. Process. Days, 1999, p. 353–6.

[80] Briccoli Bati S, Fagone M, Ranocchiai G. The elastic behavior of a rubber-like material for composite glass. XIX Congr Dell'Associazione Ital Di Mecc Teor Ed Appl 2009:1–10.

[81] Meissner M, Sackmann V. On the effect of artificial weathering on the shear bond and the tear strength of two different interlayers of laminated glass.pdf. ISAAG - Int. Symp. Appl. Archit. Glas., 2006, p. 223–33.

[82] Kott A. Zum Trag- und Resttragverhalten von Verbundsicherheitsglas 2006:189.

[83] Weller B, Kothe C, Kothe M, Wunsch J. Thermo Mechanical Behaviour of Polymeric Interlayer Materials. Glas Perform Days 2009:734–7.

[84] Bolton NP, Smith WN. Laminated safety glass 1991.

[85] Weller B, Kothe C, Kothe M. Thermal Stability of Polymeric Interlayer Materials. Challenging Glas 2 - Conf Archit Struct Appl Glas 2010:507–16.

[86] MacKnight WJ, Earnest TR. The structure and properties of ionomers. J Polym Sci Macromol Rev 1981;16:41–122. doi:10.1002/pol.1981.230160102.

[87] Hausmann K, Hayes RA, Pesek SC, Shaffer WA, Smith CA. High-clarity ionomer compositions and articles comprising the same 2010.

[88] Biolzi L, Cattaneo S, Rosati G. Progressive damage and fracture of laminated glass beams. Constr Build Mater 2010;24:577–84. doi:10.1016/j.conbuildmat.2009.09.007.

[89] Calderone I, Davies PS, Bennison SJ, Xiaokun H, Gang L. Effective laminate thickness for the design of laminated glass. Glas Perform Days 2009:1–5.

[90] Monserez S. Impact behavior of laminated glass for use in large glass facades. Universiteit Gent, 2013.

[91] Karagiannis A, Szlosek ML, Farhoudi Y. High tg monolithic poly(vinyl acetal) sheet 2016.

[92] Snedeker RH, Garty KT, Skiermont FJ. Glass-polycarbonate resin laminates 1972.

[93] Savineau GF, Sauvineau GF, Savineau GF, Sauvineau GF. Fundamentals of Laminating Process and Quality Requirements. Glas Process Days 1997:13–5.

[94] Adams RD, Wake WC. Adhesive Joints in Engineering. London and New York: Elsevier Applied Science; 1984.

[95] ASTM-D3983-98. Standard test method for measuring strength and shear modulus of nonrigid adhesives by the thick-adherend tensile-lap specimen. 2011.

[96] Louter C. Metal-to-glass bonding properties of an acrylate adhesive (DELO GB368) and an ionoplast interlayer (SentryGlas) at 23 , -20 and 60 ° C. Glas. Perform. Days, 2009, p. 139–43.

[97] Vert M, Doi Y, Hellwich K-H, Hess M, Hodge P, Kubisa P, et al. Terminology for biorelated polymers and applications (IUPAC Recommendations 2012). Pure Appl Chem 2012;84. doi:10.1351/PAC-REC-10-12-04.

[98] Froli M, Lani L. Adhesion , creep and relaxation properties of PVB in laminated safety glass. Glas. Perfomance Days, 2011, p. 1–4.

[99] Chapuis V, Pélisset S, Raeis-Barnéoud M, Li H-Y, Ballif C, Perret-Aebi L-E. Compressive-shear adhesion characterization of polyvinyl-butyral and ethylene-vinyl acetate at different curing times before and after exposure to damp-heat conditions. Prog Photovoltaics Res Appl 2014;22:405–14. doi:10.1002/pip.2270.

[100] Suchy TA. Adhesion quality control of laminated safety glass using ultrasonic velocity and attenuation measurements. University of Illinois at Urbana-Champaign, 2011.

[101] Willham JEC, Brewster MH. Architectural panels with organic photovoltaic interlayers and methods of forming the same 2015.

[102] Bennison SJ, Smith CA, Duser A Van, Jagota A. Structural Performance of Laminated Glass Made with a “Stiff” Interlayer. Use Glas. Build., 100 Barr Harbor Drive, PO Box C700, West Conshohocken, PA 19428-2959: ASTM International; 2002, p. 57-57–9. doi:10.1520/STP11056S.

[103] CEN. EN 1990 Eurocode : Basis of structural design. 2002.

[104] Galuppi L, Royer-Carfagni G. A homogenized model for the post-breakage tensile behavior of laminated glass. Compos Struct 2016;154:600–15. doi:10.1016/j.compstruct.2016.07.052.

[105] Delincé D, Callewaert D, Vanlaere W, Belis J, Depauw J. Plastic deformation of polymer interlayers during post- breakage behavior of laminated glass. Int J Mod Phys B 2008;22:5447–5452/.

[106] Castori G, Speranzini E. Structural analysis of failure behavior of laminated glass. Compos Part B Eng 2017;125:89–99. doi:10.1016/j.compositesb.2017.05.062.

[107] Aenelle ML, Pelayo F, Ismael G. Damping of laminated glass beams with polyvinil butiral interlayer. 7th Int. Oper. Modal Anal. Conf., 2017.

[108] Sable L, Skukis E, Japins G, Kalnins K. Correlation between Numerical and Experimental Tests of Laminated Glass Panels with Visco-elastic Interlayer. Procedia Eng 2017;172:945–52. doi:10.1016/j.proeng.2017.02.107.

[109] Delincé D, Belis J. Experimental assessment of polymers in glass constructions. COST Action TU0905 Mid-term Conf. Struct. Glas., CRC Press/Balkema; 2013, p. 323–30.

[110] Piscitelli LR. Campagna sperimentale sul vetro stratificato: studio del comportamento viscoelastico ed applicazione a un caso studio. Università degli Studi di Firenze, 2014.

[111] Wu P, Zhou D, Liu W, Wan L, Liu D. Elasticity solution of two-layer beam with a viscoelastic interlayer considering memory effect. Int J Solids Struct 2016;94–95:76–86. doi:10.1016/j.ijsolstr.2016.05.007.

[112] Galuppi L, Royer-Carfagni G. The design of laminated glass under time-dependent loading. Int J Mech Sci 2013;68:67–75. doi:10.1016/j.ijmecsci.2012.12.019.

[113] Galuppi L, Royer-Carfagni GF. Effective thickness of laminated glass beams: New expression via a variational approach. Eng Struct 2012;38:53–67. doi:10.1016/j.engstruct.2011.12.039.

[114] Ferry JD. Viscoelastic Properties of Polymers. New York: 1980. doi:10.1080/00914037208075296.

[115] Aklonis JJ, Shaw MT, William MJ. Introduction to polymer viscoelasticity. vol. 59.

1972. doi:10.1016/j.matchar.2007.05.008.

[116] AS 1288-2006 Australian Australian Standard : Glass in buildings - Selection and installation 2006.

[117] ASTM E1300-16 : Standard Practice for Determining Load Resistance of Glass in Buildings. West Conshohocken, PA: ASTM International; 2016. doi:10.1520/E1300-16.

[118] Giovanna R, Zulli F, Andreozzi L, Fagone M. Test Methods for the Determination of Interlayer Properties in Laminated Glass. J Mater Civ Eng 2017;29:04016268. doi:10.1061/(ASCE)MT.1943-5533.0001802.

[119] International Organization for Standardization. ISO 6721:2011 Plastics -- Determination of dynamic mechanical properties. 2011.

[120] Widman JC. Recent Developments in Penetration Resistance of Windshield Glass 1965. doi:10.4271/650474.

[121] Rieser RG, Chabal J. Safety Performance of Laminated Glass Configurations 1967. doi:10.4271/670912.

[122] Yeomans D. The pre-history of the curtain wall. Constr Hist 1998;14:59–82. doi:10.2307/41601861.

[123] Barakat MA, Hetherington JG. New architectural forms to reduce the effects of blast waves and fragments on structures. Struct Under Shock Impact V 1998;32:53–62.

[124] Katsuki K, Shibaoka K, Onishi S, Miwa T. Laminated sheet composed of thin glass and plastic sheets. J Non Cryst Solids 1980;42:619–36.

[125] Sha Y, Hui CY, Kramer EJ, Garrett PD, Knapczyk JW. Analysis of adhesion and interface debonding in laminated safety glass. J Adhes Sci Technol 2012;11:49–63. doi:10.1163/156856197X01010.

[126] Pelfrene J, Van Dam S, Van Paepegem W. Numerical and experimental study of the peel test for assessment of the glass-PVB interface properties in laminated glass. Challenging Glas. 4 COST Action TU0905 Final Conf., CRC Press; 2014, p. 513–9. doi:10.1201/b16499-74.

[127] Dural E. Experimental and numerical treatment of delamination in laminated glass plate structures. J Reinf Plast Compos 2016;35:56–70. doi:10.1177/0731684415613163.

[128] Santarsiero M, Louter C, Nussbaumer A. Laminated connections under tensile load at different temperatures and strain rates. Int J Adhes Adhes 2017;79:23–49. doi:10.1016/j.ijadhadh.2017.09.002.

[129] Serafinavicius T, Lebet J-P, Louter C, Kuranovas A, Lenkimas T. The effects of environmental impacts on durability of laminated glass plates with interlayers (SG, EVA, PVB). Challenging Glas. 4 COST Action TU0905 Final Conf., CRC Press; 2014, p. 455–62. doi:10.1201/b16499-66.

[130] Santarsiero M, Louter C, Nussbaumer A. Laminated connections for structural glass applications under shear loading at different temperatures and strain rates. Constr Build Mater 2016;128:214–37. doi:10.1016/j.conbuildmat.2016.10.045.

[131] Andreozzi L, Briccoli Bati S, Fagone M, Ranocchiai G, Zulli F. Analysis of environmental damage consequences on viscous thermo elastic properties of a polymer interlayer. XXI Congr. AIMETA Assoc. Ital. di Mecc. Teor. e Appl., Torino, Italy: 2013.

[132] Andreozzi L, Zulli F, Briccoli Bati S, Fagone M, Ranocchiai G. Weathering of laminated glass – Degradation of interlayer mechanical properties. Challenging Glas. 4 COST Action TU0905 Final Conf., CRC Press; 2014, p. 419–24. doi:10.1201/b16499-61.

[133] Andreozzi L, Briccoli Bati S, Fagone M, Ranocchiai G, Zulli F. Weathering action on thermo-viscoelastic properties of polymer interlayers for laminated glass. Constr Build Mater 2015;98:757–66. doi:10.1016/j.conbuildmat.2015.08.010.

[134] Huntsberger JR. Adhesion of Plasticized Polyvinyl Butyral to Glass. J Adhes 1981;13:107–29.

[135] Vallabhan C, Das YC, Ramasamudra M. Properties of PVB Interlayer Used in

Laminated Glass. J Mater Civ Eng 1992;4:71–6. doi:10.1061/(ASCE)0899-1561(1992)4:1(71).

[136] El-Din NMS, Sabaa MW. Thermal degradation of poly(vinylbutyral) laminated safety glass. Polym Degrad Stab 1995;41:283–8. doi:10.1016/0141-3910(94)00118-R.

[137] Sobek W, Kutterer M, Messmer R. Shear stiffness of the interlayer in laminated glass. Glas. Process. Days, Tampere, Finland: 1999, p. 360–5.

[138] D'Haene P. Flexural Stiffness of Laminated Glass Panels Under Dynamic Conditions. GPD - Glas. Perform. Days, Tampere, Finland: 2003.

[139] Gräf H, Schuler C, Albrecht G, Bucak O. The Influence of Various Support Conditions on the Structural Behaviour of Laminated Glass. Glas Process Days 2003:408–11.

[140] Weller B, Wünsch J, Härth K. Experimental Study on Different Interlayer Materials for Laminated Glass. Glas Process Days 2005:120–3.

[141] Delincé D, Belis J, Zarmati G, Parmentier B. Structural behaviour of laminated glass elements – a step towards standardization. Glas Perform Days 2007:658–63.

[142] Callewaert D, Belis J, Van Impe R, Lagae G, Vanlaere W. Refined test set-up for pure torsion of laminated glass. GPD - Glas. Perform. Days, Tampere, Finland: 2007, p. 118–21.

[143] D'Haene P, Savineau G. Mechanical properties of laminated safety glass - FEM Study. Glas. Perform. Days, 2007, p. 594–8.

[144] Decourcelle R, Nugue JC, Levasseur F. Mechanical participation of interlayer on laminated glass for building applications. Glas Perform Days 2009:718–21.

[145] Briccoli Bati S, Ranocchiai G, Reale C, Rovero L. Time-Dependent Behavior of Laminated Glass. J Mater Civ Eng 2009;22:389–96. doi:10.1061/(ASCE)MT.1943-5533.0000032.

[146] Biolzi L, Cagnacci E, Muciaccia G, Orlando M, Piscitelli LR. Experimental evaluation on long-term behaviour of cold-bent laminated glass. XXVII A.T.I.V. Conf., Parma, Italy: 2014.

[147] Hooper PA, Blackman BRK, Dear JP. The mechanical behaviour of poly (vinyl butyral) at different strain magnitudes and strain rates. J Mater Sci 2012;47:3564–76.

[148] Andreozzi L, Briccoli Bati S, Fagone M, Ranocchiai G, Zulli F. Dynamic torsion tests to characterize the thermo-viscoelastic properties of polymeric interlayers for laminated glass. Constr Build Mater 2014;65:1–13. doi:10.1016/j.conbuildmat.2014.04.003.

[149] Xu X, Liu B, Li Y. Experimental Studies on Viscoelasticity of Film Materials in Laminated Glass Sheets. SAE Int J Mater Manuf 2015;8:2015-01–0709. doi:10.4271/2015-01-0709.

[150] Nawar M, Salim H, Lafta M, Elshihy A. Quasi-Static Performance of Interlayer Systems for Laminated Glass. J Mater Civ Eng 2016;28:04015084. doi:10.1061/(ASCE)MT.1943-5533.0001348.

[151] Brinson HF, Brinson LC. Polymer engineering science and viscoelasticity: An introduction, Second edition. 2015. doi:10.1007/978-1-4899-7485-3.

[152] Qi HJ, Boyce MC. Stress–strain behavior of thermoplastic polyurethanes. Mech Mater 2005;37:817–39. doi:10.1016/j.mechmat.2004.08.001.

[153] Şerban DA, Weber G, Marşavina L, Silberschmidt V V., Hufenbach W. Tensile properties of semi-crystalline thermoplastic polymers: Effects of temperature and strain rates. Polym Test 2013;32:413–25. doi:10.1016/j.polymertesting.2012.12.002.

[154] Denault J, Vu-Khanh T, Foster B. Tensile properties of injection molded long fiber thermoplastic composites. Polym Compos 1989;10:313–21. doi:10.1002/pc.750100507.

[155] van der Vegt AK, Govaert LE. Polymeren : van keten tot kunststof. 2003.

[156] Klompen ETJ. Mechanical properties of solid polymers. Eindhoven University, The Netherlands, 2005.

[157] Hutchinson JM. Physical aging of polymers. Prog Polym Sci 1995;20:703–60. doi:10.1016/0079-6700(94)00001-I.

[158] Behr RA, Minor JE, Norville SH. Structural Behavior of Architectural Laminated Glass. J Struct Eng 1993;119:202–22. doi:10.1061/(ASCE)0733-9445(1993)119:1(202).

[159] Minor JE, Reznik PL, Fellow, ASCE. Failure Strengths of Laminated Glass. J Struct Eng 1990;116:1030–9. doi:10.1061/(ASCE)0733-9445(1990)116:4(1030).

[160] Newmark NM, Siess CP, Viest IM. Tests and analysis of composite beams with incomplete interaction. Proc Soc Exp Stress Anal 1951:75–92.

[161] Reissner E. Finite defections of sandwich plates. J Aeronaut Sci 1948;15:435–40.

[162] Wang C-T. Principle and application of complementary energy method for thin homogeneous and sandwich plates and shells with finite defections. NACA Natl. Advis. Comm. Aeronaut. TN 2620, Washington, D.C.: 1952.

[163] Pister KS, Dong SB. Elastic bending of layered plates. J Engrg Mech Div 1959;85:1–10.

[164] Timoshenko S. History of Strength of Materials: With a Brief Account of the History of Theory of Elasticity and Theory of Structures. Dover Publications; 1953.

[165] Minor JE. Developments in the Design of Architectural Glazing Systems. First Natl. Struct. Eng. Conf. 1987 Prepr. Pap., Institution of Engineers, Australia; 1987, p. 77.

[166] Behr RA, Minor JE, Linden MP. Load Duration and Interlayer Thickness Effects on Laminated Glass. J Struct Eng 1986;112:1441–53. doi:10.1061/(ASCE)0733-9445(1986)112:6(1441).

[167] Vallabhan CVG, Minor JE, Nagalla SR. Stresses in Layered Glass Units and Monolithic Glass Plates. J Struct Eng 1987;113:36–43. doi:10.1061/(ASCE)0733-9445(1987)113:1(36).

[168] Vallabhan CVG, Das YC, Magdi M, Aşık MZ, Bailey JR. Analysis of Laminated Glass Units. J Struct Eng 1993;119:1572–85. doi:10.1061/(ASCE)0733-9445(1993)119:5(1572).

[169] Shutov AI, Novikov IA, Frank AN. Strength of Laminated Safety Glass for Construction Purposes. Glas Ceram 2001;58:368–71. doi:10.1023/a:1012338931087.

[170] Pang S, Ma J, Ma Z, Liu X, Ren S. Correlation Between Temperature and Bending Behavior of Laminated Glass. J Wuhan Univ Technol 2010;22:4.

[171] Louter C, Belis J, Bos F, Callewaert D, Veer F. Experimental investigation of the temperature effect on the structural response of SG-laminated reinforced glass beams. Eng Struct 2010;32:1590–9. doi:10.1016/j.engstruct.2010.02.007.

[172] Pankhardt K, Balázs GL. Temperature dependent load bearing capacity of laminated glass panes. Civ Eng 2010;1:11–22. doi:10.3311/pp.ci.2010-1.02.

[173] Foraboschi P. Analytical model for laminated-glass plate. Compos Part B Eng 2012;43:2094–106. doi:10.1016/j.compositesb.2012.03.010.

[174] Galuppi L, Manara G, Royer Carfagni G. Practical expressions for the design of laminated glass. Compos Part B Eng 2013;45:1677–88. doi:10.1016/j.compositesb.2012.09.073.

[175] Aşık MZ. Laminated glass plates: Revealing of nonlinear behavior. Comput Struct 2003;81:2659–71. doi:10.1016/S0045-7949(03)00325-0.

[176] Aşık MZ, Tezcan S. A mathematical model for the behavior of laminated glass beams. Comput Struct 2005;83:1742–53. doi:10.1016/j.compstruc.2005.02.020.

[177] Aşık MZ, Tezcan S. Laminated glass beams: Strength factor and temperature effect. Comput Struct 2006;84:364–73. doi:10.1016/j.compstruc.2005.09.025.

[178] Aşık MZ, Bayar G. Free Vibration Analysis of the Laminated Curved Glass Beams. 2nd South East Eur. Conf. Comput. Mech., 2009, p. 256–62.

[179] Bedon C, Amadio C, Sinico A. Numerical and analytical investigation on the dynamic buckling behavior of glass columns under blast. Eng Struct 2014;79:322–40. doi:10.1016/j.engstruct.2014.08.024.

[180] Bedon C, Belis J, Luible A. Assessment of existing analytical models for the lateral torsional buckling analysis of PVB and SG laminated glass beams via viscoelastic simulations and experiments. Eng Struct 2014;60:52–67. doi:10.1016/j.engstruct.2013.12.012.

[181] Bedon C, Louter C. Exploratory numerical analysis of SG-laminated reinforced glass beam experiments. Eng Struct 2014;75:457–68. doi:10.1016/j.engstruct.2014.06.022.

[182] Bedon C, Amadio C. Buckling of flat laminated glass panels under in-plane compression or shear. Eng Struct 2012;36:185–97. doi:10.1016/j.engstruct.2011.12.010.

[183] Amadio C, Bedon C. A buckling verification approach for monolithic and laminated glass elements under combined in-plane compression and bending. Eng Struct 2013;52:220–9. doi:10.1016/j.engstruct.2013.02.022.

[184] Bedon C, Louter C. Finite Element analysis of post-tensioned SG-laminated glass beams with adhesively bonded steel tendons. Compos Struct 2017;167:238–50. doi:10.1016/j.compstruct.2017.01.086.

[185] Amadio C, Bedon C. Buckling of laminated glass elements in out-of-plane bending. Eng Struct 2010;32:3780–8. doi:10.1016/j.engstruct.2010.08.022.

[186] Louter C, Cupac J, Lebet J-P. Exploratory experimental investigations on post-tensioned structural glass beams. J Facade Des Eng 2014;2:3–18. doi:10.3233/FDE-130012.

[187] Veer FA, Rijgersberg H, Ruytenbeek D, Louter PC, Zuidema J. Composite Glass Beams, the Third Chapter. Glas Process Days 2003 2003:307–10.

[188] Feirabend S, Sobek W. Reinforced laminated safety glass (original title: Bewehrtes Verbundsicherheitsglas). Stahlbau 2008;77:16–22. doi:10.1002/stab.200810027.

[189] Wellershoff F, Sedlacek G. Structural use of glass in hybrid elements, steel-glass-beams, glass-GFRP-plates. Glas. Process. days, 2003, p. 268–70.

[190] Flinterhoff A. Load carrying behaviour of hybrid steel-glass beams in bending. University of Dortmund, 2003.

[191] Freytag B. Glass-Concrete Composite Technology. Struct Eng Int 2004;14:111–7. doi:10.2749/101686604777963991.

[192] Louter PC. Adhesively bonded reinforced glass beams. Heron 2007;52:31–57.

[193] Feirabend S, Sobek W. Reinforced laminated glass. Challenging Glas. Conf. Archit. Struct. Appl., 2008, p. 469–77.

[194] Palumbo D, Palumbo M, Mazzuchelli M, Schiavon A, Rebeschini A. A New Roof for the XIII th Century " Loggia de Vicari " (Arquà Petrarca -PD – Italy) Based on Structural Glass Trusses : a Case Study. Proc Glas Process Days 2005 2005:1–3.

[195] Speranzini E, Agnetti S. Post-cracking behaviour of reinforced glass beams. Proc COST Action TU 2013;905:285–92.

[196] Correia JR, Valarinho L, Branco FA. Post-cracking strength and ductility of glass-GFRP composite beams. Compos Struct 2011;93:2299–309. doi:10.1016/j.compstruct.2011.03.018.

[197] Speranzini E, Agnetti S. Flexural performance of hybrid beams made of glass and pultruded GFRP. Constr Build Mater 2015;94:249–62. doi:10.1016/j.conbuildmat.2015.06.008.

[198] Kozłowski M, Kadela M, Hulimka J. Numerical Investigation of Structural Behaviour of Timber-Glass Composite Beams. Procedia Eng 2016;161:990–1000. doi:10.1016/j.proeng.2016.08.838.

[199] Koz M, Hulimka J. Load-Bearing Capacity of Hybrid Timber-Glass Beams. Archit Civ Eng Environ 2014;2:61–71.

[200] Kozłowski M. Experimental and numerical analysis of hybrid timber-glass beams. Silesian University of Technology, 2014.

[201] Veer FA, van Liebergen MAC, de Vries SM. Designing and engineering transparent building components with high residual strength. Proc 5th Glas Process Days, Tampere, Finl 1997.

[202] Veer FA, Riemslag AC, Ting CN. Structurally Efficient Glass Laminated Composite Beams. Glas Process Days 2001 2001:363–7.

[203] Louter C, Belis J, Veer F, Lebet JP. Structural response of SG-laminated reinforced glass beams; experimental investigations on the effects of glass type, reinforcement percentage and beam size. Eng Struct 2012;36:292–301.

doi:10.1016/j.engstruct.2011.12.016.

[204] Louter C. Fragile yet ductile, structural aspects of reinforced glass beams. Delft University of Technology; 2011.

[205] Martens K, Caspeele R, Belis J. Performance of statically indeterminate reinforced glass beams – Experimental comparison with determinate systems and effect of a discontinuous glass section. Constr Build Mater 2017;146:251–9. doi:10.1016/j.conbuildmat.2017.03.186.

[206] Martens K, Caspeele R, Belis J. Development of Reinforced & Post-Tensioned Glass Beams - Review. J Struct Eng 2015;142:1–23. doi:10.1061/(ASCE)ST.1943-541X.0001453.

[207] Louter C, Cupac J, Debonnaire M. Structural glass beams prestressed by externally bonded tendons. Glas. Glob. Conf. Proc., 2014, p. 450–9.

[208] Veer FA. 10 years of Zappi research. Proc. Glas. Process. Days, 2005.

[209] Antonelli A, Cagnacci E, Giordano S, Orlando M, Spinelli P. Experimental and Theoretical Analysis of C-FRP Reinforced Glass Beams. ISAAG 2008 - Int. Symp. Appl. Archit. Glas., Munich: 2008.

[210] Cagnacci E, Orlando M, Spinelli P. Experimental investigation on Reinforced Glass Beams. ICCST/7 - Seventh Int. Conf. Compos. Sci. Technol., Sharjah, United Arab Emirates: 2008.

[211] Cagnacci E, Orlando M, Spinelli P. Experimental campaign and numerical simulation of the behaviour of reinforced glass beams. Glas. Perform. Days, Tampere (Fi): 2009, p. 484–7.

[212] Galuppi L, Royer-Carfagni G. Rheology of cold-lamination-bending for curved glazing. Eng Struct 2014;61:140–52. doi:10.1016/j.engstruct.2014.01.003.

[213] Vakar LI, Gaal M. Cold bendable, laminated glass - New possibilities in design. Struct Eng Int J Int Assoc Bridg Struct Eng 2004;14:95–7. doi:10.2749/101686604777963946.

[214] Belis J, Inghelbrecht B, Van Impe R, Callewaert D. Cold bending of laminated glass panels. Heron 2007;52:123–46.

[215] Baraldi D, Cecchi A, Foraboschi P. Broken tempered laminated glass: Non-linear discrete element modeling. Compos Struct 2016;140:278–95. doi:10.1016/j.compstruct.2015.12.050.

[216] Louter C. Bewehrte Glasträger. Stahlbau 2008;77:23–7. doi:10.1002/stab.200810028.

[217] Foraboschi P. Behavior and Failure Strength of Laminated Glass Beams. J Eng Mech 2007;133:1290–301. doi:10.1061/(ASCE)0733-9399(2007)133:12(1290).

[218] Oda J, Toru T, Yamamoto H. A Study on Impact Strength of Laminated Glass with Initial Crack. Trans Japan Soc Mech Eng Ser A 2000;66:1308–13. doi:10.1248/cpb.37.3229.

[219] Xu J, Sun Y, Liu B, Zhu M, Yao X, Yan Y, et al. Experimental and macroscopic investigation of dynamic crack patterns in PVB laminated glass sheets subject to light-weight impact. Eng Fail Anal 2011;18:1605–12. doi:10.1016/j.engfailanal.2011.05.004.

[220] Xu X, Xu J, Chen J, Li P, Liu B, Li Y. Investigation of dynamic multi-cracking behavior in PVB laminated glass plates. Int J Impact Eng 2017;100:62–74. doi:10.1016/j.ijimpeng.2016.10.013.

[221] Huang X, Liu Q, Liu G, Zhou Z, Li G. Experimental investigation of multi-layered laminated glass beams under in-plane bending. Struct Eng Mech 2016;60:781–94. doi:10.12989/sem.2016.60.5.781.

[222] Ali A, Hosseini M, Sahari BB. A review and comparison on some rubber elasticity models. J Sci Ind Res (India) 2010;69:495–500.

[223] Viola E. Scienza delle costruzioni. Pitagora; 1990.

[224] Treloar LRG. The physics of rubber elasticity. Oxford University Press, USA; 1975.

[225] Steinmann P, Hossain M, Possart G. Hyperelastic models for rubber-like materials: Consistent tangent operators and suitability for Treloar's data. Arch Appl Mech

2012;82:1183–217. doi:10.1007/s00419-012-0610-z.

[226] Nunes LCS. Mechanical characterization of hyperelastic polydimethylsiloxane by simple shear test. Mater Sci Eng A 2011;528:1799–804. doi:10.1016/j.msea.2010.11.025.

[227] Bower AF. Applied Mechanics of Solids. CRC Press; 2009.

[228] Yeoh OH. Some Forms of the Strain Energy Function for Rubber. Rubber Chem Technol 1993;66:754–71. doi:10.5254/1.3538343.

[229] Moreira DC, Nunes LCS. Comparison of simple and pure shear for an incompressible isotropic hyperelastic material under large deformation. Polym Test 2013;32:240–8. doi:10.1016/j.polymertesting.2012.11.005.

[230] Tobajas R, Ibartz E, Gracia L. A comparative study of hyperelastic constitutive models to characterize the behavior of a polymer used in automotive engines. Proc 2nd Int Electron Conf Mater 2016:A002. doi:10.3390/ecm-2-A002.

[231] Rivlin RS, Saunders DW. Large Elastic Deformations of Isotropic Materials. Collect. Pap. R.S. Rivlin, New York, NY: Springer New York; 1997, p. 157–94. doi:10.1007/978-1-4612-2416-7_12.

[232] Sadd MH. Elasticity: theory, applications, and numerics. Academic Press; 2009.

[233] Attard MM. Finite strain - isotropic hyperelasticity. Int J Solids Struct 2003;40:4353–78. doi:10.1016/S0020-7683(03)00217-8.

[234] Hackett RM. Hyperelasticity Primer. Cham: Springer International Publishing; 2016. doi:10.1007/978-3-319-23273-7.

[235] Mooney M. A Theory of Large Elastic Deformation. J Appl Phys 1940;11:582–92. doi:10.1063/1.1712836.

[236] Ogden RW. Large Deformation Isotropic Elasticity - On the Correlation of Theory and Experiment for Incompressible Rubberlike Solids. Proc R Soc A Math Phys Eng Sci 1972;326:565–84. doi:10.1098/rspa.1972.0026.

[237] Bergstrom JS. Mechanics of solid polymers: theory and computational modeling. William Andrew; 2015.

[238] Christensen R. Theory of viscoelasticity: an introduction. Elsevier; 2012.

[239] Perzyna P. Fundamental Problems in Viscoplasticity, 1966, p. 243–377. doi:10.1016/S0065-2156(08)70009-7.

[240] Landel RF, Nielsen LE. Mechanical properties of polymers and composites. Crc Press; 1993.

[241] Roylance D. Mechanics of materials. New York: Wiley; 1996.

[242] Simo JC, Hughes TJR. Computational inelasticity. vol. 7. Springer Science & Business Media; 2006.

[243] Gant FS, Bower MV. Domain of Influence Method: A New Method for Approximating Prony Series Coefficients and Exponents for Viscoelastic Materials. J Polym Eng 1997;17:1–22. doi:10.1515/POLYENG.1997.17.1.1.

[244] Soussou JE, Moavenzadeh F, Gradowczyk MH. Application of Prony Series to Linear Viscoelasticity. Trans Soc Rheol 1970;14:573–84. doi:10.1122/1.549179.

[245] Cost TL, Becker EB. A multidata method of approximate Laplace transform inversion. Int J Numer Methods Eng 1970;2:207–19.

[246] Bradshaw RD, Brinson LC. A Sign Control Method For Fitting And Interconverting Material Functions For Linearly Viscoelastic Solids "A Sign Control Method for Fitting and Interconverting Material Functions for Linear Viscoelastic Solids Introduction and Background. Mech Time Dep Matls 1997;1:85–108. doi:10.1023/A:1009772018066.

[247] Tzikang C. Determining Viscoelastic Strain Data a Prony Material Series for a From Time Varying. US Army Res Lab Veh Technol Dir Langley Res Center, Hampton, Virginia 2000.

[248] Park SW, Kim YR. Fitting Prony-Series Viscoelastic Models with Power-Law Presmoothing. J Mater Civ Eng 2001;13:26–32. doi:10.1061/(ASCE)0899-1561(2001)13:1(26).

[249] Tarefder RA, Rahman ASMA, University of New Mexico A, Center SUT, Technology O of the AS for R and, Transportation ND of, et al. Interconversion of Dynamic Modulus to Creep Compliance and Relaxation Modulus: Numerical Modeling and Laboratory Validation - Final Report 2016:61p.

[250] Schapery RA, Park SW. Methods of interconversion between linear viscoelastic material functions. Part II—an approximate analytical method. Int J Solids Struct 1999;36:1677–99.

[251] Park SW, Schapery RA. Methods of interconversion between linear viscoelastic material functions. Part I—A numerical method based on Prony series. Int J Solids Struct 1999;36:1653–75.

[252] Mun S, Chehab GR, Kim YR. Determination of Time-domain Viscoelastic Functions using Optimized Interconversion Techniques. Road Mater Pavement Des 2007;8:351–65. doi:10.1080/14680629.2007.9690078.

[253] Rouse PE. A Theory of the Linear Viscoelastic Properties of Dilute Solutions of Coiling Polymers. J Chem Phys 1953;21:1272–80. doi:10.1063/1.1699180.

[254] Williams ML, Landel RF, Ferry JD. The Temperature Dependence of Relaxation Mechanisms in Amorphous Polymers and Other Glass-forming Liquids. J Am Chem Soc 1955;77:3701–3707. doi:10.1021/ja01619a008.

[255] Save MA, Massonnet CE. Plastic analysis and design of plates, shells and disks 1972.

[256] Służalec A. Theory of Metal Forming Plasticity. Berlin, Heidelberg: Springer Berlin Heidelberg; 2004. doi:10.1007/978-3-662-10449-1.

[257] Bailey D. Ductile Fracture 1997;73:2003.

[258] Mirkhalaf SM, Andrade Pires FM, Simoes R. An elasto-viscoplastic constitutive model for polymers at finite strains: Formulation and computational aspects. Comput Struct 2016;166:60–74. doi:10.1016/j.compstruc.2016.01.002.

[259] Irgens F. Continuum mechanics. Springer Science & Business Media; 2008.

[260] CEN. EN ISO 12543-4, Glass in building. Laminated glass and laminated safety glass. Part 4: Test methods for durability. 2011.

[261] Biolzi L, Cagnacci E, Orlando M, Piscitelli LR. Laminated glass specimen under long-term push-out loads. XXVII A.T.I.V. Conf., 2012, p. 95–100.

[262] Cottone A, Giambanco G, Spada A. Valutazione della resistenza di adesione e della lunghezza efficace di incollaggio nei giunti adesivi tramite le leggi dell'effetto scala. XVIII GIMC Conf 2010:1–4.

[263] Moore DR, Turner S. Mechanical Evaluation Strategies for Plastics. Elsevier Science; 2001.

[264] International Organization for Standardization. ISO 527:2012 Plastics - Determination of tensile properties. Genève, CH: 2012.

[265] Weber F. Curved glass structures. GPD - Glas. Perform. Days, 2009, p. 375–80.

[266] Ensslen F. Influences of weathering on the durability of laminated safety glass. Int. Symp. Appl. Archit. Glas., Munich: 2006, p. 183–94.

[267] Wurm J. Glass Structures. Birkhauser; 2007.

[268] O'Regan C. Structural use of glass in buildings (Second edition) - The Institution of Structural Engineers. 2014.

[269] Hai ND, Mutsuyoshi H. Structural behavior of double-lap joints of steel splice plates bolted/bonded to pultruded hybrid CFRP/GFRP laminates. Constr Build Mater 2012;30:347–59. doi:10.1016/j.conbuildmat.2011.12.001.

[270] Visser R. Residual lifetime assessment of uPVC gas pipes. Enschede, Netherland: 2009. doi:10.3990/1.9789036529587.

[271] Morris JW. Laminating techniques 1966.

[272] Benedictus E. Verre feuilleté de sécurité Triplex (registered November 25, 1909). 405,881, 1906.

[273] Overend M, Zammit K. A computer algorithm for determining the tensile strength of float glass. Eng Struct 2012;45:68–77. doi:10.1016/j.engstruct.2012.05.039.

[274] Brown WG, Research NRCCD of B. A Practicable Formulation for the Strength of Glass and Its Special Application to Large Plates. National Research Council Canada; 1974.

[275] Beason WL, Research TTUI for D, (U.S.) NSF. A Failure Prediction Model for Window Glass. NTIS; 1980.

[276] Technology S of G, Gesellschaft DG. Glass Technology. The Society; 1985.

[277] Pagano NJ. Stress fields in composite laminates. Int J Solids Struct 1978;14:385–400. doi:10.1016/0020-7683(78)90020-3.

[278] BS EN 572-9. 2004.

[279] DIN 53457. 1987.

[280] Charlton DJ, Yang J, Teh KK. A Review of Methods to Characterize Rubber Elastic Behavior for Use in Finite Element Analysis. Rubber Chem Technol 1994;67:481–503. doi:10.5254/1.3538686.

[281] Luible A. Stabilität von Tragelementen aus Glas 2004;3014:264. doi:10.5075/epfl-thesis-3014.

[282] Yang LM, Shim VPW, Lim CT. A visco-hyperelastic approach to modelling the constitutive behaviour of rubber. Int J Impact Eng 2000;24:545–60. doi:10.1016/S0734-743X(99)00044-5.

[283] Kott A, Vogel T. Safety of laminated glass structures after initial failure. IABSE Symp Rep 2004;88:67–72. doi:10.2749/222137804796302563.

[284] Lenci S, Clementi F, Warminski J. Nonlinear free dynamics of a two-layer composite beam with different boundary conditions. Meccanica 2015;50:675–88. doi:10.1007/s11012-014-9945-6.

[285] Ivanov I V., Velchev DS, Sadowski T, Kneć M. Computational Models of Laminated Glass Plate under Transverse Static Loading (in: Altenbach H, Eremeyev V (eds) Shell-Like Structures Non-classical Theories and Applications). Adv Struct Mater Springer Berlin 2011:469–90. doi:10.1007/978-3-642-21855-2.

[286] Jia Z, Hui D, Yuan G, Lair J, Lau K, Xu F. Mechanical properties of an epoxy-based adhesive under high strain rate loadings at low temperature environment. Compos Part B Eng 2016;105:132–7. doi:10.1016/j.compositesb.2016.08.034.

[287] Chiu WK, Chalkley PD, Jones R. Effects of temperature on the shear stress-strain behaviour of structural adhesives (FM73). Comput Struct 1994;53:483–9. doi:10.1016/0045-7949(94)90095-7.

[288] Jia Z, Yuan G, Ma H, Hui D, Lau K. Tensile properties of a polymer-based adhesive at low temperature with different strain rates. Compos Part B Eng 2016;87:227–32. doi:10.1016/j.compositesb.2015.10.013.

[289] Giboreau A, Cuvelier G, Launay B. Rheological behaviour of three biopolymer/water systems,with emphasis on yield stress and viscoelastic properties. J Texture Stud 1994;25:119–38. doi:10.1111/j.1745-4603.1994.tb01321.x.

[290] Kolednik O. The yield stress gradient effect in inhomogeneous materials. Int J Solids Struct 2000;37:781–808. doi:10.1016/S0020-7683(99)00060-8.

[291] Premamoy G. Polymer Science and Techology of Plastics and Rubbers. New Delhi: McGraw-Hill; 1990.

[292] Graessley WW. The entanglement concept in polymer rheology. Entanglement Concept Polym. Rheol., Berlin/Heidelberg: Springer-Verlag; n.d., p. 1–179. doi:10.1007/BFb0031037.

[293] Elzière P, Dalle-Ferrier C, Creton C, Barthel É, Ciccotti M. Large strain viscoelastic dissipation during interfacial rupture in laminated glass. Soft Matter 2017;13:1624–33. doi:10.1039/C6SM02785G.

[294] Mittal KL, Kern W. Selected bibliography on adhesion measurement of films and coatings. J Adhes Sci Technol 1987;1:247–62. doi:10.1163/156856187X00265.

[295] Mittal KL. Adhesion Measurement of Thin Films, Thick Films, and Bulk Coatings. 100 Barr Harbor Drive, PO Box C700, West Conshohocken, PA 19428-2959: ASTM International; 1978. doi:10.1520/STP640-EB.

[296] Young WC, Budynas RG. Roark's formulas for stress and strain. New York: 2002.

[297] UNI EN 12150: Vetro di silicato-calcico di sicurezza temperato termicamente. 2015.

[298] Ministero delle Infrastrutture e dei Trasporti. NTC - Norme Tecniche per le Costruzioni (GU n. 29 04/02/2008 - Suppl. Ordinario n. 30), 2008.

[299] Ministero delle Infrastrutture e dei Trasporti. circolare applicativa del 2 febbraio 2009 , n. 617 per le "NTC - Norme Tecniche per le Costruzioni" (GU n.47 26/02/2009 - Suppl. Ordinario n.27). 2009.

[300] PREN 16612:2013 - Glass In Building - Determination Of The Load Resistance Of Glass Panes By Calculation And Testing. Comite Europeen de Normalisation; 2013.

[301] Palmgren AZ. Die Lebensdauer von Kugellagcrn. Z Ver Deutsch Ing 1924;68:339.

[302] Miner MA. Cumulative Damage in Fatigue. J Appl Mech 1945;12:159.

[303] CEN. FprEN 16613:2016 Glass in building - Laminated glass and laminated safetu glass - Determination of interlayer mechanical properties 2016.

[304] James AG, Green A, Simpson GM. Strain Energy Function of Rubber. I. Characterization of Gum Vulcanizates. J Appl Polim Sci 1975;19:2033–58. doi:10.1002/app.1975.070190723.

[305] Ericksen JL. Theoretical elasticity. Bull Am Math Soc 1955;61:362–4.

[306] Kott A, Vogel T. Remaining structural capacity of broken laminated safety glass. Proc. 8th Int. Conf. Archit. Automot. Glas. (Glass Process. Days), Tampere, Finl., 2003, p. 403–7.

[307] Belis J, Depauw J, Callewaert D, Delincé D, Van Impe R. Failure mechanisms and residual capacity of annealed glass/SGP laminated beams at room temperature. Eng Fail Anal 2009;16:1866–75. doi:10.1016/j.engfailanal.2008.09.023.

[308] Hagl A. Experimental and Numerical Analysis of Edge Seal Spacers of Insulated Glass Units for Structural Sealant Glazing Applications 2012.

[309] Baldridge DB. Laminated glass having electrically operated instrument indicator means embedded in the interlayer. US003317906A, 1964.

[310] Kenichi A, Naoki U, Hirofumi O. Interlayers for use in sound-insulating laminated glasses. US005190826A, 1993.

[311] Klafka G, Wieme R. Interlayer structure for laminated glass. US006451435B1, 2002.

[312] Aben H, Anton J, Õis M, Viswanathan K, Chandrasekar S, Chaudhri MM. On the extraordinary strength of Prince Rupert's drops. Appl Phys Lett 2016;109:231903. doi:10.1063/1.4971339.

[313] Hugh Chisholm, editor. The Encyclopaedia Britannica: A Dictionary of Arts, Sciences, Literature and General Information (11th edition). Philadelphia: Encyclopaedia Britannica Company; 1910.

[314] Cathers WP, Ferretti JS. Vacuum channel method of laminating glass sheets 1983.

[315] Moran JR. No autoclave process for forming a safety glass laminate 1996.

[316] Meneguzzo F, Ciriminna R, Albanese L, Pagliaro M. The great solar boom: a global perspective into the far reaching impact of an unexpected energy revolution. Energy Sci Eng 2015;3:499–509. doi:10.1002/ese3.98.

[317] Liao S-H, Jhuo H-J, Yeh P-N, Cheng Y-S, Li Y-L, Lee Y-H, et al. Single Junction Inverted Polymer Solar Cell Reaching Power Conversion Efficiency 10.31% by Employing Dual-Doped Zinc Oxide Nano-Film as Cathode Interlayer, 2015. doi:10.1038/srep06813.

[318] Thompson BB, D'Errico JJ. Polymer interlayers comprising uv absorbers 2015.

[319] Kurtz S. Progress and Strategies for Testing of Materials for Solar Panels, Shangai, China: 2017.

[320] Tripathy AR, Chen W, Kukureka SN, MacKnight WJ. Novel poly(butylene terephthalate)/poly(vinyl butyral) blends prepared by in situ polymerization of cyclic poly(butylene terephthalate) oligomers. Polymer (Guildf) 2003;44:1835–42. doi:10.1016/S0032-3861(03)00029-6.

[321] Alvarez G, Flores JJ, Aguilar JO, Gómez-Daza O, Estrada CA, Nair MTS, et al.

Spectrally selective laminated glazing consisting of solar control and heat mirror coated glass: preparation, characterization and modelling of heat transfer. Sol Energy 2005;78:113–24. doi:10.1016/j.solener.2004.06.021.

[322] Kuhn TS. The Structure of Scientific Revolutions. vol. II. 1970. doi:10.1119/1.1969660.

[323] Wölfel E. Nachgiebiger Verbund Eine Näherungslösung und deren Anwendungsmöglichkeiten. Stahlbau 1987;56:173–80.

[324] Nonlinear Viscoelasticity. Polym. Eng. Sci. Viscoelasticity, Boston, MA: Springer US; 2008, p. 327–64. doi:10.1007/978-0-387-73861-1_10.

[325] Koutsawa Y, Daya EM. Static and free vibration analysis of laminated glass beam on viscoelastic supports. Int J Solids Struct 2007;44:8735–50. doi:10.1016/j.ijsolstr.2007.07.009.

[326] Galuppi L, Royer-Carfagni G. The effective thickness of laminated glass: Inconsistency of the formulation in a proposal of EN-standards. Compos Part B Eng 2013;55:109–18. doi:10.1016/j.compositesb.2013.05.025.

[327] El-Shami MM, Norville SH, Ibrahim YE. Stress analysis of laminated glass with different interlayer materials. Alexandria Eng J 2012;51:61–7. doi:10.1016/j.aej.2012.07.008.

[328] Molnár G, Vigh LG, Stocker G, Dunai L. Finite element analysis of laminated structural glass plates with polyvinyl butyral (PVB) interlayer. Period Polytech Civ Eng 2012;56:35–42. doi:10.3311/pp.ci.2012-1.04.

[329] Pelayo F, Lopez-Aenlle M, Ismael G, Fernandez-Canteli A. Buckling of multilayered laminated glass beams: Validation of the effective thickness concept. Compos Struct 2017;169:2–9. doi:10.1016/j.compstruct.2017.01.040.

[330] Gräf H, Albrecht G, Sackmann V, Schuler C, Bucak Ö. Structural behaviour of point-supported and clamped laminated glass. Struct Eng Int 2004;14:129–33.

[331] Freddi F, Royer-Carfagni G, Silvestri M. Full-Scale Experiments for Point-Fixing Frameless Laminated Glass. Int J Appl Glas Sci 2010;1:257–72. doi:10.1111/j.2041-1294.2010.00028.x.

[332] Pottmann H, Schiftner A, Bo P, Schmiedhofer H, Wang W, Baldassini N, et al. Freeform surfaces from single curved panels. ACM Trans Graph 2008;27:76. doi:10.1145/1360612.1360675.

[333] Schiftner A, Baldassini N, Bo P, Pottmann H. Architectural freeform structures from single curved panels. Adv Archit Geom 2008;3:45–8.

[334] Eigensatz M, Kilian M, Schiftner A, Mitra NJ, Pottmann H, Pauly M. Paneling architectural freeform surfaces. ACM Trans Graph 2010;29:45. doi:10.1145/1778765.1778782.

[335] Press WH, Flannery BP, Teukolsky SA, Vetterling WT. Numerical recipes. vol. 3. cambridge University Press, cambridge; 1989.

[336] Boyce MC, Parks DM, Argon AS. Large inelastic deformation of glassy polymers. Part I: rate dependent constitutive model. Mech Mater 1988;7:15–33.

[337] Arruda EM, Boyce MC. A three-dimensional constitutive model for the large stretch behavior of rubber elastic materials. J Mech Phys Solids 1993;41:389–412.

[338] Wu PD, Van Der Giessen E. On improved network models for rubber elasticity and their applications to orientation hardening in glassy polymers. J Mech Phys Solids 1993;41:427–56.

[339] Ghorbel E. A viscoplastic constitutive model for polymeric materials. Int J Plast 2008;24:2032–58. doi:10.1016/j.ijplas.2008.01.003.

[340] Van Dommelen JAW, Parks DM, Boyce MC, Brekelmans WAM, Baaijens FPT. Micromechanical modeling of the elasto-viscoplastic behavior of semi-crystalline polymers. J Mech Phys Solids 2003;51:519–41. doi:10.1016/S0022-5096(02)00063-7.

[341] Parks DM, Ahzi S. Polycrystalline plastic deformation and texture evolution for crystals lacking five independent slip systems. J Mech Phys Solids 1990;38:701–24.

[342] Nikolov S, Doghri I. A micro/macro constitutive model for the small-deformation behavior of polyethylene. Polymer (Guildf) 2000;41:1883–91.

[343] Drozdov AD, Gupta RK. Non-linear viscoelasticity and viscoplasticity of isotactic polypropylene. Int J Eng Sci 2003;41:2335–61.

[344] Drabousky DP, Dwight D. Prony series representation and interconversion of viscoelastic material functions of equine cortical bone. Case Western Reserve University, 2009.

[345] Sarva SS, Deschanel S, Boyce MC, Chen W. Stress–strain behavior of a polyurea and a polyurethane from low to high strain rates. Polymer (Guildf) 2007;48:2208–13. doi:10.1016/j.polymer.2007.02.058.

[346] Blatz PJ, Ko WL. Application of Finite Elastic Theory to the Deformation of Rubbery Materials. Trans Soc Rheol 1962;6:223–52. doi:10.1122/1.548937.

[347] Bourcier DP, Koran FA, Crommen JHL. Glass Lamination Process, 2003.

[348] Treloar LRG. The elasticity of a network of long-chain molecules. I. Trans Faraday Soc 1943:36–41.

[349] Yeoh OH. Characterization of Elastic Properties of Carbon-Black-Filled Rubber Vulcanizates. Rubber Chem Technol 1990;63:792–805. doi:10.5254/1.3538289.

[350] Clay SB. Characterization of crazing properties of polycarbonate. Blacksburg, Virginia, 2000.